Doctoral theses at NTNU, 2020:237

Kun Xu

Design and Analysis of Mooring Systems for Semi-submersible Floating Wind Turbines in Shallow Water

Doctoral Thesis

NTNU
Norwegian University of Science and Technology

Kun Xu

Doctoral Thesis

Doctoral theses at NTNU, 2020:237

NTNU
Norwegian University of
Science and Technology
Faculty of Engineering
Department of MarineTechnology

NTNU

ISBN 978-82-326-4822-1 (printed version)
ISBN 978-82-326-4823-8 (electronic version)
ISSN 1503-8181

NTNU
Norwegian University of
Science and Technology

Kun Xu

Design and Analysis of Mooring Systems for Semi-submersible Floating Wind Turbines in Shallow Water

Thesis for the degree of Philosophiae Doctor

Trondheim, September 2020

Norwegian University of Science and Technology
Faculty of Engineering
Department of MarineTechnology

NTNU
Norwegian University of
Science and Technology

NTNU
Norwegian University of Science and Technology

Thesis for the degree of Philosophiae Doctor

Faculty of Engineering
Department of MarineTechnology

© Kun Xu

ISBN 978-82-326-4822-1 (printed version)
ISBN 978-82-326-4823-8 (electronic version)
ISSN 1503-8181

Doctoral theses at NTNU, 2020:237

Printed by Skipnes Kommunikasjon as

Abstract

Floating wind turbines are necessary to produce power from wind in deeper water where bottom-fixed wind turbines are not economically competitive. However, it is still not clear to which water depth a floating wind turbine is cheaper than a bottom-fixed one. The semi-submersible is an attractive floating concept with wide applicable range of water depths because of its small draft. The thesis deals with the challenge of designing mooring system for semi-submersible floating wind turbine in shallow water, including a study of different hydrodynamic load models for shallow water conditions, especially with respect to the higher order wave effects based on second-order and fully nonlinear wave theories.

While significant efforts have been made on design of mooring systems for offshore structures in deep water, there has been quite limited study on mooring system design for floating wind turbines in shallow water especially when the water depth is around 50 m to 80 m. Therefore, one of the focuses in this thesis is to study the mooring line behavior in different water depths and propose feasible mooring design concepts for semi-submersible floating wind turbines in shallow water. In this connection, different mooring line materials like chain and synthetic fibre rope, mooring components like clump weight and buoy, anchors like drag embedment anchor and suction anchor are used. The nonlinear material behavior of synthetic fibre rope is described with the state-of-the-art numerical model - 'Syrope'. Based on numerical analysis in serviceability and ultimate limit state conditions, the performance of different mooring designs are compared from a number of perspectives: static performance, dynamic response as well as capital costs etc. Second-order difference-frequency wave effect is considered while sum-frequency effect is neglected in view of the relevant large natural periods of the mooring systems considered. For taut mooring made of fibre rope, the mooring line tension increases linearly as offset increases. Meanwhile, the tension increases nonlinearly for catenary mooring made of chain as offset increases and the nonlinear increment is more significant in shallow water than deep water. It is found in this study that a taut mooring consisting of pure fibre rope, and a catenary mooring consisting of chain with additional clump weight and buoy are recommendable concepts.

Calculation of second-order difference-frequency wave load effect in shallow water based on Newman's approximation method and full quadratic transfer function (QTF) method are compared and it is found that it is important to apply the full QTF method in shallow water. While the effect of nonlinear wave kinematics is not significant for small waves and deep water, it becomes important for large wave and shallow water. Due to the difficulty and excessive computational costs of analyzing fully nonlinear wave-structure interaction which deals with fully nonlinear free surface conditions and body boundary conditions, the state-of-the-art method is to generate the wave trains in a separate numerical wave tank, which neglects the effect of the presence of the structure on the wave field. In this study, the wave realizations are generated in a 2D Harmonic Polynomial Cell (HPC) wave tank with horizontal flat seabed. The coupled dynamic response analysis is then performed based on the imported wave kinematics data in HAWC2 where the hydrodynamic load is calculated using Morison's equation and the wave kinematic is integrated up to the instantaneous wave surface. To increase the computational efficiency, the wave kinematics data generated from 2D HPC wave tank is approximated by polynomial fitting method before being imported into HAWC2 for determination of wave loads. The link between wave kinematics database and HAWC2 is extended from one dimensional case which is limited to bottom-fixed structure to two dimensional case which is applicable for floating structure as well. The whole numerical code package has been verified against stream function wave and linear Airy wave. In the end, fully nonlinear irregular wave trains are applied in the dynamic analysis to study the effect of wave nonlinearity on the floater motion, internal structural tower force and mooring line tension for different load cases. The results not only demonstrate the importance of considering wave nonlinearity effect in hydrodynamic analysis in shallow water but also prove the applicability and efficiency of the proposed numerical tool.

Preface

This thesis is submitted to the Norwegian University of Science and Technology (NTNU) for partial fulfilment of the requirements for the degree of philosophiae doctor.

This doctoral work has been performed at Department of Marine Technology, NTNU, Trondheim. Professor Torgeir Moan from Department of Marine Technology, NTNU is the main supervisor. Professor Zhen Gao from Department of Marine Technology, NTNU and Associate Professor Yanlin Shao from Department of Mechanical Engineering, DTU are the co-supervisors.

The work was financially supported by a scholarship from China Scholarship Council (CSC) from July 2016 to June 2018 and a scholarship from Department of Marine Technology, NTNU from June 2018 to August 2019, which are greatly appreciated. The financial support from the Norwegian Ship-owners' Association Fund and Equinor to attend academic conferences are also acknowledged.

Acknowledgement

It is not the destination, it is the journey that matters. My PhD journey would have been impossible without the help and support from many people.

First of all, I would like to express my sincere gratitude to my main supervisor Prof. Torgeir Moan. He not only offered me the opportunity to pursue my PhD study but also provided me with his remarkable experience and knowledge on my research work. I learnt from him how to systematically solve problems as well as being critical about the results.

I would like to extend my gratitude to my co-supervisor Prof. Zhen Gao. During the PhD study, he was always there to give me support and answer my questions. He set a perfect example for me regarding how to become an independent researcher.

I would also like to thank my co-supervisor Prof. Yanlin Shao. Getting him involved is definitely a turning point for my PhD study when exciting results started to come out. His generosity in sharing his expertise gave me a lot of inspirations when things did not work.

I am thankful to Prof. Min Zhang for her great collaboration and valuable discussion during her stay in Trondheim. The encouragement I received from her motivated me to move forward.

I also greatly appreciate the help from Prof. Kjell Larsen. He contributed a lot of his time and expertise on my PhD study. His constructive advice was very influential to me.

Many thanks go to Prof. Erin Bachynski for her kind ideas and suggestions when I was stuck with software. The help means a lot to me.

I would like to appreciate the time and work of my thesis committee members: Prof. Lars Johanning, Assoc. Prof. Madjid Karimirad and Prof. Svein Sævik.

I also would like to acknowledge my dear friends and colleagues who accompany me through all the days and nights in Trondheim. All the support and memory have become the highlights of my life.

Finally, I want to express my deep gratitude to my family: my parents, sister and brother-in-law. Your love and understanding means everything to me.

List of Appended Papers

This thesis consists of an introductory part and five papers, which are appended.

Paper 1:
Design and comparative analysis of alternative mooring systems for floating wind turbines in shallow water with emphasis on ultimate limit state design.
Authors: Kun Xu, Kjell Larsen, Yanlin Shao, Min Zhang, Zhen Gao, Torgeir Moan
Submitted to *Ocean Engineering*, 2020

Paper 2:
Effect of hydrodynamic load modelling on the response of floating wind turbines and its mooring system in small water depths.
Authors: Kun Xu, Zhen Gao, Torgeir Moan
Published in *Journal of Physics: Conference Series*, 2018
DOI: 10.1088/1742-6596/1104/1/012006

Paper 3:
Fully nonlinear wave effect on a semi-submersible floating wind turbine using wave kinematics from 2D Harmonic Polynomial Cell wave tank.
Authors: Kun Xu, Yanlin Shao, Zhen Gao, Torgeir Moan
Published in *Proceedings of the 3rd International Conference on Offshore Renewable-energy (CORE 2018)*, Glasgow, United Kingdom, August 29-30, 2018

Paper 4:
A study on fully nonlinear wave load effects on floating wind turbine.
Authors: Kun Xu, Yanlin Shao, Zhen Gao, Torgeir Moan
Published in *Journal of Fluids and Structures*, 2019
DOI: https://doi.org/10.1016/j.jfluidstructs.2019.05.008

Paper 5:
Effect of wave nonlinearity on fatigue damage and extreme responses of a semi-submersible floating wind turbine.
Authors: Kun Xu, Min Zhang, Yanlin Shao, Zhen Gao, Torgeir Moan
Published in *Applied Ocean Research*, 2019
DOI: https://doi.org/10.1016/j.apor.2019.101879

Declaration of authorship

All the five papers that serve as the core content of this thesis are co-authored. In all these papers, I was the first author and responsible for initiating ideas, performing the analysis and calculations, providing the results and writing the papers. Professor Torgeir Moan and Professor Zhen Gao have contributed to all the papers regarding the support, corrections and constructive comments to increase the scientific quality of the publications. Professor Yanlin Shao contributed with his expertise of the 2D HPC numerical wave tank in Paper 3, 4 & 5 as well as industrial insight of fibre rope in Paper 1. Professor Min Zhang performed the fatigue analysis in Paper 5 and offered helpful discussions for Paper 1. Professor Kjell Larsen was involved in Paper 1 by providing important knowledge regarding the experimental data of synthetic fibre rope.

Abbreviations

ACER	Average Conditional Exceedance Rate
AHV	Anchor Handling Vessel
ALS	Accidental Limit State
BEM	Blade Element Momentum
BFWT	Bottom-Fixed Wind Turbine
CFD	Computational Fluid Dynamics
DEA	Drag Embedment Anchor
DLL	Dynamic Link Library
DOF	Degree of Freedom
EU	European Union
EWEA	The European Wind Energy Association
FEM	Finite Element Method
FLS	Fatigue Limit State
FSBC	Free Surface Bouncary Condition
FWT	Floating Wind Turbine
GWEC	Global Wind Energy Council
HAWC2	Horizontal Axis Wind turbine simulation Code 2nd generation
HPC	Harmonic Polynomial Cell

IEA	International Energy Agency
LCCA	Life Cycle Cost Analysis
LCOE	Levelised Cost of Electricity
NOWITECH	Norwegian Research Centre for Offshore Wind Technology
NWT	Numerical Wave Tank
OC4	Offshore Code Comparison Collaboration Continuation
QTF	Quadratic Transfer Function
RAO	Response Amplitude Operator
SIMA	Simulation of Marine Application
SWL	Still Water Level
TLP	Tension Leg Platform
TRL	Technology Readiness Level
ULS	Ultimate Limit State

Contents

List of Tables **xvii**

List of Figures **xix**

1 Introduction **1**
- 1.1 Background and motivation 1
- 1.2 Semi-submersible floating wind turbine 6
- 1.3 Review of research work on mooring system design and coupled analysis in shallow water 8
- 1.4 Challenges & objectives 11
- 1.5 Thesis outline 15

2 Design of mooring system in shallow water **17**
- 2.1 Guidelines and standards for mooring system 18
- 2.2 Introduction of mooring system and components 19
  - 2.2.1 Mooring configuration 19
  - 2.2.2 Mooring anchor 19
  - 2.2.3 Mooring line 22
  - 2.2.4 Mooring component 23
  - 2.2.5 Mooring connector 24
- 2.3 Design criteria 25
- 2.4 Design challenges for shallow water conditions 25
- 2.5 Mooring design concept proposals in shallow water 31

3 Numerical modelling and analysis method **35**
- 3.1 General 35
- 3.2 Aerodynamics 35
- 3.3 Hydrodynamics 37
  - 3.3.1 Wave theory 37
    - 3.3.1.1 Linear wave theory 39

3.3.1.2 Fully nonlinear wave theory 39
3.3.2 Wave kinematics 41
3.3.2.1 Wave generation 41
3.3.2.2 Polynomial fitting method 43
3.3.3 Hydrodynamic load modelling 46
3.3.3.1 Radiation/diffraction theory 47
3.3.3.2 Morison's equation 49
3.3.3.3 Computational fluid dynamics 49
3.4 Mooring dynamics 50
3.5 Fully coupled analysis method 53
3.5.1 Numerical tools 54
3.6 Fatigue damage calculation 57
3.7 Extreme value prediction 57

4 Coupled analysis results 63
4.1 General 63
4.2 Design load case 63
4.3 Performance comparison of mooring designs for floating wind turbine in shallow water 66
4.3.1 Static analysis 66
4.3.2 Decay analysis 69
4.3.3 Dynamic analysis 70
4.3.4 Cost analysis 72
4.3.5 Conclusion and recommendation 74
4.4 Second-order wave load effect 75
4.5 Fully nonlinear wave effect 76
4.5.1 Verification - regular wave 79
4.5.2 Comparison - irregular wave 83
4.5.2.1 Wave realization 85
4.5.2.2 Floater motion 87
4.5.2.3 Tower base shear force and bending moment 88
4.5.2.4 Mooring line tension 89
4.5.2.5 Fatigue damage 91
4.5.2.6 Extreme value prediction 92

5 Conclusions and recommendations for future work 95
5.1 Conclusions 95
5.2 Original contributions 98
5.3 Recommendations for future work 99

References 101

A Appended papers 113
A.1 Paper 1 113
A.2 Paper 2 161
A.3 Paper 3 177
A.4 Paper 4 193
A.5 Paper 5 221

B List of previous PhD theses at Dept. of Marine Tech. 243

List of Tables

1.1 Summary of the characteristics for 5MW-NREL, 8MW-LW, 10MW-DTU and 15MW-IEA wind turbines. 4
1.2 Commercial-scale floating offshore wind farms worldwide . . . 5
1.3 Properties of semi-submersible floating wind turbines 7
1.4 Properties of 5-MW-CSC and OC4 floating wind turbines . . 8
1.5 Numerical codes and hydrodynamic theories used in the papers 13

2.1 Offshore standards regarding mooring system 18
2.2 Properties of chain and steel wire ropes 22
2.3 Mooring concept introduction 33
2.4 Mooring line properties 33

3.1 Polynomial function 45
3.2 Overview of offshore wind code capabilities 54

4.1 Design load cases in the thesis 64
4.2 Horizontal pre-tension (KN) 67
4.3 Price for chain, steel wire rope and polyester fibre rope (€/N) 73
4.4 Cost breakdown for mooring system 73
4.5 Summary of Pros and Cons for all shallow water mooring concepts 75
4.6 Hydrodynamic load models 76
4.7 Statistics of wave realization and responses 90

List of Figures

1.1 Annual global gross onshore and offshore wind installations . 1
1.2 LCOE changes with water depth for different offshore wind turbine types 3
1.3 Average water depth and distance to shore of bottom-fixed offshore wind farms in Europe by 2018. 3
1.4 Thrust curves for the 5MW-NREL, 8MW-LW, 10MW-DTU and 15MW-IEA wind turbines 4
1.5 Floating wind turbine types 6
1.6 Semi-submersible floating wind turbine concepts 7
1.7 Thesis scope 13

2.1 Mooring configuration 20
2.2 Typical anchor types 21
2.3 Mooring connectors 24
2.4 Catenary mooring configuration 26
2.5 Mooring line tension characteristics at 50 m, 100 m and 200 m 27
2.6 The influence of water depth on horizontal mooring stiffness . 27
2.7 Challenge of catenary mooring line top angles 28
2.8 The change rate of top angle α with increasing x-offsets at different water depths 29
2.9 The spring-dashpot model for synthetic fibre rope 30
2.10 Lower-bound and upper-bound stiffness model 31
2.11 Mooring configurations 32

3.1 Local element velocities and flow angles 36
3.2 Applicability of various wave theories 38
3.3 Wave generation 42
3.4 Example of boundary-fitted grid, which deforms with the instantaneous wave profile. 43
3.5 Horizontal velocity of wave particles 44

3.6 Fitting surface and original data 46
3.7 Mesh of floater and free surface in HydroD 48
3.8 Syrope model for synthetic fibre rope 51
3.9 Linearized static and dynamic elastic stiffness of fibre rope . . 53
3.10 Wave field structure of wkin.dll in HAWC2 56
3.11 Global maxima and extreme peak from time series 58
3.12 Gumbel probability paper 59
3.13 ACER function for k=1,2,...,6 60
3.14 Confidence interval for ACER function with k=1 60

4.1 OC4 semi-submersible and its mooring configuration 67
4.2 Offset-tension relation for a single mooring line 68
4.3 Angle between mooring line and vertical plane 69
4.4 Natural period 69
4.5 Dynamic analysis results 71
4.6 Spectrum of floater motion and mooring line tension 77
4.7 Statistics of floater motion and mooring line tension 78
4.8 Work flow of proposed numerical code 80
4.9 Comparison of wave kinematics 81
4.10 Comparison of motion and tension response 82
4.11 Time series of wave elevation, surge motion and mooring line tension due to linear and fully nonlinear wave in two conditions. 83
4.12 Selection of global maxima 84
4.13 Exceedance probability for global maxima of wave peaks at (0m, 0m, 0m) 85
4.14 Wave spectrum 86
4.15 Wave spectra at different frequency ranges 86
4.16 Exceedance probability for global maxima of floater motions . 87
4.17 Motion spectrum 88
4.18 Exceedance probability for global maxima of tower base shear force and bending moment 89
4.19 Tower base bending moment spectrum 89
4.20 Exceedance probability for global maxima of upwind mooring line tension 91
4.21 Mooring line tension spectrum 91
4.22 Hourly fatigue damage at the tower base and the mooring line 92
4.23 Exceedance probability for wave elevation and surge motion . 93
4.24 Extreme response 94

Chapter 1

Introduction

1.1 Background and motivation

Climate change and global warming have drawn a lot of attention all over the world, which has increased the demand for renewable and environmentally friendly energy supply. Wind energy characterized as clean and reliable has experienced a rapid development and it has become important energy supply in many countries [1]. According to Global Wind Energy Council (GWEC), the total installed wind power capacity all over the world has reached 650 GW by the end of 2019 and the annual wind power installation over last ten years is given in Figure 1.1 where expeditious progress have been witnessed in both onshore and offshore sectors. In terms of new and cumulative installations, the world's top five markets are China, US, UK, India and Spain [2].

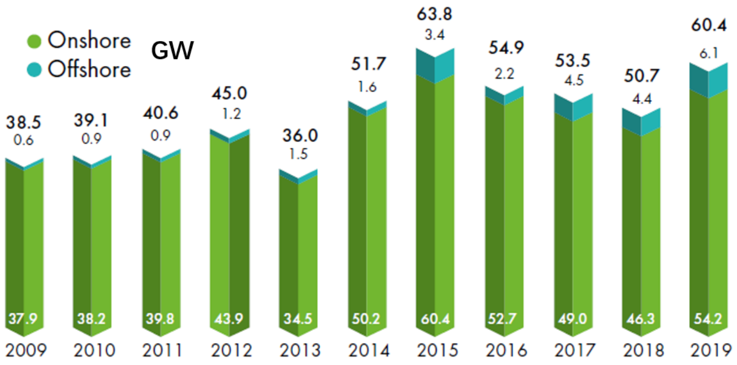

Figure 1.1: Annual global gross onshore and offshore wind installations (Source: GWEC) [2].

Compared with onshore wind, several attributes for offshore wind make it quite favorable such as immense stable resource, great area availability, easy transportation, little visual disturbance and noise etc. Offshore wind technology is developing with higher efficiency and lower cost. The current Levelised Cost of Electricity (LCOE) for offshore wind has been significantly reduced by almost 50% compared with 2012 [3].

According to the IEA offshore wind outlook [4], the offshore wind potential globally is 420878 TWh per year while 79.3% of the resource is located in deep water. As for Europe, the annual wind power potential is 71845 TWh with 93.0% in deep water. Offshore wind resource for many countries is found at water depth above 50 m [5] where bottom-fixed wind turbine (BFWT) becomes excessively expensive. On ther other hand, floating wind turbine (FWT) as a more economically attractive solution comes into the picture as shown in Figure 1.2. The cost advantage of applying floating concepts around 50 m water depth, which is considered as the limiting water depth for installing bottom-fixed structures was further investigated by WindEurope former The European Wind Energy Association (EWEA) in [6]. From the current industrial practice's point of view, the average water depth and distance to shore of current operating commercial bottom-fixed offshore wind farms in Europe is shown in Figure 1.3 where the projects are organised by development status and the size of the bubble indicates the overall capacity of the site. It is clearly seen that there is almost no bottom-fixed wind projects designed at water depth above 50 m, which again proves the potential for floating wind turbine to take over at deeper water. In this thesis, the term 'shallow water' is often mentioned which refers to water depth around 50 m to 80 m for floating wind turbine.

Alongside the trend of moving into deeper water, offshore wind sector is also developing towards larger turbines. Ever since the well known NREL 5MW reference wind turbine was proposed in 2009 [9], the concept has been implemented into industrial application by Repower, Areva, Bard, XEMC, Goldwind, and Gamesa etc. [10]. Afterwards, there was a booming development of increasing turbine size: Siemens Gamesa and GE designed a 6MW turbine; Samsung and Vestas developed 7MW and 8MW models respectively; Senvion, AMSC and Siemens Gamesa collabrated on a 10MW turbines; GE proposed the Haliade-X 12MW design; Siemens Gamesa launched a 14MW direct-drive wind turbine; A 15MW reference wind turbine was proposed in IEA wind task 37 [11], sponsored by the European Union's H2020 Program. Based on the information from WindEurope [12], the offshore turbine capacity has increased by 16% every year since 2014. The average rated capacity of installed offshore wind turbines in 2019 is 7.8 MW.

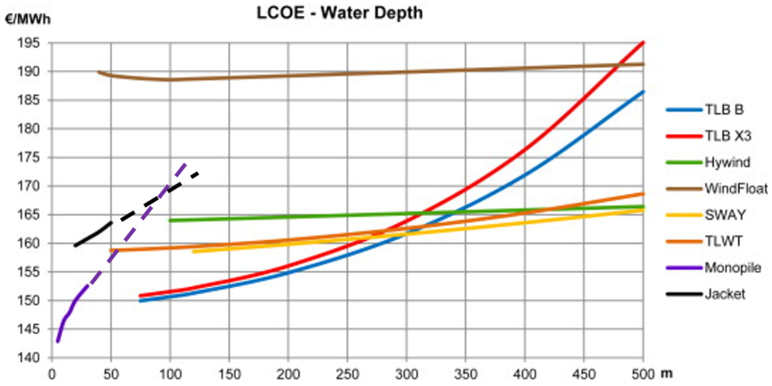

Figure 1.2: LCOE changes with water depth for different offshore wind turbine types [7]. (The results are based on numerical studies in 2014 and the actual values might be different for specific project.)

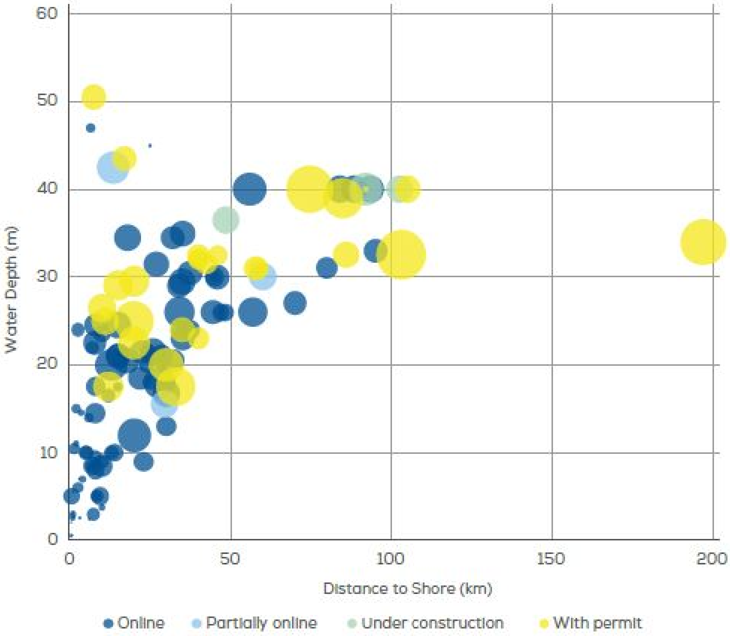

Figure 1.3: Average water depth and distance to shore of bottom-fixed offshore wind farms in Europe by 2018 [8].

Four representative reference wind turbine models i.e. 5MW-NREL [9], 8MW-LW [13], 10MW-DTU [14] and 15MW-IEA [11] are compared with respect to their structural properties in Table 1.1 and thrust curves at different wind speeds in Figure 1.4. As rated power of turbine increases, both rotor size and structural mass increase. Meanwhile, the resulting thrust force at different wind speeds also significantly increases. As a result, a larger size of supporting structure is normally required, which makes floating supporting structure more preferable than bottom-fixed type. However, it will also lead to challenges of designing the mooring system as the size of floater increases.

Table 1.1: Summary of the characteristics for 5MW-NREL, 8MW-LW, 10MW-DTU and 15MW-IEA wind turbines.

Turbine	NREL	LW	DTU	IEA
Rating (MW)	5	8	10	15
Rotor diameter (m)	126	164	178.3	240
Hub height (m)	90	110	119	150
Hub mass (kg)	56.78	90	105.52	190
Nacelle mass (kg)	240	285	446	630
Blade mass (kg)	17.74	35	41.7	65
Tower mass (kg)	347.46	558	605	860

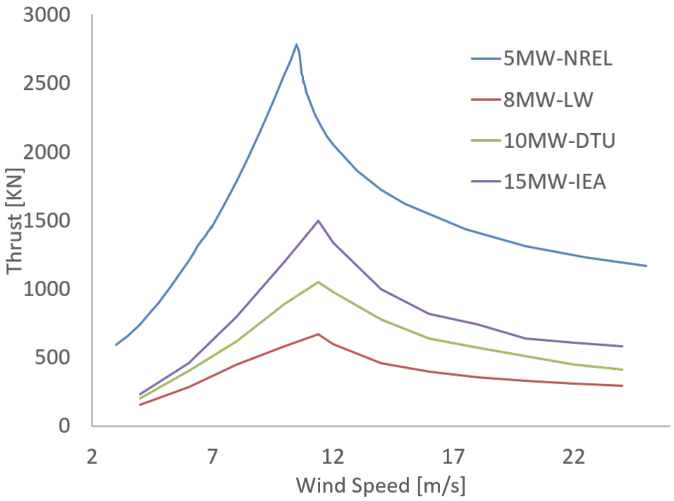

Figure 1.4: Thrust curves for the 5MW-NREL, 8MW-LW, 10MW-DTU and 15MW-IEA wind turbines [11, 13].

Floating wind industry has experienced a decent development all over the world during the last decade [15], there are a number of commercial-scale floating offshore wind farms under different phases of development as shown in Table 1.2. As the world's first operational floating wind farm, Hywind Scotland consists of five 6MW Hywind spars and it was commissioned in October 2017. In August 2019, Hywind Tampen project was launched with the purpose of supplying power to the Snorre and Gullfaks oil fields from 2022 [16]. The WindFloat Atlantic wind farm in Portugal is the world's second commercial floating wind farm which consists of three 8.4MW WindFloat semi-submersibles and it started to supply power to Portuguese grid since the end of 2019 [17]. The 50MW Kincardine offshore wind farm in UK features a total of six WindFloat semi-submersible platforms supporting five MHI Vestas V164-9.525MW turbines and one MHI Vestas V80-2.0MW turbine. The 2MW turbine was connected to British grid in October 2018 while the rest of the project is scheduled to operate in 2020 [18]. The two recently announced large-scale floating wind projects in South Korea brought the total floating offshore wind development pipeline to be around 1 GW.

Table 1.2: Commercial-scale floating offshore wind farms worldwide [15]

Project	MW	Location	Turbine	Status	Commission
Hywind Scotland	30	UK	Siemens Gamesa SG 8.0-167	Operation	2017
WindFloat Atlantic	25	PT	MHI Vestas V164-8.4MW	Construction	2020
Kincardine	50	UK	MHI Vestas V164-9.5MW	Construction	2020
Provence Grand Large	24	FR	Siemens Gamesa SG 8.0-167	Development	2021
EolMed	24.8	FR	Senvion 6.2MW	Development	2021
Groix-Belle-lle	28.5	FR	MHI Vestas V164-9.5MW	Development	2022
EFGL	30	FR	MHI Vestas V164-10.0MW	Development	2022
Hywind Tampen	88	NO	Siemens Gamesa SG 8.0-167	Development	2022
Donghae 1	200	KR	-	Development	2024+
Ulsan Metropolitan City	500	KR	-	Development	2025+

There are mainly four substructure designs for floating wind turbine in current industry: barge, tension leg platform (TLP), spar and semi-submersible as shown in Figure 1.5. Among the four floating concepts, the development of semi-submersible and spar are in the leading positions with higher enough 'technology readiness level' (TRL) ready for launch and operations compared with barge and TLP [19]. Furthermore, spar is constrained to deep water locations because of its large draft while semi-submersible is more flexible regarding applicable water depth thanks to its small draft. Considering the fact that marginal transition water depth from BFWT to FWT is approximately around 50 m [6], semi-submersible stands out among the four floating types in terms of TRL and suitable working water depth range and will be focused in this thesis.

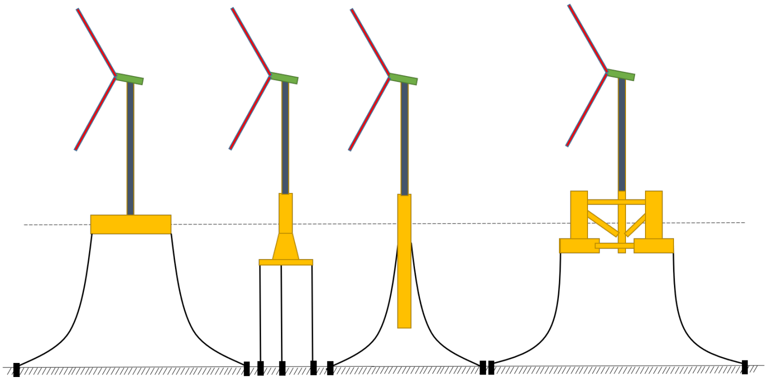

Figure 1.5: Floating wind turbine types: barge, TLP, spar and semi-submersible.

1.2 Semi-submersible floating wind turbine

There are a number of semi-submersible FWT concepts that either have been commissioned or are under development. Three or four columns are commonly used in the semi-submersible floater design while braces are also implemented in some of the popular concepts. Both horizontal-axis and vertical-axis wind turbines can be accommodated on side column or central column, while horizontal-axis wind turbine is more developed and will be focused in this thesis. Some representative concepts are shown in Figure 1.6 including WindFloat [20], Tri-floater [21], Compact Semi-Sub [22], V-Shape Semi-sub [22], NAUTILUS [23], OO-Star [23], CSC [24] and OC4 [25]. Among them, WindFloat has been successfully implemented in Kincardine wind farm since October 2018 [18] and WindFloat Atlantic wind farm since 2019 [17] while the other concepts are still under development phase. Some general properties of the concepts are provided in Table 1.3. In this thesis, CSC and OC4 semi-submersible floaters are used for different case studies and their general properties are described in Table 1.4.

The 5-MW-CSC concept (Figure 1.6 g) was first proposed by Luan et al. [24] in the NOWITECH (Norwegian Research Centre for Offshore Wind Technology) project. The 5-MW-CSC semi-submersible floater consists of three pontoons, three side columns and one central column supporting the tower and the wind turbine. Restoring stiffness is provided by the side columns. The pontoons are used to provide buoyancy and space for ballast, which leads to a low centre of gravity and floater motion features are improved as a result. No brace structure is used, which is favourable from the fabrication point of view. The 5-MW-CSC model was used to study

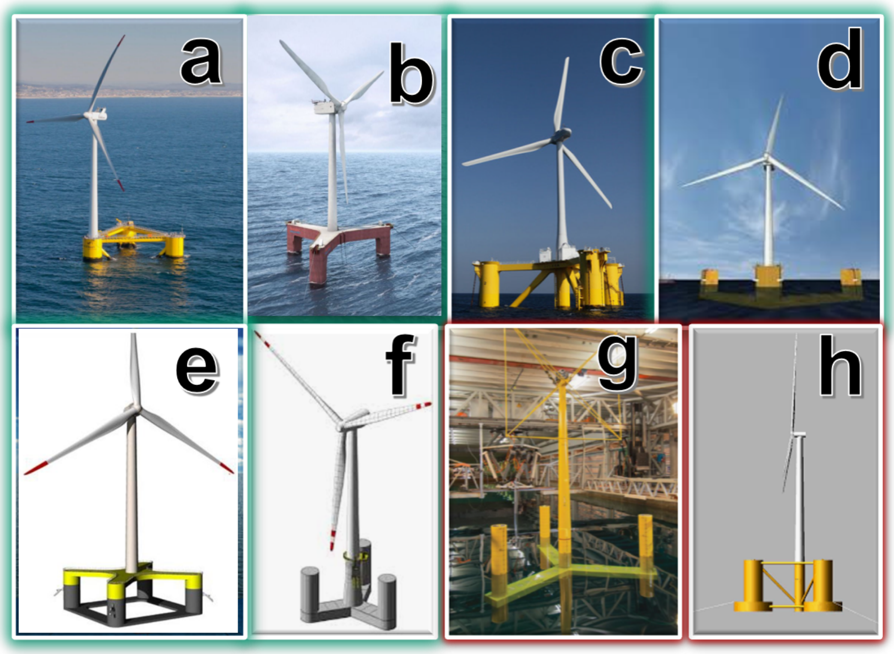

Figure 1.6: Semi-submersible floating wind turbine concepts: (a) WindFloat (b) Tri-floater (c) Compact Semi-sub (d) V-Shape Semi-sub (e) NAUTILUS (f) OO-Star (g) CSC (h) OC4

Table 1.3: Properties of semi-submersible floating wind turbines

	Country	Material	Capacity	Mooring	Water depth
WindFloat	Portugal	Steel	2 MW	3 Catenary	50 m +
Tri-floater	Netherlands	Steel	5 MW	3 Catenary	100 m
Compact	Japan	Steel	2 MW	6 Catenary	Undisclosed
V-Shape	Japan	Steel	7 MW	8 Catenary	Undisclosed
NAUTILUS	EU	Concrete & Steel	10 MW	4 Catenary	130 m
OO Star	EU	Concrete	10 MW	3 Catenary	130 m
CSC	Norway	Steel	5 MW	3 Catenary	200 m +
OC4	US	Steel	5 MW	3 Catenary	200 m +

second-order wave effects (*Paper 2*).

The OC4 concept (Figure 1.6 h) was proposed in the International Energy Agency Wind Task 30 Offshore Code Comparison Collaboration Continuation (OC4) project [25] and has been frequently referred to ever since. The floater consists of a centre column connecting the tower and three side columns which is connected with main column through a number of smaller pontoons and braces. The draft of the platform is 20 m and the tower is mounted on the top of the main column with an elevation of 10 m above the mean water level. The OC4 model was used in the study of mooring system design in shallow water (*Paper 1*) and fully nonlinear wave effect (*Paper 3, 4, 5*).

Table 1.4: Properties of 5-MW-CSC and OC4 floating wind turbines

	5-MW-CSC	OC4	
Mass with ballast	9738 t	13473 t	Mass with ballast
Floater draft	30 m	20 m	Floater draft
CoG below water level	24.36 m	13.46 m	CoG below water level
Diameter of columns	6.5 m	6.5 m	Diameter of main column
Length of center columns	34 m	12 m	Diameter of upper columns
Length of side columns	44 m	24 m	Diameter of base columns
Width of pontoons	9 m	26 m	Length of upper columns
Height of pontoons	6 m	6 m	Length of base columns
Length of pontoons	41 m	50 m	Length of pontoons

1.3 Review of research work on mooring system design and coupled analysis in shallow water

In order to successfully implement semi-submersible wind turbine in shallow water, there are a number of issues that need to be addressed. Compared with deep water mooring, the structural characteristics and corresponding design philosophy is quite different for shallow water mooring. Nonlinear behavior of synthetic fibre rope is difficult to be implemented in the numerical code. The slow-drift excitation forces can induce large horizontal excursion for semi-submersible platform, which is important to consider in the analysis. Meanwhile, the nonlinear wave effect becomes more significant as water depth decreases. These issues have been investigated by several researchers from different sectors including offshore oil & gas platform, floating wind turbine and wave energy converter etc. A brief review of previous research work is provided in this section.

Mooring system design in shallow water

Brommundt et al. [26] developed an optimization tool for catenary mooring system to study the optimal line length, angle and anchor radius with a case study at two water depths (75 m and 330 m). Benassai et al. [27, 28, 29] compared the motion control performance of catenary and tensioned line mooring systems for the Dutch tri-floater wind turbine at water depth between 50 m and 200 m. The influence of line number, platform maximum admissible offset and mooring line pattern were investigated. More catenary mooring design concepts were proposed by Campanile et al. [30] at water depth from 50 m to 80 m and from 200 m to 350 m. A preliminary cost analysis regarding installation and maintenance cost was also performed.

Clump weight and buoy have been considered in the mooring design to improve the mooring performance. Finn [31] implemented clump weight in the mooring system for ‘the guyed tower’. When platform experiences large motions in extreme condition, the clump weight will be lifted from the seabed to establish an extended catenary shape to minimize the floater motion. The benefit of attaching buoy to mooring line was studied by Mavrakos et al. [32] and confirmed that the reduction of mooring line dynamics can be achieved when the size, number and location of buoy are properly selected. Comparative mooring configurations consisting of catenary chain with or without additional clump weight or buoy were compared by Vicente et al. [33] for a floating point absorber. A hybrid mooring concept consisting of clump weights and buoys attached to the lower and upper end of the line respectively was developed by Yuan et al. [34] for a semi-submersible platform in deep water. In order to artificially increase the effective water depth from fairlead to seabed and further improve the mooring line tension characteristics, the technique of moving fairlead from underwater to above water level have been adopted by two collaborative research projects: INNWIND.EU [35] and LIFES50+ [36] for designing floating wind turbines.

Considerable efforts have also been made regarding utilizing different mooring line materials. Compared with traditional chain cable and steel wire rope, synthetic fibre ropes is regarded as a cost-competitive mooring solution. It was widely applied in deep water mooring in offshore oil & gas industry [37, 38] and it is being considered by more and more offshore renewable projects. Currently, there are only a few projects that are actually considering fibre rope as mooring solutions including the CETO wave energy converter [39] and the Floatgen wind turbine [40]. Johanning and Smith [41] studied the feasibility of applying fibre rope on wave energy converter by comparing with other mooring materials. Weller et al. [42] looked into the influence of load history on synthetic rope where different initial bedding-in levels were used to investigate the immediate quasi-static and dynamic properties of the rope. An overview of the application of synthetic ropes for marine renewable project was provided by Weller et al. [43] including classification, model testing, installation, degradation and maintenance etc.

Coupled dynamic analysis

Currently, several approaches are available to calculate the second-order difference-frequency wave load with different approximations and levels of accuracy. Newman's approximation method [44] is widely accepted in offshore industry, which is based on the assumption that the natural frequency of slow-drift motion is sufficiently small so that the exact quadratic transfer function (QTF) for difference-frequency forces can be approximated by the mean drift force value which is a second-order effect depending only on the first-order velocity potential and motions. The accuracy of Newman's approximation method to calculate horizontal slow-drift excitation force on a ship in irregular beam sea waves was confirmed by Faltinsen and Løken [45, 46], which proved that the contribution from the second-order velocity potential to the slow-drift excitation forces was small to be neglected. The second-order velocity potential was incorporated in Pinkster's approximation [47], which managed to provide the right order of magnitude to the slow-drift excitation forces due to the contribution of the second-order velocity potential. The difference-frequency QTF was approximated by Chen and Duan [48] into two parts, while one depends on the quadratic products of the first-order wave fields and the other one depends on the second-order velocity potential. Shao [49] studied the second-order wave-body interaction problems with a higher-order Boundary Element Method (BEM) where a new formulation of the boundary value problem based on body-fixed coordinate system was proposed to avoid the inconsistency in the traditional formulation while increase the accuracy. You [50] studied the second-order surge response of a moored vessel in shallow water by comparing a time domain BEM with Newman's approximation and Pinkster's approximation.

As water depth decreases, wave nonlinearity effect becomes more important to consider in the coupled analysis. According to Gibson and Swan [51], the wave nonlinearity effect can be divided into higher-order bound nonlinearity and resonant nonlinearity at third order and above by. The bound nonlinearities in regular waves are the higher-order terms derived by Stokes [52] which are phase locked to the corresponding linear wave component and intend to sharpen the wave peak and broaden the wave trough. Fully nonlinear wave effect on monopile wind turbine has been systematically investigated by Schløer et al. [53, 54, 55]. Inline force and overturning moment are compared between linear wave theory, stream function theory and fully nonlinear irregular wave. The influence on fatigue damage of the monopile and tower was studied in [54]. Redistribution of energy at different frequency range was discovered in [55]. Similar approach was used by Larsen et al. [56] to investigate jacket supported wind turbine. Nematbakhsh et al. [57] extended the nonlinear wave study to TLP wind turbine using computational fluid dynamics (CFD) method and the results was compared with results from potential flow solver. The coupled FLEX5-OceanWave3D tool was applied on a TLP wind turbine in the INNWIND project [58] to compare response exposed to different wave models including fully nonlinear wave and the result was further compared with experimental data by Pegalajar-Jurado et al. [59].

1.4 Challenges & objectives

The marginal water depth between BFWT and FWT might be in the range of 50 m - 80 m, which is quite shallow for a floating structure. It is challenging to implement floating wind turbine around this water depth mainly due to the design of mooring system. In order to further promote the development of semi-submersible floating wind turbine in shallow water, some of the remaining work will be focused in this thesis:

1. The challenges of mooring system design in shallow water were not studied into details before. Regarding the mooring application for floating wind turbine in shallow water, there is a lack of comparison between different mooring materials and sophisticated design proposals for industrial guidance.

2. The previous mooring design studies for shallow water were mainly made of pure chain cable while the hybrid mooring concepts consisting of clump weights and buoys were mainly designed for deep water and the application in shallow water mooring was not considered.

3. The experience regarding fibre rope from oil & gas sector was mainly for deep and ultra-deep water, however there is also great potential for fibre rope to be used in shallow water mooring due to its lower elastic stiffness and capital cost, which has not been discussed much before.

4. Current industrial practice for modelling fibre rope is to use the upper-bound and lower-bound method [60], which is not only conservative but also inconsistent because the offset is obtained based on a lower-bound stiffness model while the dynamic tension is estimated through another upper-bound stiffness model. There is still a lack of commercially available mooring analysis programs with the capability to simulate the non-linear change-in-length response.
5. Different methods are available to calculate second-order difference-frequency wave load. The applicability and limitation of these methods is of interest to study for the hydrodynamic analysis of floating wind turbine in shallow water.
6. Previous study of fully nonlinear wave effect on offshore wind turbine mainly focused on bottom-fixed wind turbine and there is a lack of engineering-practical numerical code that is applicable for floating wind turbine too.

Accordingly, the main objectives of this thesis are summarized as:

1. Systematically compare the different mooring system characteristics in deep and shallow water. Identify the challenges of designing mooring system in shallow water for both catenary and taut mooring systems.
2. Make recommendation of preferable mooring designs for floating wind turbine in shallow water depth for industrial guidance through comparative studies of different mooring designs.
3. Considering the limitation of traditional conservative and inconsistent method of modelling fibre rope, improve the numerical method that can better describe its structural behavior.
4. Study the feasibility of applying Newman's approximation method to describe second-order difference-frequency wave effect in shallow water by comparing with results from full QTF method.
5. Investigate the significance of wave nonlinearity in shallow water and develop an efficient numerical tool to study its effect on floating wind turbine. Quantify the wave nonlinearity effect for different structural responses.

Semi-submersible is selected as the targeting floater type because of its applicability in shallow water as mentioned before. This thesis is written as a summary of three journal articles and two conference papers as attached in the Appendix A. The scope of the thesis is shown in Figure 1.7 where the main topics and the interconnection between appended papers are illustrated. In addition, the numerical codes and hydrodynamic theories applied in the individual papers are summarized in Table 1.5.

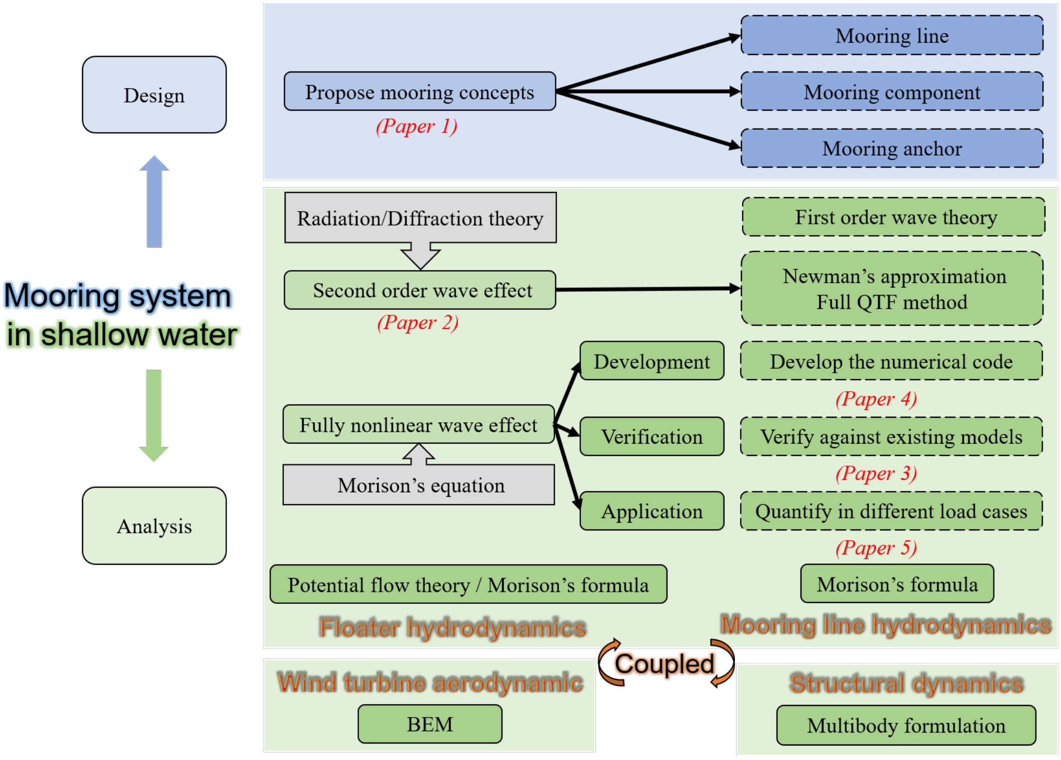

Figure 1.7: Scope of the thesis

Table 1.5: Numerical codes and hydrodynamic theories used in the papers

	Numerical code	Hydrodynamic theory
P1	SIMA	Potential flow theory (second-order difference-frequency effect)
P2	SIMA	Potential flow theory (second-order difference-frequency effect)
P3	2D HPC/HAWC2	Morison's equation (fully nonlinear wave effect)
P4	2D HPC/HAWC2	Morison's equation (fully nonlinear wave effect)
P5	2D HPC/HAWC2	Morison's equation (fully nonlinear wave effect)

The contents of the five papers in the Appendix A are summarized as follows:

Paper 1:
This paper studied the design challenges of mooring system for semi-submersible FWT in shallow water and proposed preferable mooring design concepts. Seven mooring design concepts were proposed at 50 m for the OC4 semi-submersible with original design at 200 m as a reference. Different mooring line materials were compared together with other mooring components and anchors. Based on experimental data, a state-of-the-art numerical model was used to describe the stiffness characteristics of fibre rope. The comparison was performed from different perspectives: static performance, dynamic response and cost analysis. Preferable mooring designs were recommended for engineering guidance.

Paper 2:
Apart from first-order wave load, second-order difference-frequency wave load effect is important for semi-submersible platforms. This paper mainly compares different hydrodynamic load modelling methods of second-order wave drift force: Newman's approximation method and full QTF method. Three water depths were considered: 50 m, 100 m, 200 m. The floater motion, mooring line tension and non-Gaussian property of the response were studied.

Paper 3:
The main purpose of this paper is to verify the numerical tool proposed in Paper 4 which is used to study fully nonlinear wave effects. Three wave models were compared: stream function wave, fully nonlinear wave and linear Airy wave. The comparison between the first two wave models was able to verify the accuracy of the proposed model since they satisfy the same free surface boundary conditions (FSBCs). The comparison between the latter two models was meant to indicate the effect due to wave nonlinearity. Three load cases characterized with different wave steepness were considered.

Paper 4:
This paper outlines an engineering-practical numerical tool to study fully nonlinear wave effect on floating wind turbine. 2D HPC numerical wave tank was used to generate the irregular linear and fully nonlinear wave trains. A polynomial fitting method was proposed to scale down the size of wave kinematics data file in order to satisfy the virtual memory requirement of HAWC2. The link between the wave kinematics database and HAWC2

was extended from one dimensional (Wkin.dll) to two dimensional (Wkin.dll 2D) which enables the application to not only BFWT but also FWT. Two wave-only extreme irregular wave conditions are studied as example to illustrate the wave nonlinearity effect.

Paper 5:
Based on the numerical tool developed in Paper 4, the focus of this paper is a systematic study of the wave nonlinearity effect in different load cases where both wind and wave are considered. In operational conditions, floater motion, tower base bending moment, pontoon axial force and mooring line tension as well as the fatigue damage of mooring line and at tower base are studied. In extreme conditions, the extreme value of critical responses are predicted based on Gumbel fitting method and ACER method.

1.5 Thesis outline

The thesis consists of five chapters. A brief description of each chapter is provided as follow:

Chapter 1: Introduction
This chapter includes research background and motivation, an overview of state-of-the-art semi-submersible floating wind turbine concepts, a review of previous research work on mooring system design and coupled analysis method in shallow water, remaining challenges to be solved and main objectives of the thesis.

Chapter 2: Design of mooring system in shallow water
This chapter mainly introduces the design perspectives of mooring system in shallow water as well as modelling technique in numerical program. Currently available offshore guidelines and standards regarding mooring system from different authorities are introduced as well as basis information of different components of mooring system. The design challenges of mooring system for floating wind turbine in shallow water are mentioned. Seven feasible mooring design concepts including different mooring line materials, anchors and mooring components are proposed for floating wind turbine in shallow water.

Chapter 3: Numerical modelling and analysis method
The theoretical background of the fully coupled analysis method used in this thesis is introduced in this chapter. The aerodynamic theory is briefly

mentioned while the hydrodynamic theory is described into details including different wave theories, processing of wave kinematics data and different hydrodynamic load modelling methods. The main features of the numerical tools used in this thesis is introduced. An improved numerical model of fibre rope are described. The approaches of calculating fatigue damage and predicting extreme value are described.

Chapter 4: Coupled analysis results
This chapter mainly presents the results and outcomes of this thesis. The determination of the design load cases is also provided in this chapter. The performance of mooring concepts proposed in Chapter 2 are compared in this chapter from different perspectives including static analysis, dynamic analysis and cost analysis. Advantages and disadvantages of different concepts are summarized and recommendation of preferable designs are made. The results of calculating second-order wave load using Newman's approximation and full QTF method at different water depths are compared. A numerical tool to study fully nonlinear wave effect on floating wind turbine is proposed and verified. The wave nonlinearity effect is further studied from several aspects including fatigue damage and extreme value for critical responses.

Chapter 5: Conclusions and recommendations for future work
Conclusions, original contributions and recommendations for future work are presented in this chapter.

Chapter 2

Design of mooring system in shallow water

Precise positioning and motion control is critical for safe operation of the floating wind turbine considering the integrity of electric power cable. The purpose of the mooring system is primarily to provide station-keeping, especially to prevent drift-off under steady environmental loads, as well as possibly limit motions - especially for tension-leg or taut mooring systems. Moreover, for the tension-leg system the mooring system is crucial in providing stability of the floater.

The total restoring force of the mooring system in quasi-static condition is related to geometric stiffness and elastic stiffness. Geometric stiffness mainly comes from the weight and pre-tension of the mooring line which is the main source of restoring force in catenary mooring system. Elastic stiffness is mainly due to line elongation which is the main source of restoring force in taut mooring system with synthetic fibre rope. The stiffness for each mooring line is referred to as the in-plane stiffness while the out-of-plane stiffness is normally very small. The stiffness for catenary mooring becomes quite nonlinear when floater horizontal offset is large. Moreover, the line laying on the seabed should be long enough to prevent being totally lifted up. In dynamic conditions, mooring line tension response can be divided into mean tension and dynamic tension which can be further decomposed into wave frequency and low frequency components. Mooring line motion will also lead to a drag force and an inertial force which contribute to the damping and inertial effect of the mooring line respectively. The damping effect is particularly important for floater's low frequency motions which are associated with a small potential damping.

2.1 Guidelines and standards for mooring system

Currently, there are a number of offshore guidelines and standards available for designing mooring system for offshore oil & gas platform, floating wind turbine and wave energy converter etc. Some representative standards from different authority organizations are given in Table 2.1. Referring to these standards, redundancy in mooring system for offshore oil & gas platform is normally required because the failure of mooring line could lead to unacceptable consequences such as loss of life and environmental pollution etc. As for the floating wind turbine, mooring system failure will most likely lead to just economic loss, therefore the number of mooring line is normally kept as few as possible for economical purpose. Design rules for floating wind turbine is also required to check when designing its mooring system through coupled analysis method. In this thesis, the standards from DNVGL are mainly referred to.

Table 2.1: Offshore standards regarding mooring system

Authority	Guidelines and standards
DNVGL	DNVGL-OS-E301 Position mooring 2018 DNVGL-OS-E302 Offshore mooring chain 2018 DNVGL-OS-E303 Offshore fibre ropes 2018 DNVGL-OS-E304 Offshore mooring steel wire ropes 2015 DNVGL-ST-0119 Floating wind turbine structures 2018 DNVGL-RP-E301 Design and installation of fluke anchors 2017 DNVGL-RP-E302 Design and installation of plate anchors in clay 2017 DNVGL-RP-E303 Geotechnical design and installation of suction anchors in clay 2017
BV	NR493DTR02E Classification of mooring system for permanent offshore units. 2012 NI432DTOR01E Certification of fibre ropes for deepwater offshore services 2007 NR494DTR02E Rules for the classification of offshore loading and offloading buoys 2006
ISO	ISO19901-7:2013 Stationkeeping system for floating offshore structures and mobile offshore units. 2013 ISO18692:2007 Fibre ropes for offshore stationkeeping: polyester 2007 ISO1704:2008 Ships and marine technology - stud-link anchor chains 2008
API	API RP 2SK Recommended practice for design and analysis of stationkeeping systems for floating structures 2008 API RP 2SM Recommended practice for design, manufacture, installation, and maintenance of synthetic fibre ropes for offshore mooring 2014
ABS	Guidance note on the application of fiber rope for offshore mooring 2014

2.2 Introduction of mooring system and components

2.2.1 Mooring configuration

- *Catenary mooring system* (Figure 2.1a) is the earliest and most common mooring system that is used in current industry. The restoring force is provided by the self-weight of mooring line. A number of mooring lines are uniformly arranged around the floating structure. Normally, there is a significant part of mooring line lying on the seabed to avoid the mooring line being totally lifted up. Therefore, the anchor is designed to take only horizontal forces. Moreover, the friction force due to the relative movement between mooring line and the seabed should be taken into account.

- *Taut mooring system* (Figure 2.1b) consists of a group of stretched mooring lines whose net weight is so small that the catenary properties of the line could be ignored. The restoring force depends on the elastic stretch of the line. Taut mooring arrives at the seabed at an angle, which means that the anchor has to undertake both horizontal and vertical forces. Compared with catenary mooring, the footprint of taut mooring system is smaller, which could result in reduction of material quantity, cost and weight of the total mooring system.

- *Tension leg mooring system* (Figure 2.1c) is specially used for tension leg platform. The buoyancy of the platform is larger than its gravity which leads to a net upward force to be balanced by the the mooring line tension. Associated anchors are normally suction anchor or anchor piles which can take vertical forces. The pre-tension in the line is often obtained by the use of winches on the floating structure. The horizontal motion of the floating structure is quite limited because of the tethers while vertical motion of the floater could lead to large snapping load which should be carefully dealt with.

2.2.2 Mooring anchor

The primary function of an anchor is to fix the mooring line to the seabed at a given position. The choice of anchor depends on a couple of factors, such as the water depth to be applied, the soil condition, the loading acting on the anchor, anchor positioning accuracy and the cost of installation etc. [62]. Many different types of anchors are applied in the offshore industry and the most common anchor types are illustrated in Figure 2.2 including

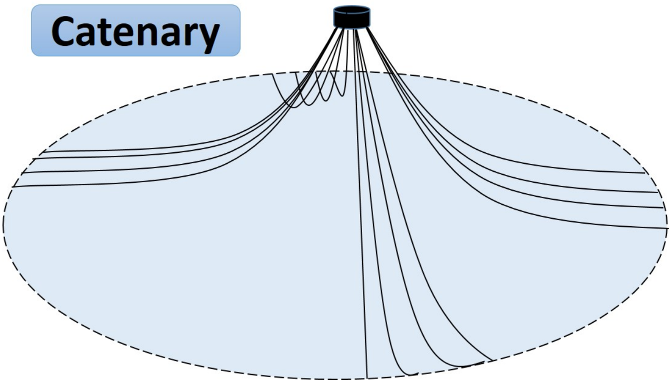

(a) Catenary mooring system

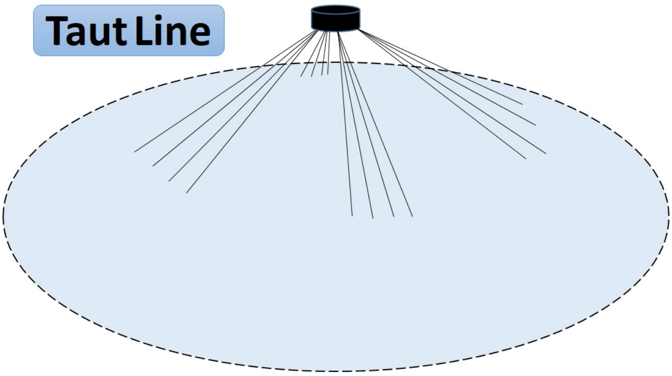

(b) Taut mooring system

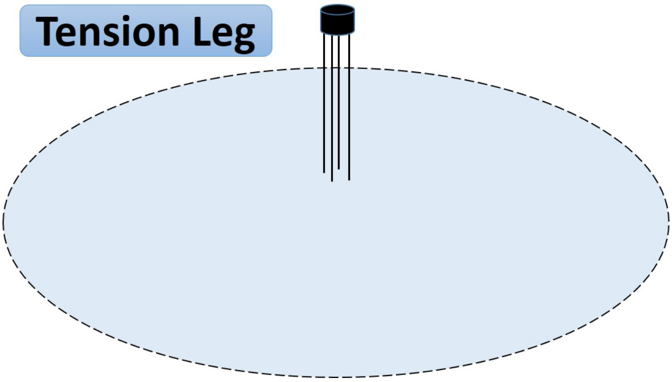

(c) Tension leg mooring system

Figure 2.1: Mooring configuration [61]

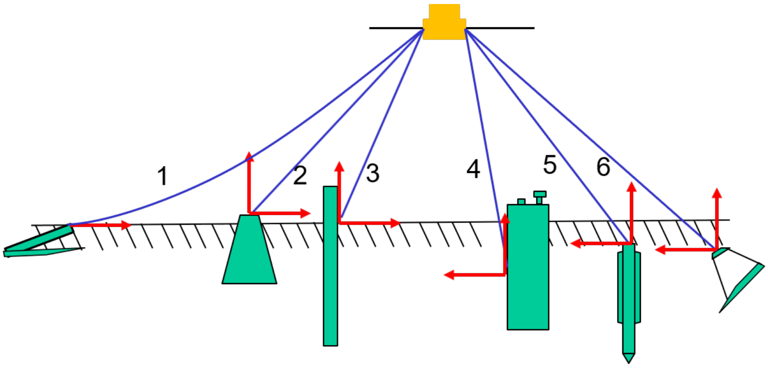

Figure 2.2: Typical anchor types

drag embedment anchor (DEA) (No.1), dead weight anchor (No.2), pile anchor (No.3), suction anchor (No.4), torpedo anchor (No.5) and vertical load anchor (No.6). The red arrows indicate in which direction the anchor can take the force.

- *Drag embedment anchor* is the most popular anchor type available in the industry. It is designed to partly or fully penetrate into the seabed. The hold capacity is determined by the resistance of the soil in front of the anchor. It serves perfectly for resisting large horizontal loads, but not for large vertical loads. DEA is a quite attractive option for mooring solution because of its high efficiency while the installation procedure is not simple. The installation normally requires pulling operation using an anchor handling vessel (AHV) with sufficient bollard pull and a pulling force equal to the 100 year intact mooring line tension is required at Norwegian continental shelf.

- *Pile anchor* is a hollow steel pipe which is penetrated into soil with a piling hammer or vibrator. The vertical and horizontal holding capacity is determined by the friction of the soil along the pile and lateral soil resistance respectively. Horizontal capacity can be further increased by adding additional elements such as skirts or wings to the pile top. For the sake of safety consideration, the pile is preferred to be installed well underneath the seabed to ensure the holding capacity.

- *Suction anchor* is a caisson foundation with an open bottom and closed top whose holding capacity is generated by friction of the soil along the suction anchor and lateral soil resistance which enable it to cope with both horizontal and vertical loads. During the installation, a pump is connected to the top of the pipe in order to pump the water out of the anchor which will create a pressure difference between the outside and the inside of the pipe and further force the pipe into the seabed to a target depth. The pump is removed after installation is completed. Suction pile length to diameter ratios may range from 2:1 for stiff clay soil to 7:1 for soft clay soil.

2.2.3 Mooring line

As the most important component in the mooring system, mooring line is used to provide the restoring force by connecting the floater and anchor. The most popular mooring line materials that are widely used in offshore industry are chain, steel wire rope and synthetic fibre rope.

• *Chain* is the most common product used for catenary mooring lines which is characterized with different diameters and grades [61]. The weight of chain can be quite large compared with other mooring line material which make it more suitable to be used in shallow water where the length of suspended mooring line is quite short. According to [63], the submerged weight per unit length (w), axial stiffness (EA) and catalogue break strength (CBS) of a chain link can be expressed as in Table 2.2:

Table 2.2: Properties of chain and steel wire ropes [63]

	Chain	Six strand wire	Spiral strand wire
w (N/m)	0.1875 D^2	0.034 D^2	0.043 D^2
EA (N)	90000 D^2	45000 D^2	90000 D^2
CBS (N)	c(44-0.08D) D^2	525 D^2	900 D^2

where D is the nominal diameter with unit of mm and c is coefficient which should be selected according to the material grade.

• *Steel wire rope* used in offshore mooring line are normally structured as six strand, spiral strand or multi-strand. Six strand independent wire rope core is the most popular construction for mobile drilling units because of its lateral flexibility and spiral strand construction is more commonly utilized in floating production systems, where it shows great longitudinal stiffness, torque balance and lower spinning loss performance. Multi-strand rope construction is not commonly used in offshore industry. For the same breaking load, steel wire rope is light-weighted. Meanwhile, zink and plastic sheathing can protect steel wire rope from corrosion. In some cases, steel wire ropes are implemented in a taut mooring system to provide axial elasticity for the restoring effect. The properties of wire ropes are influenced by not only rope construction but also the manufacturer's professionalism. The properties of six strand and spiral strand ropes are compared in Table 2.2 where D is the nominal diameter of the rope with unit of mm.

• *Synthetic fibre rope* is made of polyester or other high-strength fibres and it has been a popular material for deep water mooring solution thanks to its light weight and high elasticity [43]. Moreover, it also has great potential in shallow water mooring design due to its linear tension increment behavior. The properties of fibre rope are more complex than traditional chain or steel wire rope. The change-in-length response is nonlinear and load-sequence dependent while the length of the line is also affected by the loading rate and duration. Even though there has been a long history of application of fibre rope mooring in offshore industry, current industrial practice is normally conservative and inconsistent using an upper and a lower bound axial stiffness method. Comprehensive understanding of the material behaviour is still limited and so are relevant analytical methods.

2.2.4 Mooring component

In order to satisfy required performance criteria, additional mooring components such as clump weights and buoys are quite helpful in achieving the desired restoring force by adjusting the geometric stiffness of the line.

• *Clump weight* is a concentrated weight which can be used to improve the geometric stiffness properties of the line by incorporating with lighter mooring line to achieve same required pre-tension. With implementation of clump weight, heavy chain can be replaced which is quite beneficial in shallow water where mooring line tension will increase quite significantly at large offset.

• *Buoy* is a structure whose buoyancy is larger than gravity which can be connected to a mooring line in order to reduce the weight of the line, improve the geometric stiffness and increase vertical clearance to any equipment on the seabed. The application of buoy has been widely accepted in deep water mooring where the weight of the mooring line is a limiting factor for design consideration. Meanwhile, the utilization of buoy in shallow water mooring is also quite favorable to prevent extreme tension at large offset due to a favorable change of line geometric stiffness which however was hardly discussed before.

2.2.5 Mooring connector

Mooring connectors are used to connect different mooring line sections such as chain links with different diameters, chain to steel wire rope, mooring line to anchors or vessels etc. Mooring connectors are designed to take the full breaking strength of the mooring line while their fatigue properties require special attention. The connectors are typically designed as ‘fit for purpose’ for each project [61].

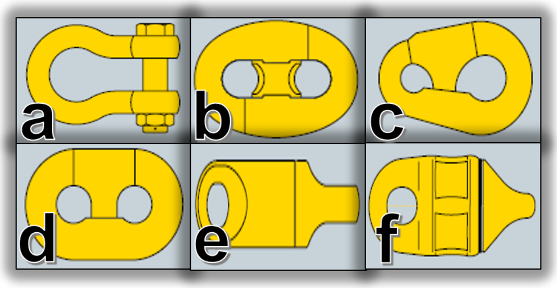

Figure 2.3: Mooring connectors [61]

Some examples of mooring connectors are shown in Figure 2.3:

- *Shackle (Figure 2.3a)* is a universal connector with many different types. It consists of a bow which is closed by a pin.
- *Kenter-type link (Figure 2.3b)* is used for connecting two pieces of chain links whose termination dimensions are same. Normally it is not recommended for permanent mooring system because of their shorter fatigue life than chain.
- *Pear-shaped link (Figure 2.3c)* is used for connecting two pieces of chain links with different termination dimensions.
- *C-type link (Figure 2.3d)* is similar to Kenter-type link while the major difference is the way that the connector is opened and closed.
- *Mooring swivel (Figure 2.3e)* is used to relieve the twist and torque that builds up in the mooring line. It can be placed a few links away from the anchor point or between sections of chain or wire rope.
- *Anchor handling swivel (Figure 2.3f)* is used to compensate the load impact during handling process. The slim geometry allows the swivel to run through fairlead, chaser ring or over an anchor handler stern roller without damage to the bearing system or any other swivel part.

2.3 Design criteria

Design of a mooring system normally consists of many aspects such as environmental condition, water depth, floater excursion limit, structure lifetime, installability and component cost etc. A systematic design of mooring system normally include Ultimate Limit State (ULS), Fatigue Limit State (FLS) and Accidental Limit State (ALS) [64]. Detailed mooring design criteria have been mentioned by many offshore standards, such as API RP 2SK [62] and DNV-OS-E301 [64] etc. In this thesis, the main criteria in the mooring design process are:

1. Considering the safety of power cable and the power production efficiency of wind turbine, the offsets of the floater have to be limited to a reasonable range.
2. All mooring lines have to be able to withstand the load effects in all the environmental conditions considered which means that the maximum mooring line tension can not exceed the maximum breaking strength taking into account an appropriate safety factor.
3. The catenary mooring line lying on the seabed should be long enough to prevent drag anchor taking vertical load even in the most extreme condition during lifetime. Because when it is fully lifted up, it will be the stretching of the line that provides the restoring effect which will lead to a very large tension in the lines. The requirement becomes more important for anchors in sand and hard soil where the anchor penetration is quite shallow.
4. The leeward mooring line should not experience slack which may lead to large tension.
5. The properties of a deep water mooring system designed for a semi-submersible floating wind turbine at 200 m is considered as reference for shallow water mooring (50 m) such as: pretension, line length etc. Comparative models with clump weight and buoy are included to explore whether additional mooring components can improve the mooring performance.

2.4 Design challenges for shallow water conditions

The integrity of the mooring system should be ensured by proper design, fabrication, installation, use as well as condition assessment in the lifecycle at minimum lifecycle costs. On one hand, the mooring system should be stiff enough to limit the floater offset under the mean wind and wave loads and the floater slowly-varying motions due to the second-order wave loads and the wind loads. On the other hand, it should be compliant enough to allow wave-frequency floater motions and avoid large mooring line tension induced by the first order wave loads on the floater. These features are relatively easy to achieve in deep water while it is more challenging in shallow water for both catenary and taut mooring systems [65]:

Catenary mooring system

1: The vertical span from fairlead to seabed in shallow water is much shorter than deep water as shown in Figure 2.4, which directly affects the length of suspended mooring line that provides pre-tension. Taking the OC4 semi-submersible floating wind turbine as an example, the fairlead is located at 14 m below mean water level. The effective vertical distances for suspended mooring line are 36 m and 186 m when water depths are 50 m and 200 m respectively. In order to achieve reasonable pre-tension as deep water, the size of mooring line has to be increased in shallow water.

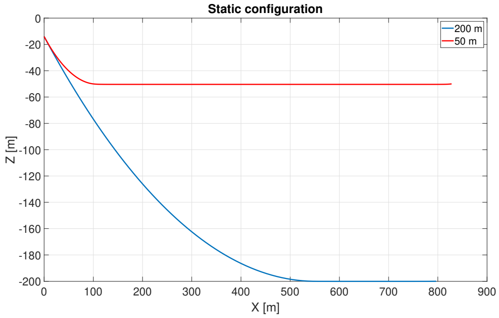

Figure 2.4: Catenary mooring configuration

2: With the same offset increment at fairlead, longer line in shallow water will be lifted up than that in deep water. Given the same pre-tension and stiffness at zero offset, the mooring line tension characteristics at different water depths are provided in Figure 2.5. The comparison illustrates that the mooring line stiffness increases faster with increasing offset for shallow water mooring than deep water mooring, meaning that if the same wave frequency motions are triggered, larger tension will be induced in shallow water mooring line. The dramatic increase in line stiffness and associated sudden increase of line tension may lead to potential line breaking.

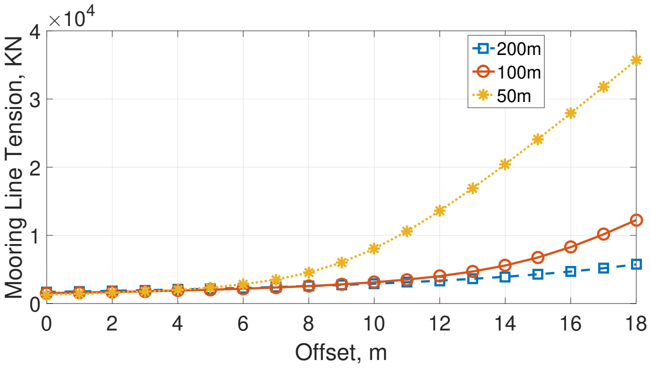

Figure 2.5: Mooring line tension characteristics at 50 m, 100 m and 200 m [66]

3: According to [67], the horizontal, geometric, in-elastic stiffness k_G of a catenary mooring line can be expressed as:

$$k_G = \frac{\partial T_H}{\partial x} = \omega[-\frac{2}{\sqrt{1+2\frac{T_H}{\omega h}}} + cosh^{-1}(1+\frac{\omega h}{T_H})]^{-1} \tag{2.1}$$

where ω is the unit weight of mooring line, x is the horizontal offset, h is water depth and T_H is the horizontal tension. Given the same horizontal tension T_H, the horizontal stiffness increases as water depth decreases as shown in Figure 2.6. The mooring system is designed to be compliant to the wave-frequency motions of the floating wind turbines. A stiffer mooring system will lead to higher natural frequencies of the horizontal motions, which are more easily excited by difference-frequency wave loads.

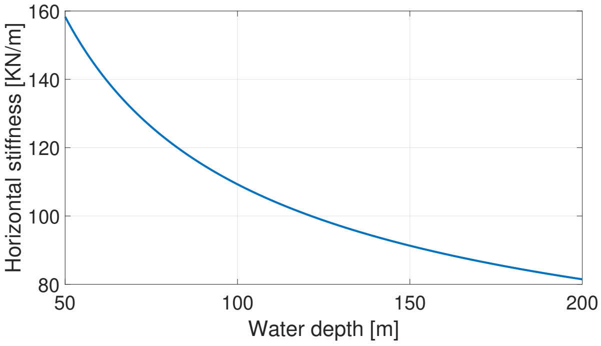

Figure 2.6: The influence of water depth on horizontal mooring stiffness

4: The top angles between mooring line and axes, α and β, indicate the level of catenary shape of mooring line as shown in Figure 2.7 (a). The bigger α is and the smaller β is, the less catenary shape is left while the tighter and the more stretched the line is. The initial values for α and β at static position are determined by mooring line tightness which is influenced by the horizontal span s (distance between fairlead and touch down point), effective water depth h (distance between fairlead and seabed) and length of suspended mooring line l_s as given in Equation 2.2:

$$tan\beta = sinh(\frac{2sh}{l_s^2 - h^2}) \tag{2.2}$$

Normally deep water mooring is designed with small tightness and reasonable horizontal pre-tension can be achieved even with small angle α. This keeps a high level of catenary shape, which means it is quite rare that the mooring line will be totally stretched even for large horizontal x-offset. On the other hand, shallow water mooring is usually quite tight because the effective water depth is much smaller compared with horizontal span. In order to obtain reasonable horizontal pre-tension as deep water, the angle α has to be increased even with heavier mooring line, which as a result will eliminate certain level of catenary shape.

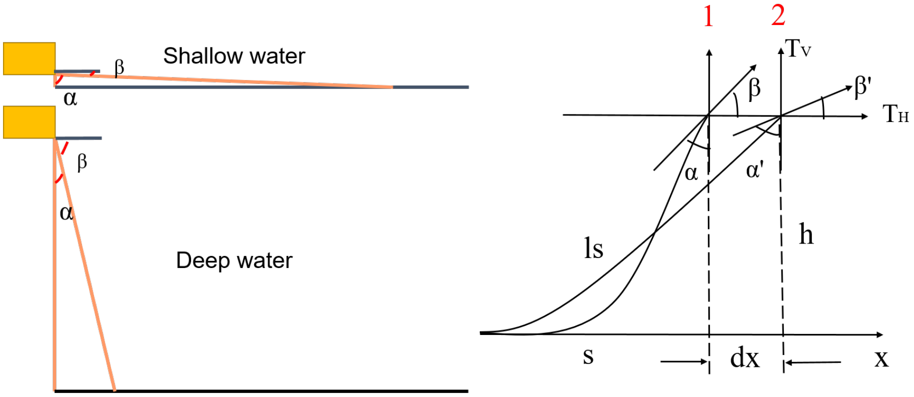

(a) Mooring line catenary shape in shallow and deep water

(b) Influence of x-offset on the top angles

Figure 2.7: Challenge of catenary mooring line top angles

From dynamic perspective, the increase of x-offset at fairlead will enlarge α and decrease β, but the change rate varies at different water depths. As an example given in Figure 2.7 (b), when the fairlead moves from position

1 to position 2 with a horizontal offset d_x, the angle α and β will change to α' and β'. Similar as deriving the mooring line horizontal stiffness in Equation 2.1, the average change rate of the angle β can be represented by the derivative of $tan\beta$ with respect to horizontal offset x:

$$\begin{aligned}\beta_x = \frac{\mathrm{d}tan\beta}{\mathrm{d}x} = \frac{\mathrm{d}\frac{T_V}{T_H}}{\mathrm{d}x} = \frac{\frac{T_V \cdot dT_H - T_H \cdot dT_V}{(T_H)^2}}{dx} &= \frac{1}{(T_H)^2} \cdot (T_V \cdot \frac{\mathrm{d}T_H}{\mathrm{d}x} - T_H \cdot \frac{\mathrm{d}T_V}{\mathrm{d}x}) \\ &= \frac{k_G}{(T_H)^2} \cdot (\omega\sqrt{h^2 + 2ah} - T_H \cdot \sqrt{\frac{1}{1+2ah}})\end{aligned} \tag{2.3}$$

where k_G is horizontal stiffness as described in Equation 2.1, ω is the unit weight of mooring line, x is the x-offset, h is water depth, a is a coefficient expressed as $a = T_H/\omega$. As a result, the average change rate for angle α expressed with unit degree can be written as:

$$\alpha_x = 90 - arctan(\frac{\mathrm{d}tan\beta}{\mathrm{d}x}) \tag{2.4}$$

Based on Equation 2.3 and 2.4, given the same horizontal tension T_H, the change rate of top angle, α_x, at different water depths are given in Figure 2.8. The angle change rate tends to increase as water depth decreases, which means shallow water mooring is more vulnerable to lose catenary shape and be stretched to straight line than deep water mooring. It will lead to potential vertical force on the anchor which is quite dangerous. As a result, large footprint of the mooring system is normally required for shallow water with long chains laying on the seabed.

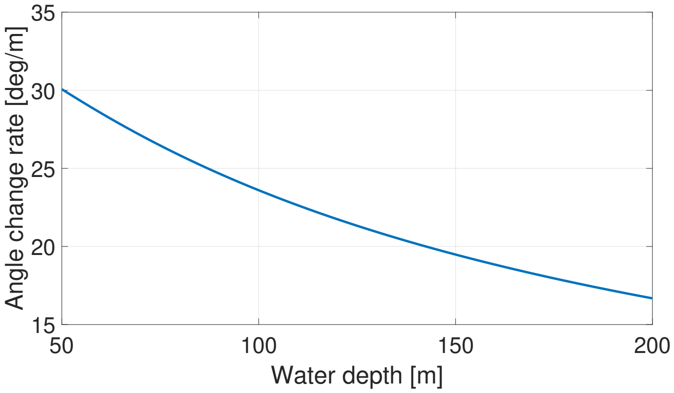

Figure 2.8: The change rate of top angle α with increasing x-offsets at different water depths

Taut mooring system

1: In taut mooring system, the restoring force mainly comes from the stretch of the line so that the horizontal, elastic stiffness, k_E, assuming a linearized elasticity, can be expressed as:

$$k_E = EA\frac{1}{l}sin\alpha \tag{2.5}$$

where E is the Young's modulus, A is the cross sectional area, l is the total line length and α is the angle between mooring line and vertical plane. Normally when water depth goes from deep to shallow, the total length of mooring line l will become shorter which will lead to a larger stiffness k_E. Therefore, when experiencing same amplitude of wave-frequency motion, the induced tension will be larger in shallow water mooring line.

2: Synthetic fiber rope as the most popular material used in taut mooring system is more complicated than chain and steel wire rope regarding the structural property. The change-in-length nonlinear behavior of synthetic fibre rope can be illustrated with the a spring-dashpot model as shown in Figure 2.9. The elastic stretch consists of instant-elastic and visco-elastic stretch which can be considered as a spring without and with a damper separately. The permanent stretch on the other hand includes visco-plastic stretch which is irreversible when exposed to tension and construction stretch where the ratchet allows the spring to extend above previous highest tension without retraction.

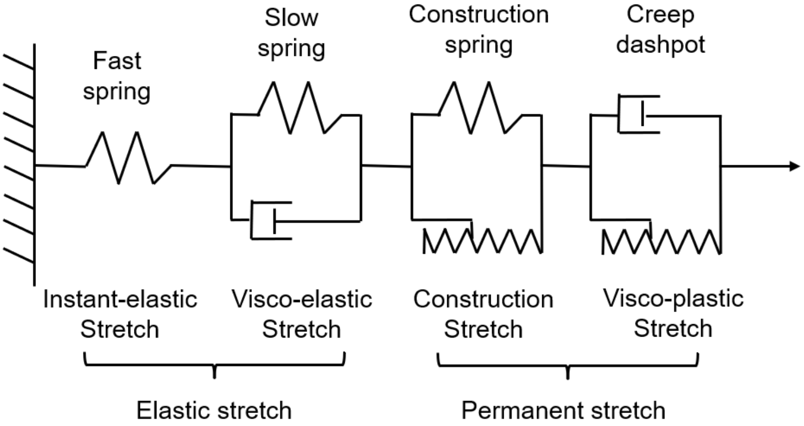

Figure 2.9: The spring-dashpot model for synthetic fibre rope [68]

As shown in Figure 2.10, the current industrial design practice is to use a lower-bound stiffness to calculate extreme offset and an upper-bound stiffness to calculate extreme tension. The influence of mean tension level on the stiffness is not taken into account. This conservative and inconsistent approach has been mentioned in several offshore standards including DNVGL-RP-E305 [69] and API-RP-2SM [60]. There is a lack of comprehensive understanding of the fibre rope performance and well-established numerical program that can include the nonlinear behavior of synthetic fibre rope.

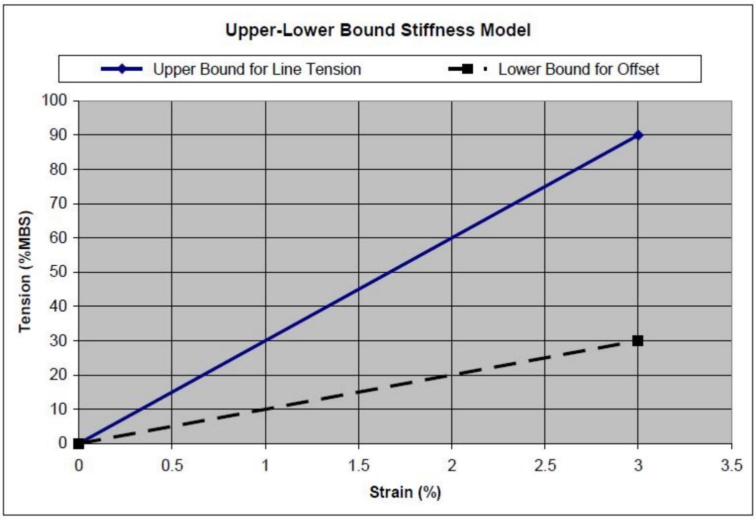

Figure 2.10: *Lower-bound and upper-bound stiffness model [60]*

2.5 Mooring design concept proposals in shallow water

In view of the design challenges in section 2.4 and the design criteria in section 2.3, seven initial mooring design concepts are proposed as potential mooring solutions in shallow water for floating wind turbine as shown in Figure 2.11. The black lines and blue lines indicate mooring lines made of chain links and synthetic fibre rope respectively. The red square and green circles stand for clump weights and buoys respectively. The concepts are designed at water depth of 50 m (shallow water) while a mooring model at 200 m (deep water) is used as a reference model. Because of the decent performance of the reference model, the mooring line length, pre-tension, offset-tension characteristics etc. of the reference models are selected as design criteria when the shallow water mooring concepts are proposed. The detailed performance of the seven concepts are further compared in Chapter 4.

The features of the models are introduced in Table 2.3, while the detailed properties of the mooring line are summarized in Table 2.4. Among the seven designs, the first four concepts are catenary moorings using chain cable while the last three are taut moorings using synthetic fibre rope. In addition, clump weight and buoy are also included in the comparative designs to check the influence on the overall performance. The parameters of the chain is determined according to Vryhof [61] and the parameter for the fibre rope is according to BRIDON [70]. The diameter of chain refers to the size of the steel bar, while the diameter of fibre rope refers to the size of the rope. The weight of mooring line is given as the unit weight in water. The anchor radius refers to the distance of anchor from the center of the platform. The property of buoy is given as the net buoyancy. The numerical modelling technique for synthetic fibre rope is introduced in Section 3.4 especially regarding the axial stiffness in static and dynamic conditions. EAs and EAd stands for axial stiffness used in static analysis and dynamic analysis respectively as described in Equation 3.27 & 3.29.

Meanwhile, drag embedment anchor is used for the four catenary mooring designs. To be more specific, 17 ton Stevshark Mk5 anchor designed by Vryhof [61] is selected. This anchor can be adjusted for varying soil conditions through modifying the shank angle. The selection is based on two reference projects: Hywind II project [71] and WindFloat project [20] where same anchor was used. In order to better take the vertical load from the fibre rope and achieve accurate anchor location, suction anchor is chosen for the three taut mooring designs. Similar to the conceptual TLWT project [72], a 50 ton suction anchor is chosen. More details regarding the comparison of different mooring designs are available in appended paper 1.

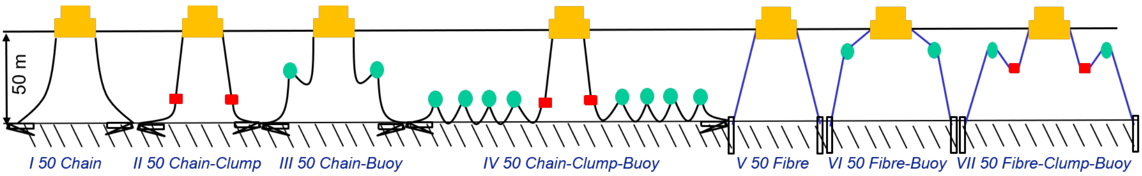

Figure 2.11: Mooring configurations

Table 2.3: Mooring concept introduction

Model	Description	Feature
I	Chain	The weight is quite heavy in order to achieve reasonable pre-tension as deep water mooring.
II	Chain-Clump	Clump weight can contribute to pre-tension, so the weight of mooring line can be reduced.
III	Chain-Buoy	Buoy can influence the catenary shape by introducing more geometric stiffness.
IV	Chain-Clump-Buoy	The attachment of buoys at the resting line can help to decrease the weight of lifted line and decrease the extreme tension at large offset.
V	Fibre	Pure fibre rope is used.
VI	Fibre-Buoy	Buoy is included as comparative design to include geometric stiffness.
VII	Fibre-Clump-Buoy	Both clump weight and buoy are included as comparative design.

Table 2.4: Mooring line properties

	Material	Weight	Diameter	MBS	Length	Radius	Clump	Buoy	EAs	EAd
		kg/m	m	KN	m	m	t	KN	KN	KN
200	Chain	113.35	0.0766	6001	835.5	837.6	No	No	7.54E5	
I	Chain	613	0.175	25174	835.5	868.8	No	No	2.62E6	
II	Chain	308	0.124	14358	835.5	868.8	28	No	1.31E6	
III	Chain	308	0.124	14358	835.5	868.8	No	330	1.31E6	
IV	Chain	308	0.124	14358	935.5	965.4	28	330	1.31E6	
V	Fibre	26.5	0.203	11772	1000	1048.9	No	No	Eq 3.27	Eq 3.29
VI	Fibre	26.5	0.203	11772	1000	1048.9	No	70	Eq 3.27	Eq 3.29
VII	Fibre	26.5	0.203	11772	1000	1048.9	15	70	Eq 3.27	Eq 3.29

Chapter 3

Numerical modelling and analysis method

3.1 General

Floating wind turbine normally consists of several structural components including blades, nacelle, rotor, floater and mooring system etc. In order to better account for the aerodynamics, hydrodynamics, structural dynamics, control system dynamics and mooring line dynamics, a coupled aero-hydro-servo-elastic analysis method is required to perform the time domain simulations. As most of current available hydrodynamic analysis codes for floating wind turbine are based on linear wave theory which is more applicable for deep water, there is a need of developing new numerical method that can better consider the significant nonlinear wave effect in shallow water for floating wind turbine.

3.2 Aerodynamics

The tower, nacelle and rotor of wind turbine are subjected to aerodynamic loads. The loads acting on tower and nacelle can be defined as drag force, while the loads on rotor consists of both lift and drag loads which can be calculated with different level of accuracy and efficiency: 1D momentum theory, 2D blade element momentum (BEM) theory and 3D blade structure with a Navier-Stokes's solution etc [73]. Currently, most of the available numerical tool for floating wind turbines are based on BEM theory to calculate aerodynamic loads including SIMA and HAWC2 which are used in this study.

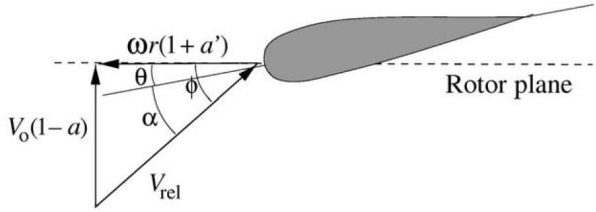

Figure 3.1: Local element velocities and flow angles

The BEM theory is based on coupling momentum theory with blade element theory, which considers the flow across a given section as two-dimensional. Since the blades are slender structures and the span-wise velocity component is much lower than the stream-wise component, the forces at a specific point on the blades can be calculated based on two-dimensional aerodynamic properties with lift force, drag force and pitching moment on each element [74]. It can be illustrated by breaking the blades into many elements along the span as shown in Figure 3.1 where θ is the local twist angle which is the sum of original section twist angle and blade pitch angle, r is the distance to the center of rotation, ω is the rotating angular velocity, V_0 is the wind velocity perpendicular to the rotor plane, ϕ is the flow angle and α is the attacking angle which is defined as:

$$\alpha = \phi - \theta, \qquad tan\phi = \frac{V_0}{\omega\, r}\frac{1-a}{1+a'} \tag{3.1}$$

where a and a' are axial and rotational induction factors given as:

$$a = [1 + \frac{4sin^2\phi}{\sigma C_n}]^{-1}, \qquad a' = [-1 + \frac{4\, sin\phi\, cos\phi}{\sigma\, C_t}]^{-1} \tag{3.2}$$

where σ is solidity, normal and tangential force coefficients are defined as $C_n = C_L\, cos\phi - C_D\, sin\phi$, $C_t = C_L\, sin\phi - C_D\, cos\phi$ respectively. At last, the lift and drag coefficients can be described as:

$$C_L(\alpha) = \frac{f_L}{0.5\rho V_{rel}^2 c}, \qquad C_D(\alpha) = \frac{f_D}{0.5\rho V_{rel}^2 c} \tag{3.3}$$

where f_L and f_D are lift and drag loads on the section, ρ is air density, c is chord length of the section, V_{rel} is the relative wind velocity which is defined as:

$$V_{rel} = V_0\sqrt{(1-a)^2 + (\frac{r\omega_r}{V_0}(1+a'))^2} \tag{3.4}$$

The above equations serves as the basis of classic BEM theory which are based on several assumptions [74]. For example, the flow over the blades is assumed to be in equilibrium all the time, which disregards the dynamics of the wake. Pressure gradients in the span-wise direction of the blade are ignored which will lead to a difference when the tip speed ratios are high. In practice, several extensions can be made to the BEM theory in order to handle more features, such as dynamic inflow, skew inflow, shear effect on induction, large blade deflections, tip loss correction, dynamic stall etc. In particular, three models are available to account for dynamic stall: Stig Øye model which accounts for stall separation lag, modified Beddoes-Leishmann model which also considers the effects of shed vorticity from the trailing edge and ATEFlap dynamic stall model that calculates the unsteady lift, drag and moment on a 2D airfoil section equipped with adaptive trailing edge flap. In this thesis, the modified Beddoes-Leishmann model is used to account for the dynamic stall. The flexibility of tower and blades are considered in the aeroelasticity calculation of the aerodynamic loads for bottom-fixed offshore wind turbine. As for floating wind turbine, the platform motion should also be considered in the dynamic analysis.

3.3 Hydrodynamics

The hydrodynamic analysis of an offshore structure normally consists of determining the sea states at the relevant site depth; selecting applicable wave theory; choosing appropriate hydrodynamic load computation method; calculating structural response.

Ocean wave behaves quite differently at different water depths which as a result requires different numerical models to properly describe its property. At the same time, the hydrodynamic force model for offshore wind turbine should be sophisticated enough to capture the structural complexity and efficient enough to be engineering practical. Suitable wave theory and hydrodynamic load modelling method for semi-submersible FWT should be carefully determined when the water depth is shallow. Normally, Morison's formula is used for slender structures while panel methods with potential flow theory are used for large volume structures.

3.3.1 Wave theory

In reality, ocean waves are random, nonlinear and irregular which varies in height, length, propagation speed and traveling directions. Wave theories used to predict the wave kinematics can be divided into linear and nonlinear groups according to the simplification level of boundary conditions. The theories differ in the functional formulation and in the degree to which they satisfy the nonlinear kinematic and dynamic FSBCs.

A linear regular wave has a sinusoidal surface profile with small amplitude and steepness, while a nonlinear wave has sharper crests and flatter troughs. The nonlinearity of wave can be described by higher order bound and resonant nonlinearities [75]. Bound nonlinearities are induced by higher order nonlinear harmonics which are phase locked to the first order wave component. They tend to modify the free surface profile by sharpening the peaks and flattening the troughs. Resonant nonlinearities on the other hand influence the energy distribution within the wave spectrum by adjusting the phases and amplitudes of the first order wave components and produces new wave components satisfying the dispersion relation. The nonlinear regular waves can be described by Stokes, cnoidal, stream function or solitary wave theories. The applicable water depth for various wave theories is discussed in IEC 61400-3 [76] as shown in Figure 3.2. Horizontal axis is a non-dimensional measure of depth shallowness and the vertical axis is a measure of wave steepness.

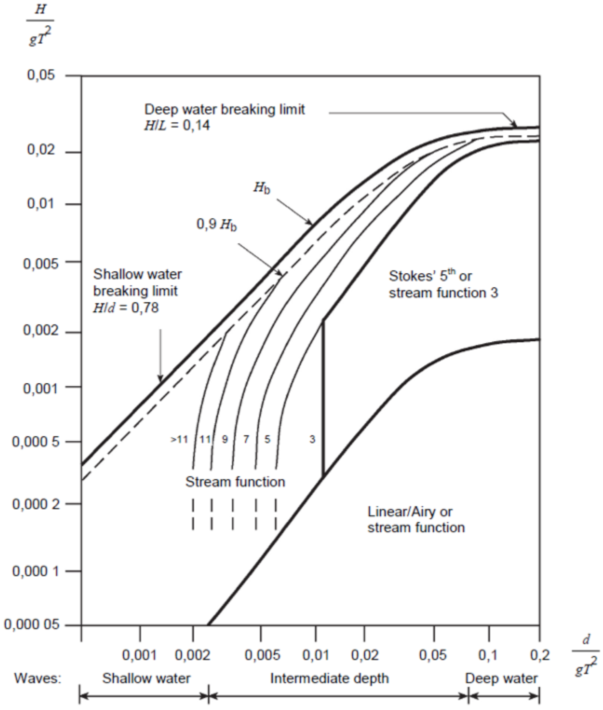

Figure 3.2: Applicability of various wave theories [76]

3.3.1.1 Linear wave theory

Linear wave theory also known as Airy wave theory is the most widely used wave theory in offshore industry especially for medium and large water depth. It is based on the assumption that the contribution from the nonlinear terms in FSBCs is negligible. The mathematical expression can be derived considering a incompressible, inviscid and irrotational fluid.

1. Laplace equation is the governing equation in the fluid domain:

$$\bigtriangledown^2 \phi = 0 \tag{3.5}$$

2. Considering wave elevation, η which is proportional to wave height H is small, the FSBCs can be linearized and described at the still water level (SWL) $z = 0$ instead of $z = \eta$ using Taylor's expansion. Dynamic FSBC is written as:

$$\frac{\partial \phi}{\partial t} = -g\eta \quad \text{on} \quad z = 0 \tag{3.6}$$

   where the atmospheric pressure is assumed to be zero on the free surface.

3. Kinematic FSBC is expressed as

$$\frac{\partial \eta}{\partial t} = \frac{\partial \phi}{\partial z} \quad \text{on} \quad z = 0 \tag{3.7}$$

4. The impermeability condition, such as sea bottom and fixed body surfaces is described as:

$$\frac{\partial \phi}{\partial n} = 0 \tag{3.8}$$

3.3.1.2 Fully nonlinear wave theory

According to Shao and Faltinsen [77], different from linear wave theory, fully nonlinear wave theory provides more accurate mathematical expressions by including the nonlinear terms at FSBCs which are written as:

- Fully nonlinear dynamic FSBC

$$\frac{\partial \phi}{\partial t} = -g\eta - \frac{1}{2} \bigtriangledown \phi \cdot \bigtriangledown \phi \qquad \text{on} \qquad z = \eta(x, y) \tag{3.9}$$

- Fully nonlinear kinematic FSBC

$$\frac{\partial \eta}{\partial t} = \frac{\partial \phi}{\partial z} - \overline{\bigtriangledown}\phi \cdot \overline{\bigtriangledown}\eta \qquad \text{on} \qquad z = \eta(x, y) \tag{3.10}$$

Here $\bigtriangledown = \vec{i}\frac{\partial}{\partial x} + \vec{j}\frac{\partial}{\partial y} + \vec{k}\frac{\partial}{\partial z}$ and $\overline{\bigtriangledown} = \vec{i}\frac{\partial}{\partial x} + \vec{j}\frac{\partial}{\partial y}$. $\vec{i}$, $\vec{j}$ and $\vec{k}$ are unit vectors along x-, y- and z- axis respectively.

When a material derivative following an arbitrary velocity $\vec{v} = \{v_x, v_y, v_z\}$ is introduced, the fully nonlinear FSBCs can be rewritten as:

$$\frac{\mathrm{D}\phi}{\mathrm{D}t} = -g\eta - \frac{1}{2} \bigtriangledown \phi \cdot \bigtriangledown\phi + \vec{v} \cdot \bigtriangledown\phi \qquad \text{on} \qquad z = \eta(x, y) \tag{3.11}$$

$$\frac{\mathrm{D}\eta}{\mathrm{D}t} = \frac{\partial\phi}{\partial z} - \overline{\bigtriangledown}\phi \cdot \overline{\bigtriangledown}\eta + \{v_x, v_y\}^T \cdot \overline{\bigtriangledown}\eta \qquad \text{on} \qquad z = \eta(x, y) \tag{3.12}$$

A semi-Lagrangian approach can be used by following the vertical velocities of fluid particles on the free surface, which means in 2D case the following FSBCs shall be applied in the numerical implementation:

$$\frac{\mathrm{D}\phi}{\mathrm{D}t} = -g\eta - \frac{1}{2} \bigtriangledown \phi \cdot \bigtriangledown\phi + \frac{\partial\phi}{\partial z}(\frac{\partial\phi}{\partial z} - \frac{\partial\phi}{\partial x}\frac{\partial\eta}{\partial x}) - \mu(x)\phi \quad \text{on} \quad z = \eta(x) \tag{3.13}$$

$$\frac{\mathrm{D}\eta}{\mathrm{D}t} = \frac{\partial\phi}{\partial z} - \frac{\partial\phi}{\partial x} \cdot \frac{\partial\eta}{\partial x} - \mu(x)\eta \quad \text{on} \quad z = \eta(x) \tag{3.14}$$

Here $\mu(x)$ is a damping coefficient to dissipate the energy of the waves which exists only in the damping zone at the end of the numerical wave tank.

Except linear Airy wave, the other periodic wave theories shown in Figure 3.2 are restricted to a regular form which makes them not suitable to represent the realistic irregular wave realizations. Meanwhile, linear wave theory is formulated on the basis that only the linear terms are kept in FSBCs while nonlinear terms are totally neglected. It can provide good estimation of the wave kinematics for small waves in deep water. However, the wave profiles will become quite nonlinear due to the significant contribution from nonlinear terms when the wave height increases or water depth decreases. In such case, fully nonlinear wave theory can provide better description of wave profiles and water particle kinematics. Therefore, irregular wave train simulated from fully nonlinear models is supposed to be the best wave option to describe large waves in shallow water. The difference of structural response when exposed to irregular linear and fully nonlinear wave is one of the main focuses of this study.

3.3.2 Wave kinematics

Wave kinematics including wave elevation, velocity potential, velocity and acceleration of wave particles are important properties of ocean waves. A proper handling of the wave kinematics data can not only guarantee the accuracy of the calculation of the hydrodynamic load but also increase the efficiency of the process.

3.3.2.1 Wave generation

The fully nonlinear wave kinematics in this thesis is generated using 2D HPC method which is developed by Shao and Faltinsen [77, 78, 79]. It is a potential flow solver dividing the fluid domain into quadrilateral cells associated with harmonic polynomials which are used to describe the velocity potential in each cell. An explicit 4^{th} order Runge-Kutta method is applied to integrate the FSBCs in time to update the wave elevation and velocity potential on the free surface. Wavemaker at left end of the numerical wave tank is used to generate the target waves. A sudden start of a wavemaker will introduce instability and breakdown of the simulation eventually. Thus, a ramp function $r(t)$ is applied to the wavemaker signal $s(t)$ so that the modified signal becomes $s(t) = \overline{s}(t) \cdot r(t)$. In this study, the following ramp function is applied

$$r(t) = \begin{cases} \frac{1}{2}[1 - cos(\pi \frac{t}{T_{ramp}})], & t < T_{ramp} \\ 1, & t \geq T_{ramp} \end{cases} \tag{3.15}$$

Here T_{ramp} is the duration of the ramp, which is taken as 2 times of the peak period T_p of the wave spectrum. A numerical damping zone is implemented at the end of the numerical wave tank to dissipate the energy of the waves. A quadratic function, which has been suggested by Ning and Teng [80] is applied:

$$\mu(x) = \begin{cases} \mu_0(\frac{x-x_b}{\lambda_b})^2, & x > x_b \\ 0, & x \leq x_b \end{cases} \tag{3.16}$$

Here x is the coordinate measured from the location of the wavemaker. x_b is the location where the damping zone starts and λ_b is the length of the damping zone. The length of the damping zone and the damping strength μ_0 are so chosen to minimize the wave reflection from the wall at the end of the tank.

A free-surface filter is implemented in order to simulate nonlinear steep waves over a long time duration without any instability developing. Without such a filter, sawtooth instability will eventually occur for waves over a certain steepness as consequence of aliasing effects due to the quadratic terms in fully nonlinear free surface conditions. In this study, the simulated wave elevation along the numerical wave tank is projected into wave number space through FFT technique, and the following filter is then applied to the resulting wave numbers

$$\gamma(k) = exp(-(\frac{k}{\alpha \cdot k_0})^{\beta}) \tag{3.17}$$

Here k_0 is a reference wave number, which normally corresponds to a characteristic wave number of the considered wave spectrum. In this study, k_0 is taken as k_p, which is the root of the dispersion relationship $\omega_p^2 = k_p h \cdot \tanh(k_p h)$. Here $\omega_p = 2\pi/T_p$, h is the water depth. α and β are constant coefficients.

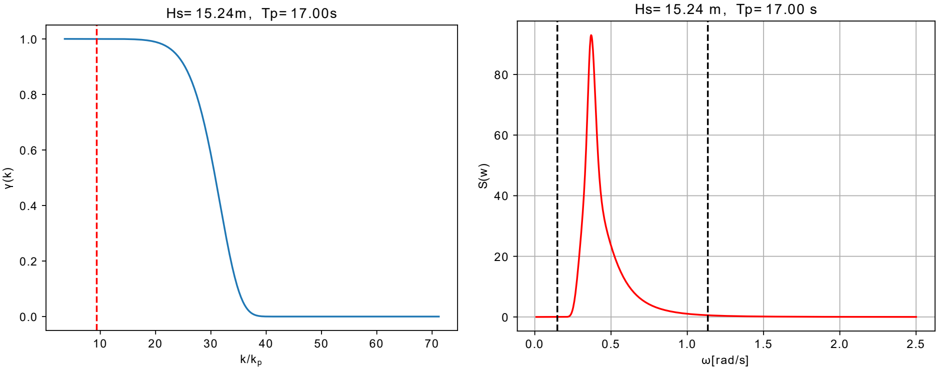

(a) Filter strength *(b) Cut-off of wave spectra*

Figure 3.3: Wave generation

An ideal filter should be able to sufficiently remove energy from very short waves while keep the important waves unchanged. α and β are determined through $\gamma(k_{max}) = 0.01$ and $\gamma(k_{min}) = 0.99$ which indicate that the filter takes away 99% wave amplitude from a short wave with wave number k_{max} and only 1% wave amplitude from a wave with wave number k_{min}. In this study, $k_{max} = 2\pi/(4\Delta x)$ and $k_{min} = 2\pi/(10\Delta x)$ are used in all the analysis with irregular waves. Δx is the size of the element along horizontal direction of the numerical wave tank. Figure 3.3 (a) is an example of the filter strength $\gamma(k)$ as function of k/k_p for a sea state with H_s =*15.24 m* and T_p =*17.0 s*. The filter strength is dependent on the discretization and the characteristic wave number $k_0 = k_p$. The horizontal discretization is defined with $\Delta x = \frac{\lambda_p}{40} = \frac{2\pi}{k_p} \cdot \frac{1}{40}$, which means that 40 elements are uniformly distributed within a characteristic wave length, which corresponds to the peak-frequency of the spectrum. According to figure 3.3 (a), the filter completely removes energy for waves with $k/k_p \geq 40$ while it has almost no effect for waves with $k/k_p \leq 20$.

When a wave spectrum is used to generate irregular waves in the time domain, it is common practice to truncate the wave spectrum by a lower-limit frequency ω_l and upper-limit frequency ω_u. The cut-off frequency limit in this thesis is determined mainly based on two aspects: the important waves containing most of the energy cannot be cut off and extremely short wave which requires quite fine mesh should be cut off in order to avoid numerical breakdown and increase of CPU time. As recommended by Stansberg et al. [81] and DNV-RP-C205 [82], the cut-off limit defined in this study is: $\omega_u = \sqrt{2g/H_s}$ and $\omega_l = 0.4 * \omega_p$, which leads to only 1.1% loss of the zero-th moments of the wave spectra for the condition. The vertical dashed lines in Figure 3.3 (b) represent the cut-off frequencies while the red lines represent the wave spectra.

3.3.2.2 Polynomial fitting method

The velocity potential, wave elevation, velocity are directly calculated from 2D HPC wave tank, while acceleration is available by post-processing velocity and grid deformation. All the grids are fixed in the tank in linear wave making problem, while the grids deform vertically in nonlinear case as shown in Figure 3.4, which leads to the different technique when calculating the acceleration.

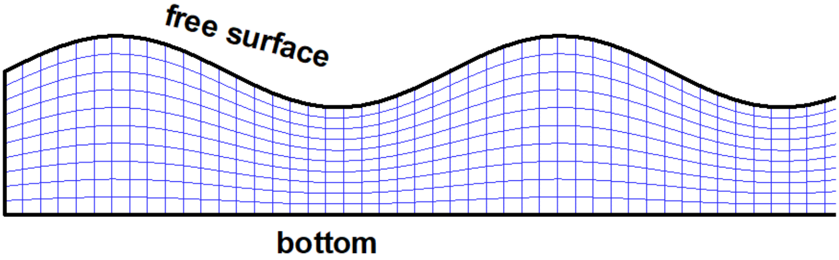

Figure 3.4: Example of boundary-fitted grid, which deforms with the instantaneous wave profile [77].

Bernoulli's equation is only valid in an inertial system. Therefore, material derivative is introduced to calculate the acceleration [72]:

$$\frac{\partial U}{\partial t} = \frac{\delta U}{\delta t} - w_{grid} \cdot \bigtriangledown U \tag{3.18}$$

Since the grid deformation only appears in vertical direction, Equation 3.18 can be further written as:

$$\frac{\partial U}{\partial t} = \frac{\delta U}{\delta t} - \frac{\partial z}{\partial t} \cdot \frac{\partial U}{\partial z} \tag{3.19}$$

where U is the velocity, $\frac{\partial z}{\partial t}$ is the relative velocity representing the grid deformation in vertical direction.

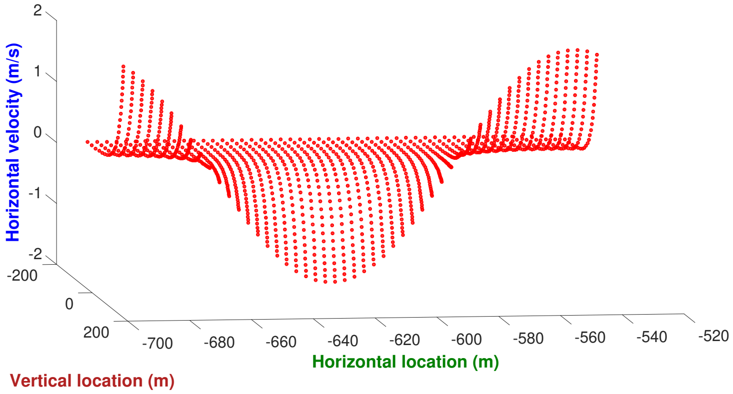

Figure 3.5: Horizontal velocity of wave particles

The wave kinematics data obtained from the wave tank at each time step is expressed at discrete grid points across the whole wave field. Figure 3.5 is an example of the horizontal velocity of wave particles in the wave field with corresponding horizontal and vertical coordinates at a certain time step. At the same time step, there are three other similar figures representing vertical velocity, horizontal acceleration and vertical acceleration which are not shown here. It takes about 18 hours to generate a 1 hour irregular wave realization with 148 grids horizontally and 22 grids vertically on a normal computer when only 2 processors are engaged. However, the size of resulting wave kinematics files including wave elevation, velocity and acceleration in both horizontal and vertical directions is around 8 Gbyte, which exceeds the memory requirement of the simulation tool for wind turbine, HAWC2 in this study. Besides, huge occupation of virtual memory will slow down the computation especially for floating wind turbine whose element number is normally very large.

Table 3.1: Polynomial function

order	polynomial
0	1
1	$x \quad z$
2	$x^2 \quad xz \quad z^2$
3	$x^3 \quad x^2z \quad xz^2 \quad z^3$
...	...
n	$x^n \quad x^{n-1}z \quad x^{n-2}z^2 \quad ... \quad x^2z^{n-2} \quad xz^{n-1} \quad z^n$

Accordingly, a polynomial fitting method to deal with the wave kinematics is developed. First of all, the vertical and horizontal dimensions of the wave field are determined by water depth and footprint of the mooring system respectively. Normally, it is sufficient to use 50 grids horizontally per wavelength and 30 grids along water depth. Then the whole wave field is divided into a number of horizontal divisions based on the wavelength. Within each division, a 2 dimensional polynomial function representing horizontal and vertical coordinates up to a certain order n is introduced as shown in Table 3.1. The corresponding coefficients using least-squares method are calculated and arranged in a descending power regarding x coordinate. As a result, the kinematics data at each time step can be expressed in a function form instead with location coordinates as input variables:

$$U = c_1 x^n + c_2 x^{n-1} z + ... + c_{\frac{(n+1)(n+2)}{2}-2} x z^{n-1} + c_{\frac{(n+1)(n+2)}{2}-1} z^n + c_{\frac{(n+1)(n+2)}{2}} \tag{3.20}$$

Here x represents horizontal coordinate, z represents vertical coordinate and c_i is corresponding polynomial coefficient.

In nonlinear wave problem, the vertical coordinates of the grid points can be directly applied as input for z, since the grids deform vertically following instantaneous wave elevation up to the free surface. Meanwhile, in linear wave problem, the grid is fixed and the kinematics is calculated below mean water level. Therefore, Wheeler stretching method is applied to obtain the kinematics up to the free surface by scaling vertical coordinate:

$$z^{'} = (z - \eta)\frac{d}{d + \eta} \tag{3.21}$$

where z is original grid coordinate, $z^{'}$ is scaled coordinate, η is the instantaneous free surface elevation and d is water depth.

As a result, the wave kinematics at any locations in the whole wave field at each time step can be calculated based on Equation 3.20, which include not only the original grid points directly from the wave tank as shown in

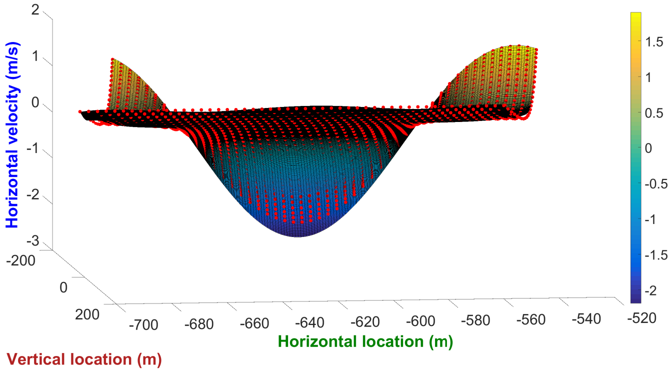

Figure 3.6: Fitting surface and original data

Figure 3.5 but also at the locations between the grid points. The resulting wave kinematics information can be expressed with a fitting surface where different color represent different amplitude of the kinematics. Figure 3.6 is an example of the fitting surface for horizontal velocity and it can be seen that the velocity between the grid points are available as well represented by the fitting surface. The same procedure is applied to acceleration and velocity in both horizontal and vertical directions.

In the end, the original wave kinematics expressed at discrete grid points are replaced by coefficients c_i and corresponding polynomial functions x_i, z_i representing horizontal and vertical coordinates. The size of data is decreased from 8 Gbyte to 1 Gbyte for a 1 hour irregular wave problem using 148 grids horizontally and 22 grids vertically, which fulfills the memory requirement of HAWC2 to import pre-generated wave kinematics. The order of the polynomial function applied should be carefully chosen in order to achieve good result especially for irregular wave problems whose variation of wave kinematics is harder to predict.

3.3.3 Hydrodynamic load modelling

Once proper wave model is determined, the resulting hydrodynamic load on the structure can be calculated using different theories mainly depending on the size of the structure. Radiation/diffraction theory and Morison's equation are widely applied in current offshore industry because of their accuracy and efficiency.

3.3.3.1 Radiation/diffraction theory

Radiation/diffraction theory is mainly for large-volume structure to describe the wave-body interaction. It is used to study second-order wave load effect in this thesis [66]. A linear radiation/diffraction theory solves the Laplace equation in the fluid domain with linearized boundary conditions. The solution consists of independent velocity potentials representing incident, diffraction and radiation wave problems which are expressed with frequency-dependent added mass, damping and restoring coefficients in frequency domain. The results can be further applied in time domain simulation through Cummins equation [83]. Take a floating single degree-of-freedom system including mooring system as an example, the motion equation in time domain can be written as:

$$(\mathbf{M}+\mathbf{A}_\infty)\ddot{\vec{x}}(t)+\int_0^t \kappa(t-\tau)\dot{\vec{x}}(\tau)d\tau+\mathbf{C}\vec{x}(t)+\mathbf{K}(\vec{x}(t)) = \vec{F}^{FK+D}(t)+\vec{F}^{Aero+Drag}(\dot{\vec{x}}(t),\ddot{\vec{x}}(t)) \tag{3.22}$$

where $\mathbf{M}$ is the mass matrix of the body, $\mathbf{A}_\infty$ is the added mass matrix at infinite frequency, $\kappa(t-\tau)$ is the retardation function consisting of frequency-dependent added mass and damping coefficient, $\mathbf{C}$ is the hydrostatic restoring matrix, $\mathbf{K}(\vec{x}(t))$ is the nonlinear restoring matrix from the mooring system, $\vec{F}^{FK}$ is the Froude-Krylov force, $\vec{F}^{D}$ stands for the diffraction force, $\vec{F}^{Aero}$ is the aerodynamic load and $\vec{F}^{Drag}$ is the viscous drag force, $\vec{x}, \dot{\vec{x}}, \ddot{\vec{x}}$ are the displacement, velocity and acceleration.

Based on linear radiation/diffraction theory, the first-order wave load can be solved at the mean position of the body with linearized boundary conditions and the resulting loads and motions oscillate with the incident wave frequency. second-order wave loads on the other hand are proportional to the square of the wave amplitude and the frequency is equal to the sum or the difference of incident wave frequency pairs. Generally, the second-order hydrodynamic load is small in magnitude but it may lead to the resonance of structure with large response. When it comes to loads and motions of a semi-submersible platform, the second-order difference-frequency load also known as wave drift load becomes important consisting of mean wave drift load and slowly-varying drift load.

The second-order wave loads can be described by either full QTF method or Newman's approximation. Similar to response amplitude operator (RAO) to each individual wave component for the first order problem, QTF is based on each pair of wave components and represents the contribution from the wave pair to the second-order wave load. QTF is expressed with a complex-valued function of wave directions β_1 & β_2 and wave periods τ_1 & τ_2 of the wave pair. Then the difference-frequency second-order wave loads are the sums of contributions from all the combination of wave pairs in the sea state:

$$F_{drift} = \sum_{i=1}^{n}\sum_{j=1}^{n} \mathbb{R}\left\{Q_d(\beta_i,\beta_j,\tau_i,\tau_j)\cdot a_i \cdot a_j \cdot exp\left[i(\omega_i-\omega_j)t-(\phi_i-\phi_j)\right]\right\} \quad (3.23)$$

where $\mathbb{R}$ means taking the real part of the complex number, $Q_d(\beta_i,\beta_j,\tau_i,\tau_j)$ is wave drift QTF for wave components i and j, a_i and a_j are the wave amplitudes, ω_i and ω_j are the wave frequencies and ϕ_i and ϕ_j are the wave phases.

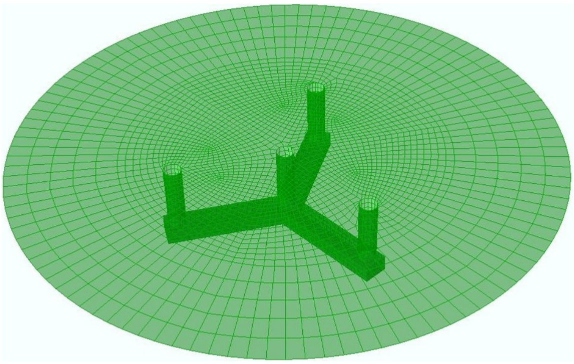

Figure 3.7: Mesh of floater and free surface in HydroD

Despite QTF can provide an accurate estimation of second-order wave loads, the calculation of QTF is however quite intensive because it not only involves analysis in diffraction/radiation code for N*(N+1)/2 wave pairs but also calculates the double summation in Equation 3.23. The computation in numerical code normally requires an additional mesh of free surface as shown in Figure 3.7. Newman's approximation on the other hand only requires wave pairs of equal direction and periods which are the diagonal values of the full QTF data representing the mean wave drift load. The off-diagonal values defining the slowly-varying drift load are thereafter extrapolated based on the diagonal terms, which reduces the calculation time significantly.

Newman's approximation can provide accurate result for low difference frequencies when $\Delta\omega = |\omega_i - \omega_j|$ is small, which normally is the case for massive structures such as barges or FPSO in surge, sway and yaw, and for which the drift forces in regular wave are large. However, the accuracy is limited for responses whose natural period is small such as heave, roll and pitch for slowly-varying resonant excitation forces. Since the second-order incident potential is not taken into account at all for Newman's approximation, there may be inaccuracy in shallow water calculation even for small $\Delta\omega$, which has been demonstrated by You (2012) [50] and de Hauteclocque et al. (2012) [84].

3.3.3.2 Morison's equation

The structure can be considered as slender structure when the diameter-to-wavelength ratio is less than 1/5. Under such case, Morison's equation which is a semi-empirical method can be used to calculate the resulting hydrodynamic loads. It has been mostly applied on slender vertical surface-piercing cylinders such as monopile and spar. Some recent research results also proved the applicability for small-diameter floating wind turbine like semi-submersible in high sea states compared to model scale measurements [85]. The hydrodynamic loading according to Morison's equation is expressed in terms of the undisturbed fluid-particle velocity and accelerations which provides a straightforward manner to consider nonlinear wave kinematics models and it is used to study fully nonlinear wave load effect in this thesis [86, 87, 88]. The wave force dF on a strip of length dz of a rigid moving circular cylinder can be written as:

$$dF = \rho\frac{\pi D^2}{4}C_M\frac{\mathrm{d}u_w}{\mathrm{d}t}dz - \rho\frac{\pi D^2}{4}(C_M-1)\frac{\mathrm{d}\dot{x}}{\mathrm{d}t}dz + \frac{\rho}{2}C_D D\left|u_w-\dot{x}\right|(u_w-\dot{x})dz \tag{3.24}$$

where D is the cylinder diameter, u_w is velocity of the undisturbed incident wave, $\dot{x}$ is velocity of the moving of cylinder, C_D is the drag coefficient and C_M is the inertia coefficient which is related to the added mass coefficient C_A as $C_M = C_A + 1$. C_D and C_M are dependent of several parameters such as Reynolds number, the roughness number and the Keulegan-Carpenter number. They should be determined empirically and C_M specifically can be determined according to the result from potential flow theory. In conclusion, Morison force as shown in Equation 3.24 can be interpreted as three component: Froude-Kriloff force, hydrodynamic added mass force and drag force.

3.3.3.3 Computational fluid dynamics

Computational fluid dynamics (CFD) method with proper turbulence modelling considered as a highly sophisticated numerical method to study floating wind turbine can inherently takes into account relevant linear and non-linear hydrodynamic effects including viscous effects [57]. Despite the accuracy in hydrodynamic wave modeling with CFD method, high computational effort is expected which still requires a lot of effort before engineering application. CFD method is not the focus of this study, therefore only a brief introduction is given in this section.

A numerical CFD code normally consists of a fluid-structure interaction part which solves Navier-Stokes equations and a structural part which models the structural components. Navier-Stokes equations supplemented with continuity equation is the basis for CFD method which can be written as follows for incompressible flows:

$$\rho\left(\frac{\partial \mathbf{u}}{\partial t} + \bigtriangledown \cdot (\mathbf{uu})\right) = -\bigtriangledown p + \rho \mathbf{g} + \bigtriangledown \cdot \mu(\bigtriangledown \mathbf{u} + \bigtriangledown \mathbf{u}^T) + \mathbf{F} \tag{3.25}$$

$$\bigtriangledown \cdot \mathbf{u} = 0 \tag{3.26}$$

where ρ is the density, $\mathbf{u}$ is velocity, $\mathbf{g}$ is gravitational acceleration, μ is dynamic viscosity, p is pressure and $\mathbf{F}$ is the force term that couples the fluid-structure part with the structural part. The Navier-Stokes equations are analytical equations and discretization is needed to be implemented into numerical codes. Typical discretization methods include finite difference method, finite element method and finite volume methods.

3.4 Mooring dynamics

Finite element method (FEM) approach is normally used in the numerical code to model the mooring line [89]. The modelling technique for catenary is to use 3-D bar element which consists of a node with 3 spatial degree of freedoms at each element end. For catenary mooring consisting of chain link or steel wire rope, the numerical model is specified in terms of sequence of segments with homogeneous cross sectional properties. Cross sectional component type, length and number of elements to be used for finite element discretization are specified for each segment. The seafloor contact is modelled by nonlinear stiffness which is implemented as springs at the nodal points that may touch the seafloor. The horizontal contact force with the seabed will be modeled as independent with respect to axial and lateral direction.

With respect to the current conservative approach of fibre rope analysis in offshore industry as mentioned in Section 2.4, many recent research projects have been launched with the objective to improve the modelling method for safe and reliable fibre rope mooring system. Among them, Syrope JIP [68] project led by DNV GL provided specific and practical guidelines based on extensive laboratory testing.

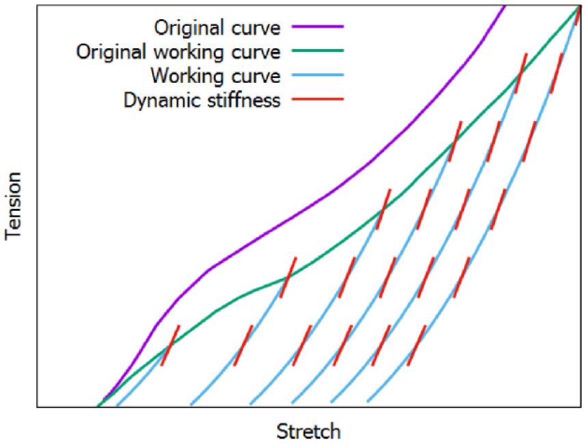

Figure 3.8: Syrope model for synthetic fibre rope [68]

The 'Syrope' model as shown in Figure 3.8, was proposed in the JIP [68] to better describe the tension-stretch and axial stiffness characteristics for synthetic fibre rope used in mooring analysis. Based on the results from full scale testing, the 'Syrope' model can be interpreted as a combination of four curves:

- **Original curve** represents the tension-stretch relationship during the first, rapid loading of the new rope, which can be considered as the upper limit of the tension-stretch curve.
- **Original working curve** represents the stationary curve when the rope is at the mean tension with permanent stretch taken out.
- **Working curve** represents the curve when the rope is at a lower mean tension than the previous historical maximum mean tension. In a stationary sea state, the working curve is determined by the historically highest mean tension level while the exact working point on the curve is determined by the mean tension level.
- **Dynamic stiffness** represents the slope of the linearized stiffness curve for a given mean tension. It increases with mean tension and is used to calculate the tension dynamics due to low-frequency (LF) and wave-frequency (WF) top end motions.

More details about the model can be found in [68] while the determination of static and dynamic stiffness is focused in this paper. The static stiffness is represented by the nonlinear working curve depending on previous highest mean tension. It describes a nonlinear relation between mean tension and mean stretch which is used to estimate the offset due to mean environmental loads. The dynamic stiffness, applied for both LF and WF load effects, is linear and increases with mean tension. The proposed models are linearly dependent on mean tension only. The analytical expression of the linearized static stiffness EA_s can be expressed as:

$$EA_s = \frac{dT_{mean}}{d\epsilon} = a \cdot T_{mean} + b \cdot MBS \tag{3.27}$$

where ϵ is stretch, MBS is minimum breaking strength of the rope, T_{mean} is the mean tension, a and b are constants estimated from full scale testing. It is a linear differential equation and the solution is a nonlinear exponential relation between the mean tension and the stretch. By assuming zero mean tension for zero stretch, it can be further described as:

$$\frac{T_{mean}}{MBS} = \frac{b}{a} \cdot [exp\,(a \cdot \epsilon) - 1] \tag{3.28}$$

The analytical expression of the linearized dynamic stiffness, EA_d is expressed as:

$$EA_d = \frac{dT_{dyn}}{d\epsilon} = f \cdot T_{mean} + g \cdot MBS \tag{3.29}$$

where T_{mean} is the mean tension determined from previous static analysis using linearized static stiffness, f and g are constants estimated from full scale testing. Examples of linearized static and dynamic stiffness curves are given in Figure 3.9.

Static stiffness is nonlinear with stretch (Equation 3.28) while both static and dynamic stiffness vary with mean tension level and the mean tension is also influenced by the stiffness. Drawing lessons from [90], the mooring analysis procedure applied in this thesis work is explained as follows:

- **Step 1:** Determine the parameters of the static and dynamic stiffness models; i.e. a, b, f and g. Select pre-tension and determine anchor positions.

- **Step 2:** Perform static analysis where wind turbine is exposed to mean environmental forces using the nonlinear static stiffness model in Equation 3.28. Calculate mean offset and mean tension in the lines.

- **Step 3:** Based on the mean tension in each line, calculate the dynamic stiffness and apply them in the final dynamic analysis of the mooring lines to document dynamic tension.

- **Step 4:** Calculate total tension by adding the results from Step 2 and 3.

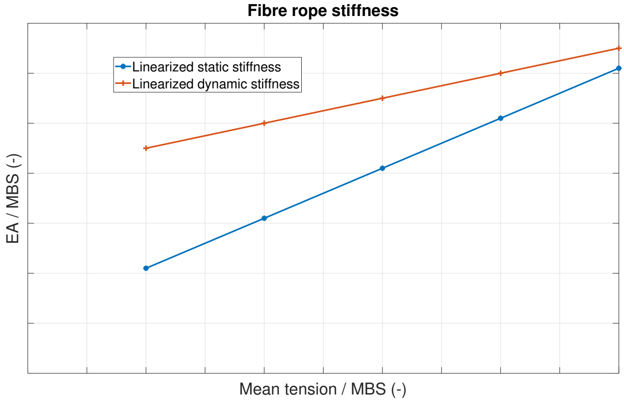

Figure 3.9: Linearized static and dynamic elastic stiffness of fibre rope. Typical curve shapes from full-scale 'Syrope' testing and internal work in Equinor. [91]

3.5 Fully coupled analysis method

The analysis of floating wind turbine system is a complicated process which should consider many aspects such as turbulent wind field, nonlinear wave loading, nonlinear structural behaviour, mooring line dynamics and servo control etc. Therefore, it is recommended to perform fully coupled aero-hydro-servo-elastic dynamic analysis to capture the nonlinear responses [92]. The dynamic motion equation of the floater can be written as:

$$(M+A_\infty)\ddot{x}(t)+\int_0^t \kappa(t-\tau)\dot{x}(\tau)d\tau+(K_m(x,t)+K_h)x(t) = q(t,x,\dot{x}) \quad (3.30)$$

where M is the mass matrix, A_∞ is the added mass matrix at infinite frequencies, $\kappa(t-\tau)$ is the retardation function which is calculated from frequency-dependent added mass or potential damping, K_h is the hydrostatic restoring matrix, K_m is the nonlinear restoring matrix from mooring system, $x, \dot{x}, \ddot{x}$ are the displacement, velocity and acceleration, q is the external force which includes wave excitation force, wind force and any other external forces. All the forces are functions of floater motions, velocities and acceleration, in addition to time. The aerodynamic and hydrodynamic loads and corresponding structural responses are considered simultaneously in the coupled time-domain analysis, including the wind turbine controller.

The Newton-Raphson iteration is used to achieve equilibrium at every time steps between external and internal forces. The solution of Equation 3.30 in time domain can be obtained through an incremental procedure using the dynamic time integration algorithm. Every sub-solution is calculated by utilizing the start condition from previous time step and assuming a new motion pattern, which will make the solution become the start condition for the following time step. The Newton-Raphson iteration is normally used to calculate equilibrium at every time steps between external and internal forces. It recalculates the mass, damping and stiffness matrices at each iteration cycle and the phases between wind and wave excitation and structural responses can be reasonably considered. Meanwhile, all sources of damping, e.g. aerodynamic, hydrodynamic, soil and structural damping can be included correctly. Moreover, the variation of wind turbine loads due to the change of rotor speed or blade pitch angle through the controller could be properly considered as well.

3.5.1 Numerical tools

Currently, a number of numerical analysis tools are available to perform coupled dynamic analysis for FWT. Some of them originate from wind industry while others are originally from offshore industry. Table 3.2 summarizes the features of some popular existing numerical codes [93].

Table 3.2: Overview of offshore wind code capabilities

Code	Developer	Aerodynamics	Hydrodynamics	Mooring
SIMA	SINTEF Ocean	(BEM^1 or GDW^2)+DS^3	PF^5+ME^6	FEM^{10}/Dyn^{11}
HAWC2	DTU	(BEM or GDW)+DS	PF/ME	FEM/Dyn
FAST	NREL	(BEM or GDW)+DS	PF+QD^7	QS^{12}
Bladed	GH	(BEM or GDW)+DS	ME+(IWL^8+IP^9)	QS
OcraFlex	Orcina	BEM or GDW or FDT^4	PF+ME	LM^{13}/Dyn

1 - blade element momentum; 2 - generalized dynamic wake; 3 - dynamic stall; 4 - filtered dynamic thrust; 5 - potential flow; 6 - Morison's equation; 7 - quadratic drag; 8 - instantaneous water level; 9 - instantaneous position; 10 - finite element method; 11 - dynamic; 12 - quasi-static; 13 - lumped mass.

In this thesis, the numerical codes used include existing tools as well as self-developed code packages and the time-domain simulations are mainly carried out in SIMA and HAWC2.

SIMA

SIMA (Simulation of Marine Application) developed by MARINTEK (SINTEF Ocean) is a simulation and analysis tool for marine operations and floating systems from modelling to post-processing [94]. For the time-domain dynamic analysis of FWT, three main built-in modules are engaged: Simo, Riflex and AeroDyn. Simo bodies are used for large-volume hydrodynamic calculations based on frequency-domain potential flow coefficients and distributed Morison elements. Riflex is used to model the mooring system, tower, shaft and blades as flexible beam elements according to finite element formulation. AeroDyn handles the aerodynamic forces and moments on the blades based on the BEM (Blade Element Momentum) theory. The fully coupled aero-hydro-servo-elastic analysis is achieved through links between separate modules. In this thesis, SIMA is used to compare different mooring design concepts (*Paper 1*) thanks to its capability to model clump weight and buoy. It is also used to compare Newman's approximation and full QTF method regarding second-order wave effect (*Paper 2*).

HAWC2

HAWC2 (Horizontal Axis Wind turbine simulation Code 2nd generation) is an aeroelastic code developed at DTU Wind Energy which is intended to calculate the response of offshore floating and fixed wind turbines in time domain [95]. In HAWC2, multi-body formulation is the basis of the structural modelling strategy and each body is modeled using a number of Timoshenko beam elements. The coupling constraints connecting individual bodies make it possible to account for the nonlinear structural effects due to body rotation or deformation. The aerodynamic modelling is based on BEM theory and was extended by Hansen et al. [96] to include dynamic stall, skew inflow and operation in sheared inflow etc. The hydrodynamic load can be calculated by either potential flow theory or Morison's equation. Buoyancy loads are included through integration of external pressure contribution and inserted as concentrated forces on end nodes and distributed forces over conical sections. Higher-order hydrodynamic effects include nonlinear wave kinematics, instantaneous water level, instantaneous structure position. Mooring lines can be modelled with either quasi-static or dynamic manner [97]. HAWC2 in this thesis is mainly used to study the fully nonlinear wave effect (*Paper 3, 4 and 5*) on FWT.

The wave kinematics applied in HAWC2 are provided externally through a DLL interface named Wkin.dll. In the current version Wkin.dll 2.4, the input wave types can be: linear airy waves with Wheeler stretching; irregular Airy waves based on JONSWAP or PM spectrum with directional spreading; stream function wave and pre-generated wave kinematics.

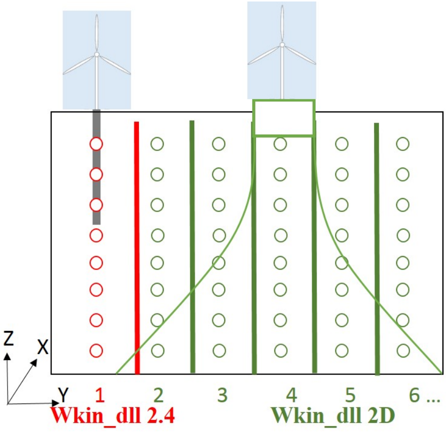

Figure 3.10: Wave field structure of wkin.dll in HAWC2

When importing pre-generated wave kinematics, the wave field that Wkin.dll 2.4 is able to handle can be considered as a one dimensional field since the data are imported at discrete grid points at only one horizontal location along the water depth as the red part in Figure 3.10. The wave kinematics variation only exists in one dimension. The kinematics at any point and the wave elevation are linearly interpolated using the neighbouring points. This works sufficiently for bottom fixed wind turbine such as monopile where only the wave kinematics at the centre of the structure is needed since the movement of monopile is very small.

However, it is not applicable for floating wind turbine where the variation along horizontal direction is needed as well due to the mooring system. Therefore, the Wkin.dll 2.4 is further extended in this thesis to include wave kinematics variation in horizontal direction in order to implement on floating wind turbine (green part in Figure 3.10). It is named Wkin.dll 2D because it is able to handle wave field in two dimensions. Wave elevation is linearly interpolated at different horizontal locations. The wave kinematics including velocity and acceleration are first calculated in numerical wave tank and then fit into polynomial coefficients to scale down the size as introduced in section 3.3.2.2. The extension of the wave field from one dimensional to two dimensional makes it possible to perform hydrodynamic analysis for floating wind turbine using pre-generated wave kinematics method, which is the basis for fully nonlinear wave effect study.

3.6 Fatigue damage calculation

Fatigue analysis can be performed in frequency domain with acceptable accuracy and efficiency [98]. However, due to nonlinear loading, nonlinear fluid-structure-interaction, the damping/excitation from wave-wind-induced motions and nonlinearity of the responses, the fatigue analysis for floating wind turbine is preferably performed in the time domain despite the computational efforts [99].

The fatigue damage for mooring line and tower base due to axial stress can be calculated using T-N and S-N curve methods respectively. The total structural fatigue damage can be determined as the sum of the fatigue damage that arises from each individual design sea state. The damage for each sea state can be calculated based on Miner-Palmgren hypothesis by adding together the damage from each stress or tension level.

$$D = \sum_{j}^{N_{total}} \frac{n_j}{N_j} \tag{3.31}$$

where n_j is the number of cycles at the j-th stress range in the time history and N_j is the number of cycles to failure at corresponding stress range according to the design curve. According to Wöhler [100], the number of cycles until fatigue failure (N) is given by:

$$N = JS^{-m} \quad \text{or} \quad N = KT^{-m} \tag{3.32}$$

where N is the number of permissible cycles of stress or tension range, J, K are the coefficients in the curves, m is the inverse slope factor and S is the stress range while T is the tension range in the time history. The number of load cycles can be determined using Rainflow counting method. Normally, number of cycles to failure for high level stress cycles is fewer compared to lower level stress cycles. If the applied stress level is below the endurance limit of the material, the structure is assumed to be able to function infinitely. Therefore a two-sloped S-N curve is normally preferred to account for different stress levels [101].

3.7 Extreme value prediction

By taking a random stochastic process $X(t)$ over a time period T as an example, the extreme value of the process is defined as the largest maximum from a sequence of individual maxima.

$$X_e = max\left\{X_{m1}, X_{m2}, ..., X_{mn}\right\} \tag{3.33}$$

where X_e stands for the largest maximum value and X_{mi} represents the individual maxima as shown in Figure 3.11. Based on the assumption that all the individual maxima are independent and identically distributed with a common distribution function $F_{Xm}(x)$, the distribution for X_e is described as:

$$F_{Xe}(x) = Prob\left\{X_e \leq x\right\} = [F_{Xm}(x)]^n \tag{3.34}$$

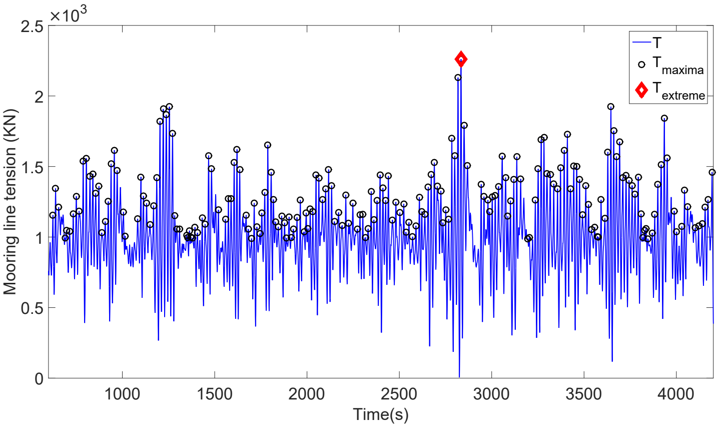

Figure 3.11: Global maxima and extreme peak from time series

Several methods have been developed for predicting the extreme value distribution, while two of them are used in this paper: type I asymptotic extreme value distribution i.e. the Gumbel fitting method and ACER (average conditional exceedance rate) method.

Gumbel fitting method

When the sample number n is large enough, the extreme value distribution Equation 3.34 has been proved that it will converge towards one of three types of distributions : Gumbel, Fréchet and Weibull also known as type I, II and III extreme value distributions whose cumulative distribution probability can be assembled as the generalized extreme value (GEV) distribution:

$$F_{Xe}(x) = exp\left\{-1 + \gamma(\frac{x-\mu}{\sigma})^{-\frac{1}{\gamma}}\right\} \tag{3.35}$$

Here μ is the location parameter, σ is the scale parameter and γ is the shape parameter. The limiting case when $\gamma \to 0$ will result in the Gumbel distribution which is the most recommended model for marine structures

[102].

$$F_{Xe}(x) = exp(-exp(-\alpha(x-\mu))) \tag{3.36}$$

where α is the scale parameter and μ is the location parameter which can be determined by Gumbel probability paper method. Rewrite Equation 3.36 with logarithm of both sides, a linear function is introduced as:

$$-ln[-ln(F_{Xe}(x))] = \alpha(x-\mu) \tag{3.37}$$

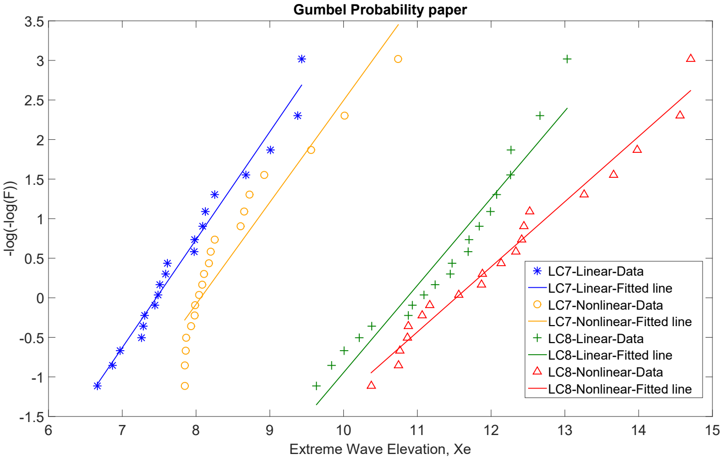

Figure 3.12: Gumbel probability paper

The cumulative distribution probability is represented by a straight line in the probability paper where parameters α and μ can be estimated by the least-square fitting method of original data [103]. An example of Gumbel probability paper for extreme wave elevation is shown in Figure 3.12.

Average conditional exceedance rate method

The average conditional exceedance rate (ACER) method proposed by Næss and Gaidai [104] predicts the exact extreme value distribution by building up a sequence of non-parametric distribution functions known as ACER functions instead of the parametric distribution functions. It considers all the global maxima peaks while the dependence between successive peaks in a sampled time-series are taken into account as well which makes it available for both the stationary and non-stationary process.

The extreme value probability distribution according to ACER method is written as:

$$F_{Xe}(x) \approx P_k(x) \approx exp\{-(N-k+1)\hat{\varepsilon}(x)\} \tag{3.38}$$

where k is the order of the ACER function which represents the immediately preceding non-exceedances, $\hat{\varepsilon}(x)$ is the empirical ACER function of order k which is determined by fitting available global maxima peaks from time series [105].

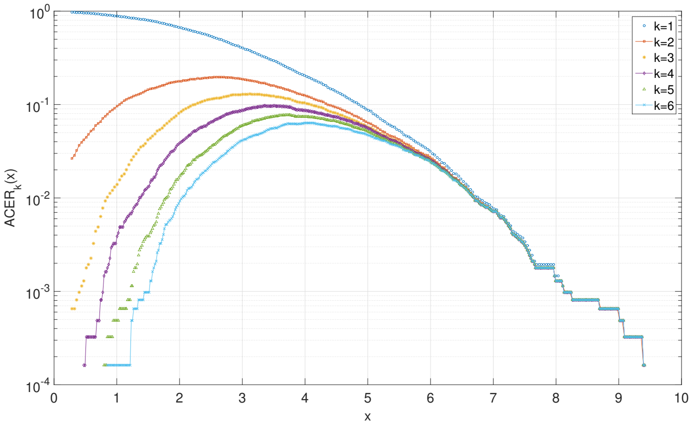

Figure 3.13: ACER function for k=1,2,...,6

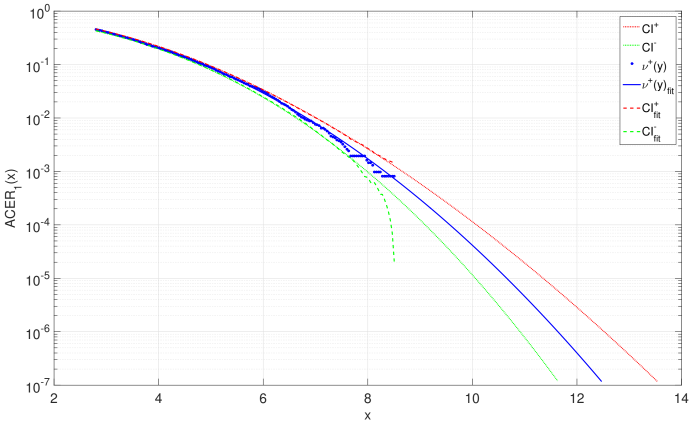

Figure 3.14: Confidence interval for ACER function with k=1

The empirical ACER function follows the form:

$$\hat{\varepsilon}(x) = q_k \cdot exp\left\{-a_k(x-b_k)^{c_k}\right\}, \qquad x \geq x_0 \tag{3.39}$$

Due to the fact that the ACER function behaves close to $exp\left\{-a(x-b)^c\right\}$ in the upper tail region, the coefficients a_k, b_k,c_k and q_k depending on the order k can be determined by extrapolation using mean-square-error function:

$$F(q_k, a_k, b_k, c_k) = \sum_{i=1}^{N} \rho_j |ln\hat{\varepsilon_k}(x_{mi}) - \ln q + a(x_{mi-b})^c|^2 \tag{3.40}$$

The weight factor ρ_j is described as $\rho_j = (\ln CI^+(x_i) - \ln CI^-(x_i))^{-2}$ where it represents the 95% confidence interval:

$$CI^{\pm}(x_{mi}) = \hat{\varepsilon_k}(x_{mi}) \left\{ \frac{1.96}{\sqrt{(N-k+1)\hat{\varepsilon_k}(x_{mi})}} \right\} \tag{3.41}$$

An example of the ACER function is given in Figure 3.13 representing the empirical ACER function for different orders of k from 1 to 6. Noticeable variation of ACER function with different order is discovered at lower range of the individual maxima indicating the significant dependence between data points. However, the variation disappears in the tail region for all functions which allows the first-order ACER function $\hat{\varepsilon_1}(x)$ to be chosen for extrapolation which involves most data for estimation and offers same level of accuracy as higher order functions at the same time.

The empirical function $\hat{\varepsilon_1}(x)$ is presented in Figure 3.14 including the 95% confidence interval fitted by time series peaks as well as the estimation from extrapolation scheme. Previous study by Fu et al. [103] shows that the prediction is not sensitive to the choice of the tail marker x_0 which is used to define the tail region, therefore the default value can be used. Finally, the extrapolation scheme leads to the estimation of all the coefficients required in ACER function.

Chapter 4

Coupled analysis results

4.1 General

In this chapter, the environmental parameters defined in the load cases are introduced. The performance of proposed mooring design concepts in shallow water as mentioned in Section 2.5 is compared and recommendation of preferable proposals is also made (Paper 1). In addition, the dynamic response characteristics of semi-submersible FWT in shallow water are investigated and demonstrated based on fully coupled time domain simulations. It mainly addresses the second-order wave load effect (Paper 2) and the fully nonlinear wave load effect which consists of proposing the numerical code (Paper 4), verifying against well-known wave models (Paper 3) and studying the fully nonlinear wave effect with perspective of fatigue damage and extreme values (Paper 5).

4.2 Design load case

A number of representative load cases are selected in this thesis to perform different analyses with different purposes. The environmental conditions defined in the five appended papers are summarized in Table 4.1.

Paper 1: The load cases used to compare shallow water mooring design concepts are referred to the wind and wave data at Statfjord site in the Northern North Sea where a joint wind and wave distributions was established by Johannessen et al. [106] considering 1-hour mean wind speed at 10 m above sea water level (U_{10}), the significant wave height (H_s) and the spectral peak period (T_p).

Table 4.1: Design load cases in the thesis

		U_w m/s	H_s m	T_p s	U_c m/s	Seeds -	Time s	Turbine Status
Paper 1	LC1	4	1.96	9.72	-	10	12000	Operational
	LC2	8	2.53	9.85	-	10	12000	Operational
	LC3	12	3.20	10.11	-	10	12000	Operational
	LC4	16	3.97	10.44	-	10	12000	Operational
	LC5	20	4.80	10.82	-	10	12000	Operational
	LC6	24	5.69	11.23	-	10	12000	Operational
	LC7	32	7.64	12.08	-	10	12000	Parked
	LC8	40	9.77	12.95	-	10	12000	Parked
	LC9	40	9.77	12.95	1.0	10	12000	Parked
Paper 2	ULS-1	41.86	13.4	13.1	1.05	10	12000	Parked
	ULS-2	38.87	15.6	14.5	1.05	10	12000	Parked
Paper 3	H6T7	-	6	7	-	-	4200	Parked
	H6T10	-	6	10	-	-	4200	Parked
	H12T15	-	12	15	-	-	4200	Parked
Paper 4	ULS1	-	9.14	13.6	-	20	4200	Parked
	ULS2	-	15.24	17	-	20	4200	Parked
Paper 5	LC1	4	1.96	9.72	-	10	4200	Operational
	LC2	8	2.53	9.85	-	10	4200	Operational
	LC3	12	3.20	10.11	-	10	4200	Operational
	LC4	16	3.97	10.44	-	10	4200	Operational
	LC5	20	4.80	10.82	-	10	4200	Operational
	LC5_2	24	4.80	10.82	-	10	4200	Operational
	LC6	24	5.69	11.23	-	10	4200	Operational
	LC6_2	20	5.69	11.23	-	10	4200	Operational
	LC7	40	9.77	12.95	-	20	4200	Parked
	LC8	60	15.75	15.10	-	20	4200	Parked

$$f_{U_{10}H_sT_p}(u_{10}, h_s, t_p) = f_{U_{10}}(u_{10}) \cdot f_{H_s|U_{10}}(h_s \mid u_{10}) \cdot f_{T_p|H_sU_{10}}(t_p \mid h_s, u_{10}) \tag{4.1}$$

The joint distribution representing 100-year wind and 100-year wave condition consists of a marginal distribution of wind speed U_{10}, a conditional distribution of H_s for given U_{10} and a conditional distribution of T_p for given U_{10} and H_s. Design wind speed is first determined and the expected significant wave height can then be calculated based on the conditional distribution of H_s for given U_{10} which is a two-parameter Weibull distribution. Likewise, the expected spectral peak period T_p can then be calculated according to the conditional distribution of T_p for given H_s and U_{10} as a log-normal distribution proposed by Johannessen et al. [106].

The wind speed considered ranges from cut-in, rated and cut-out wind speed. The turbulence intensity is determined according to IEC Class C [76]. The vertical wind shear as the variation of the mean wind speed U_z with height z above the ground is considered using the normal wind profile model proposed in [107]:

$$U(z) = U_{ref}(\frac{z}{z_{ref}})^{\alpha} \tag{4.2}$$

where U_{ref} is the reference wind speed and z_{ref} is the height of the reference wind speed and α is the power law coefficient. The reference height is as the center of rotor and α was chosen to be 0.14 for floating wind turbine based on IEC 61400-1 [107].

In addition, current load effect is also considered in Paper 1. According to DNVGL-OS-E301 [64], the current can be categorized as tidal, circulational, wind-generated, soliton and loop currents, depending on the site location. A surface current speed (U_c) with 10-year return period is recommended for mooring analysis. Based on the typical surface current speeds as given in DNVGL-OS-E301 [64], 1.0 m/s is chosen as a representative surface current velocity in this paper. The variation is considered as a linear profile from still water level to *z= -50 m* as shown in Equation 4.3. The current is assumed to vanish at water depth deeper than 50 m and same current profile is used for both 50 m and 200 m water depth.

$$U_c(z) = 1.0 \cdot \left(\frac{50+z}{50}\right) \quad \text{for} \quad -50 \leq z \leq 0 \tag{4.3}$$

Paper 2: The two load cases used for comparing hydrodynamic load modelling methods regarding second-order wave load effect are determined based on the data at Norway site 5 [108]. The two extreme environmental conditions corresponds to 50 years return period with one refers to the condition with maximum mean wind speed and one condition with maximum significant wave height. The current speed is defined as 1.05 m/s as representative value for the Norway site 5.

Paper 3: The load cases used to verify the numerical code for studying fully nonlinear wave effects are three wave-only regular wave conditions. The most significant difference of the three sea states is the nonlinearity of the wave considering wave steepness. Meanwhile, the first two sea states represent moderate condition while the last one stands for severe condition.

Paper 4: The two extreme load cases to study the fully nonlinear wave effect on floating wind turbine are determined according to the original design load case definition for OC4 semi-submersible [25].

Paper 5: The environmental condition to study the effect of wave nonlinearity on fatigue damage and extreme responses are also determined based on the wind and wave data at Statfjord site in the Northern North Sea which is the same as Paper 1. The most probable normal operational conditions with directionally aligned wind and wave are labeled as LCs 1–6 while LCs 7–8 are extreme conditions where wind turbine is under parked condition. In addition, two more operational conditions with specific wind and wave parameters are chosen to study the wind and wave effect labeled as LC5_2 and LC6_2.

4.3 Performance comparison of mooring designs for floating wind turbine in shallow water

The mooring design concepts proposed for floating wind turbine in shallow water as presented in Section 2.5 are compared in this section regarding their overall performance. The OC4 semi-submersible [25] was selected as the reference floating wind turbine to evaluate these mooring designs. The mooring system consists of three mooring lines which spread symmetrically about a vertical axis through the platform center with an angle of 120 degree between each line. The fairlead is located at the top of the base columns which is 14 m below the still water level as shown in Figure 4.1 where a bird view of the mooring system is also given. The evaluation includes static analysis, dynamic analysis and a preliminary cost analysis.

4.3.1 Static analysis

In the following analysis, mooring line tension refers to the total tension when x-offset at fairlead is non-zero and its horizontal component is termed horizontal tension. Similarly, pre-tension and horizontal pre-tension refer to the case when the x-offset at fairlead is zero.

Pre-tension

Sufficient pre-tension can avoid large floater offset due to mean and LF environmental load. It is influenced by the submerged weight of the suspended mooring line for catenary mooring system and initial line stretching

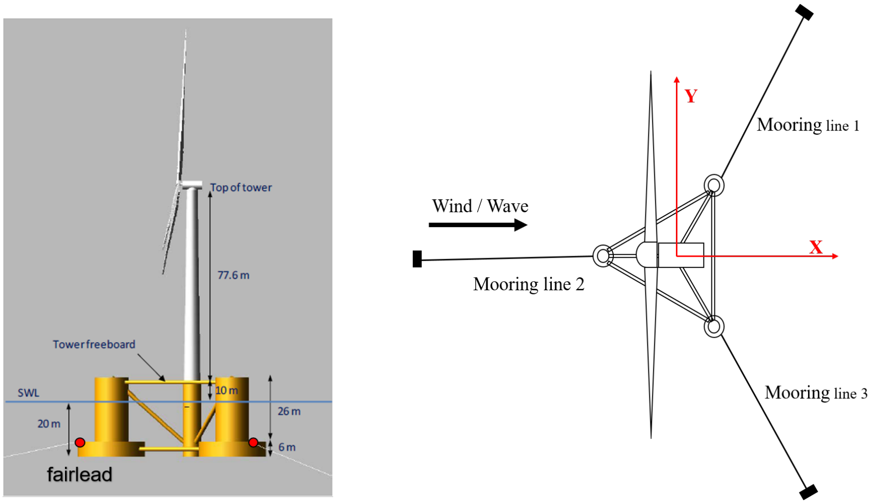

(a) Fairlead position *(b) A bird view of mooring system*

Figure 4.1: OC4 semi-submersible and its mooring configuration

for taut mooring system. The horizontal pre-tension for the seven designs are listed in Table 4.2 where the value for 200 m is set as a reference. As expected, the horizontal pre-tension for Model III is smaller compared with other models because of the buoy attached to the suspended line.

Table 4.2: Horizontal pre-tension (KN)

200 m	I	II	III	IV	V	VI	VII
914	868	910	462	859	1048	1152	1145

Offset-tension characteristics

The tension properties of single mooring line are compared in Figure 4.2. It provides an example of the tension characteristics for mooring line 2 when it is exposed to increasing x-offsets in positive x direction as shown in Figure 4.1 (b). According to Campanile et al. [30], the recommended admissible floater offset to water depth ratio is 0.3 at 50 m depth, therefore the static mooring line tension characteristics is compared up to 15 m offset. The amplitude of typical low-frequency and wave frequency motions is in the range between 2 m to 4 m for operational conditions, while the extreme motion is just below 15 m as shown in Figure 4.5. The tension for the three taut moorings increases linearly with increasing offset while the effect due to the implementation of clump weight and buoy is not significant. As for the four catenary moorings, the tension increases linearly at small offset while the increment becomes nonlinear at large offset. This is a typical characteristics for catenary mooring system and it is more significant for shallow water (50 m) than deep water (200 m) [66]. Among the four catenary moorings, the nonlinear increment of Model I is the most noticeable due to large unit weight while Model IV is the least noticeable thanks to the buoy attached at the resting line. The performance of Model IV, V, VI, VII are quite close to the reference model 200 m.

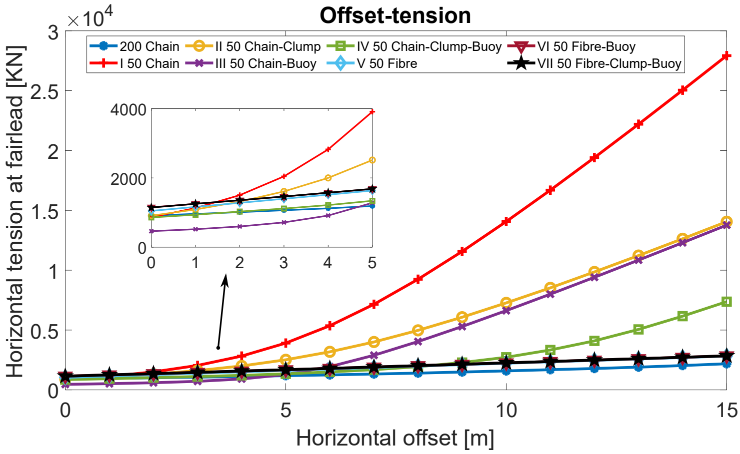

Figure 4.2: Offset-tension relation for a single mooring line

Vertical angle

The issue regarding the angle between mooring line and vertical axis has been introduced in Section 2.4. The change of the angle α (as shown in Figure 2.7) for mooring line 2 with increasing x-offset at fairlead is shown in Figure 4.3. Since the water depth is quite small (50 m) compared with mooring line footprint (about 900 m), the stretched synthetic fibre rope mooring line is almost parallel to the seabed with angle close to 90 degree, while the influence of adding clump weight and buoy is quite limited. As for the four catenary moorings in 50 m, the initial angles are around 60 degree, indicating a significant catenary shape. As x-offset increases, the angles starts to approach 90 degree indicating the loss of catenary shape and the likely stretching of the line. Better performance is achieved by Model IV because of the application of buoys. Meanwhile, the angle problem is not significant for the catenary mooring in 200 m.

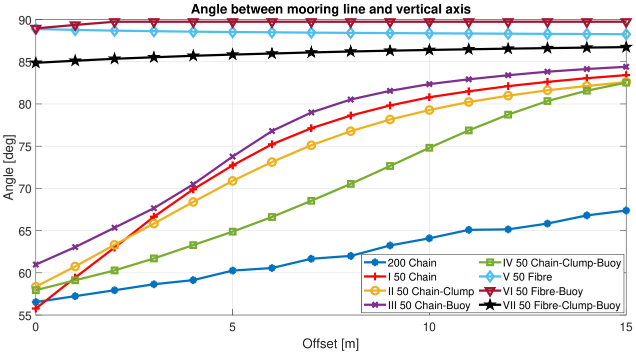

Figure 4.3: Angle between mooring line and vertical plane

4.3.2 Decay analysis

Free decay test in calm water were performed to compare the natural periods for the different concepts and the results are summarized in Figure 4.4. The natural periods in heave, roll and pitch degrees of freedom (dof) are quite close for different concepts while the natural periods for surge, sway and yaw dofs vary significantly among different mooring concepts. In addition, it is worthy noticing that the natural periods for horizontal dofs are larger than typical wave periods. Therefore, difference-frequency wave effect is of more interest than sum-frequency wave effect to check when second-order wave effect is considered in the hydrodynamic analysis.

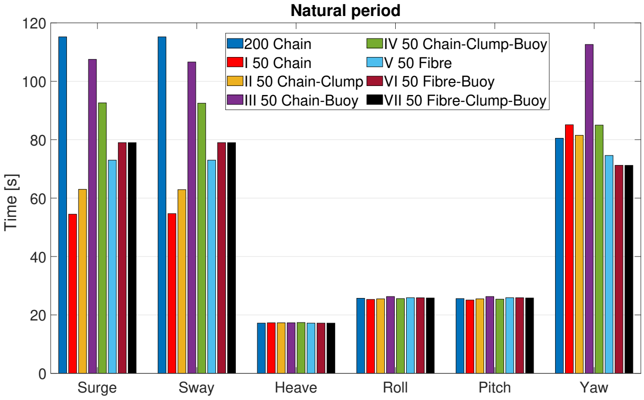

Figure 4.4: Natural period

4.3.3 Dynamic analysis

The environmental parameters for the dynamic analysis are given in Table 4.1 labeled as Paper 1 where six operational conditions and three extreme conditions are considered. The results are achieved for 3-h response by running each simulation for 12000 s while the first 1200 s is excluded because of transient effect. Ten different realisations of turbulent wind and irregular wave are generated for each load case to account for the stochastic variability. The final statistics are taken as the average of the ten realisations. The floater surge and pitch motion and mooring line tension are shown in Figure 4.5, while the rest of the results are available in appended paper 1.

In operational condition where the turbine is rotating, the mean value of surge and pitch motions are clearly non-zero due to the mean wind and wave force. As for extreme condition where the blades are feathered, the mean wind force acting on the wind turbine is quite limited. Mean motions which is then mainly due to second-order wave drift load or current load effect. Surge response for the reference model in 200 m is in general larger than all the models in 50 m. Mean value of surge motion is relatively large when wind speed is around rated wind speed (LC3) or current load is considered (LC9) while the standard deviation and maximum increase as wave becomes more and more severe. For the seven designs in 50 m, the mean and maximum value for Model III and IV are relatively larger than others, which will directly influence the mooring line tension. The standard deviations for all the designs are quite close. Similar to surge motion, the mean value of pitch motion is also wind-dominated while the standard deviation and maximum increase as environmental condition becomes more severe. There is no big discrepancy from different models in all load cases even the taut mooring systems do not show any disadvantages.

The tension of windward mooring line which is also the most loaded mooring line is selected for comparison in Figure 4.5. The mean tensions for Model I II and IV are quite close while smaller value for Model III and larger value for Model V VI VII are observed for all the load cases. Noticeable standard deviation and maximum is found for Model I compared with others in LC9. Similar surge motion leads to quite different maximum mooring line tension in extreme condition is the best prove of different mooring line behaviors when exposed to same environmental condition. Among the four catenary designs, smaller extreme tension is obtained for Model IV thanks to the implementation of buoy. As for the three taut moorings, the extreme tensions are slightly higher than the catenary moorings.

Considering different capacity associated with different mooring materials, utilization factor recommended by DNVGL-ST-0119 [109] can provide

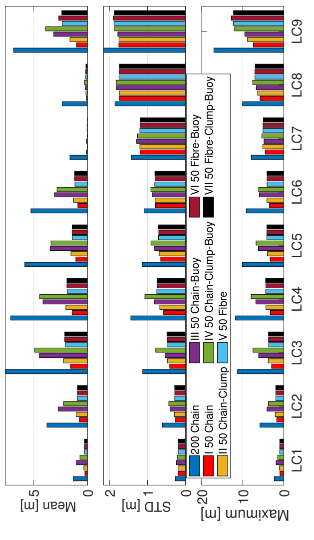

(a) Floater surge motion

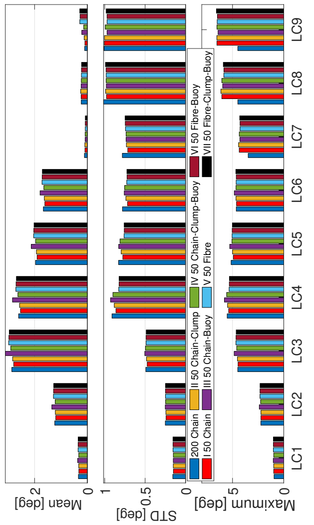

(b) Floater pitch motion

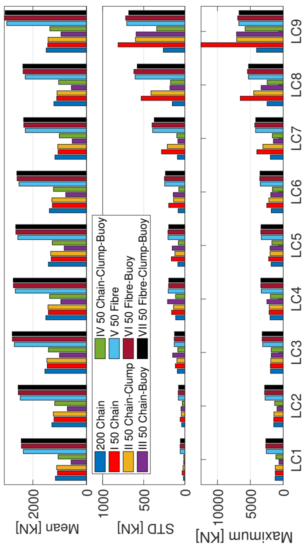

(c) Mooring line tension

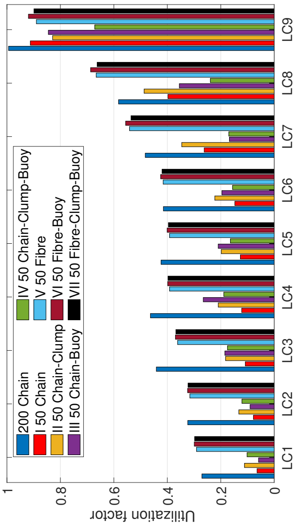

(d) Mooring line utilization factor

Figure 4.5: Dynamic analysis results

another perspective of tension responses to their material limit apart from the direct comparison of the statistics. The utilization factor u is defined as:

$$u = \frac{T_{pret}\gamma_{pret} + T_{C-env}\gamma_{env}}{S_C} \tag{4.4}$$

where T_{pret} is the mooring line pre-tension, T_{C-env} is the characteristic environmental tension due to mean, low-frequency and wave-frequency load which is calculated as $T_{MPM} - T_{pret}$, where T_{MPM} is the most probable maximum tension, S_C is the characteristic mooring line strength defined as 95% of the minimum breaking strength S_{MBS}, γ_{pret} and γ_{env} are safety factors which are set as 1.3 & 1.75 respectively in this study based on the assumption of level 1 consequence class [109].

The resulting utilization factors for all the models in all load cases are shown in Figure 4.5. First of all, all the utilization factors are below 1 which means the line capacities are not exceeded for all the models and they are close to 1 in the most extreme condition meaning that line redundancy is within acceptable range. In operational conditions where the tension level is small, the utilization factors for taut moorings are slightly larger than catenary moorings. However in extreme conditions when the tension level is high, the utilization factors for catenary moorings increase dramatically compared with taut moorings. Speaking of individual mooring performance, almost no difference is found among Model V VI VII and clearly better performance is found for Model IV.

4.3.4 Cost analysis

Economic consideration plays an important role in the mooring decision. The expense of an offshore wind project can be evaluated by capital expenditures (CAPEX) and operating expenditures (OPEX) [7]. When a complete time span is considered for different phases of the project, life cycle cost analysis (LCCA) is preferred for evaluation. Since the focus of this thesis is to compare different mooring design concepts for the same floating wind turbine, the LCCA analysis will focus on the mooring system rather than the whole wind turbine. In addition, the comparison is performed mainly for manufacture and installation in LCCA. An elementary cost analysis is performed in this study based on a number of different sources and the main purpose is to provide a general cost-wise ranking of the seven mooring designs. The total cost also takes into account the utilization factor of mooring line as shown in Figure 4.5. Certain costs can be subject to variations given particular project, location and timing.

The detailed anchor capacity design is not the focus of this study, therefore anchors from well-proven industrial projects are referred. According to [110], the price of a 17 ton Stevshark Mk5 anchor from Vryhof Anchors is approximately € 114000, while a 50 ton suction anchor costs around € 512500.

The price for mooring line is estimated according to the objective function in [111] which is based on data provided by Equinor. The prices for chain, polyester and steel wire basically can be described by a common expression with different coefficients.

$$Cost = Length * Weight * Price \tag{4.5}$$

where length is given in m, weight in the air is given in N/m and the price is given in $€/N$ for different materials as shown in Table 4.3.

Table 4.3: Price for chain, steel wire rope and polyester fibre rope (€/N)

	Chain	Steel wire rope	Polyester fibre rope
Price	0.25	0.5	0.7

The price for two clump weights are estimated as heavy chain using Equation 4.5 while the price for two buoys are estimated using data from Defender [112] with a linear interpolation.

The installation procedure for all the models is assumed to be performed by one large anchor handling tug supply vessel with sufficient holding capacity. According to [113], the installation time for a DEA anchor is about 8 hours including deck rigging, launching, lowering, seabed penetrating and tensioning while it takes about 12 hours to install a suction anchor including seabed penetrating and deck handling. Based on many other pre-defined assumption as listed in [110], the baseline mooring system installation costs for different concepts are obtained.

Table 4.4: Cost breakdown for mooring system (€)

	Anchor	Line	u	Clump	Buoy	Installation	Total
200 m	114k*3	236.8k*3	0.972	0	0	55k*3	**1.20m**
I	114k*3	1280.4k*3	0.982	0	0	55k*3	4.28m
II	114k*3	643.3k*3	0.992	70k*3	0	55k*3	2.63m
III	114k*3	643.3k*3	0.93	0	1.3k*3	55k*3	2.31m
IV	114k*3	720.3k*3	0.654	70k*3	1.3k*4*3	55k*3	**2.15m**
V	512.5k*3	185.5k*3	0.974	0	0	88k*3	**2.34m**
VI	512.5k*3	185.5k*3	0.977	0	0.8k*3	88k*3	2.35m
VII	512.5k*3	185.5k*3	0.997	37.5k*3	0.8k*3	88k*3	2.47m

The total cost for all the mooring models are calculated in Table 4.4 by summing up the manufacture and installation costs. The price is listed in Euro (€), k stands for 10^3 and m stands for 10^6. u indicates the utilization factor of the mooring line as shown in Figure 4.5.

Generally, the catenary mooring is competitive regarding the cost of anchor and installation but the capital cost for the mooring line is quite high. The taut mooring on the other hand is favorable with respect to the cost of synthetic fibre rope, however the cost for the suction anchor and installation is quite high. Clearly, the cost of the reference model in 200 m is quite low compared with the models in 50 m since the cost of the mooring line is low. Model I is the most expensive model because of the high price for the heavy chain. Model IV and V are more cost-competitive designs of their types.

4.3.5 Conclusion and recommendation

From static analysis, heavy chain or clump weight have to be used in order to achieve reasonable pre-tension. The tension for traditional catenary mooring increases nonlinearly with increasing offset while the tension increment for fibre rope is linearly predictable. The implementation of clump weight and buoy clearly improves the catenary concepts by decreasing the size of mooring line and reducing the peak line tension. However, its benefit is not significant for taut moorings. From decay analysis, the influence of mooring system on the natural periods of the floater is more significant for horizontal dofs (surge, sway and yaw) than vertical dofs (heave, roll and pitch). From dynamic analysis, the extreme tension for pure chain mooring is extraordinarily large. Judging from the mooring utilization factor, hybrid catenary mooring (Model IV) clearly stands out. From the cost analysis, the capital cost of mooring chain is high while the cost of its DEA anchor and installation is relatively low. On the contrary, the cost of fibre rope mooring line is quite low, however the cost for the suction anchor and installation is quite high. When combining with the utilization factor, Model IV and V are cost-competitive concepts. The advantages and disadvantages of the seven mooring designs are further summarized in Table 4.5.

In conclusion, considering both the structural performance and capital cost, the hybrid catenary mooring concept made of chain and combined with clump weight and buoy (Model IV) and taut mooring concept with pure fibre rope (Model V) are preferable and recommended for floating wind mooring design in shallow water in the future.

Table 4.5: Summary of Pros and Cons for all shallow water mooring concepts

Model	Pors and Cons	Recommend
I-Chain	Mooring line is heavy, the extreme mooring line tension is quite large and the cost is very high.	NO
II-Chain-Clump	Clump weight can contribute to pre-tension, but line tension in extreme condition is not improved. The cost is lower than pure chain cable mooring.	NO
III-Chain-Buoy	Buoy can reduce the extreme tension, but it will decrease the pre-tension. The reduction of extreme tension is not significant.	NO
IV-Chain-Clump-Buoy	The merits of clump weight and buoy are included. The extreme tension at large offset is avoided. The cost is competitive thanks to lower utilization.	**YES**
V-Fibre	Desired pre-tension is much easier to achieve than catenary mooring. The tension increment is linear even for large offset. The cost is acceptable considering its performance.	**YES**
VI-Fibre-Buoy	The effect of adding extra buoy to fibre rope is quite limited.	NO
VII-Fibre-Clump-Buoy	The effect of adding buoy and clump weight to fibre rope is not significant.	NO

4.4 Second-order wave load effect

As described in Section 3.3.3.1, Newman's approximation may provide satisfactory results for massive structures in deep water compared with full QTF method. However, it becomes inaccurate in shallow water where full QTF is a better option. As part of the thesis work, both of the two methods are used to calculate the second-order difference-frequency wave load for the CSC semi-submersible floating wind turbine and the comparison is performed at three water depths (50 m, 100 m and 200 m). Two extreme conditions with 50-year return period are considered as shown in Table 4.1 labeled as Paper 2. Four numerical models as shown in Table 4.6 are compared, where Newman's approximation is applied in horizontal plane i.e. surge, sway and yaw while Full QTF method is implemented in all 6 degree of freedoms (DOFs). Effect due to turbulent wind is also studied since it is located at similar low-frequency range as the difference-frequency wave effect. The details of the three reference mooring line models can be found in appended paper 2 [66].

Table 4.6: Hydrodynamic load models

No	Wave		Wind	Current
	First-order	second-order		
1	Included	Not included	Not included	Included
2	Included	Newman's approximation (3 DOFs)	Not included	Included
3	Included	Full QTF (6 DOFs)	Not included	Included
4	Included	Full QTF (6 DOFs)	Included	Included

The final results in ULS-1 condition are shown in Figure 4.6 and 4.7 regarding the spectrum and statistics respectively as an example. The wave-frequency response is similar for different load models. As for the low-frequency motion, Newman's approximation clearly underestimate all the motions compared with full QTF method. As for the mooring line tension, the difference are not significant in 200 m where wave-frequency response is dominating over low-frequency response. However, low-frequency response becomes more significant at shallower water depth (100 m and 50m) where Newman's approximation underestimate the response compared with full QTF method.

In conclusion, full QTF method is preferable over Newman's approximation to describe second-order difference-frequency wave effect for semi-submersible wind turbine in shallow water [66].

4.5 Fully nonlinear wave effect

As mentioned in section 3.3.1, fully nonlinear wave is better than linear Airy wave to describe large wave in shallow water where nonlinear wave effect becomes significant. The fully nonlinear irregular wave effect on monopile wind turbine has been intensively studied by Schløer et al. [114, 115, 116] using OceanWave3D [117] wave tank. However, it is more challenging to apply fully nonlinear wave on FWT than BFWT in terms of accuracy and efficiency. One of the reasons is that the footprint of floating wind turbines is larger due to its mooring system which requires larger database for pre-generated wave kinematics to be used in a global response analysis. Normally the database is so large that it may exceed the virtual memory limit of the simulation tool for wind turbine. In addition, it is so demanding to obtain accurate fully nonlinear wave kinematics due to complicated fully nonlinear FSBCs that a separate numerical wave tank (NWT) is needed to generate the wave. Building a link between the wave kinematics database and the simulation tool is also quite important.

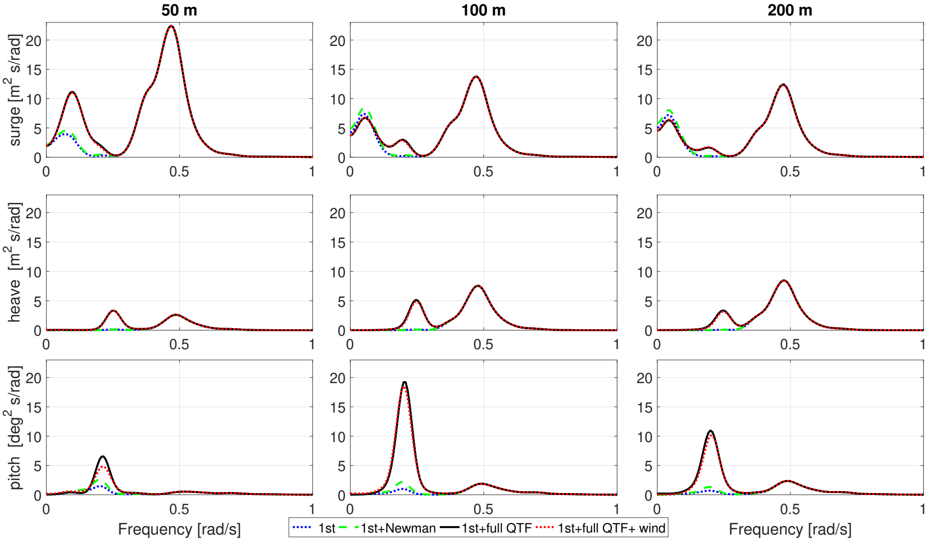

(a) Motion spectrum

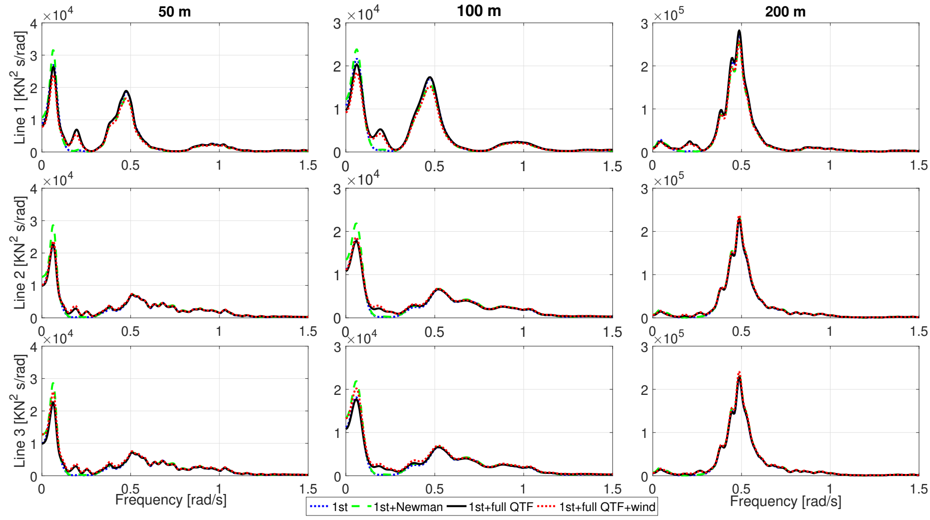

(b) Tension spectrum

Figure 4.6: Spectrum of floater motion and mooring line tension

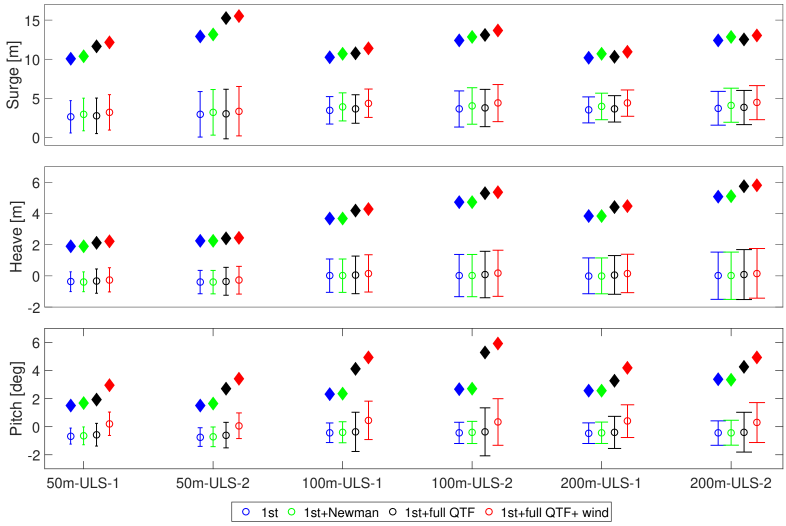

(a) Motion statistics

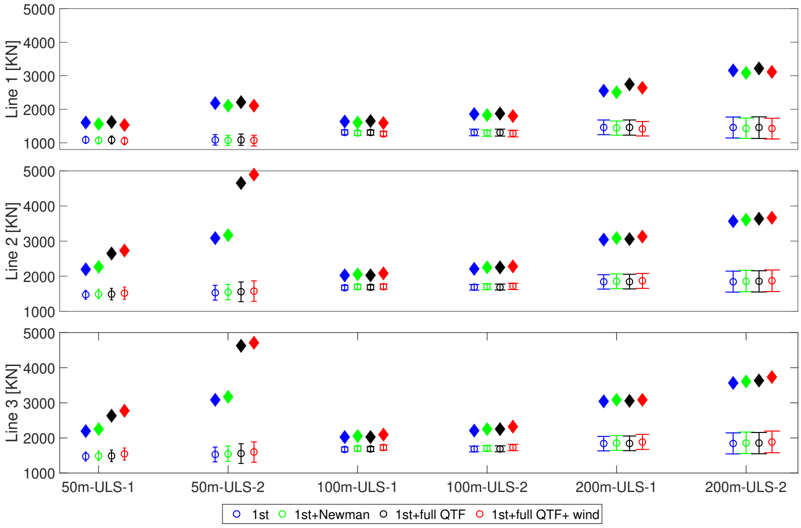

(b) Tension statistics

Figure 4.7: Statistics of floater motion and mooring line tension

As an important part of the thesis work, fully nonlinear wave effect on the OC4 semi-submersible floating wind turbine is studied at 200 m water depth using HAWC2 to carry out the coupled dynamic analysis and the fully nonlinear waves are generated in the 2D HPC numerical wave tank which is proposed by Shao and Faltinsen [77, 78, 79]. The properties of the mooring system has been mentioned in the Table 2.4 in Section 2.5. In order to decrease the wave kinematics data size and solve the software memory problem, a polynomial fitting method is developed by Xu et al. [86] to fit the kinematics data at grid points in the whole wave field to polynomial functions representing location coordinates and corresponding polynomial coefficients, which is described in details in section 3.3.2.2. At the same time, the dynamic link library (DLL) between wave kinematics database and HAWC2 is extended from one dimensional to two dimensional so that it can be applied to not only BFWT but also FWT.

4.5.1 Verification - regular wave

The proposed numerical to study fully nonlinear wave effect on floating wind turbine is achieved by connecting several individual numerical codes. The analysis procedure is demonstrated in Figure 4.8 where the main contribution of this thesis is marked with red color. The details of the process are further explained as follows:

Step 1: 2D HPC numerical wave tank is first used to generate regular or irregular wave with linear or fully nonlinear FSBCs. Wave elevation, velocity and velocity potential are directly available from the tank while the acceleration is obtained through post-processing based on information of velocity and grid location. The calculation of acceleration is based on Equation 3.19 and performed in Python.

Step 2: A Matlab code package based on polynomial fitting method (Equation 3.20) is developed and applied to fit wave velocity and acceleration data. The polynomial coefficients are stored as a wave kinematics database.

Step 3: Finally the coupled dynamic time domain analysis is carried out in HAWC2 based on Morison's equation. The wave kinematics at required location is calculated through Wkin.dll 2D using location coordinates sent from HAWC2 and polynomial coefficients sent from wave kinematics database.

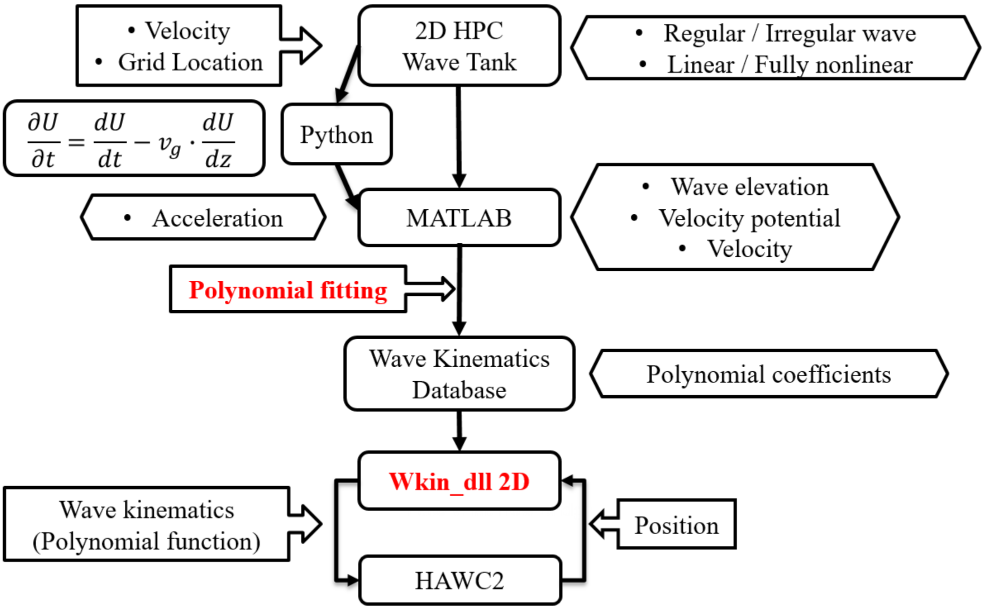

Figure 4.8: Work flow of proposed numerical code

The procedure is first verified against stream function wave developed by Dean [118] and linear Airy wave in regular wave condition as listed in Table 4.1 labeled as Paper 3. The most significant difference of the three load cases is the nonlinearity of the wave defined as wave steepness which is the ratio of wave height to its wavelength. The latter two wave models are available in HAWC2 as default input options.

On one hand, the comparison between regular fully nonlinear wave and stream function wave can indicate how good the proposed method is since both of the two wave models satisfy fully nonlinear FSBCs and they should provide the same prediction in theory. On the other hand, the comparison with linear Airy wave can illustrate how significant the wave nonlinear effect is in different load cases. The comparison is performed with respect to wave elevation, wave particle velocity and acceleration detected at location (0 m, 0 m, 0 m), floater motions and mooring line tensions.

The wave elevations are compared in the left column of Figure 4.9. Wave period detected is the same for all the three wave models while equal peak and trough is predicted from linear wave and smaller trough and higher peak are estimated from stream function wave and fully nonlinear wave due to the nonlinear effect. The wave particle velocity and acceleration are detected at fixed location whose coordinates are (0 m, 0 m, 0 m), therefore the values will become zero when instantaneous water level drops below zero. Stream function wave and fully nonlinear wave generated by the HPC wave tank clearly provide larger kinematics than linear wave.

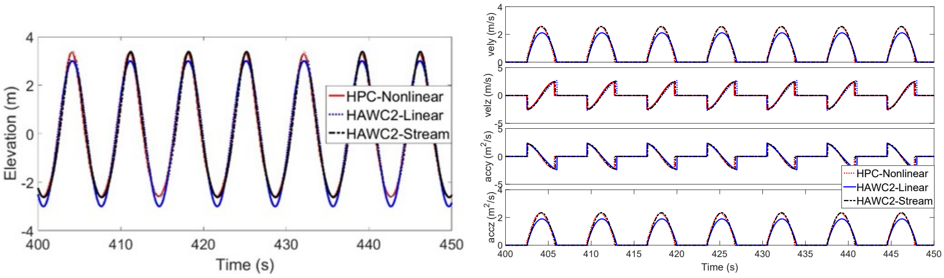

(a) Wave elevation - H6T7 *(b) Velocity/acceleration - H6T7*

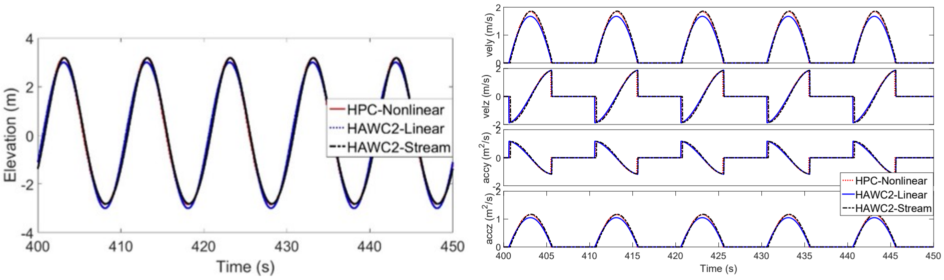

(c) Wave elevation - H6T10 *(d) Velocity/acceleration - H6T10*

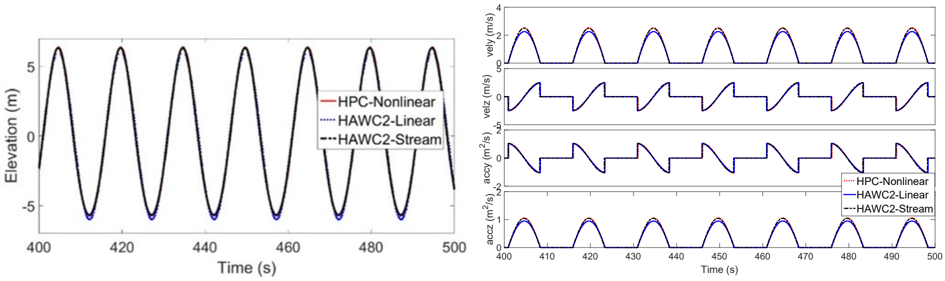

(e) Wave elevation - H12T15 *(f) Velocity/acceleration - H12T15*

Figure 4.9: Comparison of wave kinematics

The floater motion and mooring line tension is compared in Figure 4.10. For linear wave, the integration will be done up to the instantaneous wave elevation with the help of stretching the wave kinematics. The mean surge response is non-zero due to the viscous wave effect which is third-order of incident wave. Surge and heave response from fully nonlinear wave and stream function wave are almost the same and clearly larger than linear wave response. The difference is less significant for pitch motion. Mooring line tension which is greatly influenced by the floater motion especially in the horizontal plane basically follows the same trend as surge motion.

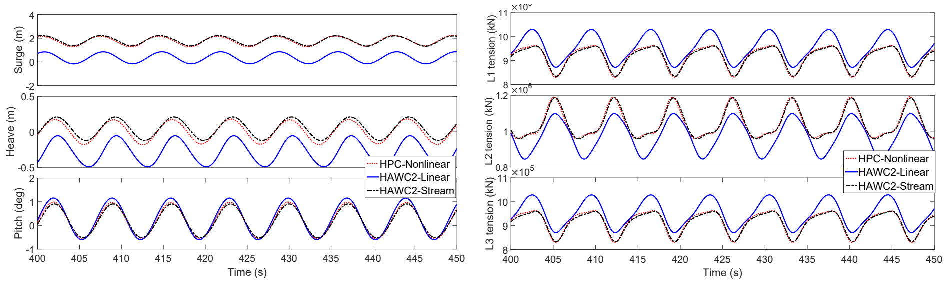

(a) Floater motion - H6T7 *(b) Mooring line tension- H6T7*

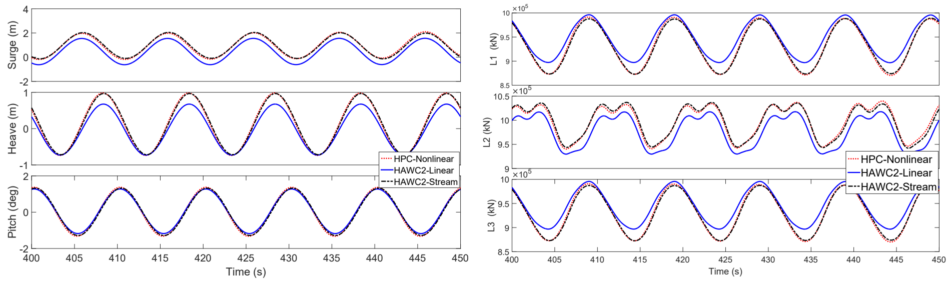

(c) Floater motion - H6T10 *(d) Mooring line tension - H6T10*

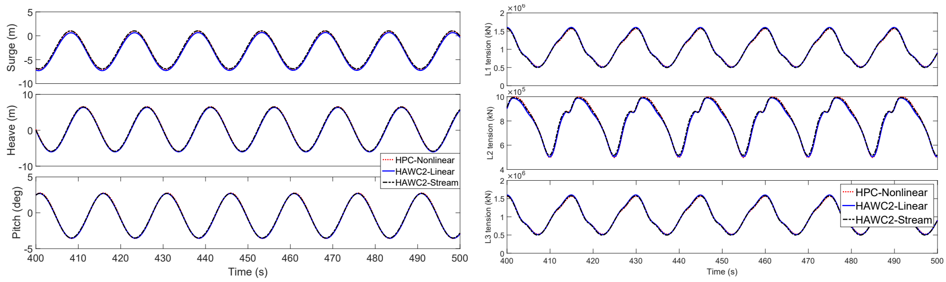

(e) Floater motion - H12T15 *(f) Mooring line tension - H12T15*

Figure 4.10: Comparison of motion and tension response

In conclusion, the comparison between the three wave models in different load cases proves the accuracy and applicability of the proposed method to study fully nonlinear wave load effect. At the same time, the wave nonlinear effect is shown to influence the structural response and it is more significant in conditions with larger wave steepness.

4.5.2 Comparison - irregular wave

Based on the verified method, the fully nonlinear wave model is implemented in irregular wave trains based on JONSWAP wave spectrum and compared with irregular linear wave model in this section. As shown in Table 4.1, two wave-only extreme load cases ULS1 & ULS2 are first compared to specifically study the influence due to the wave nonlinearity. Afterwards, eight wind-wave load cases labeled as LC1-8 are used to include the wind effect as well.

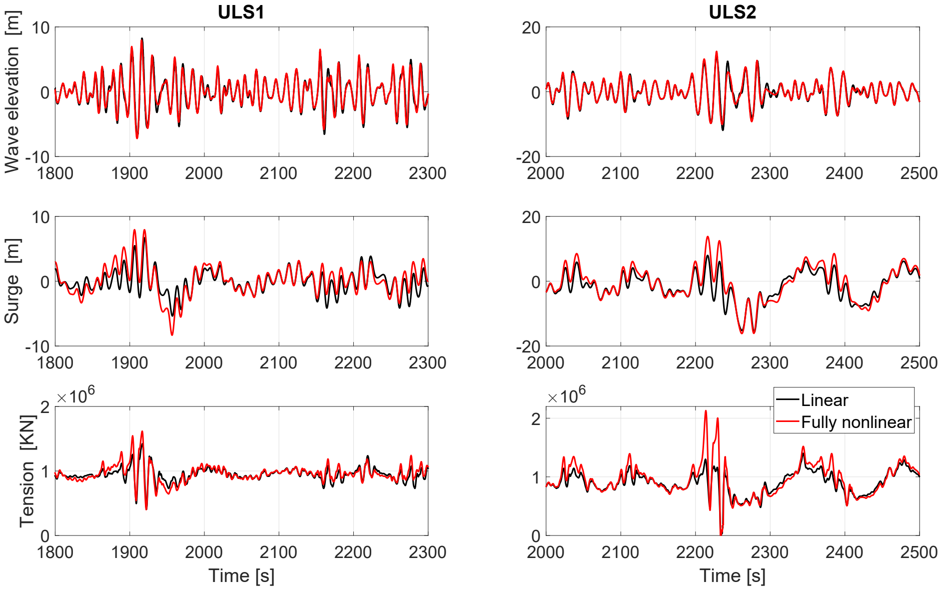

Figure 4.11: Time series of wave elevation, surge motion and mooring line tension due to linear and fully nonlinear wave in two conditions.

An example of time series for wave elevation, floater surge motion and mooring line tension are given in Figure 4.11. Black line represents results due to linear wave and red line represents results due to fully nonlinear wave. Since the same seed number is used to generate the wave for linear and fully nonlinear wave, the time series of the wave and response follow the same trend just with different amplitudes due to wave nonlinearity effect.

The peak amplitude illustrates the difference between the two wave models, which is the basis of the statistical comparison in this section. From statistical point of view, probability of exceeding a given threshold by a random maximum provides direct indication of the distribution of maximum response and it can be fit with asymptotic extreme value probability distribution model when the number of sample is large enough. Accordingly, the occurrence probability of a certain level of response can be then predicted. The probability of exceedance is calculated as:

$$P(X_i) = 1 - \frac{i}{N+1} \tag{4.6}$$

Where X_i is the response sorted in an increasing order. N is the total number of peaks.

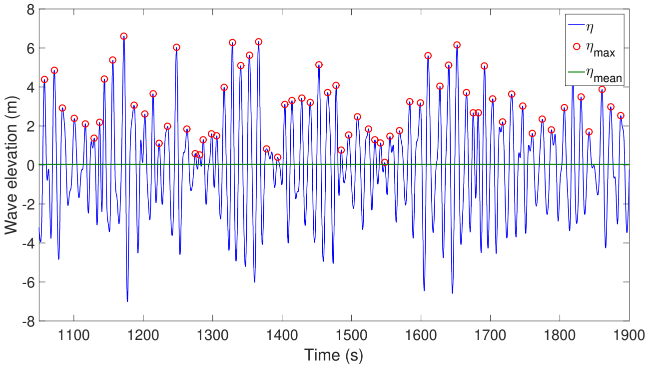

Figure 4.12: Selection of global maxima

Normally, global response maxima of a stationary Gaussian narrow-band process can be well modelled by a Rayleigh distribution [103]. However, when non-Gaussian and nonlinear property of the process increases, in order to get an accurate expression of the upper tail distribution, Weibull distribution is preferred instead of Rayleigh distribution. In this study, the largest maximum response between adjacent zero-up-crossing above the mean response level is selected as the global response maxima. Figure 4.12 is an example of the global maxima selection of the wave elevation. Blue line is the realization of the wave elevation and green line is the level of mean value and the red dots represent the selected global maxima. The exceedance probability above 0.1 is fitted with Rayleigh distribution while the tail part with probability below 0.1 is decided to be fitted with Weibull distribution. In the following section, results of linear and nonlinear wave from ULS1 and ULS2 conditions are shown together with different colors and markers. The fitting probability distribution are plotted using dashed line with the same color as the original maxima data. The horizontal axis represents the global maxima of the response and the vertical axis representing the probability of exceedance is expressed in a logarithmic scale for better representation.

4.5.2.1 Wave realization

The property of the wave observed at location (0m, 0m, 0m) is first compared with time realization and wave spectrum. Figure 4.13 shows the probability of exceedance for positive wave peaks observed at (0m, 0m, 0m) obtained from linear and nonlinear wave in two conditions. In general, distinction is not obvious between linear and nonlinear curves at probability level larger than 0.1 for smaller wave peaks. It is mainly the higher maxima with probability level below 0.1 that has clear difference. Higher peaks are predicted from nonlinear wave than linear wave and the difference is more obvious in higher sea state (ULS2). When the same exceedance probability is considered, fully nonlinear wave tends to predict higher value. The mixed Rayleigh-Weibull distributions is able to predict the probability of the original data quite well. The statistics of wave realization is presented in Table 4.7. Nonlinear wave in general predicts larger maximum elevations than linear wave for both cases, which is mainly due to the additional contribution from the nonlinear terms in the fully nonlinear FSBCs and the fact that the conditions are satisfied on the instantaneous wave surface.

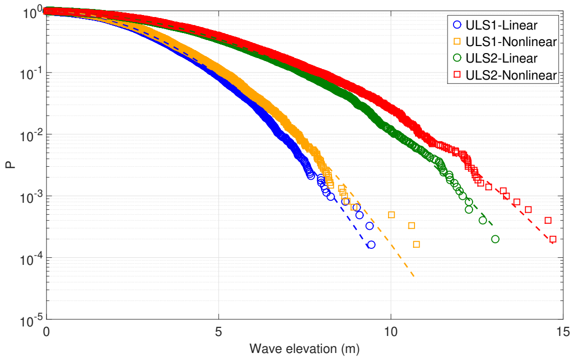

Figure 4.13: Exceedance probability for global maxima of wave peaks at (0m, 0m, 0m)

Wave spectrum determines the energy distribution of the wave at different frequencies. The linear and nonlinear spectrum of wave elevation for both cases are compared in Figure 4.14. The spectra at wave frequency range (ULS1: [0.3 rad/s - 1 rad/s] & ULS2: [0.25 rad/s - 1 rad/s]) are quite similar for linear and nonlinear wave containing most of the energy. The main difference is located at higher and lower frequency. The wave spectra are zoomed in at three frequency ranges as shown in Figure 4.15. It is seen that linear wave tends to have more energy at range [0.5 rad/s -

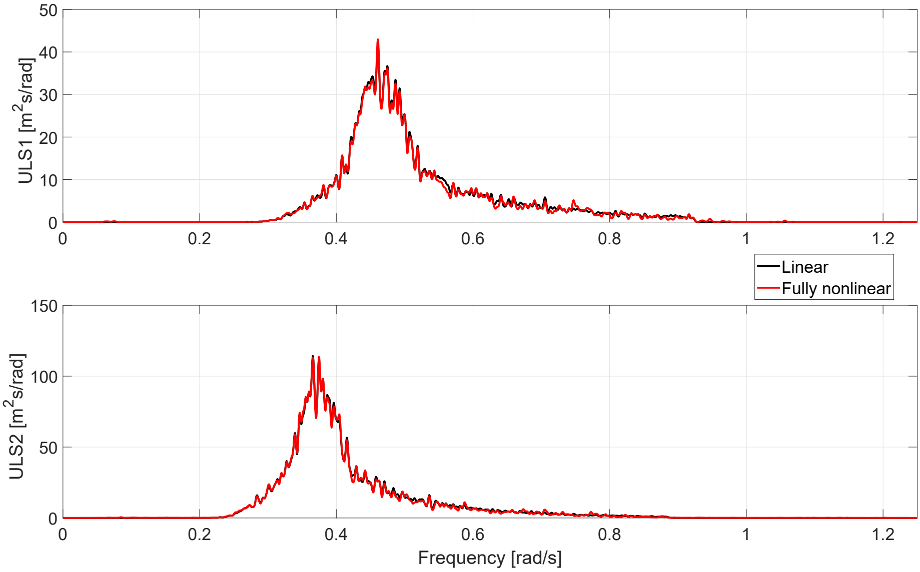

Figure 4.14: Wave spectrum

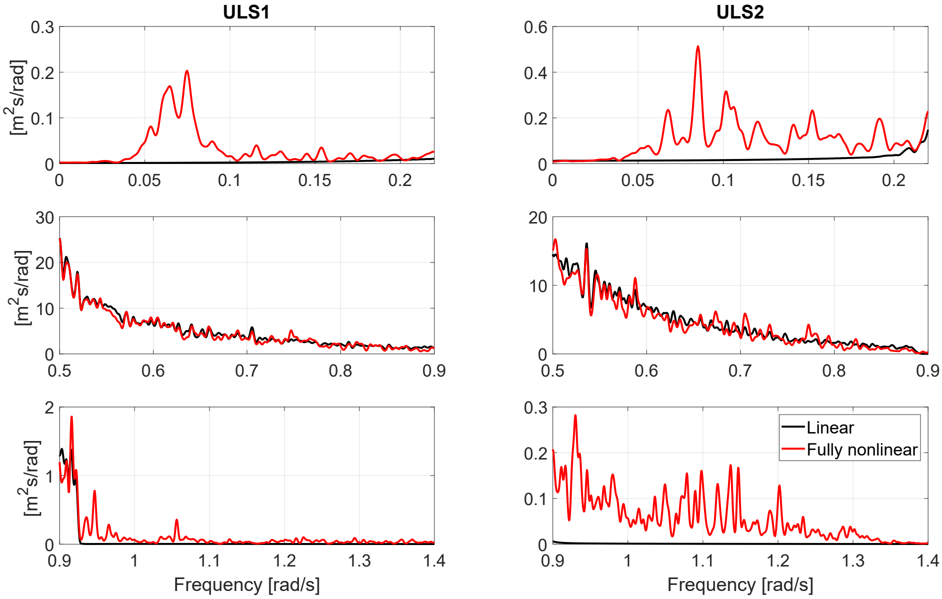

Figure 4.15: Wave spectra at different frequency ranges

0.9 rad/s] than nonlinear wave. At the same time, nonlinear wave relocates more energy at higher range [0.9 rad/s - 1.4 rad/s] and lower range [0 rad/s - 0.2 rad/s]. Initially, the wave spectrum used for generating the irregular wave is the same for linear and fully nonlinear wave and the difference of the energy distribution in the resulting wave spectrum for different frequency range is indeed due to nonlinear free surface effect and contact effect from seabed during wave development. Different responses are directly affected by wave energy distribution at corresponding range, such as surge motion in low frequency range and tower base shear force and bending moment at wave frequency range.

4.5.2.2 Floater motion

Floater motion of a semi-submersible floating wind turbine is influenced by not only the wave-frequency wave load but also higher-order (low-frequency) wave load. The statistics of motion response is given in Table 4.7. Larger motion response is observed at higher sea states as expected in Figure 4.16. Limited difference is found in heave and pitch motion from the two wave models while significant difference is observed for surge motion.

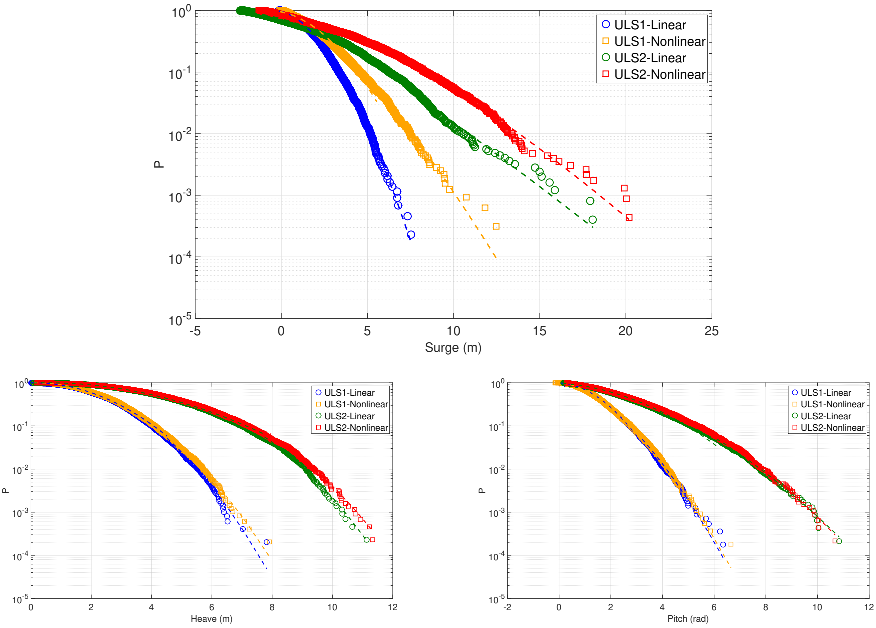

Figure 4.16: Exceedance probability for global maxima of floater motions

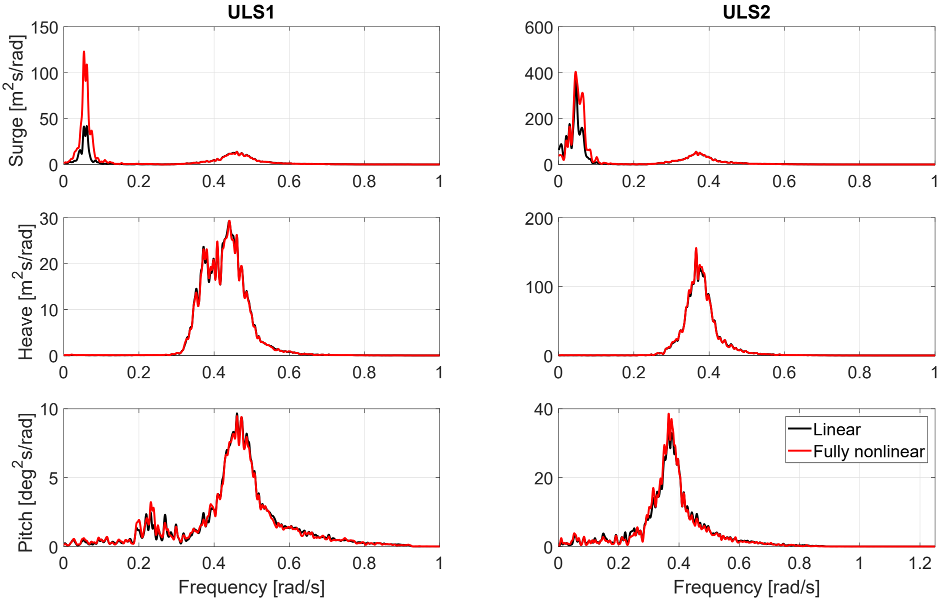

Figure 4.17: Motion spectrum

The motion response spectra are compared in Figure 4.17. For surge motion, little contribution is from wave frequency component while significant contribution is from surge resonance whose natural frequency is located between [0 rad/s - 0.2 rad/s] where fully nonlinear wave contains more energy than linear wave due to energy relocation as shown in Figure 4.15. Therefore, linear wave underestimates surge response compared with fully nonlinear wave, which is one of the most important findings in this study. As for heave and pitch motion, both of them are governed by wave frequency response where linear and fully nonlinear wave contains similar energy and very little contribution is due to motion resonance.

4.5.2.3 Tower base shear force and bending moment

The shear force and bending moment parallel to incoming wave direction at the tower base are studied in Figure 4.18. It is very interesting to notice that both shear force and bending moment predicted from linear wave model are in general larger than from nonlinear wave model. This is because both of them are mainly influenced by the wave frequency effect where linear wave contains more energy as shown in Figure 4.15.

Figure 4.19 shows the power spectrum for the bending moment which is shown to be sensitive to wave-frequency load. In this region, linear wave contains more energy than fully nonlinear wave which transfers energy to the frequency that tower base response is not very sensitive to.

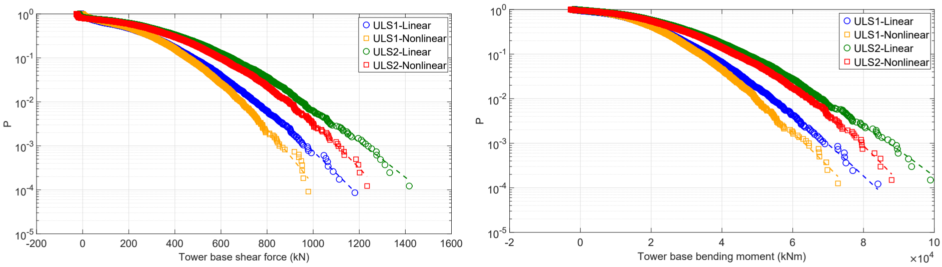

Figure 4.18: Exceedance probability for global maxima of tower base shear force and bending moment

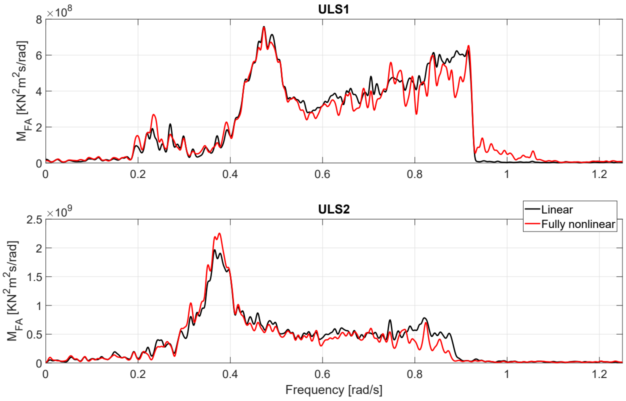

Figure 4.19: Tower base bending moment spectrum

4.5.2.4 Mooring line tension

As shown in the bird view of the mooring system configuration in Figure 4.1 (b), mooring line 2 is located in upwind direction and it is exposed to the largest tension. Linear wave clearly underestimate the tension and the difference is quite obvious even for smaller sea state. The statistics of tension response is provided in Table 4.7. The power spectrum for mooring line 2 is compared in Figure 4.21. Surge resonance dominates the mooring line tension response with additional contribution from wave frequency. The difference from linear and fully nonlinear wave is more significant in the surge resonant range (low frequency range) than wave frequency range.

Table 4.7: Statistics of wave realization and responses

		ULS1 Linear	ULS1 Nonlinear	ULS2 Linear	ULS2 Nonlinear
Wave	Mean [m]	9.79e-5	6.27e-4	3.55e-4	7.36e-3
	Maximum [m]	7.85	8.67	11.3	12.2
	Std [m]	2.24	2.23	3.43	3.40
	Skewness	0.00287	0.120	0.00883	0.170
	Kurtosis	3.02	3.05	2.90	2.94
	Extreme 10^{-4} [m]	9.79	10.60	13.78	15.59
Surge	Mean [m]	0.0981	0.126	0.921	1.96
	Maximum [m]	5.94	8.80	10.2	14.0
	Std [m]	1.56	2.10	4.09	4.41
	Skewness	0.152	0.242	-0.268	-0.0493
	Kurtosis	3.29	3.59	3.09	4.07
	Extreme 10^{-4} [m]	7.99	13.67	23.87	26.74
Heave	Mean [m]	0.0189	0.112	0.0482	0.179
	Maximum [m]	6.21	6.43	9.63	10.0
	Std [m]	1.85	1.84	3.29	3.29
	Skewness	0.0760	0.122	0.0435	0.0931
	Kurtosis	2.73	2.74	2.48	2.48
	Extreme 10^{-4} [m]	7.53	7.81	11.29	11.78
Pitch	Mean [deg]	0.0713	0.0606	0.203	0.295
	Maximum [deg]	5.13	5.10	8.70	8.86
	Std [deg]	1.19	1.18	2.10	2.11
	Skewness	0.249	0.313	0.415	0.519
	Kurtosis	3.35	3.38	3.56	3.51
	Extreme 10^{-4} [deg]	6.58	6.55	11.58	11.33
Mooring	Mean [KN]	8.64e+05	9.12e+05	9.48e+05	9.61e+05
	Maximum [KN]	1.403e+06	1.758e+06	1.706e+06	2.458e+06
	Std [KN]	8.215e+04	1.130e+05	1.687e+05	2.096e+05
	Skewness	0.214	1.01	0.743	1.08
	Kurtosis	5.31	5.91	6.46	10.1
	Extreme 10^{-4} [KN]	1.657e+06	2.438e+06	2.732e+06	3.215e+06

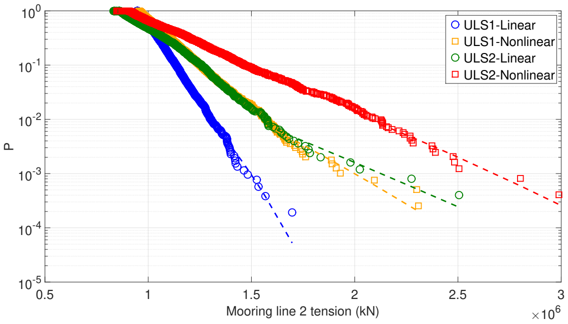

Figure 4.20: Exceedance probability for global maxima of upwind mooring line tension

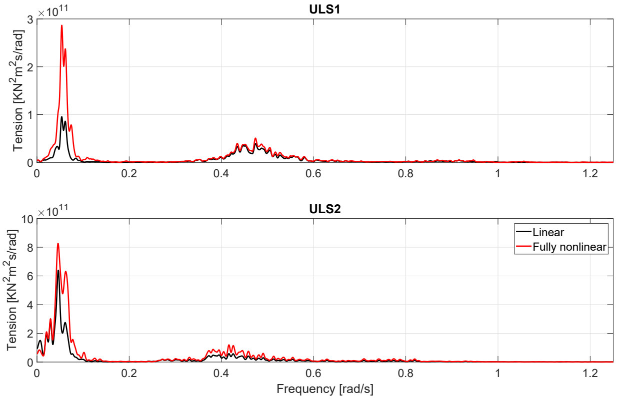

Figure 4.21: Mooring line tension spectrum

4.5.2.5 Fatigue damage

The effect of wave nonlinearity on the fatigue damage of mooring line and tower base is studied for the representative operational conditions as shown in Table 4.1 and the final results are given in Figure 4.22. Generally, the fatigue damage at conditions with lower wind speed and smaller wave than LC1 can be expected not significant. The fatigue damage at the tower base increases as sea state increases, which is mainly due to increase of wind speed. The excitation of the tower natural bending mode in LC2 significantly increases the fatigue damage level compared with other LCs. Linear wave predicts slightly higher fatigue damage than fully nonlinear wave because more energy is located around wave frequency range for linear wave. However, the difference is only noticeable in higher sea state.

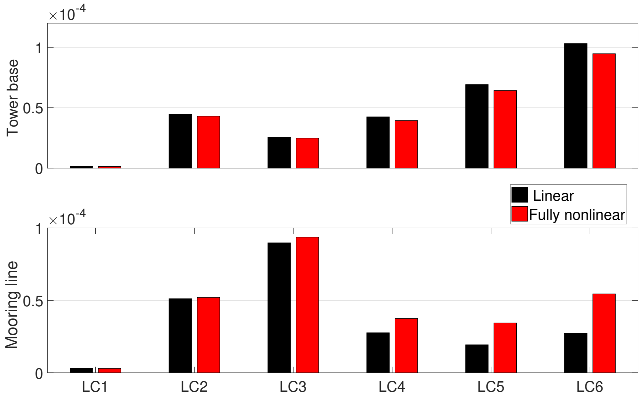

Figure 4.22: Hourly fatigue damage at the tower base and the mooring line

The fatigue damage of the mooring line on the other hand is normally proportional to wave height and inversely proportional to wave period when exposed to wave only condition. From Figure 4.22, the fatigue damage level of mooring line which are wind dominated reaches the maximum at LC3. From LC4 to LC6, the increase of wind speed actually leads to decreasing fatigue damage while the increase of wave condition on the contrary leads to increasing fatigue damage. As a result, the fatigue damage level in LC6 is found to be higher than in LC4 and LC5, which marks the greater contribution of fatigue damage due to wave nonlinearity.

4.5.2.6 Extreme value prediction

As shown in previous results, the wave nonlinear effect becomes more significant as environmental condition becomes more severe. Therefore, the extreme values of critical responses in the representative load cases LC7 & LC8 are further compared from the two wave models. Gumbel fitting method and ACER method as described in Section 3.7 are used. The purpose of this study is to quantify the wave nonlinear effect into numbers to better describe the significance.

The maximum value identified are plotted in Gumbel probability paper as shown in Figure 3.12 where the shape and location parameters can be determined accordingly. Once the unknown coefficients are estimated, the probability distribution function for Gumbel distribution is available. A large simulation sample is required in order to predict the Gumbel distribution with acceptable accuracy. Meanwhile, only the largest maxima is used for estimation while the other maxima peaks did not really contribute. Different from the Gumbel fitting method, all individual global peaks are involved in ACER method for predicting the extreme value.

Once all the coefficients for both methods are determined, the exceedance probability is plotted in Figure 4.23 for wave elevation and surge motion as examples where the solid line represents ACER function and dashed line stands for Gumbel function while original maximum peaks from each simulations are shown as markers with different colors. Exceedance probability not only indicates how well the probability models fit with original data but also provides a direct way to determine the extreme value over a certain probability occurrence level. In general, linear wave models predicts smaller extreme value than fully nonlinear wave model for a given exceedance level while the predictions from ACER method and Gumbel method are pretty close to each other.

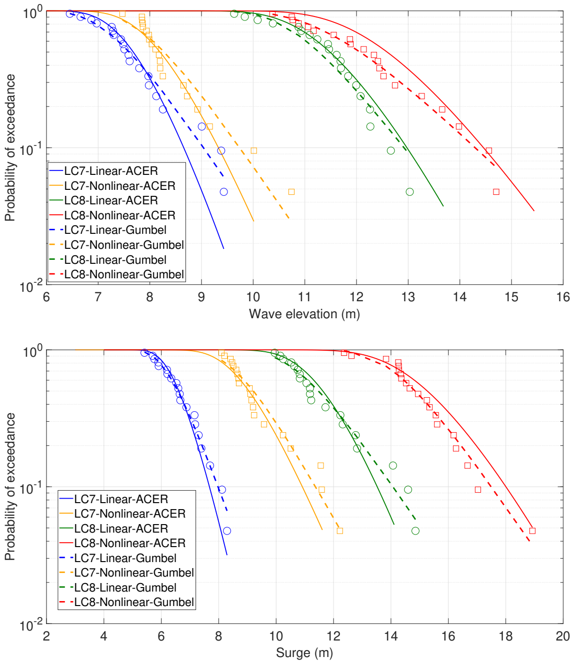

Figure 4.23: Exceedance probability for wave elevation and surge motion

Thereafter, the expected maximum value of two methods for the given short-term condition can be determined based on the derived probability density functions as shown in Figure 4.24 where different colors are used to represent the predictions from two methods in two load cases. The notations are explained with more details in appended paper 5 [87]. The responses which are sensitive to nonlinear wave effect are distinguished from others. First of all, as wave height increases, the extreme response due to higher sea states (LC8) is predicted larger than smaller sea states (LC7). Secondly, Gumbel fitting method generally predicts quite close results as ACER method for all cases even though latter method utilizes more data from time series. Most importantly, linear wave model significantly underpredicts extreme floater surge motion and mooring line tension compared with the fully nonlinear wave model for both LC7 and LC8 conditions and it becomes more significant as sea state becomes more severe. Underestimation is found for wave elevation, surge motion and mooring line tension with approximately 10%, 25% and 25% respectively. Meanwhile, the extreme value predictions are quite close for other responses which indicating they are not sensitive to wave nonlinearity effect.

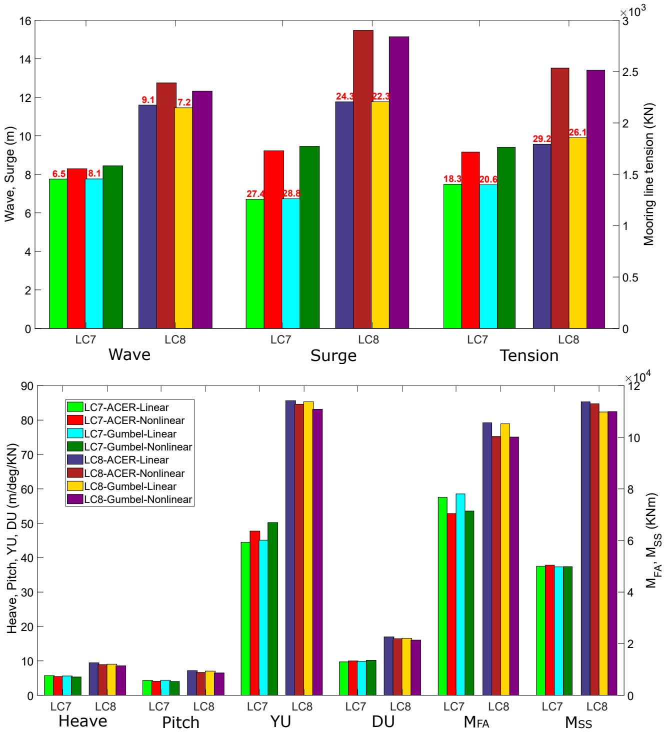

Figure 4.24: Extreme response (The red numbers on top of the bar column quantify the under-estimation of linear wave theory as the percentage of the difference to the results of fully nonlinear wave theory) [87]

Chapter 5

Conclusions and recommendations for future work

This thesis studies the design challenge of mooring system for semi-submersible FWT in shallow water as well as different hydrodynamic load modelling methods in shallow water especially regarding the higher-order wave effect such as second-order and fully nonlinear wave effect. Novel mooring design concepts consisting of different mooring line materials and components are systematically compared and feasible solutions are recommended. Newman's approximation method and full QTF method are compared regarding their applicability and limitation of calculating second-order difference-frequency wave load effect in shallow water. Fully nonlinear wave effect is studied based on an external numerical wave tank, a recent-proposed fitting method and a link between wave kinematics database and the dynamic analysis numerical tool. The final chapter presents the conclusions, original contributions and recommendation for future work.

5.1 Conclusions

The main conclusions of the thesis can be summarized as follow:

- Seven new mooring system design concepts are proposed for 50 m in order to discover the marginal water depth to deploy floating wind project. Different mooring line materials and additional mooring components are cooperated with different anchors for concept proposals by taking full advantage of both geometric and elastic mooring stiffness. Due to smaller effective water depth in shallow water, the weight of catenary chain mooring line has to be increased in order to achieve reasonable pre-tension as deep water. It can be improved by replacing with clump weight while the inclusion of buoy can further decrease the mooring line tension but will increase the floater motion. For catenary mooring system, the mooring line lying on the seabed need to be long enough to prevent anchor taking vertical load. Otherwise, strong nonlinear resorting effect will lead to large mooring line tension. Taut mooring system consisting of fibre rope on the other hand proves its advantage over traditional catenary mooring line with its linear tension increment even for large offset. The restoring stiffness of synthetic fibre rope mooring system is small compared with strictly taut mooring system, since the total length of the mooring line is quite long considering the water depth. The restoring stiffness will be too large if a shorter line is used. From the cost perspective, the capital cost of heavy chain is high while the DEA and the installation is cheap. The cost of fibre rope is low while the suction anchor and installation is high. In the end, two preferable mooring designs with better performance and competitive cost are recommended for industrial application in the future: one hybrid catenary mooring made of chain, clump weight and buoy; one taut mooring made of pure fibre rope.

- Newman's approximation and full QTF method have been comparatively studied for the second-order wave drift force for the CSC semi-submersible floating wind turbine in three water depths. Newman's approximation is applied in horizontal plane i.e. surge, sway and yaw while full QTF method involves calculation in all six DOFs. Compared with full QTF method, Newman's approximation is less computation-intensive which requires only the diagonal terms of full QTF matrix and the accuracy is acceptable in relatively deep water while the underestimation increases as environmental condition becomes more severe and water depth decreases. Therefore, full QTF method is recommended to describe the second-order wave drift force for semi-submersible FWT in shallow water.

- The linear and fully nonlinear irregular wave using same random seed are first generated in the 2D HPC numerical wave tank with linear and fully nonlinear FSBCs respectively. A number of problems have been properly handled such as time integration, wave generation and wave absorption. Before importing wave kinematics data into HAWC2 where the time-domain dynamic simulation is carried out, the enormous data is first fitted into polynomial functions representing location coordinates associated with polynomial coefficients which significantly decreases the size of the data. The external dynamic link library used to provide wave kinematics to HAWC2 is further extended from one dimensional (Wkin.dll 2.4) to two dimensional (Wkin.dll 2D) in order to include the variation of wave kinematics along horizontal direction which is relevant for floating wind turbine. The fully nonlinear wave kinematics is imported through the extended DLL to HAWC2 in the form of polynomial coefficients. Wkin.dll 2D receives location coordinates from HAWC2 and sends back the exact wave kinematics value for hydrodynamic wave load calculation.

- The numerical tool to include fully nonlinear wave model is verified against stream function wave and linear Airy wave which are two well-proven models. Three regular wave conditions with different degree of nonlinearity are considered. The comparison with stream function wave proves the accuracy and applicability of the proposed method since both of them satisfy the fully nonlinear FSBCs and their properties including wave elevation and wave kinematics are the same in regular form theoretically. The comparison with linear Airy wave at the same time indicates the influence due to wave nonlinearity. The results did show the difference regarding not only wave kinematics but also structural response and the difference increases as wave becomes more nonlinear.

- Based on the verified numerical tool, the significance of wave nonlinearity effect is systematically studied based on irregular wave simulations in both operational and extreme conditions respectively. In operational condition, linear wave predicts slightly higher heave & pitch motions, tower based bending moment & shear force and tower base fatigue damage while fully nonlinear wave theory predicts larger surge motion, mooring line tension and mooring line fatigue damage. This is because fully nonlinear wave distributes more wave energy to higher and lower frequency range than wave frequency due to wave nonlinearity effects which greatly influences responses whose natural period is in the low frequency range and the difference increases significantly as the sea state becomes more severe. In extreme conditions, Gumbel fitting method and ACER method are able to provide similar extreme predictions. Linear wave generally underestimates wave elevation, floater surge motion and mooring line tension compared with fully nonlinear wave by 10%, 25% and 25% respectively.

5.2 Original contributions

This thesis mainly deals with the design and analysis of mooring system for semi-submersible floating wind turbine when water depth is shallow. The main original contributions include both design concept proposal and analysis method development. It can be summarized as follow:

• Propose different mooring system design concepts for semi-submersible floating wind turbine in shallow water. The performance is compared from different perspectives including cost analysis. An innovative catenary mooring concept combined with clump weight and buoy is developed and its performance is proved to be improved compared with traditional catenary mooring designs.

A state-of-the-art numerical model for the stiffness of synthetic fibre rope is implemented in the numerical simulation to better describe its behavior.

• Study the applicability of different second-order wave load modelling methods for semi-submersible floating wind turbine at different water depths. Newman's approximation and Full QTF method are compared while three water depth including 200 m, 100 m and 50 m are considered.

• In order to study the fully nonlinear wave effect on floating wind turbine, an engineering-practical numerical tool is developed. The dynamic link library (Wkin.dll) between the wave kinematics database generated from numerical wave tank (2D HPC) and the time-domain dynamic analysis code (HAWC2) is extended from one-dimensional to two-dimensional in order to be applicable for floating structures.

• The size of the wave kinematics data from the numerical wave tank is quite large which not only exceeds the virtual memory requirement of the code but also decreases the computation efficiency. Therefore, a polynomial fitting method is proposed to fit the data at discrete grid point to polynomial coefficients associated with location coordinates.

• The numerical code to study fully nonlinear wave effect is verified against existing regular wave models including Airy wave and stream function wave. The verification not only proves the accuracy of the code but also indicate the significance of nonlinear wave effect.

• Compare the wave nonlinearity effect in realistic environment described by irregular wave. Different load cases characterized by different wave parameters are considered while fatigue damage and extreme values for critical responses are also predicted in order to give a full picture of the wave nonlinearity effect.

5.3 Recommendations for future work

Based on the work that has been done in this thesis, the following topics are recommended for future work:

• *Comparative analysis of mooring system with emphasis on fatigue limit state design*

The comparative analysis of the proposed mooring system in paper 1 is limited to ultimate limit state design while it can be extended to include fatigue analysis where a sufficient number of environmental conditions are considered. Then a more complete picture of the performance of the mooring concepts can be expected.

• *Further optimization of proposed mooring system concepts*

The seven mooring concepts in Paper 1 are proposed comparatively which means improvement of design modification will decrease the utilization factor of the mooring line and make it less optimized. Further optimization of individual design can be performed in order to decrease the cost of the concept.

• *Sensitivity study of specific mooring line properties*

Mooring system design is a huge project involving many different design parameters. The influence of the change of a specific mooring line property is of interest to check, such as the size and location of clump weight and buoy.

• *Compare the mooring concepts with model test*

Apart from the numerical analysis, it will be quite meaningful to extend the comparison further with model test and check the performance of different concepts in order to get a better understanding.

• *Wave kinematics fitting method*

The order of the polynomial used in the fitting method in this thesis is selected as 6, it is interesting to check whether the increase of order could improve the fitting accuracy and efficiency. Meanwhile, other fitting method based on different philosophies can be compared, such as sigmma transformation method.

- *Effect due to different order wave kinematics*

  It is possible to describe the wave kinematics up to a certain order based on Stokes theory, such as second-order, fifth-order etc. It is of interest to compare the different wave kinematics models and check how much contribution is from each order. The applicable regime for different wave theories is also of interest to analyze.

- *Validate the fully nonlinear wave model with model tests or field measurements*

  The developed numerical tool for fully nonlinear wave effect has been verified against different numerical wave models. Further validation is necessary through comparisons with model tests or field measurements.

- *Hydrodynamic load modelling method*

  The reason for choosing Morison's equation as the hydrodynamic load calculation method for fully nonlinear wave kinematics is because Morison's equation is the only option in HAWC2 to combine with importing wave velocity and acceleration. It will be interesting to extend the approach by considering a different load model, such as Rainey model [119], FNV model [120] etc. Another potential modelling method could be a combination of diffraction/radiation theory for potential flow part and Morison' equation to integrating the drag term up to instantaneous incident wave surface.

- *The selection of drag coefficients*

  The drag coefficients for the Morison's equation are dependent on KC numbers, Reynolds numbers etc. The uncertainty of the empirical coefficients should be addressed in the future through calibration against model test or CFD analysis with proper turbulence modelling in order to establish a decent database for drag coefficients that can be used in the time domain simulation in the future.

References

[1] Global Wind Energy Council, *Global Wind Report 2018.* 2019. Brussels, Belgium.

[2] Global Wind Energy Council, *Global Wind Report 2019.* 2020. Brussels, Belgium.

[3] Wind Europe, *Wind energy in Europe in 2018.* 2019. Brussels, Belgium.

[4] International Energy Agency, *Offshore Wind Outlook 2019.* 2019. Paris, France.

[5] DNVGL, *Floating wind technology - Future development.* 2014. Oslo, Norway.

[6] European Wind Energy Association, *Deep water - The next step for offshore wind energy.* 2013. Brussels, Belgium.

[7] A. Myhr, C. Bjerkseter, A. Ågotnes, and T. A. Nygaard, "Levelised cost of energy for offshore floating wind turbines in a life cycle perspective," *Renewable Energy*, vol. 66, pp. 714–728, 2014.

[8] Wind Europe, *Offshore Wind in Europe Key trends and statistics 2018.* 2019. Brussels, Belgium.

[9] J. Jonkman, S. Butterfield, W. Musial, and G. Scott, *Definition of a 5MW Reference Wind Turbine for Offshore System Development.* 2009. National Renewable Energy Laboratory, US.

[10] P. Bortolotti1, H. C. Tarres, K. Dykes, K. Merz, L. Sethuraman, D. Verelst, and F. Zahle, *IEA Wind Task 37 on Systems Engineering in Wind Energy WP2.1 Reference Wind Turbines* . 2009.

[11] IEA Wind, *Definition of the IEA Wind 15-Megawatt Offshore Reference Wind Turbine.* 2020. Denver, US.

[12] Wind Europe, *Offshore Wind in Europe Key trends and statistics 2019.* 2020. Brussels, Belgium.

[13] LEANWIND, *LEANWIND deliverable - project no. 614020 Summary description of LEANWIND 8 MW reference turbine.* 2015. University College Cork, UK.

[14] C. Bak, F. Zahle, R. Bitsche, T. Kim, A. Yde, L. C. Henriksen, M. H. Hansen, J. P. A. A. Blasques, M. Gaunaa, and A. Natarajan, *The DTU 10-MW Reference Wind Turbine.* 2013. DTU Wind Energy, Denmark.

[15] Wold Forum Offshore Wind, *Global Offshore Wind Report 2019.* 2020. Hamburg, Germany.

[16] equinor, "Statoil to build the world's first floating wind farm: Hywind scotland," 2020. https://www.equinor.com/en/news/hywindscotland.html (accessed on 2020.02.14).

[17] edp renewable, "Windfloat atlantic project starts supplying clean energy in portugal," 2020. https://www.edpr.com/en/news/2020/01/02/windfloat-atlantic-project-starts-supplying-clean-energy-portugal (accessed on 2020.02.14).

[18] NS ENERGY, "Kincardine Floating Offshore Wind Farm, Scotland," 2020. https://www.nsenergybusiness.com/projects/kincardine-floating-offshore-wind-farm-scotland/ (accessed on 2020.02.14).

[19] Wind Europe, *Floating Offshore Wind Vision Statement.* 2017. Brussels, Belgium.

[20] Principle Power, "Windfloat," 2020. http://www.principlepowerinc.com/en/windfloat (accessed on 2020.02.14).

[21] B. Bulder, M. T. Van Hees, A. Henderson, R. Huijsmans, J. Pierik, E. Snijders, G. Wijnants, and M. Wolf, "Study on feasibility of and boundary conditions for floating offshore wind turbines," *ECN, MARIN, TNO, TUD, MSC, Lagerway the Windmaster*, vol. 26, pp. 70–81, 2002.

[22] Fukushima Offshore Wind Consortium, “Fukushima Floating Offshore Wind Farm Demonstration Project,” 2020. http://www.fukushima-forward.jp/english/ (accessed on 2020.02.14).

[23] LIFES50+, *Deliverable D4.2 Public Definition of the Two LIFES50+ 10MW Floater Concepts.* 2018.

[24] C. Luan, Z. Gao, and T. Moan, “Design and analysis of a braceless steel 5-mw semi-submersible wind turbine,” in *ASME 35th International Conference on Ocean, Offshore and Arctic Engineering*, American Society of Mechanical Engineers (ASME), 2016. Busan, South Korea.

[25] A. Robertson, J. Jonkman, M. Masciola, H. Song, A. Goupee, A. Coulling, and C. Luan, “Definition of the semisubmersible floating system for phase II of OC4,” 2014. National Renewable Energy Lab (NREL), Golden, Colorado, US.

[26] M. Brommundt, L. Krause, K. Merz, and M. Muskulus, “Mooring system optimization for floating wind turbines using frequency domain analysis,” *Energy Procedia*, vol. 24, pp. 289–296, 2012.

[27] G. Benassai, A. Campanile, V. Piscopo, and A. Scamardella, “Mooring control of semi-submersible structures for wind turbines,” *Procedia Engineering*, vol. 70, pp. 132–141, 2014.

[28] G. Benassai, A. Campanile, V. Piscopo, and A. Scamardella, “Ultimate and accidental limit state design for mooring systems of floating offshore wind turbines,” *Ocean Engineering*, vol. 92, pp. 64 – 74, 2014.

[29] G. Benassai, A. Campanile, V. Piscopo, and A. Scamardella, “Optimization of mooring systems for floating offshore wind turbines,” *Coastal Engineering Journal*, vol. 57, no. 4, 2015.

[30] A. Campanile, V. Piscopo, and A. Scamardella, “Mooring design and selection for floating offshore wind turbines on intermediate and deep water depths,” *Ocean Engineering*, vol. 148, pp. 349 – 360, 2018.

[31] L. Finn, “A new deepwater offshore platform - the guyed tower,” in *Offshore technology conference*, 1976. Houston, Texas.

[32] S. Mavrakos, V. Papazoglou, M. Triantafyllou, and J. Hatjigeorgiou, “Deep water mooring dynamics,” *Marine structures*, vol. 9, no. 2, pp. 181–209, 1996.

[33] P. C. Vicente, A. F. de O. Falcal, and P. A. Justino, “Slack-chain mooring configuration analysis of a floating wave energy converter,” in *Proceeding of 26th international workshop on water waves and floating bodies.*, (Athens, Greece), 2011.

[34] Z. M. Yuan, A. Incecik, and C. Ji, “Numerical study on a hybrid mooring system with clump weights and buoys,” *Ocean Engineering*, vol. 88, pp. 1–11, 2014.

[35] INNWIND.EU, *Deliverable D4.3.7 Design Solutions for 10MW Floating Offshore Wind Turbines.* 2017.

[36] LIFES50+, *Deliverable D4.5 State-of-the-art models for the two LIFES50+ 10MW floater concepts.* 2018.

[37] R. Rossi, C. J. Del Vecchio, and R. C. F. Goncalves, “Moorings with polyester ropes in petrobras: Experience and the evolutio,” in *Offshore Technology Conference 20845*, 2010.

[38] D. L. Bugg, D. Vickers, and C. Dorchak, “Mad dog project: Regulatory approval process for the new technology of synthetic (polyester) moorings in the gulf of mexico,” in *Offshore Technology Conference 16089*, 2004.

[39] Carnegie Clean Energy, “CETO Next Generation,” 2020. https://www.carnegiece.com (accessed on 2020.02.14).

[40] ideol, “France’s first offshore wind turbine and ideol’s first demonstrator,” 2020. https://www.ideol-offshore.com/en/floatgen-demonstrator (accessed on 2020.02.14).

[41] L. Johanning and G. H. Smith, *EquiMar Deliverable D7.3.2 Consideration of the cost implications for mooring MEC devices.* 2009.

[42] S. Weller, P. Davies, and L. Johanning, “The influence of load history on synthetic rope response,” in *Proceeding of the European Wave & Tidal Energy Conference*, 2013.

[43] S. Weller, L. Johanning, P. Davies, and S. Banfield, “Synthetic mooring ropes for marine renewable energy applications,” *Renewable energy*, vol. 83, pp. 1268–1278, 2015.

[44] J. N. Newman, “Second-order, slowly-varying forces on vessels in irregular waves,” in *Proceeding of International symposium dynamics of marine vehicles and structures in waves*, 1974. London, UK.

[45] O. M. Faltinsen and A. E. Løken, “Drift forces and slowly varying horizontal forces on a ship in waves,” in *Proceedings symposium on applied mathematics*, 1978. Delft, the Netherlands, pp 22-41.

[46] O. M. Faltinsen and A. E. Løken, “Slow drift oscillations of a ship in irregular waves,” 1979. Det Norske Veritas publication No. 108, Oslo.

[47] J. Pinkster, *Low frequency second order wave exciting forces on floating structures.* 1980. PhD thesis, Technical University of Delft.

[48] X. Chen and W. Duan, “Formulation of low-frequency QTF by O ($\Delta\omega$) approximation,” in *Proceedings of 22nd IWWWFB, Plitvice, Croatia*, 2007.

[49] Y. Shao, *Numerical potential-flow studies on weakly-nonlinear wave-body interactions with/without small forward speeds.* 2010. PhD thesis, NTNU.

[50] J. You, *Numerical Studies on Wave Forces and Moored Ship Motions in Intermediate and Shallow Water.* 2012. PhD thesis, NTNU.

[51] R. Gibson and C. Swan, “The evolution of large ocean waves: the role of local and rapid spectral changes,” *Proceedings of the Royal Society A: Mathematical, Physical and Engineering Sciences*, vol. 463, no. 2077, pp. 21–48, 2006.

[52] G. G. Stokes, *On the Theory of Oscillatory Waves*, vol. 1 of *Cambridge Library Collection - Mathematics*, pp. 197–229. Cambridge University Press, 2009.

[53] S. Schløer, H. Bredmose, and H. B. Bingham, “Irregular wave forces on monopile foundations. effect af full nonlinearity and bed slope,” in *30th International Conference on Ocean, Offshore and Arctic Engineering*, vol. 5, pp. 581–588, American Society of Mechanical Engineers, 2011.

[54] S. Schløer, H. Bredmose, and H. B. Bingham, “The influence of fully nonlinear wave forces on aero-hydro-elastic calculations of monopile wind turbines,” in *In Proceedings of the ASME 31st International Conference on Ocean, Offshore and Arctic Engineering*, vol. 7, pp. 393–402, 2012.

[55] S. Schløer, H. Bredmose, and H. B. Bingham, “The influence of fully nonlinear wave forces on aero-hydro-elastic calculations of monopile wind turbines,” *Marine Structures*, vol. 50, pp. 162–188, 2016.

[56] T. J. Larsen, T. Kim, S. Schløer, and H. Bredmose, "Comparisons of wave kinematics models for an offshore wind turbine mounted on a jacket substructure," in *Proceedings European Wind Energy Association (EWEA)*, 2011.

[57] A. Nematbakhsh, E. Bachynski, Z. Gao, and T. Moan, "Comparison of wave load effects on a tlp wind turbine by using computational fluid dynamics and potential flow theory approaches," *Applied Ocean Research*, vol. 53, pp. 142–154, 2015.

[58] H. Bredmose, *INNWIND.EU Deliverable 4.21 Fully nonlinear wave forcing of a TLP wind turbine.* 2013.

[59] A. Pegalajar-Jurado, M. Borg, A. Robertson, J. Jonkman, and H. Bredmose, "Effect of second-order and fully nonlinear wave kinematics on a tension-leg-platform wind turbine in extreme wave conditions," in *36th International Conference on Ocean, Offshore and Arctic Engineering*, 2017.

[60] API, *API-RP-2SM Design, Manufacture, Installation, and Maintenance of Synthetic Fiber Ropes for Offshore Mooring*, 2014.

[61] Vryhof, *Vryhof Manual - the guide to Anchoring.* 2015. Netherlands.

[62] American Petroleum Institute , *API RP 2SK Recommended practice for design and analysis of stationkeeping systems for floating structures.* 2015. Washington DC, US.

[63] N. Barltrop, *Floating Structures: a guide for design and anslysis*, vol. 2. Oilfield Publications, Inc, 1998.

[64] DNVGL, *DNVGL-OS-E301 Position mooring.* 2018. Høvik, Norway.

[65] K. Xu, K. Larsen, Y. Shao, M. Zhang, Z. Gao, and T. Moan, "Design and comparative analysis of alternative mooring systems for floating wind turbines in shallow water with emphasis on ultimate limit state design," *Submitted to Ocean Engineering*, 2020.

[66] K. Xu, Z. Gao, and T. Moan, "Effect of hydrodynamic load modelling on the response of floating wind turbines and its mooring system in small water depths," in *Journal of Physics: Conference Series*, vol. 1104, p. 012006, IOP Publishing, 2018.

[67] O. M. Faltinsen, *Sea loads on ships and offshore structures*, vol. 1. Cambridge university press, 1993.

[68] E. Falkenberg, V. Åhjem, L. Yang, *et al.*, "Best practice for analysis of polyester rope mooring systems," in *49th Offshore Technology Conference (OTC)*, 2017. Houston, US.

[69] DNVGL, *DNVGL-RP-E305 Design, testing and analysis of offshore fibre ropes* . 2015. Høvik, Norway.

[70] BRIDON, *Oil and gas, wire and fibre rope solutions for the world's most demanding applications.* 2013. Doncaster, UK.

[71] Equinor, "Equinor - the world's leading floating offshore wind developer," 2020. https://www.equinor.com/en/what-we-do/hywind-where-the-wind-takes-us.html (accessed on 2020.02.14).

[72] R. Copple, C. Capanoglu, *et al.*, "Tension leg wind turbine (TLWT) conceptual design suitable for a wide range of water depths," in *22nd International Offshore and Polar Engineering Conference*, International Society of Offshore and Polar Engineers, 2012. Rhodes, Greece.

[73] J. Manwell, J. McGowan, and A. Rogers, *Wind Energy Explained: Theory, Design and Application.* John Wiley & Sons, 2010.

[74] M. O. L. Hansen, *Aerodynamics of Wind Turbines.* Earthscan, 2008.

[75] R. Gibson and C. Swan, "The evolution of large ocean waves: the role of local and rapid spectral changes," *Proceedings of the Royal Society A: Mathematical, Physical and Engineering Sciences*, vol. 463, no. 2077, pp. 21–48, 2006.

[76] International Electrotechnical Commission , *IEC 61400-3: Wind Turbines Part 3: Design Requirements for Offshore Wind Turbines.* 2009. Geneva, Switzerland.

[77] Y. Shao and O. M. Faltinsen, "Towards efficient fully-nonlinear potential-flow solvers in marine hydrodynamics," in *ASME 31st International Conference on Ocean, Offshore and Arctic Engineering*, American Society of Mechanical Engineers (ASME), 2012. Rio de Janeiro, Brazil.

[78] Y. Shao and O. M. Faltinsen, "A harmonic polynomial cell (HPC) method for 3D Laplace equation with application in marine hydrodynamics," *Journal of Computational Physics*, vol. 274, pp. 312–332, 2014.

[79] Y. Shao and O. M. Faltinsen, “Fully-nonlinear wave-current-body interaction analysis by a harmonic polynomial cell method,” *Journal of Offshore Mechanics and Arctic Engineering*, vol. 136, no. 3, p. 031301, 2014.

[80] D. Ning and B. Teng, “Numerical simulation of fully nonlinear irregular wave tank in three dimension,” *International Journal for Numerical Methods in Fluids*, vol. 53, pp. 1847–1862, 2007.

[81] C. T. Stansberg, O. T. Gudmestad, and S. K. Haver, “Kinematics under extreme waves,” *Journal of Offshore Mechanics and Arctic Engineering*, vol. 130, no. 2, p. 021010, 2008.

[82] DNVGL, *DNV-RP-C205 Environmental conditions and environmental loads*. 2017. Høvik, Norway.

[83] W. E. Cummins, “The impulse response function and ship motions,” in *Symposium on ship theory, University Hamburg*, 1962.

[84] G. D. Hauteclocque, F. Rezende, O. Waals, and X. B. Chen, “Review of approximations to evaluate second-order low-frequency load,” in *ASME 31st International Conference on Ocean, Offshore and Arctic Engineering*, American Society of Mechanical Engineers (ASME), 2012. Rio de Janeiro, Brazil.

[85] A. Robertson, J. Jonkman, M. Masciola, P. Molta, A. Goupee, A. Coulling, I. Prowell, and J. Browning, “Summary of conclusions and recommendations drawn from the deepcwind scaled floating offshore wind system test campaign,” in *ASME 32nd International Conference on Ocean, Offshore and Arctic Engineering*, American Society of Mechanical Engineers (ASME), 2013. Nantes, France.

[86] K. Xu, Y. Shao, Z. Gao, and T. Moan, “A study on fully nonlinear wave load effects on floating wind turbine,” *Journal of Fluids and Structures*, vol. 88, pp. 216–240, 2019.

[87] K. Xu, M. Zhang, Y. Shao, Z. Gao, and T. Moan, “Effect of wave nonlinearity on fatigue damage and extreme responses of a semi-submersible floating wind turbine,” *Applied Ocean Research*, vol. 91, p. 101879, 2019.

[88] K. Xu, Y. Shao, Z. Gao, and T. Moan, “Fully nonlinear wave effect on a semi-submersible floating wind turbine using wave kinematics from

2d Harmonic Polynomial Cell wave tank," in *2018 3rd Conference on Offshore Renewable Energy (CORE)*, 2018. Glasgow, UK.

[89] SINTEF Ocean, *RIFLEX 4.14.0 User Guide*, nov 2018. Trondheim, Norway.

[90] D. Qiao and J. Ou, "Comparative analysis on dynamic characteristics of deepwater hybrid mooring line," *Journal of Ship Mechanics*, vol. 15, no. 11, 2011.

[91] T. Stenlund, *Mooring System Design for a Large Floating Wind Turbine in Shallow Water.* 2018. Master thesis, NTNU.

[92] Z. Cheng, *Integrated Dynamic Analysis of Floating Vertical Axis Wind Turbines.* PhD thesis, NTNU, 2016.

[93] T. Moan, Z. Gao, E. Bachynski, and A. Nejad, "Recent advances in response analysis of floating wind turbines in a reliability perspective," in *International Offshore Wind Technical Conference (IOWTC)*, 2018. San Francisco, US.

[94] SINTEF, "Sima." https://www.sintef.no/en/software/sima/ (accessed on 2020.02.14).

[95] T. Larsen and A. Hansen, *How 2 HAWC2, the user's manual.* Risø National Laboratory, 2007. Copenhagen, Denmark.

[96] M. Hansen, M. Gaunaa, and H. Madsen, *A Beddoes-Leishman type dynamic stall model in state-space and indicial formulations.* Risø National Laboratory, 2004. Copenhagen, Denmark.

[97] B. Kallesøe and A. Hansen, "Dynamic mooring line modeling in hydro-aero-elasticwind turbine simulations," in *21st International Offshore and Polar Engineering Conference*, International Society of Offshore and Polar Engineers, 2011. Maui, Hawaii, US.

[98] Z. Gao and T. Moan, "Frequency-domain fatigue analysis of wide-band stationary gaussian processes using a trimodal spectral formulation," *International Journal of Fatigue*, vol. 30, no. 10-11, pp. 1944–1955, 2008.

[99] M. I. Kvittem and T. Moan, "Time domain analysis procedures for fatigue assessment of a semi-submersible wind turbine," *Marine Structures*, vol. 40, pp. 38–59, 2015.

[100] A. Wöhler, *Über die festigkeitsversuche mit eisen und stahl.* Ernst & Korn, 1870.

[101] DNVGL, *DNVGL-RP-C203 Fatigue design of offshore steel structures.* 2019. Høvik, Norway.

[102] A. Næss and T. Moan, *Stochastic dynamics of marine structures.* Cambridge University Press, 2013.

[103] P. Fu, B. J. Leira, and D. Myrhaug, "Reliability analysis of wake-induced collision of flexible risers," *Applied Ocean Research*, vol. 62, pp. 49 – 56, 2017.

[104] A. Næss and O. Gaidai, "Estimation of extreme values from sampled time series," *Structural Safety*, vol. 31, no. 4, pp. 325–334, 2009.

[105] P. Fu, B. J. Leira, and D. Myrhaug, "Assessment of methods for short-term extreme value analysis of riser collision," in *ASME 37th International Conference on Ocean, Offshore and Arctic Engineering*, American Society of Mechanical Engineers, 2018. Madrid,Spain.

[106] K. Johannessen, T. Meling, S. Haver, *et al.*, "Joint distribution for wind and waves in the northern north sea," in *11th International Offshore and Polar Engineering Conference*, International Society of Offshore and Polar Engineers, 2001. Stavanger, Norway.

[107] International Electrotechnical Commission , *IEC 61400-1: Wind turbines part 1: Design requirements.* 2005. Geneva, Switzerland.

[108] L. Li, Z. Gao, and T. Moan, "Joint distribution of environmental condition at five european offshore sites for design of combined wind and wave energy devices," *Journal of Offshore Mechanics and Arctic Engineering*, vol. 137, p. 031901, 2015.

[109] *DNVGL-ST-0119 Floating wind turbine structures.* DNVGL, 2018. Høvik, Norway.

[110] C. Bjerkseter and A. Ågotnes, "Levelised costs of energy for offshore floating wind turbine concepts," Master's thesis, Norwegian University of Life Sciences, Ås, 2013.

[111] K. E. Klingan, *Automated Optimization and Design of Mooring Systems for Deep Water.* 2016. Mater thesis, NTNU.

[112] Defender, "The marine outfitter of choice for boating enthusiasts since 1938," 2019. https://www.defender.com/ (accessed on 2020.02.14).

[113] J. M. Audibert, E. Clukey, J. Huang, *et al.*, "Suction caisson installation at horn mountain–a case history," in *The Thirteenth International Offshore and Polar Engineering Conference*, International Society of Offshore and Polar Engineers, 2003.

[114] S. Schløer, H. Bredmose, and H. B. Bingham, "Irregular wave forces on monopile foundations. effect of full nonlinearity and bed slope," in *ASME 30th International Conference on Ocean, Offshore and Arctic Engineering*, American Society of Mechanical Engineers (ASME), 2011. Rotterdam, Netherlands.

[115] S. Schløer, H. Bredmose, and H. B. Bingham, "The influence of fully nonlinear wave forces on aero-hydro-elastic calculations of monopile wind turbines," in *ASME 31st International Conference on Ocean, Offshore and Arctic Engineering*, American Society of Mechanical Engineers (ASME), 2012. Rio de Janeiro, Brazil.

[116] S. Schløer, H. Bredmose, and H. B. Bingham, "The influence of fully nonlinear wave forces on aero-hydro-elastic calculations of monopile wind turbines," *Marine Structures*, vol. 50, pp. 162–188, 2016.

[117] A. P. Engsig-Karup, H. B. Bingham, and O. Lindberg, "An efficient flexible-order model for 3d nonlinear water waves," *Journal of Computational Physics*, vol. 228, pp. 2100–2118, 2009.

[118] R. G. Dean, "Stream function representation of nonlinear ocean waves," *Journal of Geophysical Research Atmospheres*, vol. 70, no. 18, 1965.

[119] Rainey and R. C. T., "A new equation for calculating wave loads on offshore structures," *Journal of Fluid Mechanics*, vol. 204, no. -1, p. 295, 1989.

[120] O. M. Faltinsen, J. N. Newman, and T. Vinje, "Nonlinear wave loads on a slender vertical cylinder," *Journal of Fluid Mechanics*, vol. 289, no. -1, p. 179, 1995.

Appendix A

Appended papers

A.1 Paper 1

Paper 1:
Design and comparative analysis of alternative mooring systems for floating wind turbines in shallow water with emphasis on ultimate limit state design.
Authors: Kun Xu, Kjell Larsen, Yanlin Shao, Min Zhang, Zhen Gao, Torgeir Moan
Submitted to *Ocean Engineering*, 2020

This paper is awaiting publication and is therefore not included.

A.2 Paper 2

Paper 2:
Effect of hydrodynamic load modelling on the response of floating wind turbines and its mooring system in small water depths.
Authors: Kun Xu, Zhen Gao, Torgeir Moan
Published in *Journal of Physics: Conference Series*, 2018
DOI: 10.1088/1742-6596/1104/1/012006.

Effect of hydrodynamic load modelling on the response of floating wind turbines and its mooring system in small water depths

Kun Xu[1], **Zhen Gao**[1,2], **Torgeir Moan**[1,2]

[1] Department of Marine Technology, Norwegian University of Science and Technology (NTNU), Trondheim, NO-7491, Norway

[2] Centre for Autonomous Marine Operations and Systems (AMOS), NTNU, Trondheim, NO-7491, Norway

E-mail: `kun.xu@ntnu.no`

Abstract. A large number of offshore wind turbines have been installed recently, mostly in water depth up to 30 m based on monopile foundations. It is expected that floating wind turbine becomes more competitive than bottom fixed wind turbine when the water depth exceeds 50 m. In this paper, the focus is on the environmental loads and responses of mooring systems for a semi-submersible in water depths from 50 m to 200 m. Mooring design for moderate water depths is relatively easy to achieve, but it is challenging for shallow water. The effect of environmental load modelling should be studied based on designing a reasonable mooring system. With a mooring system design for 200 m water depth as a reference, two mooring system design concepts in 100 m and 50 m water depth have been proposed for a 5-MW-CSC semi-submersible floating wind turbine. Preliminary design has been carried out to determine mooring line properties, mooring system configurations and document the static performances. A fully coupled time domain dynamic analysis for extreme environmental conditions was performed using Simo-Riflex-AeroDyn. Four different load models were applied in order to check the influence of different load components including the effect of wind, current and second order wave forces by means of Newman's approximation and a full QTF method.

1. Introduction

In the last decades, more and more offshore wind energy projects have emerged with the purpose to accommodate more wind power with better quality, avoid noise effect and visual disturbance to citizens and achieve less obstacle to transport. Through the experiences gained in the offshore oil and gas industry, the long-term survivability of offshore support structures has been successfully demonstrated in the wind energy industry. There is still a huge potential for cost reduction and technological innovation. All ongoing commercial scale offshore wind projects utilise seabed mounted substructure concepts. However in many countries there are only a limited number of suitable sites in sufficiently shallow water to allow economically viable fixed substructures to be deployed. When the water depth exceeds 50 m, floating support structures are expected to be competitive in terms of lifecycle cost. However, floating wind turbines are still at an early stage of development and it is of vital importance to identify the marginal depth to make floating wind turbines competitive.

A semi-submersible platform achieves stability by water plane stiffness and ballast in the columns or pontoons to some extent. The characteristic of small draft of semi-submersible allows it to be deployed in shallow waters. There has been several successful semi-submersible floating wind turbine projects all over the world, such as WindFloat [1], OO Star Wind Floater [2], 5-MW-CSC semi-submersible floater [3], Fukushima FORWARD demonstration project [4].

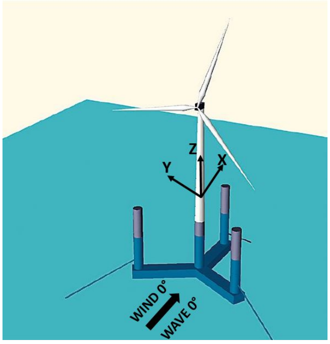

Hull steel mass	1686	t
COG	(0, 0, -24.53)	m
COB	(0, 0, -22.42)	m
Draft	30	m
Pontoon length	41	m
Pontoon height	6.0	m
Column length	24	m
Column diameter	6.5	m
Floater draft	30	m

Figure 1. Overall layout[3] and main properties[5] of 5MW-CSC floater

The 5-MW-CSC semi-submersible floating wind turbine studied in this paper includes a wind turbine, a tower, a semi submersible hull and three catenary mooring lines, as shown in Figure 1. The origin of the coordinate system is placed at the still water level with wave and wind direction as shown. The braceless semi hull consists of three pontoons, three side columns and one central column supporting the tower and the wind turbine [6]. The wind turbine in the study is the NREL 5 MW reference wind turbine [7] mounted on the OC3 Hywind wind tower [8] which starts from 10 meters above the waterline.

The purpose of this paper is to study the effect of different environmental loads on floating wind turbine motion and mooring system. Three water depths were considered in order to address the challenge to design mooring system at small water depth and to check the variation of responses while same environmental conditions are used. Based on preliminary design, three mooring systems were proposed to carry out the analysis. No detailed design and design optimization were performed since they served the purpose quite well.

2. Theory

2.1. Wave loads

Wave loads acting on the floating structure can be estimated based on potential flow theory or Morison formula using wave kinematics. The Morison formulation is mainly applied for slender structures with small dimensions compared to the wave length. As for large volume structures, diffraction and radiation forces are important. Therefore, in this paper, the potential flow theory is used to calculate the hydrodynamic loads acting on the floater while Morison formulation is applied to calculate wave forces on the mooring line.

Potential flow theory considers the solutions of a linearized boundary value problem for inviscid, incompressible flow. For the first order linear wave solutions, the loads and motions have zero mean value and oscillate with the frequency of the incident waves. When it comes to loads and motions of a semi-submersible platform, the slow drift motions caused by slowly-varying (slow drift) loads connected with second order difference frequency effect and mean drift effect become important [9]. The contribution from second order potential is the most difficult part to compute which is required to satisfy the second order free surface boundary condition and an additional free surface mesh is needed to solve the problem numerically. The resulting force can be written as:

$$F_j^{(2)} = \Re \sum_m \sum_n \xi_m \xi_n T_{mn}^j(\omega_m, \omega_n) e^{-i(\omega_m - \omega_n)t + (\epsilon_m - \epsilon_n)} \tag{1}$$

The function $T_{mn}^j(\omega_m, \omega_n)$ represents the complex difference frequency second order transfer function, known as the quadratic transfer function (QTF).

Since a catenary mooring system is considered, only difference frequency wave loads are used in the analysis regarding induced resonant motions in surge, pitch and heave. Due to the difficulty in calculating QTFs, some approximations have been proposed, mainly to avoid computing the second order velocity potential $\phi^{(2)}$. One of the most widely used methods is Newman's approximation, which could be used to derive the QTF matrix based on the mean drift forces which is depended only on the first order solutions.

Newman's approximation becomes inaccurate when the frequency considered is close to resonance condition with small damping and the accuracy also decreases for motions with low natural period, e.g. for heave, pitch and roll motion. Therefore in this paper:

- Newman's approximation will be only considered in horizontal motion, i.e. surge, sway and yaw motion to account for second order difference-frequency wave loads.
- Full QTF method will include the contributions from all six degree of freedoms.

2.2. Wind loads

A structure under the influence of wind will experience static and dynamic wind forces. The wind loads acting on the nacelle and tower are primarily drag forces. However, the loads acting on the blades include both lift and drag forces, which can be calculated with blade element momentum (*BEM*) and generalized dynamic wake (*GDW*) [10]. In this paper, *BEM* theory is used when the mean wind speed is below 8 *m/s*, otherwise, *GDW* theory is chosen. The wind field is generated by *TurbSim* [11] based on the Kaimal spectral model. The turbulence intensity is defined in *IEC 61400* standard [12]. *Class C* is selected in current study for offshore condition. Meanwhile, *Extreme Wind Model* is used for extreme condition related to parked model.

2.3. Current loads

The slow-drift motion of moored floating structure is greatly influenced by second order difference-frequency wave loads, wind loads and current loads. The wave drift forces will increase when current load is involved [13]. Viscous drift forces due to wave-current interaction effects is important to consider especially in extreme sea states [14]. Therefore, according to [15], the effect of current loads on mooring lines should be taken into account when relevant. Current velocity vector varies with water depth, while the profile is stretched or compressed due to surface waves. Generally, the current velocity can be considered as a steady flow field where the velocity vector is only a function of the water depth [16]. The current profile considered in this paper is wind-generated current expressed as a linear profile from still water level to a certain depth below which the current is assumed to vanish.

3. Preliminary design of mooring system

The purpose of this paper is to compare the effect of different hydrodynamic modelling on the response of mooring system and floater motion, therefore reasonable mooring systems are needed at different water depths. According to [15], the mooring system must fulfil three safety criteria: ULS, FLS and ALS. Due to the configuration, it can be quite challenging to ensure system integrity in ALS condition when losing one or more mooring lines. In this paper, ULS condition was the main criteria considered to propose mooring system design concepts. The main criteria in the preliminary design for mooring system to follow, includes:

(i) Stiffness criterion: The horizontal stiffness of the mooring system should be sufficient to keep the platform within a specific range and compliance to reduce the tension in first order waves. Moreover, there should not be vertical force acting on the anchor in order to prevent lifting up the anchor.

(ii) Resistance criterion: The mooring lines should be strong enough to ensure normal operation, in other words, the maximum line tension should not exceed the capacity of the mooring line.

(iii) Design loads are carried out based on partial safety factors for the tension (load effect) due to mean and dynamic tension depending on the consequences of failure.

(iv) In the design phase, power cable design is carried out when the mooring system configuration and the maximum offset are determined. Power cable is then designed to accommodate the possible maximum offset. This design philosophy determines that the floater motion should be limited to a reasonable range especially in horizontal plane in order to protect the power cable from taking large loads and bending moments.

Essentially, the challenge in mooring line design is to balance stiffness and strength. In this connection, the fact that the tension increases in a nonlinear fashion which will cause large tension due to geometrical effect for catenary mooring lines is an important issue to consider.

3.1. Reference mooring system - 200 m water depth

The initial 5-MW-CSC floating wind turbine is designed for 200 m water depth, which has been utilized as a reference model in order to carry out the study for 100 m and 50 m. The mooring system consists of three catenary mooring lines which are made of spiral rope and positioned with 120 degrees angle between the mooring lines. Each mooring line is attached at the outer columns of the semi at a water depth of 18 meter, where the fairlead is located. The configuration of upper part is close to a straight line because of the clump weight, while the lower part has a catenary shape. The anchor used here is a conventional fluke anchor which is mounted into the seabed.

Table 1. Mooring line properties for 200 m, 100 m and 50 m

Water Depth (m)	200	100	50
Mooring line type	Spiral rope	Spiral rope	Chain R4-RQ4
Nominal diameter (m)	0.1365	0.1365	0.18
Nominal cross-section area (m^2)	0.01465	0.01465	0.0509
Gyration radius (m)	0.03415	0.03415	0.0636
Mass/length in air (kg/m)	115.02	115.02	648
Axial stiffness per unit length (KN/mm)	3.08E6	3.08E6	2.92E9
Transversal drag coefficient	1.2	1.2	2.4
Longitudinal drag coefficient	0.02	0.02	1.15
Transversal added-mass coefficient	0	0	1
Longitudinal added-mass coefficient	1	1	2
Catalogue breaking load (KN)	16769	16769	26278

3.2. Mooring system for 100 m and 50 m water depths

Based on a satisfactory mooring system design for 200 m water depth, the evaluation criteria of preliminary design for 100 m and 50 m is to achieve the similar stiffness, catenary shape and pretension as in 200 m. Since the same floating wind turbine is utilized for 100 m and 50 m, the general mooring line configurations are kept the same as in the reference model. A longer part lying on the seabed for shallower water depth is under expectation in order to prevent mooring line from being totally lifted up and prevent vertical force acting on the anchor. For catenary mooring system, the suspended length of mooring line decreases with water depth, which will further influence the pretension which is mainly determined by self-weight of suspended mooring line and clump weight. In order to compensate for this feature, heavier mooring line material - studless chain $R4-RQ4$ is selected for 50 m and wire rope is selected for 100 m. Generally, the weight of chain is about five times of the wire rope, which could be beneficial to achieve the desired pretension in 50 m water depth. It is recommended to use spiral strand when the required service life of mooring system is more than 20 years [15]. In addition, corresponding clump weights in 100 m and 50 m have been enlarged as well. Furthermore, in order to improve the fatigue performance, a HDPE plastic sheathing is used for spiral rope and no stud is utilized to connect chain links.

Table 2. Mooring system configuration for 200 m, 100 m and 50 m

Water Depth (m)		200	100	50
Mooring line number		3	3	3
Angle between adjacent lines (deg)		120	120	120
Depth from fairlead to seabed (m)		182	82	32
Radius from fairlead to platform center (m)		44.25	44.25	44.25
Radius from anchor to platform center (m)		1184.5	917	720
Initial Configuration	Offset at fairlead (m)	0	0	0
	Angle at fairlead(deg)	59.9	56.5	40.9
	Total length (m)	1173	891.6	686.6
	Suspended length (m)	711.6	336.8	80.6
	Touchdown length (m)	461.4	554.8	606
Extreme Configuration	Offset at fairlead (m)	17	18	20
	Angle at fairlead(deg)	73.4	80.6	84.1
	Total length (m)	1173	891.6	686.6
	Suspended length (m)	1148	881.5	675.6
	Touchdown length (m)	25	10.1	11

In order to check the static performance of the proposed concepts for 100 m and 50 m water depths, a comparative study is carried out with respect to the performance of 200 m design. According to the result shows in Figure 2, the tension increases in a nonlinear behaviour which is applicable for all three water depth while it becomes more significant when water depth decreases. The behaviour occurs at smaller offset for 50 m water depth.

4. Hydrodynamic load modelling and analysis

HydroD (Wadam) based on potential wave theory is used to carry out hydrodynamic analysis of the semi-submersible platform. Additionally, second order free surface boundary condition has to be fulfilled in order to calculate full QTF, which requires an additional free surface mesh to solve the problem numerically. The hydrodynamic model is provided in Figure 3.

4.1. Free decay test

Free decay tests are carried out to estimate the natural periods of floater motions and damping. The decay tests for 5-MW-CSC floater are performed at the undisturbed position in six degrees of freedom and three water depths. The damping is very important when the load acting excites

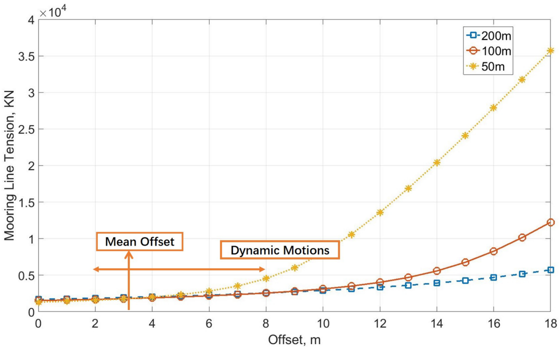

Figure 2. Mooring line tension with offsets for water depth of 200 m, 100 m and 50 m.

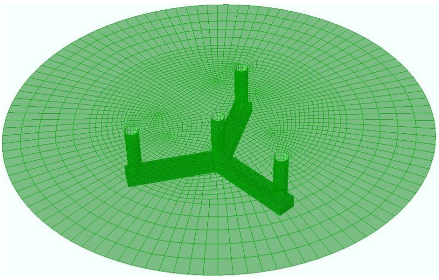

Figure 3. Hydrodynamic model in HydroD.

the resonant motion of the structure. The magnitude of the damping determines the amplitude of the resonance. The damping included in this paper includes: potential wave excitation damping, viscous damping effect acting on the floater and viscous damping on the mooring line by means of the drag force in Morison's formula.

4.2. Load cases

Based on the data from [17], Norway site 5 has been selected as a representative site for a floating wind turbine. The environmental condition corresponding to 50-year wind, wave and 10-year current conditions are listed. Two typical extreme environmental conditions corresponding to 50 years condition are provided for Norway site 5 suggested by [17] with one refers to the condition with maximum mean wind speed and one condition with maximum significant wave height as shown in Table 3.

Table 3. Extreme load cases for 50-year wind, wave[17] and 10-year current[15]

Condition	U_w	H_s	T_p	U_c	Turbine status
	[m/s]	[m]	[s]	[m/s]	
ULS-1	41.86	13.4	13.1	1.05	Parked
ULS-2	38.87	15.6	14.5	1.05	Parked

As for the current profile, a surface current speed (U_c) with a 10-year return period is recommended to use according to[15]. Currently there is no available statistical data of current speed of Norway site 5. However, it can be estimated based on the mean wind speed:

$$U_w = 0.015 \cdot U_c \tag{2}$$

Besides, Norway site 5 is located quite close to location North sea (Troll) whose recommended current speed with 10-year return period is *1.5 m/s* according to [15]. Therefore, the final current speed used in this paper is taken as the average of the estimated value and the value for location Troll platform. The variation is considered as a linear profile from *z= -50 m* to still water level and it is assumed to vanish at 50 m below the still water level. The same current profile is used for all three water depths.

$$U_c(z) = 1.05 \cdot \left(\frac{50+z}{50}\right) \quad for \quad -50 \leq z \leq 0 \tag{3}$$

In order to check the influence of the effect of different methods to include second order wave force and the effect from wind force, four different load models have been included in this paper:

Table 4. Hydrodynamic Load models

No	Wave		Wind	Current
	First-order	Second-order		
1	Included	Not included	Not included	Included
2	Included	Newman's approximation (3 DOF)	Not included	Included
3	Included	Full QTF (6 DOF)	Not included	Included
4	Included	Full QTF (6 DOF)	Included	Included

The Newman's approximation is good if the frequency difference is small, which is usually the case for horizontal motions for offshore structure especially in deep water. Newman's approximation is uncertain when it comes to shallow water. Comparing results from models 1, 2 and 3, the accuracy of Newman's approximation for second order wave forces can be judged. By comparing results from model 3 and 4, the influence from wind force could be figured out. Meanwhile, drag force on mooring line is included for all the models as the third contribution to second order response. Current is considered for all the models as well. In addition, four wave directions have been selected in order to check the influence of wave-wind misalignment: 0°, 45°,60° and 90°.

4.3. Fully coupled dynamic model

Taking the current study objective - offshore floating wind turbine into account, factors such as turbulent wind field, nonlinear wave loading, nonlinear structural behaviour and servo control make it necessary to carry out fully coupled aero-hydro-servo-elastic analysis to capture the nonlinear responses. In this paper, the fully coupled dynamic simulation is run for 4000 s with time step of 0.01 s which corresponds to a one-hour dynamic analysis while the first 400 s is eliminated because of start-up transient effects. For each load case and each wave direction, 5 identical and independent one-hour simulations with different seed numbers for the turbulent winds and irregular waves were carried out to reduce the statistical uncertainty. The final statistics e.g. maximum, mean and standard deviation were calculated by averaging the results from the five samples.

5. Results and discussions

5.1. Spectral analysis

The floater motion response spectrum with 0 deg incoming wave direction in ULS-1 condition is discussed as an example. Three water depths and four load models are listed together for comparison. Generally speaking, the second-order forces are small compared to the first-order forces. However, when the difference-frequency forces coincide with the eigenfrequencies of the structure, some resonant motions will occur. The wind force is included in the fourth model, however the effect from mean wind force is not significant because the turbine is in a parked condition. There is great similarity regarding the spectrum in ULS-1 condition and ULS-2 condition, therefore only results from ULS-1 condition is listed.

Floater motion

- For **surge** motion, the wave frequency response is dominated by the frequency range of 0.3 to 0.7 rad/s and they are larger in the 50 m case due to the intermediate wave depth effect as compared to the 100 m and 200 m cases. Similarly, the surge resonant motion is also larger. In addition, there is a low frequency response around 0.1 rad/s, which is due

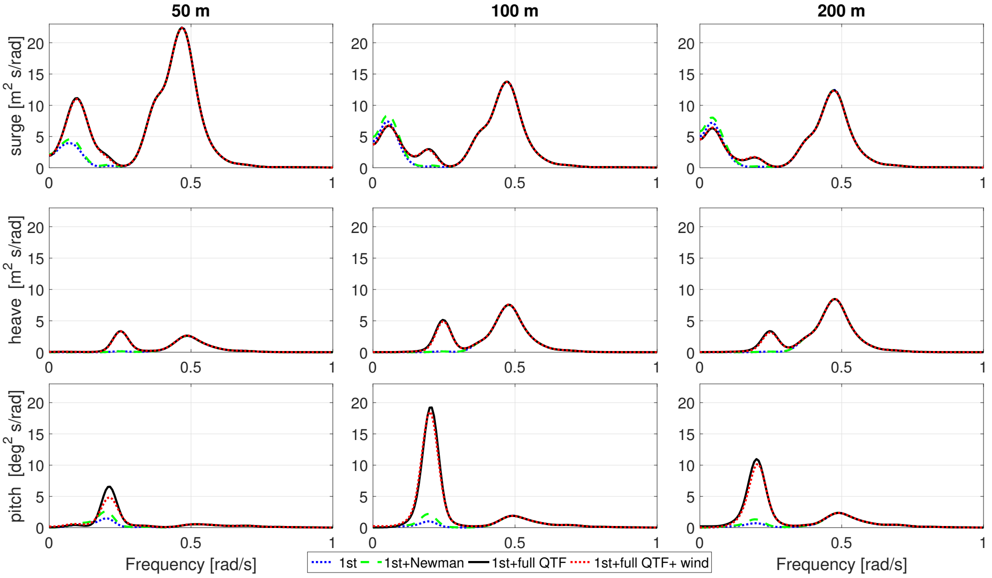

Figure 4. Floater motion spectrum in ULS-1 condition

to surge resonance. Moreover, the coupling between surge and pitch also contribute to the total motion response. A small peak is observed at about 0.2 rad/s which coincides with pitch resonant frequency. The coupling effect is not significant for the 50 m case.

- For **heave** motion, wave frequency response is still dominating in the same range. The heave resonant motion occurs at 0.25 rad/s for all three water depths. Second-order difference frequency response in heave motion is more significant than surge motion. However, the amplitude is still smaller than the wave frequency response.
- For **pitch** motion, the pitch resonant contribution is in leading position at 0.2 rad/s larger than wave frequency contribution, which makes it different from other responses. This is because pitch motion is quite sensitive to difference-frequency force and wind-induced force.

When comparing Newman's approximation and a full QTF with respect to represent second-order difference-frequency response, full QTF is supposed to provide the most accurate result for all six degrees of freedom while Newman's approximation is not good for surge resonant motion in small water depth. Besides, Newman's approximation does not apply to the resonant vertical motion, e.g. heave and pitch motion. Therefore, Newman's approximation of the low-frequency motion is clearly seen in Figure 4 to underestimate especially heave and pitch motion. A full QTF method is recommended to model difference-frequency force in order to better capture the low-frequency motion.

However, the wave-frequency range response does not seem to be influenced as expected. Therefore, the curves representing four different models coincide with each other at wave frequency in the spectrum. Since the wind turbine is in a parked condition during the ultimate limit state test, the influence from wind force is not prominent. Under such condition, the mean pitch motion is quite small. During operational condition where rotor rotates, large pitch motion due to thrust force can be expected and so is the response due to wind force.

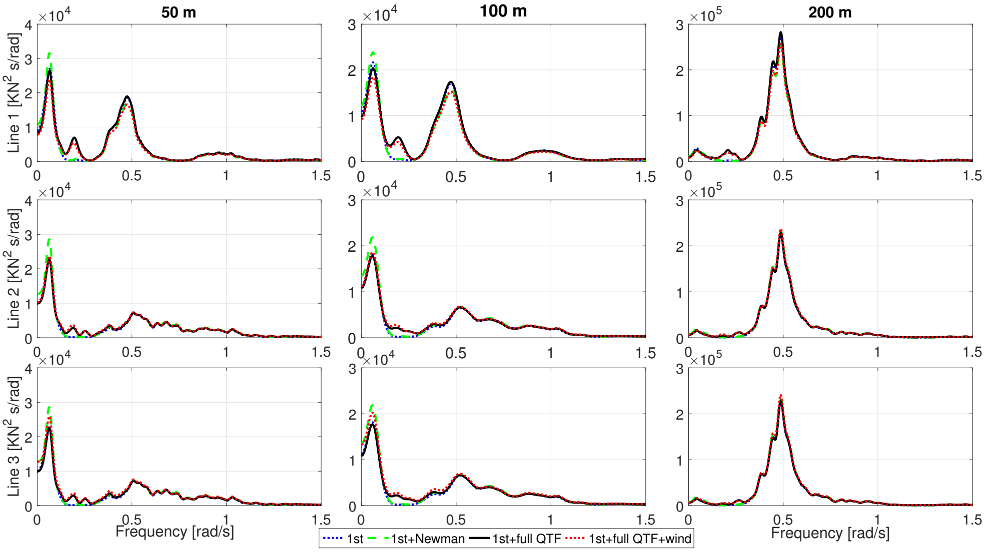

Figure 5. Mooring line tension spectrum for the ULS-1 condition

Mooring line tension

The spectrum for three mooring lines tension in head sea for the ULS-1 condition are shown in figure 5. The scales of the figure are chosen differently for different water depth for better indication due to the big difference of the magnitudes. The most significant contribution to the mooring line tension comes from wave frequency ranging from 0.3 to 0.7 rad/s, which applies to all three water depths. The difference among the four different load models are not significant in 200 m, which indicates that wave-frequency response is dominating while low-frequency response does not contribute much to the total response. However, the contribution from low-frequency response increases with decreasing water depth. The peaks between 0 to 0.3 rad/s in 100 m and 50 m stands for the contribution from difference frequency wave loads and aerodynamic loads including contribution from surge resonance around 0.1 rad/s and pitch resonance around 0.2 rad/s. Second-order surge resonant motions increase when the water depth decreases and so does the dynamic mooring line tension. Take the spectrum in 50 m as an example, the contribution from difference-frequency response does contribute a lot to the total response and it becomes more and more significant with decreasing water depth. Newman's approximation method underestimate the difference-frequency response compared with full QTF method.

5.2. Platform motion

In order to focus on the most critical motion response, only surge, heave and pitch motion were selected. The misaligned wave-wind condition was studied for all four cases, however only the result from 0° and 60° are listed because of the similarity. The effect of second order difference frequency force and wave-wind misalignment were the main focusing points as well as the water depths. Figure 6 and 7 shows the platform motion responses in three water depths with two wave incoming directions. The circle marker indicates the mean response with error bar standing for the standard deviation. The diamond marker represents the maximum response. Results for four different models at same water depth and load case are assembled together for better comparison. The total motion response is composed of a mean static response due to

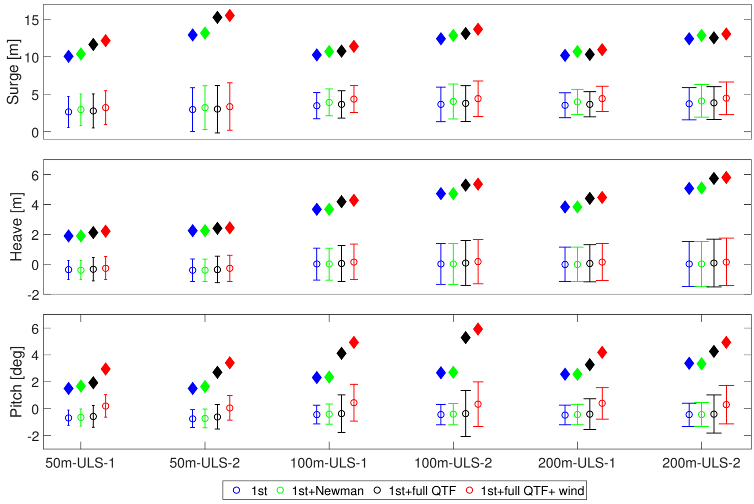

Figure 6. Motion response for three water depths with 0° wave and wind incoming direction

mean wave and wind force together with a dynamic response due to wave frequency and low frequency response. Generally speaking, the motion responses are larger in ULS-2 condition where the wave condition is more severe, which demonstrates that floater motion response is more sensitive to wave load rather than wind load. When comparing the three water depths, the amplitude is relatively larger in 50 m than 100 m and 200 m.

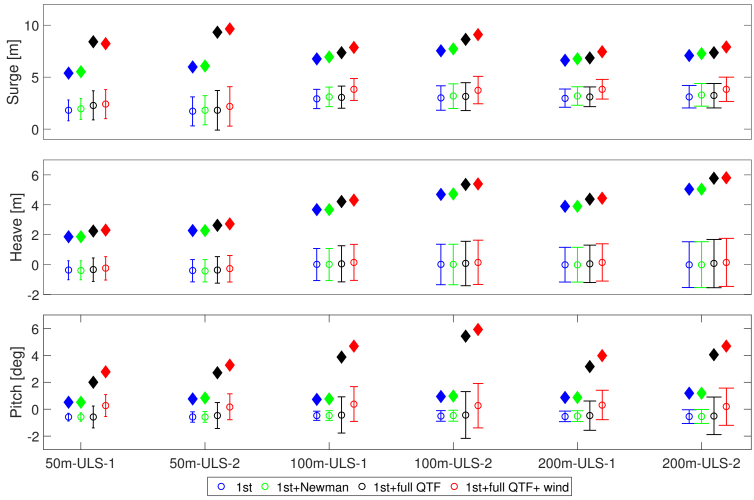

Figure 7. Motion response for three water depths with 60° wave direction and 0° wind direction

The mean values of the platform motions are mainly wind induced and the rotor is feathered in the ultimate limit case, therefore, the mean motion is not extremely large for all the cases.

However, when comparing the third and forth model, the influence from wind force did show up with slightly larger response when including wind force. The motion response is smaller when wave comes from 60° as shown in figure 7, because the load direction does not coincide with the motion direction. However, large mooring line tension is discovered because the wave load acts directly in-line with mooring system configuration. In general, the platform motion responses are larger when considering second order difference-frequency force using full QTF method. In other word, only including first order wave force or including difference-frequency force using Newman's approximation will underestimate the motion response.

5.3. Mooring line tension

Figure 8 and 9 shows the mean, maximum and standard deviation of tension in all three mooring lines in two extreme load cases. For most cases, the dynamic tension takes smaller part of the total force compared with mean tension part, which means that the mean static force due to wave and wind is dominating and the dynamic behaviour in wave frequency and low frequency are not strong. Therefore, the difference in the mean with four different load models is relatively small, which because pretension of the mooring line is dominating.

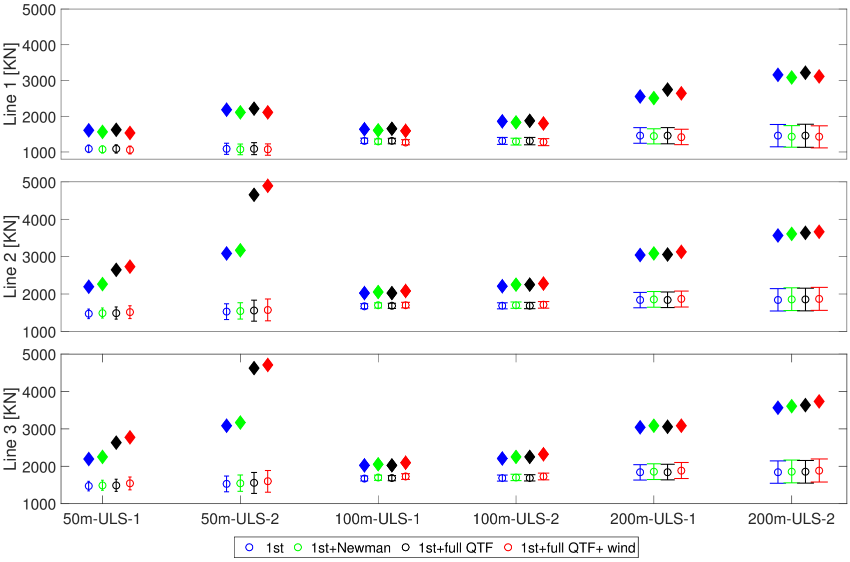

Figure 8. Mooring line tension for three water depths with wave incoming direction of 0°

However the second order difference-frequency wave force could lead to large response at resonance where damping will be important. Therefore, second order wave force did increase the maximum values and standard deviations. The maximum tension in 50 m case is much larger than the other two water depths which is due to the nonlinear tension increment when large offset was excited.

In ULS-2 condition where the significant wave height is larger, mooring line tension responses are relatively larger than those in ULS-1 condition for all the cases. Notably, the mooring line tension in 50 m increases significantly in ULS-2 condition. This is because the environmental condition, and especially the wave condition, has become severe enough to cause mooring line tension increase nonlinearly. Once the tension starts to increase nonlinearly, it will as expected be more notable in shallow water. The mooring system in 100 m shows great performance without extreme tension increment, which indicates that the nonlinear behaviour is not significant in 100 m water depth. By comparing the mooring line tension response with different wave incoming direction, it is seen that the maximum mooring line tension occurs in the case when the wave loads are acting directly towards the mooring line, i.e. for mooring line 3 with 60° wave incoming direction for both conditions.

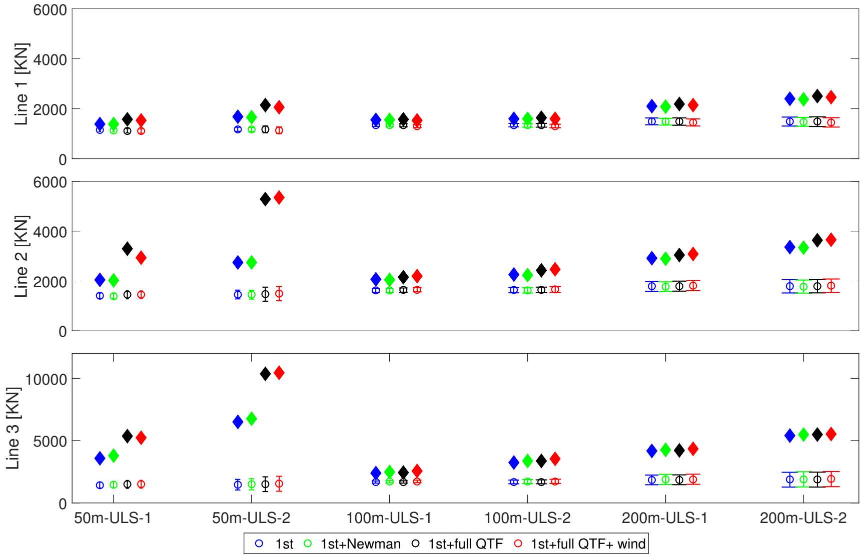

Figure 9. Mooring line tension for three water depths with wave incoming direction of 60°

It is notable that there is significant difference of maximum tension in different water depths even though the mean value and standard deviation seem quite close. When the mooring line tension follows a Gaussian process, the kurtosis of the response should be around 3 [18]. Moreover, the extreme tension can be expressed as:

$$M = \mu + k.\sigma \tag{4}$$

where M is the maximum value, μ is the mean value, σ is the standard deviation and k is coefficient with value of 4 for Gaussian process [20].

Table 5. Coefficient k and Kurtosis

	ULS-1-0			ULS-2-60		
	Moor1		Surge	Moor3		Surge
	k	Kurt	Kurt	k	Kurt	Kurt
50 m	4.3	3.4	3.5	14.7	49.0	3.7
100 m	4.4	3.5	3.2	10.8	19	3.2
200 m	5.7	5.4	3.1	6.0	6.1	2.9

The non-Gaussian nature of mooring line tension is greatly influenced by the nonlinearity of the mooring system which increases in shallow water as shown in Figure 2. Wave parameters e.g.

significant wave height and wave peak period in the meanwhile also affect the Gaussian nature of the mooring line tension [21]. Larger kurtosis coefficient is expected in severe sea states. The k values in Equation 4 estimated for mooring line 1 tension in ULS-1 condition with 0° incoming wave direction and mooring line 3 tension in ULS-2 condition with 60° incoming wave direction are shown in Table 5. The kurtosis for surge motion in both cases are listed as well. The load model used here includes current load, wind load and second order wave load based on full QTF method.

For the surge motion, the kurtosis are close to 3 for all cases, which indicates that the motion is close to Gaussian process. As for the mooring line tension, the kurtosis for 50 m and 100 m water depth is close to 3 and k value close to 4 while both kurtosis and k value are slightly larger in 200 m water depth. This indicates that when the environmental condition is not extremely severe, tension for the least loaded mooring line almost follows a Gaussian distribution. Meanwhile, as the most loaded mooring line 3 in more severe sea state ULS-2 condition, there is significant increase in both the kurtosis and k value and they increase faster with decreasing water depth which displays the high non-Gaussian character.

Larger kurtosis indicates that higher extreme values exist in the upper tails of the probability density distribution [19]. In high sea states, non-Gaussian behaviour is expected in principle in floater motions and especially mooring line tension. The property will increase when the current is included [22].

6. Conclusion

During the mooring system design phase, two factors that can influence mooring line tension significantly were mainly considered: geometrical effect and increased stiffness for large offsets. In order to achieve similar performance, heavier mooring line was chosen for the shallow water depth with longer mooring line placing on the seabed.

As for the dynamic analysis, the mean response of the platform motion and mooring line tension which is due to mean wave and wind force are not affected by the difference-frequency effect. As water depth decreases, the contribution from difference frequency becomes increasingly more significant. Therefore in order to capture the low-frequency response accurately, a full QTF method is recommended while Newman's approximation will underestimate the response.

In the extreme condition, the maximum mooring line tension occurs in the case when the wave acting aligned with the mooring line configuration direction while the direction of wind and current are considered fixed. Mooring line tension and floater motions are relatively larger in the condition where wave is more severe, which indicates that they are more sensitive to wave loads than wind loads.

The highly non-Gaussian property of responses in high sea states indicates possible extreme mooring line tension and floater motion, which makes it quite challenging to design mooring system for extreme environmental conditions especially in shallow water.

Acknowledgement

The first author is financially supported by the Chinese Scholarship Council (CSC).

References

[1] Roddier D, Peiffer A, Aubault A and Weinstein J. 2011 *Proc. of the ASME 2011 30th Int. Conf. on Ocean, Offshore and Arctic Engineering* (Rotterdam)
[2] Landbø T 2013 *OO Star Wind Floater A robust and flexible concept for floating wind*
[3] Luan C, Michailides C, Gao Z and Moan T 2014 *Proc. of the ASME 2014 33rd Int. Conf. on Ocean, Offshore and Arctic Engineering* (California)
[4] Ishihara T 2013 *Fukushima Offshore Wind Consortium* (Fukushima FORWARD)
[5] Bachynski E E, Chabaud V and Sauder T 2015 *12th Deep Sea Offshore Wind RD Conference* (Trondheim)

[6] Michailides C, Luan C, Gao Z and Moan T 2014 *Proc. of the ASME 2014 33rd Int. Conf. on Ocean, Offshore and Arctic Engineering* (California)

[7] Jonkman J M, Butterfield S, Musial W and Scott G 2009 *NREL report*

[8] Jonkam J M 2010 *NREL report*

[9] Faltinsen O M 1990 *Sea loads on ships and offshore structures* (Cambridge University Press)

[10] Hansen M O L 2008 *Aerodynamics of wind turbines* (London: Earthscan)

[11] Jonkman J M and Kilcher L 2012 *Turbsim Users' Guide*

[12] IEC 2005 *IEC 61400-1. Wind Turbine - Part 1 : Design requirements.*

[13] Zhao R and Faltinsen O M 1988 *J. Applied Ocean Research* **10** 87-99

[14] Chakrabarti S 1984 *J. Applied Ocean Research* **6** 73-82

[15] DNVGL 2013 *DNV-OS-E301,Position Mooring*

[16] DNVGL 2011 *DNV-RP-C205,Environmental Conditions and Environmental Loads*

[17] Li L, Gao Z and Moan T 2015 *J. of Offshore Mechanics and Arctic Engineering* **137** 031901-1-16

[18] Naess A and Moan T 2013 *Stochastic dynamic of marine structures* (Cambridge University Press)

[19] Gao Z and Moan T 2007 *J. of Applied Ocean Research* **29** 45-54

[20] Gao Z and Moan T 2009 *Proc. of the 10th Int. Conference on Structural Safety and Reliability* 997-1004

[21] Li H , Du J, Wang S, Sun M and Chang A 2016*J. of Ocean Engineering* **124** 204-214

[22] Stansberg C T 2008 *Proc. of the ASME 27th Int. Conf. on Offshore Mechanics and Arctic Engineering* (Estoril)

A.3 Paper 3

Paper 3:
Fully nonlinear wave effect on a semi-submersible floating wind turbine using wave kinematics from 2D Harmonic Polynomial Cell wave tank.
Authors: Kun Xu, Yanlin Shao, Zhen Gao, Torgeir Moan
Published in *Proceedings of the 3rd International Conference on Offshore Renewable-energy (CORE 2018)*, Glasgow, United Kingdom, August 29-30, 2018

FULLY NONLINEAR WAVE EFFECT ON A SEMI-SUBMERSIBLE FLOATING WIND TURBINE USING WAVE KINEMATICS FROM 2D HARMONIC POLINOMIAL CELL WAVE TANK

Kun Xu, *Norwegian University of Science and Technology, Norway*
Yanlin Shao, *Technical University of Denmark, Denmark*
Zhen Gao, *Norwegian University of Science and Technology, Norway*
Torgeir Moan, *Norwegian University of Science and Technology, Norway*

ABSTRACT

When floating wind turbines are placed at intermediate water depths (50m - 200m), the effect of nonlinear waves becomes more significant due to decreased water depth and increased wave steepness. This is the feature that a linear wave theory cannot capture. The effect of nonlinear wave loads on bottom-fixed wind turbines such as monopile and jacket has been studied using numerical wave tanks. However, there has been limited similar research work on floating wind turbines. One of the reasons is that the footprint of floating wind turbines is larger due to its mooring system which makes the database for pre-generated wave kinematics very large that normally exceeds the memory requirement of simulation tool for wind turbine. In accordance to the software memory barrier, a polynomial fitting method of wave kinematics has been developed [23] in order to scale down the data size to meet the memory requirement. The wave kinematics including wave elevation, velocity and acceleration are generated in a 2D numerical wave tank based on the Harmonic Polynomial Cell method. The wave kinematics obtained at pre-defined grid points in the wave field are fit to polynomial function representing location coordinates and corresponding coefficients. HAWC2 is used for coupled dynamic analysis with the obtained wave kinematics through polynomial fitting process as input. The hydrodynamic wave load is calculated using Morison's equation. The external DLL used to provide wave kinematics to HAWC2 is extended from 1D to 2D wave field to be applicable for floating wind turbine. Three wave-only regular wave cases with different wave steepness are selected to study the influence of fully nonlinear wave effect with different wave inputs: linear wave, fully nonlinear wave and stream function. Prediction of wave kinematics, motion and mooring line tension responses and computational efficiency are considered. The rapid development of computer capacity and numerical wave tank makes it practical to consider fully nonlinear wave effect in hydrodynamic analysis in an efficient way.

NOMENCLATURE

FOWT	Floating Offshore Wind Turbine
HPC	Harmonic Polynomial Cell
DLL	Dynamic Link Library
NWT	Numerical Wave Tank
HAWC2	Horizontal Axis Wind turbine simulation Code 2nd generation
FSBC	Free Surface Boundary Condition

1. INTRODUCTION

It has been almost three decades since Floating Offshore Wind Turbine (FOWT) concept was studied by mainstream research community. It is no longer restricted to R&D phase with a high 'technology readiness level'. One of the greatest evidence is that the world's first floating wind farm, Hywind Scotland has started to contribute to Scottish grid from October 2017 [6] and has been outerperforming expectations ever since. Through the instrumentality of onshore wind and bottom-fixed offshore wind, the cost-reduction perspective for FOWT is quite promising, which leads FOWT to be a significant part in the future energy transition.

Despite the rapid development, there are still several challenges during the design phase, one of which is the hydrodynamic load and response modelling. In current design practice, regular waves (e.g. linear Airy wave and Stokes' theory) and irregular waves (superposition of linear waves and second-order waves) are popular to use. It offers satisfactory results for deep water condition where the water depth is larger than half of the wavelength. But most FOWTs are aiming at water depth in the range from 50 m to 200 m where linear wave theory has limitations and fully nonlinear wave theory will reveal its advantage. However, fully nonlinear wave model has not been included as a default input option in state-of-the-art commercial software for integrated analysis of offshore wind turbines because of its complexity. The main procedure to apply fully nonlinear wave so far is to import the wave kinematics (velocity and acceleration) generated from Numerical Wave Tank (NWT) into the simulation tool for wind turbine and apply Morison's equation to calculate the hydrodynamic load. The effect of fully nonlinear wave loads on bottom fixed offshore wind turbine such as monopile with respect to fatigue damage and extreme response has been studied in [7] [8] [9]. However, there has been limited similar research work on floating wind turbines. One of the reason is that the footprint of floating wine turbines is much larger due to its mooring system which requires larger database for pre-generated nonlinear wave kinematics and it easily exceeds the memory requirement of the software, while only the wave kinematics at the centreline of the structure is required for monopile which is way smaller regarding the size of data needed since the movement of the monopile is very small.

In order to solve the memory limit problem and further study the fully nonlinear wave effect on floating wind turbine, a polynomial fitting method that could decrease the size of wave kinematics data has been developed and verified in [23]. The main objective of this paper is to utilize this method to study the influence of fully nonlinear wave with three regular wave sea states accompanied with different wave steepness. The NWT used in this paper to generate wave kinematics is based on 2D Harmonic Polynomial Cell (HPC) method [1], which is an efficient numerical potential-flow field solver. The selected simulation tool for floating wind turbine is HAWC2 [10]. The original Dynamic Link Library (DLL) to provide external wave kinematics was extended to handle 2D wave field. The wave kinematics are fit into polynomial coefficients with location coordinates as input variable. Three wave-only regular wave case study on a semi-submersible floating wind turbine is presented. Comparison is made between linear wave and stream function from HAWC2 and fully nonlinear wave from 2D HPC wave tank.

2. WAVE THEORY

Wave theories can be divided into linear and nonlinear group according to the simplification level of boundary conditions. A linear wave has a sinusoidal surface profile with small amplitude and steepness, while a nonlinear wave has sharper crests and flatter troughs as shown in Figure 1. The nonlinear waves can be categorized into Stokes, cnoidal, solitary and stream function according to the wave properties and the mathematical methods to solutions.

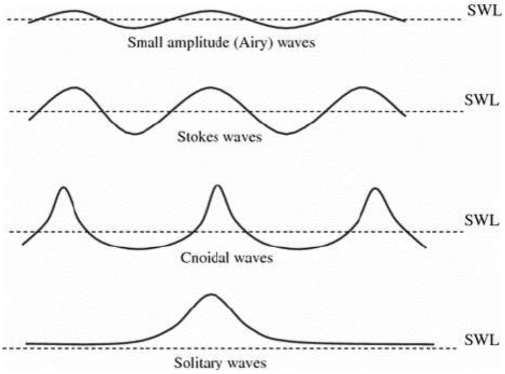

Figure 1 Wave profiles based on different wave theory [24]

2.1 LINEAR AND FULLY NONLINEAR WAVE

Linear wave theory also known as Airy wave theory is the most widely used among all. It generally provides good estimation of the wave kinematics for small wave at deep water (water depth is larger than half of the wavelength). It is based on the assumption that the contribution from the nonlinear terms in the free surface boundary conditions (FSBC) is negligible. The fluid applied in the computational domain is assumed to be homogeneous, incompressible, inviscid and irrotational and the fluid particle velocity can be expressed by the gradient of velocity potential φ which satisfies the Laplace (continuity) equation as a governing equation in the fluid domain:

$$\nabla^2\varphi = 0 \tag{1}$$

The associated boundary conditions can be described as:

- Dynamic FSBC:

  $$\frac{\partial\varphi}{\partial t} = -g\eta - \frac{1}{2}\nabla\varphi.\nabla\varphi \quad on \quad z = \eta \tag{2}$$

  Where the atmospheric pressure is assumed to be zero on the free surface.
- Kinematic FSBC:

  $$\frac{\partial\eta}{\partial t} = \frac{\partial\varphi}{\partial z} - \nabla\varphi.\nabla\eta \quad on \quad z = \eta \tag{3}$$

- Impermeability condition, such as sea bottom and fixed body surfaces:

$$\frac{\partial \varphi}{\partial n} = 0 \qquad (4)$$

When the wave height H is small enough compared with wavelength, the wave can be assumed to be linear and the dynamic and kinematic FSBCs can also be linearized. Considering wave elevation, η which is proportional to wave height H, is also small, the boundary conditions can be further simplified at $z=0$ instead of $z=\eta$ using Taylor's expansion.

$$\frac{\partial \varphi}{\partial t} = -g\eta \quad on \quad z = 0 \qquad (5)$$

$$\frac{\partial \eta}{\partial t} = \frac{\partial \varphi}{\partial z} \quad on \quad z = 0 \qquad (6)$$

On the other hand, when the wave height becomes large and water depth becomes small, the contribution from the nonlinear terms in the FSBC becomes important. In such case, **fully nonlinear wave** is preferred with fully nonlinear FSBCs as in Equation 2 and 3.

In order to satisfy fully nonlinear FSBCs in time-domain simulations, a 4th order Runge-Kutta time integration scheme and mixed Eulerian-Lagrangian method are used to obtain the velocity potential and free surface elevation at each time step.

Introducing the material derivative:

$$\frac{D}{Dt} = \frac{\partial}{\partial t} + \vec{v}.\nabla \qquad (7)$$

The fully nonlinear FSBC can be rewritten as:

$$\frac{D\varphi}{Dt} = -g\eta - \frac{1}{2}\nabla\varphi\nabla\varphi + \vec{v}.\nabla\varphi \text{ on } z = \eta \qquad (8)$$

$$\frac{D\eta}{Dt} = \frac{\partial \varphi}{\partial z} - \nabla\varphi\nabla\eta + \vec{v}.\nabla\eta \text{ on } z = \eta \qquad (9)$$

Here η indicates the wave elevation. When $\vec{v} = \nabla\varphi$ is used, the free surface particles are tracked in a Lagrangian manner, while $\vec{v} = \left\{0, \frac{D\eta}{Dt}\right\}$ indicates a semi-Lagrangian approach in which the free-surface nodes are allowed to move only in a prescribed manner. In such case, 2D FSBC can be expressed as:

$$\frac{D\varphi}{Dt} = -g\eta - \frac{1}{2}\nabla\varphi\nabla\varphi + \frac{\partial \varphi}{\partial z}\left(\frac{\partial \varphi}{\partial z} - \frac{\partial \varphi}{\partial x}\frac{\partial \eta}{\partial x}\right) z = \eta \qquad (10)$$

$$\frac{D\eta}{Dt} = \frac{\partial \varphi}{\partial z} - \frac{\partial \varphi}{\partial x}\frac{\partial \eta}{\partial x} \quad z = \eta \qquad (11)$$

The highlighted part of Equation 10 and 11 are the differences of FSBCs considered in linear and nonlinear manner. In such way, linear and fully nonlinear wave can be generated based on corresponding conditions.

2.2 NONLINEAR REGULAR WAVE

In current engineering practice, there are several available nonlinear regular wave theories with periodic nonlinear wave profiles such as Stokes wave theory, cnoidal wave theory and stream function theory.

Stokes wave theory is an analytical finite-amplitude theory for deep water area [25]. The wave parameters are expressed in terms of power series truncated at a chosen order, e.g. Stokes second order theory is truncated after the second term in the power series. First order Stokes wave theory expression is exactly the same as linear wave theory. Higher order terms for steeper Stokes waves will lead to unrealistic results.

Cnoidal wave is a long periodic wave developed by Boussinesq [27] and Korteweg and de Vries [26] for shallow and transitional water area with even shaper crests and flatter troughs than the Stokes wave. It provides additional nonlinear corrections with respect to finite depth effects. The solution is expressed in terms of elliptical integrals of the first kind. A particularly simple limiting case of cnoidal waves when L/h goes to infinity is solitary wave which physically appears as one single wave crest on an undisturbed water surface. It is the basis for some of the most advanced and successful computational wave models available nowadays.

Stream function theory presented by Dean [28] [29] is based on a truncated Fouries expansion of the exact nonlinear equation and has been further developed for the highest possible waves. In comparison with experimental results of particle velocity, stream function theory is able to provide good results especially for extreme sea states. The closer to the breaking wave height, the more terms are required in order to give an accurate representation of the wave. The required order N of the stream function wave theory is determined in a way that errors in maximum velocity and acceleration are less than one percent. Stream function is only an auxiliary function without any physical meaning in itself. In addition, it cannot be used for irregular wave simulation.

The choice of wave theory is the basis of an accurate hydrodynamic analysis. A guideline work was done by Ursell [30] and further clarified by Lin and Clark [31]. The range of application of the different wave theories is presented in DNV-RP-

C205 based on wave height, wave period and water depth as shown in Figure2. Horizontal axis is a non-dimensional measurement of depth shallowness and the vertical axis is a measurement of wave steepness.

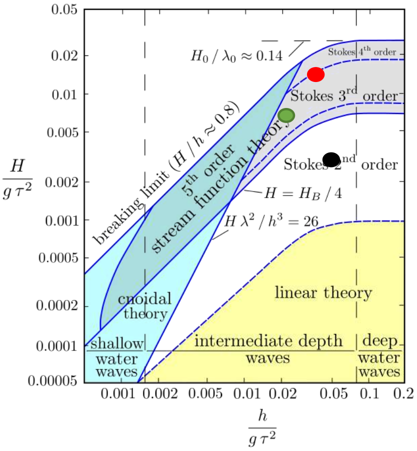

Figure 2 Applicability of various wave theories [33].

In deep water, linear wave theory is able to represent small wave and Stokes wave is applied for high wave. Meanwhile in shallow water, cnoidal wave is suitable for small wave and high wave is preferred to be described by stream function theory. In engineering practice, realistic sea profile is described by superposition of a number of regular wave components. So far, only linear Airy wave can be used and no other nonlinear-wave based irregular wave model exists. In this paper, the wave models selected are linear wave, stream function wave and fully nonlinear wave.

3. NUMERICAL WAVE TANK - HARMONIC POLYNOMIAL CELL (HPC) METHOD

3.1 NUMERICAL WAVE TANK

In the past several decades, the application of NWT in time domain has become more and more popular in solving various marine hydrodynamics problems such as linear wave-body interaction with linearized free surface boundary condition [11]; 3D fully nonlinear wave-body interaction in steady uniform currents [12]; fully nonlinear free surface problem using mixed Eulerian-Lagrangian time marching technique [13].

Recently, NWT has also been applied on offshore wind turbine mainly to study nonlinear wave effect. For example, OceanWave3D [14], a numerical tool developed at DTU which is able to solve 3D Laplace equation for the velocity potential with nonlinear free surface boundary condition has been coupled with an aeroelastic code FLEX5 [15] to study the fatigue damage and extreme response of monopile due to nonlinear wave effect. The same tool was applied on a TLP wind turbine in the INNWIND project [16] and further compared with experimental data [17].

3.2 2D HPC METHOD

The NWT used in this paper is based on 2D harmonic polynomial cell (HPC) method which was initially proposed by [1] as a potential flow solver with approximately 4th order accuracy. The highlight of HPC method is that the fluid domain is divided into quadrilateral cells associated with harmonic polynomials which are used to describe the velocity potential in each cell. It has been compared with four other methods and shown great efficiency and accuracy [1]. The HPC method was developed to 3D case by [2], and implemented in fully-nonlinear wave body interaction problems such as sloshing in 3D tanks, shallow water wave tank, influence from seabed topography and nonlinear wave diffraction by a bottom-mounted vertical circular cylinder. Promising results again proved the applicability of HPC method when dealing with potential flow problems. Later on, the current effects was studied together with nonlinear wave diffraction by multiple bottom mounted cylinder in [3]. Improvement of HPC method was made by [4] in order to account for singular flows and discontinuous problems. Domain decomposition method combing with local potential flow solution was proposed to handle the singularity at sharp corners. A double-layer node technique was developed to model the velocity potential jump in a thin free shear layer in lifting problem.

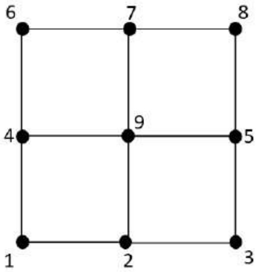

Figure 3 Grid node indexes in a cell

According to 2D HPC method, the fluid domain is discretized into quadrilateral cells within which there are four quadrilateral elements and nine grid nodes as shown in Figure 3. The stencil centre is located in the middle node with index 9 while other nodes are boundary nodes numbering from 1 to 8.

The velocity potential ϕ within the cell is expressed by harmonic polynomials which automatically satisfy Laplace equation. Therefore, the velocity potential at any point in the cell can be interpolated by a linear combination of the eight harmonic polynomials at the surrounding boundary nodes.

$$\phi(x,y) = \sum_{j=1}^{8} b_j f_j(x,y) \qquad (12)$$

Where $f_1(x,y) = 1$, $f_2(x,y) = x$, $f_3(x,y) = y$, $f_4(x,y) = x^2 - y^2$, $f_5(x,y) = xy$, $f_6(x,y) = x^3 - 3xy^2$, $f_7(x,y) = 3x^2y - y^3$, $f_8(x,y) = x^4 - 6x^2y^2 + y^4$

Including higher order polynomials could reduce the wave dispersion errors in the time domain analysis and increase the accuracy of the free surface boundary conditions.

The way to calculate the unknown coefficients b_j term is equivalent to a sub-Dirichlet boundary value problem with Laplace equation as the governing equation. Combining $x=x_j$, $y=y_j$, $\phi=\phi_j$ with Equation 12, a linear equation with a precise form is achieved:

$$b_i = \sum_{j=1}^{8} c_{i,j}\, \phi_j \quad (i = 1 \ldots, 8) \qquad (13)$$

here $c_{i,j}(i,j=1,\ldots,8)$ is the elements of the inverse of matrix $[D]$ which consists of elements $d_{i,j}=f_j(x_i,y_i)$. Therefore, the velocity potential at any grid point in the fluid domain could be described based on the eight surrounding boundary nodes in the same stencil cell. Considering the stencil centre where $x=x_9=0$ and $y=y_9=0$, the resulting harmonic polynomials is expressed as $f_1(0,0)=1$ and $f_j(0,0)=0$, $j=2,\ldots,8$. Accordingly, the velocity potential at the cell centre is described as:

$$\phi_9 = \phi(x = x_9 = 0, y = y_9 = 0) = \sum_{i=1}^{8} c_{1,i}\phi_i \quad (14)$$

The Dirichlet boundary condition is related to velocity potential at the boundary nodes, while the Neumann boundary condition is enforced by taking the normal derivative:

$$\frac{\partial\phi}{\partial n}(x,y) = \sum_{i=1}^{8}\left[\sum_{j=1}^{8} c_{j.i}\nabla f_j(x,y).n(x,y)\right]\phi_i \quad (15)$$

Where n is the normal vector, positive and points to the outside of the fluid domain.

3.3 POLYNOMIAL FITTING OF WAVE KINEMATICS

The velocity potential, wave elevation, velocity are directly calculated from 2D HPC wave tank, while acceleration is available by post-processing velocity and grid deformation. All the grids are fixed in the tank in linear wave making problem, while the grids deform vertically in nonlinear case which leads to the difference when calculating the acceleration. Bernoulli's equation is only valid in an inertial system. Therefore, material derivative is introduced to calculate the acceleration [18]:

$$\frac{\partial U}{\partial t} = \frac{\delta U}{\delta t} - w_{grid}.\nabla U \qquad (16)$$

Since the grid deformation only appears in vertical direction, Equation 5 can be further written as:

$$\frac{\partial U}{\partial t} = \frac{\delta U}{\delta t} - \frac{\partial z}{\partial t}.\frac{\partial U}{\partial z} \qquad (17)$$

Where U is the velocity, $\frac{\partial z}{\partial t}$ is the relative velocity representing the grid deformation.

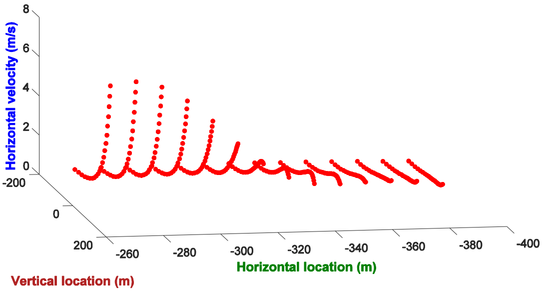

Figure 4 Horizontal velocity at 200s

The wave kinematics information obtained from the tank at each time step is expressed at discrete grid points across the whole wave filed whose dimension can be decided accordingly as shown in Figure 4. However, the size of resulting wave kinematics files including wave elevation, velocity and acceleration in both horizontal and vertical directions is around 8G for 1 hour irregular wave realization with 148 grids horizontally and 22 grids vertically, which easily exceeds the memory requirement of the simulation tool for wind turbine, HAWC2 in this paper. Besides, huge occupation of virtual memory will slow down the computation especially for floating wind turbine whose element number is normally very large. Therefore, there is an urgent need to scale down the size of input wave data.

Table 1 Polynomial function

order	polynomial
0	1
1	$x \quad z$
2	$x^2 \quad xz \quad z^2$
3	$x^3 \quad x^2z \quad xz^2 \quad z^3$
$\vdots$	$\vdots$
n	$x^n \quad x^{n-1}z \quad x^{n-2}z^2 \quad \ldots \quad x^2z^{n-2} \quad xz^{n-1} \quad z^n$

In accordance to the challenge, a polynomial fitting method has been proposed and verified in [23]. Brief introduction of the method is presented here while the verification can be referred to [23]. First of all, the vertical and horizontal dimensions of the wave field are determined by water depth and footprint of the mooring system respectively. Normally, it is sufficient to use 50 grids horizontally per wavelength and 30 grids along water depth. Then the whole wave filed is divided into a number of horizontal divisions based on the wavelength. The kinematics varies at both horizontal and vertical directions. Therefore within each division, a 2 dimensional polynomial function representing horizontal and vertical coordinates up to a certain order *n* is introduced as shown in Table 1. The corresponding coefficients using least-squares method are calculated and arranged in a descending power regarding *x* coordinate. The kinematics data at each time step can be further expressed in a function form with location coordinates as input variables:

$$U = c_1x^n + c_2x^{n-1}z + \cdots + c_{\frac{(n+1)(n+2)}{2}-2}xz^{n-1} + c_{\frac{(n+1)(n+2)}{2}-1}z^n + c_{\frac{(n+1)(n+2)}{2}} \qquad (18)$$

Here *x* represents horizontal coordinate and *z* represents vertical coordinate.

In nonlinear wave problem, the vertical coordinates of the grid points can be directly applied as input for *z*, since the grids deform vertically following instantaneous wave elevation up to the free surface. Meanwhile, in linear wave problem, the grid is fixed and the kinematics is calculated below mean water level. Therefore, Wheeler stretching method is applied to obtain the kinematics up to the free surface by scaling vertical coordinate:

$$z' = (z - \eta)\frac{d}{d+\eta} \qquad (19)$$

Where *z* is original grid coordinate, *z'* is scaled coordinate, η is the instantaneous free surface elevation and *d* is water depth.

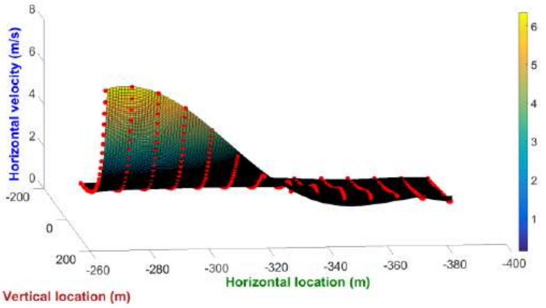

Figure 5 Fitting surface and original data

As a result, the kinematics at any locations at each time step in the field is available from Equation 18 besides original grid points as shown in Figure 5. The variance is large close to free surface and it slowly decays to zero close to seabed as expected. The same procedure is applied to acceleration and velocity in both horizontal and vertical directions.

In the end, the original wave kinematics expressed at discrete grid points are replaced by coefficients c_i and corresponding polynomial variables x_i, z_i representing horizontal and vertical coordinates. The size of data is decreased from 8G to 1G for a 1 hour irregular wave problem using 148 grids horizontally and 22 grids vertically, which satisfies the virtual memory requirement of HAWC2 and can be imported through reading pre-generated wave kinematics manner.

4. HAWC2

HAWC2 is an aero-elastic nonlinear multibody code designed for wind turbine analysis in time domain developed by DTU Wind Energy [10]. Several floating wind turbine concept have been tested in HAWC2 such as Hywind spar, OC4 Semi and a TLP concept [16].

4.1 MODELLING METHOD

Timoshenko beam elements are used to model wind turbine structure. A multibody formulation makes it possible to divide whole structure into a number of substructures in order to capture structural nonlinear effects.

Original mooring line in HAWC2 is a quasi-static model using pre-calculated results from MIMOSA where the stiffness property is described using fairlead position against restoring forces from mooring line. In each time step, the mooring line tension is iterated according to the floater position. Inertial effects and hydrodynamic drag effects from wave, current are neglected. Later on, the quasi-static model was developed to a dynamic model including a cable element with hydrodynamic drag, buoyancy forces and nonlinear spring stiffness representing the bottom contact [19].

Potential flow theory can be used in HAWC2 for hydrodynamic modelling by coupling with output results from WAMIT [20] for large volume structures. The other option for slender structures whose diameter-to-wavelength ratio is less than 1/5 is Morison's equation, which is a semi-empirical method. The diffraction and radiation effects are considered not significant. The wave force dF on a strip of length dz of a rigid moving circular cylinder can be written as [18]:

$$dF = \rho\frac{\pi D^2}{4}dzC_M a_n + \rho\frac{\pi D^2}{4}dz(C_M - 1)a_c + \frac{\rho}{2}C_D Ddz|u_{rel}|u_{n,rel} \tag{20}$$

where D is the cylinder diameter, a_n is the undisturbed wave induced acceleration components normal to the cylinder axis, a_c is the normal component of cylinder acceleration, $u_{n,rel}$ is the component of the relative velocity normal to the cylinder, C_M and C_D are the mass and drag coefficients which are dependent of several parameters such as Reynolds number, the roughness number and the Keulegan-Carpenter number. The coefficients should be determined empirically and C_M can be also decided according to the result from potential flow theory. The vertical buoyancy force is accounted for by integrating axial dynamic pressure and inserted as concentrated force on base columns.

4.2 WKIN DLL

The wave kinematics applied in HAWC2 are provided externally through a defined DLL interface named wkin.dll. In the current version 2.4, the input wave types include: linear airy waves with Wheeler stretching; irregular Airy waves of JONSWAP or PM spectrum with directional spreading; stream function wave and pre-generated wave kinematics.

When importing pre-generated wave kinematics, the wave field that wkin.dll 2.4 can handle can be considered as a 1D field since the data are imported at discrete grid points at only one horizontal location along the water depth as the red part in Figure 6. The wave kinematics variation only exists in one dimension. The kinematics at any point and wave elevation is linearly interpolated using the neighbouring points. This works sufficiently for bottom fixed wind turbine such as monopile where only the wave kinematics at the centre of the structure is needed.

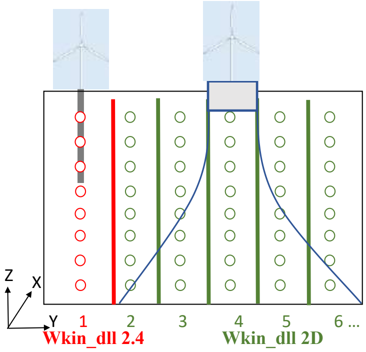

Figure 6 Wave kinematics data structure in wkin.dll

However, it is not applicable for floating wind turbine where the variation along horizontal direction is needed as well. Therefore, the wkin.dll is further extended in [23] to include wave kinematics variation in horizontal direction as well in order to implement on floating wind turbine as the green part in Figure 6. It is named Wkin.dll 2D because it is able to handle wave field in two dimensions now. The wave kinematics in the field is obtained using polynomial functions as described in section 3 and wave elevation is linearly interpolated at different horizontal locations. The wave kinematics including velocity and acceleration are used to calculate hydrodynamic loads on both floater and mooring line using Morison's equation.

5. CASE STUDY

The whole work procedure of polynomial fitting method is demonstrated in Figure 7. The wave kinematics is generated in 2D HPC wave tank where wave elevation, velocity are directly calculated while acceleration is obtained through post-processing using a Python code package based on velocity and grid location. Then a Matlab package based on polynomial fitting method is applied to fit velocity and acceleration to polynomial coefficients. Wkin.dll 2D will receive the location coordinates sent from HAWC2 and delivers the exact wave kinematics value using the polynomial fitting method. Coupled dynamic analysis is carried out in HAWC2 where hydrodynamic load acting on floater and mooring line are calculated based on Morison's equation. The three highlights in this paper are marked with red colour.

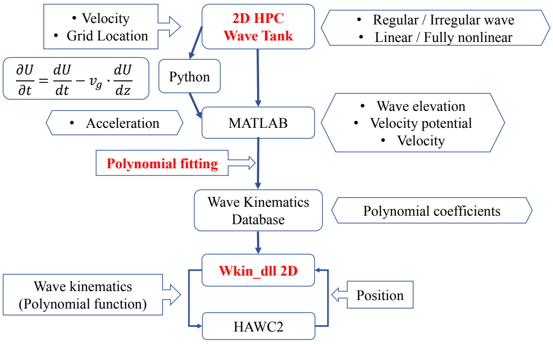

Figure 7 Flowchart

5.1 OC4 SEMI SUBMERSIBLE

OC4 is a 5MW semi-submersible floating wind turbine in 200 m as shown in Figure 8. The semi floater includes a centre column supporting the tower and three offset columns with smaller structures connecting each other [21]. Diffraction effects are important to consider when the diameter to wavelength ratio, D/λ is larger than 0.2 [5]. As for the main structure and pre-defined sea states in [21], the ratio exceeds 0.2 only for some lowest sea states, where hydrodynamic loads are small anyway. In order to compare the influence of hydrodynamic modelling methods using potential flow theory or Morison's equation, a code-to-code verification was carried out involving 23 organizations and 19 simulation tools [22]. The conclusion is that for the relevant load cases, either of the two methods or the combination is able to achieve equally accurate hydrodynamic loads on the structure. A detailed comparison is available in [22]. In this paper, Morison's equation is applied as introduced in Section 4.1.

Figure 8 OC4 Semi-submersible wind turbine [21]

Three catenary mooring lines are arranged symmetrically about the platform vertical axis with 120° angle between them. The radius from the floater centre is 837.6m to anchors and 40.87m to fairleads. Unstretched length of all three lines is 835.5m with 0.0776m diameter and 108.63 kg/m apparent mass in fluid per unit length. The detailed layout is shown in Figure 9. In this paper, the mooring line is modelled including dynamic effect [19] as introduced in Section 3.1.

5.2 RESULTS

In this paper, three wave-only regular wave cases as shown in Table 2 are selected based on the metocean data at Norway 5 site in the North Sea [33]. The most significant difference of the three sea states is the nonlinearity of the wave considering wave steepness (σ) as the ratio of wave height to its wavelength. Meanwhile, the first two sea states represent moderate condition while the last one stands for severe condition. The three conditions are also listed in Figure2 with black dot represents condition H12T15, green dot stands for condition H6T10 and red dot is for condition H6T7.

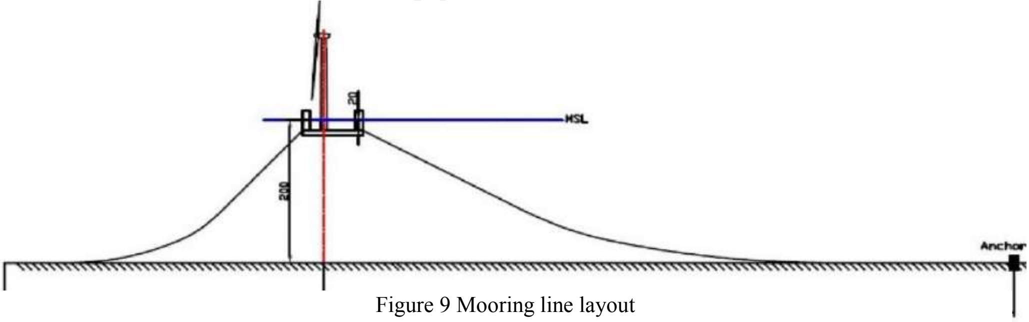

Figure 9 Mooring line layout

The water depth considered is 200m. The wave models used for comparison in this paper include:

- ***HAWC2-Linear***: linear Airy wave from HAWC2 default option;
- ***HAWC2-Stream***: stream function wave from HAWC2 default option;
- ***HPC-Nonlinear***: Fully nonlinear wave generated from HPC wave tank with fully nonlinear FSBCs.

Table 2 Load cases

	H (m)	T (s)	λ (m)	σ (H/ λ)
H6T7	6	7	76	0.078
H6T10	6	10	156	0.038
H12T15	12	15	351	0.034

Wave kinematics from the first two waves are directly calculated in HAWC2 while polynomial fitting method is used to process the wave kinematics from fully nonlinear wave and then import into HAWC2. Wheeler stretching is used for linear wave to get the value up to free surface. HAWC2-Linear wave serves as a baseline reference for the comparison. All the simulations are run with time step 0.02s and the system becomes stable after 200s.

5.2 (a) H6T7 – σ 0.078

Wave kinematics

Since HAWC2 is a 2D simulation tool, both velocity and acceleration in *x* direction are negligible. Wave elevations observed at location (0m, 0m, 0m) and horizontal and vertical velocity and acceleration are presented.

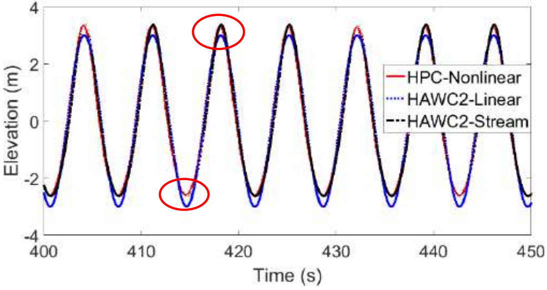

Figure 10 Wave elevation at (0m, 0m, 0m) – H6T7

Wave period detected is the same for all and the wave peaks and troughs are different as expected. Equal peak and trough is predicted from linear wave. Smaller trough and higher peak are obtained from Stream function and fully nonlinear wave.

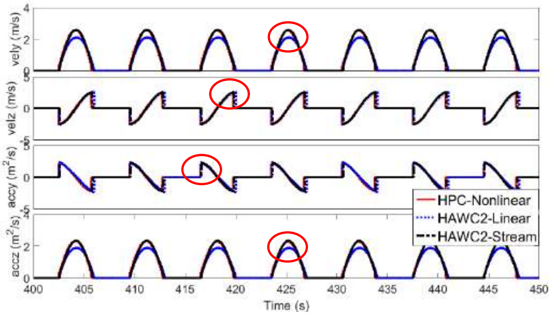

Figure 11 Velocity & acceleration at (0m, 0m, 0m) – H6T7

The kinematics at the observed point is only non-zero below instantaneous free surface, therefore it drops to zero when free surface goes below the point. Stream function and fully nonlinear wave provide almost the same prediction which is larger than linear wave.

Tower base

Shear stress and bending moment are the main sources that lead to fatigue damage at tower base. Both of them are greatly influenced by wave frequency loads. The difference from three wave models are not significant.

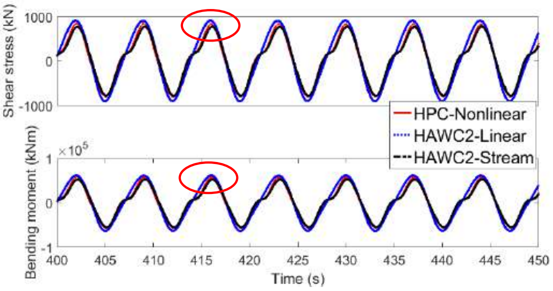

Figure 12 Shear stress & bending moment – H6T7

Floater motion

Surge, heave and pitch responses in condition H6T7 are shown in Figure 13. In theory, surge response will oscillate about zero-mean position (the dashed line) if Morison's equation is calculated at the undisplaced position of the body without wave stretching. However, there should be a slight non-zero drift surge motion in reality. The phenomenon can be captured when Morison's equation is integrated up to the instantaneous wave elevation using a stretching method as illustrated in Figure 13. Meanwhile, axial dynamic pressure is inserted as concentrated force on base columns to account for buoyancy force.

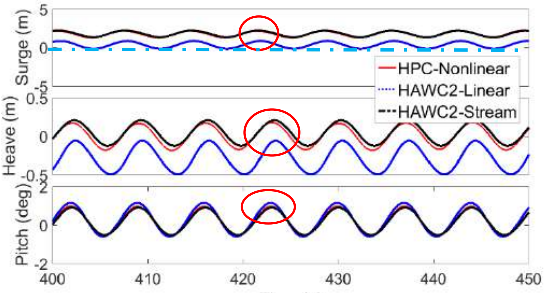

Figure 13 Motion response – H6T7

From Figure 13, surge and heave responses from fully nonlinear wave and stream function are quite close and clearly larger than linear wave response. The influence from different wave models are not significant for pitch motion.

Mooring line tension

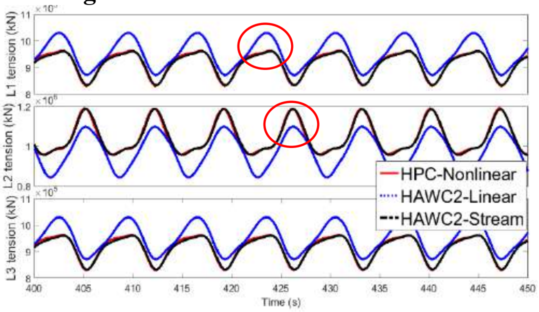

Figure 14 Tension response – H6T7

Mooring line tension is mainly due to the floater motion, therefore different surge motion prediction greatly influences the mooring line tension response. Mooring line 2 is in the upwind direction oriented with zero wind wave incoming direction while line 1 and 3 are symmetric in the downwind direction. The underestimation of surge motion from linear wave leads to underestimation of mooring line tension at upwind direction and overestimation at downwind direction. The results from Stream function and fully nonlinear wave are almost the same.

Computational efficiency

The dynamic analysis in HAWC2 is run for 700s with 0.02s time step for all methods. It takes 1.8 hours using default HAWC2 waves and 2.2 hours for HPC wave. Combining 2 hours for wave generation and 1 hours for polynomial fitting, the efficiency to run fully nonlinear wave analysis using polynomial fitting method is acceptable.

5.2 (b) H6T10 – σ 0.038

Wave kinematics

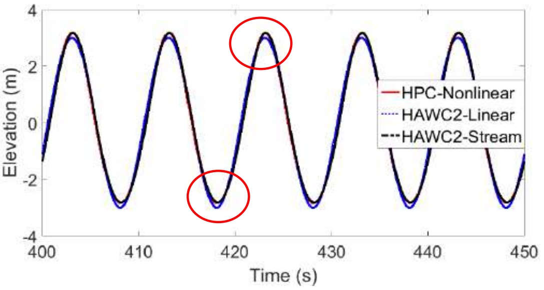

Figure 15 Wave elevation at (0m, 0m, 0m) – H6T10

Fully nonlinear wave and Stream function provide slightly larger peak and smaller trough than linear wave. Slight difference is also observed for horizontal velocity and vertical acceleration as shown in Figure 16. However, the difference is smaller compared with condition H6T7 due to smaller wave nonlinearity.

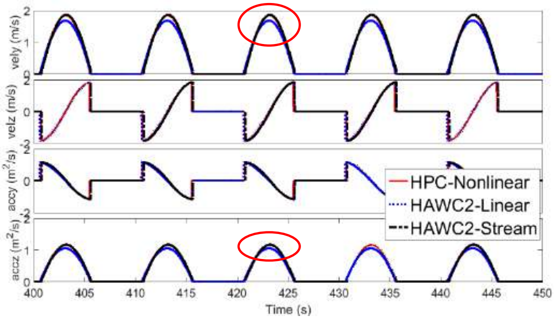

Figure 16 Velocity & acceleration at (0m, 0m, 0m) – H6T10

Floater motion

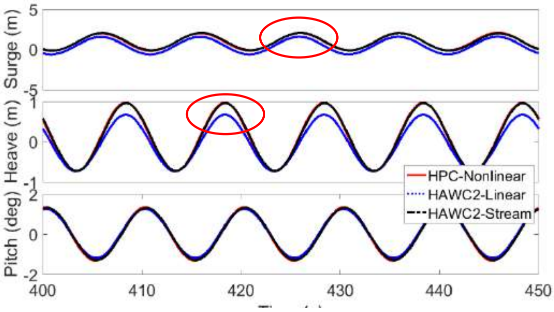

Figure 17 Motion response – H6T10

The decrease of the wave nonlinearity also affects the motion response as shown in Figure 17. The underestimation of surge and heave motion from linear wave is smaller compared with condition H6T7. Fully nonlinear wave and stream function again provides same motion prediction.

Mooring line tension

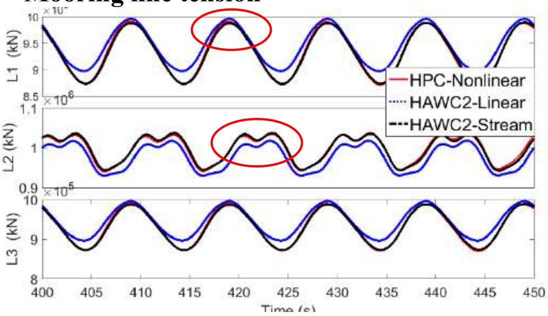

Figure 18 Tension response – H6T10

Due to the dynamic effects on mooring line, the upwind mooring line response includes more frequencies besides wave frequency as shown in Figure 18, which is captured by all wave theories. Maximum tension responses for less tensioned mooring line 1 and 3 are almost the same for all wave models. For most tensioned mooring line 2, linear wave model underestimates the maximum response compared with fully nonlinear wave and Stream function.

5.2 (c) H12T15 – σ 0.034

Wave kinematics

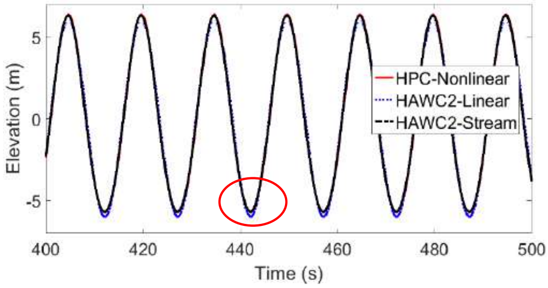

Figure 19 Wave elevation at (0m, 0m, 0m) – H12T15

There is almost no difference of wave profile from three wave models for the least nonlinear wave condition. So is the wave kinematics.

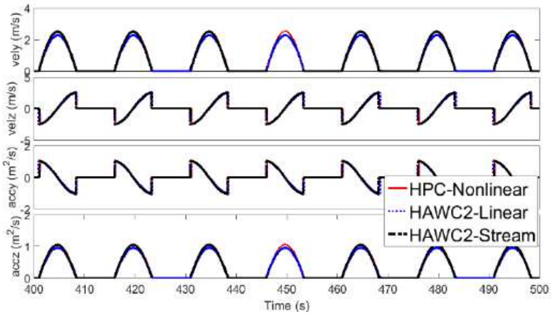

Figure 20 Velocity & acceleration at (0m, 0m, 0m) – H12T15

Floater motion

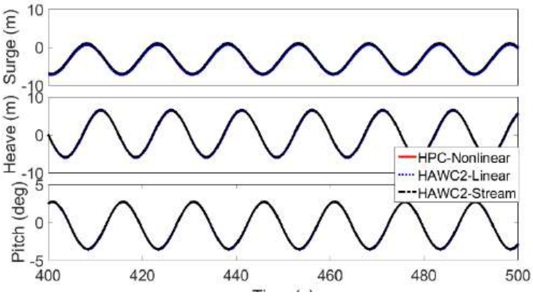

Figure 21 Motion response– H12T15

The motion response is almost the same for all three wave models which proves that linear wave can provide equally accurate results as fully nonlinear wave and Stream function for large wave in deep water.

Mooring line tension

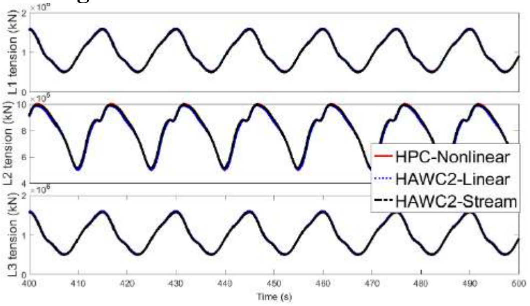

Figure 22 Tension response – H12T15

Same mooring line tension response also proves the applicability of all three wave theories when large wave is considered in deep water area.

5.2 (d) Summary

The statistics of wave elevation, surge motion and tension for mooring line at upwind direction in three sea states from all wave models are compared. The values are taken after the system becomes stable without transient phase in the beginning. The circle marker indicates the mean response. The maximum and minimum response are represented by diamond and square markers respectively.

Since both fully nonlinear wave and Stream function wave satisfy the fully nonlinear FSBC, the predictions from these two wave theories are almost the same for all three conditions. As wave steepness increases, phenomenon of smaller trough and higher peak from Stream function wave and fully nonlinear wave than linear wave becomes more significant as condition H6T7.

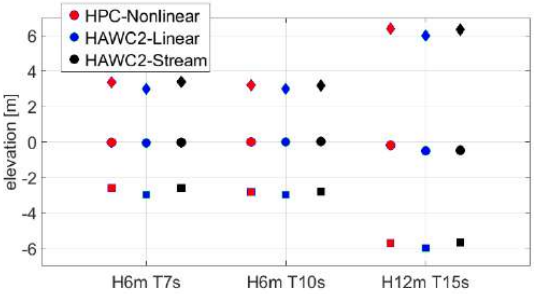

Figure 23 Wave elevation

Floater motion response is influenced not only by wave severity but also wave nonlinearity. In general, more severe wave leads to larger motion response. The mean surge motion is negative for condition H12T15 while positive for the other two conditions. Fully nonlinear wave and Stream function calculate same surge response which is clearly larger than linear wave for all three conditions. The difference increases as wave nonlinearity increases.

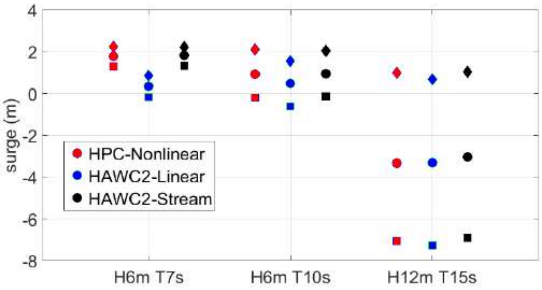

Figure 24 Surge motion

Normally, larger wave leads to higher mooring line tension. However, the mean surge motion is negative for condition H12T15 which makes the mooring line tension at upwind direction less severe. The comparison among three wave theories is same as surge motion.

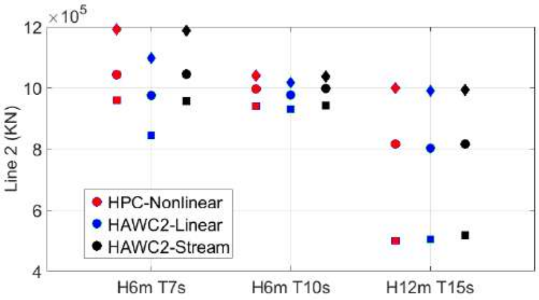

Figure 25 Mooring line tension

5. CONCLUSIONS

In order to apply an accurate wave model on floating wind turbine in intermediate water, a fully nonlinear wave model needs to be considered. To solve the memory barrier of the software for modelling floating wind turbine when applying nonlinear wave kinematics, a new wave kinematics polynomial fitting method is developed for HAWC2 using an extended 2D wkin.dll.

2D HPC wave tank is an efficient tool to generate wave kinematics for both regular and irregular wave with linear and fully nonlinear FSBCs. The polynomial fitting of obtained wave kinematics not only saves the data size but also keeps the accuracy at a high level. The wkin.dll in HAWC2 is extended to handle 2D wave field when applying pre-generated wave kinematics on a floating wind turbine and calculate hydrodynamic loads using Morison’s equation. The results of the case study show that the wave generated using different wave theories can be significantly different especially when the nonlinearity increase. However, there is almost no difference between Stream function wave and fully nonlinear wave, since both satisfy the fully nonlinear FSBCs. Linear wave theory in general underestimates the structural response compared with two nonlinear wave theories. Since Stream function cannot be used when irregular wave is considered as fully nonlinear wave, the latter is of great use in engineering project to describe realistic sea wave.

Considering the whole work procedure, from 2D HPC tank to wave kinematics database consisting of polynomial coefficients, from extended wkin.dll to hydrodynamic response calculation, computational efficiency is proved acceptable while memory requirement is fulfilled. This study not only proves the importance to consider fully nonlinear effects in hydrodynamic analysis for floating wind turbine in intermediate water depth but also offers an efficient numerical tool to make it happen.

ACKNOWLEDGEMENTS

The first author gratefully acknowledges the financial support from China Scholarship Council.

REFERENCES

1. Y. Shao and O. M. Faltinsen, 2012, 'Towards efficient fully-nonlinear potential-flow solvers in marine hydrodynamics', *In Proceedings of the 31st International Conference on Ocean, Offshore and Arctic Engineering of Reference, pp 369-380*
2. Y. Shao and O. M. Faltinsen, 2014, 'A harmonic polynomial cell (HPC) method for 3D Laplace equation with application in marine hydrodynamics' *Journal of computational physics, Vol.274, pp 312-332*
3. Y. Shao and O. M. Faltinsen, 2014, 'Fully-nonlinear wave-current-body interaction analysis by a harmonic polynomial cell method'*, Journal of Offshore Mechanics and Arctic Engineering, Vol. 136, p 031301*
4. H. Liang, O. M. Faltinsen and Y. Shao, 2015, 'Application of a 2D harmonic polynomial cell (HPC) method to singular flows and lifting problems', *Journal of Applied Ocean Research, Vol. 53, pp 75-90*
5. O. M. Faltinsen, 1990, 'Sea loads on ships and offshore structures', *Cambridge University Press.*
6. Statoil, 2017, 'World's first floating wind farm has started production', available at 'https://www.statoil.com/en/news/worlds-first-floating-wind-farm-started-production.html'
7. S. Schløer, H. Bredmose and H. B. Bingham, 2011, 'Irregular wave forces on monopile foundations. Effect of full nonlinearity and bed slope', *In proceedings of the ASME 2011 30th International Conference on Ocean, Offshore and Arctic Engineering*
8. S. Schløer, H. Bredmose, H. B. Bingham and T. J. Larsen, 2012, 'Effects from fully nonlinear irregular wave forcing on the fatigue life of an offshore wind turbine and its monopile foundation', *In the proceedings of the ASME 2012 31th International Conference on Ocean, Offshore and Arctic Engineering*
9. S. Schløer and H. Bredmose and H. B. Bingham, 2016, 'The influence of fully nonlinear wave forces on aero-hydro-elastic calculations of monopile wind turbines', *Journal of Marine Structures, Vol.50, pp162-188.*
10. T. J. Larsen and A. M. Hansen, 2007, 'How 2 HAWC2, the user's manual', Risø National Laboratory
11. D. E. Nakos, D. Kring and P. D. Sclavounos, 1994, 'Rankine panel methods for transient free surface flows', *In the proceedings of 6th International Conference on Numerical Ship Hydrodynamics', pp 251-269*
12. M. H. Kim, M. S. Celebi and D. J. Kim, 1998, 'Fully nonlinear interactions of waves with a three dimensional body in uniform currents', *Journal of Applied Ocean Research, Vol 20, pp 309-321*
13. M. S. Longuet-Higgins and E. D. Cokelet, 1976 'The deformation of steep surface waves on water – I. A numerical method of computation', *In the proceedings of Royal Society, pp1-26*
14. A. P. Engsig-Karup, H. B. Bingham and O. Lindberg, 2009, 'An efficient flexible-order model for 3D nonlinear water waves', *Journal of Computational Physics, Vol 228, pp2100-2118*
15. S. Øye, 1996, 'FLEX4 simulation of wind turbine dynamics', *In proceedings of 28th IEA meeting of experts concerning state of the art of aero-elastic codes for wind turbine calculations*
16. H. Bredmose, 2013 'Fully nonlinear wave forcing of a TLP wind turbine', *Deliverable report 4.21 on INNWIND.EU*
17. A. Pegalajar-Jurado, M. Borg, A. Robertson, J. Jonkman and H. Bredmose, 2017, 'Effects of second-order and fully nonlinear wave kinematics on a tension-leg-platform wind turbine in extreme wave conditions', *In proceedings of International Conference on Offshore Mechanics and Arctic Engineering, Vol 10*
18. O. M. Faltinsen and A. N. Timokha, 2009, 'sloshing', *Cambridge University Press*
19. B. S. Kallesøe and A. M. Hansen, 2011, 'Dynamic mooring line modeling in Hydro-Aero-Elastic wind turbine simulations', *In proceedings of 21st international offshore and polar engineering conference*
20. M. Borg, A. M. Hansen and H. Bredmose, 2016, 'Floating substructure flexibility of large-volume 10MW offshore wind turbine platforms in dynamic calculations', *Journal of Physics: Conference series, vol 753*
21. A. Robertson, J. Jokman, M. Masciola, H. Song, A Goupee, A. Coulling and C. Luan, 2014, 'Definition of the semisubmersible floating system for Phase II of OC4', *NREL technical report*
22. A. Robertson, J. Jokman, F. Vorpahl et al. 2014, 'Offshore code comparison collaboration continuation within IEA wind task 30: phase II results regarding a floating semisubmersible wind system', *In proceedings of international conference on offshore mechanics and arctic engineering, vol 9B*

23. K. Xu, Y. Shao, Z. Gao and T. Moan. 2018, ‘A study on fully nonlinear wave load effects on floating wind turbine’, *submitted for review.*

24. H. Karadeniz, 2013, ‘Stochastic analysis of offshore steel structures – An analytical appraisal’, *Springer.*

25. G. G. Stokes, 1847, ‘On the theory of oscillatory waves’, *Transactions of the Cambridge Philosophical Society, pp 441-473*

26. D. J. Korteweg and G. de Vries, 1895, ‘On the change of form of long waves advancing in a rectangular canal and on a new type of long stationary waves’, *Philosophical Magazine Series, pp 422-443*

27. J. Boussinesq, 1877, ‘Essai sur la theorie des eaux courantes’, *Mem. Pres. Acad. Sci. Paris.*

28. R. G. Dean, 1965, ‘Stream function representation of nonlinear ocean waves’, *Journal of Geophysical Research, vol 70.*

29. R. G. Dean, 1970, ‘Relative validation of water wave theories’, *Journal of Waterways and Harbours.*

30. F. Ursell, 1953, ‘The long wave paradox in the theory of gravity waves’, *Proceeding of Cambridge Philosophical Society, pp 685-694*

31. C. C. Lin and A. Clark Jr, 1959, ‘On the theory of shallow water waves’, *Tsing Hua Journal of Chinese Studies. pp 54-62*

32. DNVGL, 2017, ‘DNV-RP-C205, Environmental conditions and environmental loads’

33. L. M. Bernard, 1976, ‘An introduction to hydrodynamic and water waves’, *Springer*

34. L. Li, Z. Gao and T. Moan, 2015, ‘Joint Distribution of Environmental Condition at Five European Offshore Sites for Design of Combined Wind and Wave Energy Devices’, *Journal of Offshore Mechanics and Arctic Engineering, vol 137.*

35. C. Luan, Z. Gao and T. Moan, 2013, ‘Modelling and analysis of a semi-submersible wind turbine with a central tower with emphasis on the brace system’, *Proceedings of the ASME 2013 32nd International conference on ocean and arctic engineering, Nantes, France.*

A.4 Paper 4

Paper 4:
A study on fully nonlinear wave load effects on floating wind turbine.
Authors: Kun Xu, Yanlin Shao, Zhen Gao, Torgeir Moan
Published in *Journal of Fluids and Structures*, 2019
DOI: https://doi.org/10.1016/j.jfluidstructs.2019.05.008

Journal of Fluids and Structures 88 (2019) 216–240

Contents lists available at ScienceDirect

Journal of Fluids and Structures

journal homepage: www.elsevier.com/locate/jfs

A study on fully nonlinear wave load effects on floating wind turbine

Kun Xu [a,*], Yanlin Shao [b,c], Zhen Gao [a,d,e], Torgeir Moan [a,d,e]

[a] Department of Marine Technology, Norwegian University of Science and Technology (NTNU), Trondheim 7491, Norway
[b] Department of Mechanical Engineering, Technical University of Denmark, 2800 kgs., Lyngby, Denmark
[c] Shipbuilding Engineering Institute, Harbin Engineering University, 150001 Harbin, China
[d] Centre for Ships and Ocean Structures (CESOS), NTNU, Trondheim 7491, Norway
[e] Centre for Autonomous Marine Operations and Systems (AMOS), NTNU, Trondheim 7491, Norway

ARTICLE INFO

Article history:
Received 11 January 2019
Received in revised form 12 April 2019
Accepted 16 May 2019
Available online 30 May 2019

Keywords:
Fully nonlinear wave effect
Floating wind turbine
2D HPC method
Polynomial fitting method

ABSTRACT

The influence of fully nonlinear wave effects on floating wind turbine has been studied in this paper by comparing both floater motions and structural responses of tower base and mooring lines exposed to linear and fully nonlinear long-crested irregular waves. Wave kinematics of the linear and nonlinear wave are calculated in a 2D Harmonic Polynomial Cell wave tank. The wave kinematics are further processed by a polynomial fitting method to scale down the data size so that it fulfills the memory requirement of HAWC2 where coupled dynamic analysis is carried out. The external DLL used to provide wave kinematics to HAWC2 is extended from one dimensional (Wkin.dll 2.4) to two dimensional (Wkin.dll 2D) wave field so that fully nonlinear wave can be implemented on floating wind turbine through reading pre-generated wave kinematics manner. The whole work procedure including wave generation, polynomial fitting and implementation in HAWC2 has been verified with a linear regular wave case. Two extreme irregular wave conditions are focused to study the nonlinear wave effects regarding critical responses, such as wave elevation, floater motions and mooring line tension. The results have not only proved the accuracy and applicability of the polynomial fitting method and the extended Wkin.dll 2D for HAWC2 but also revealed the importance to consider fully nonlinear wave model in hydrodynamic analysis compared with linear wave theory especially for high sea states in shallow and intermediate water. As a result of development of computer capacity and numerical wave tank, this paper has demonstrated that fully nonlinear wave effect can be considered in an engineering manner with acceptable efficiency.

© 2019 The Authors. Published by Elsevier Ltd. This is an open access article under the CC BY-NC-ND license (http://creativecommons.org/licenses/by-nc-nd/4.0/).

1. Introduction

As floating wind turbines become more and more competitive in offshore wind energy market, the hydrodynamic behavior of floating structure in intermediate water depths (50 m–200 m) has drawn a lot of attention especially regarding the effect of the wave nonlinearity. The widely used linear Airy wave is mainly suitable for small wave in deep water and cannot provide accurate results for large wave in shallow water. The stream function wave model can capture most of the important nonlinearities. However, it does not work for irregular nonlinear waves, thus is less useful in practice

---

* Corresponding author.
E-mail address: kun.xu@ntnu.no (K. Xu).

https://doi.org/10.1016/j.jfluidstructs.2019.05.008
0889-9746/© 2019 The Authors. Published by Elsevier Ltd. This is an open access article under the CC BY-NC-ND license (http://creativecommons.org/licenses/by-nc-nd/4.0/).

when irregular waves are concerned. Larger extreme loads and load effects are expected in the case of fully nonlinear wave model in particular for extreme environmental conditions, in which wind turbine blades are parked and wave loads dominate over wind loads. It is therefore necessary to consider fully nonlinear wave in hydrodynamic analysis in order to calculate the wave loads and the structural responses of floating wind turbines properly.

Fully nonlinear wave interaction with submerged structures was investigated by Bai et al. (2014) using a three-dimensional numerical wave tank based on potential theory. The higher-order boundary element method is used to solve the mixed boundary value problem. Schløer et al. (2011) studied the effect of fully nonlinear irregular unidirectional wave acting on a monopile. Inline force and overturning moment resulted from nonlinear waves was found to be significantly larger than from linear wave. In some cases, stream function theory underestimates the wave forces compared with fully nonlinear irregular wave. The aeroelastic code used to model the wind turbine is FLEX5 Øye (1996) and the undisturbed fully nonlinear wave kinematics was obtained from OceanWave3D which is a fully nonlinear potential wave model proposed by Engsig-Karup et al. (2009) from DTU. OceanWave3D is able to solve 3D Laplace equation for the velocity potential with nonlinear free surface boundary conditions (FSBC). Schløer et al. (2012) performed comparative analysis regarding the fatigue damage of the monopile and tower due to fully nonlinear irregular wave. Fatigue damage level was seen to be significantly affected by nonlinear wave especially for misaligned wave and wind condition. In Schløer et al. (2016), linear and nonlinear wave realization were looked into detail. Redistribution of energy at different frequency range was observed from wave spectrum. The largest positive wave peaks come from nonlinear wave realization for all the condition compared with linear wave, so does the largest skewness. The difference between linear and nonlinear results increases with decreasing water depth due to increasing wave nonlinearity for reduced water depth. Nonlinear wave effects was also investigated for jacket supported wind turbine by Larsen et al. (2011). Significant increase in dynamic load effect due to nonlinear wave was found for tower bottom bending moment and axial force in both right leg and lower X-brace.

Despite all the previous work on bottom fixed wind turbine, there has been limited similar research work on floating wind turbines. Computational fluid dynamics (CFD) method has been used to study the fully nonlinear wave effect on a TLP floating wind turbine by Nematbakhsh et al. (2015). The results was compared with results from potential flow solver — Simo-Riflex. However, aerodynamic load was not included, nor does aeroelastic response of the wind turbine due to high computational cost. The coupled FLEX5-OceanWave3D tool was applied on a TLP wind turbine in the INNWIND project (Bredmose, 2013) to compare response exposed to different wave models including fully nonlinear wave. The result was further compared with experimental data in Pegalajar-Jurado et al. (2017). Pegalajar-Jurado et al. (2017) concluded that it was quite difficult to determine which wave model included was the most accurate because the wave models with different sets of wave kinematics cannot provide consistent prediction. Therefore, it is more challenging to apply fully nonlinear wave on floating wind turbine than bottom fixed wind turbine in terms of accuracy and efficiency. One of the reasons is that the footprint of floating wind turbines is larger due to its mooring system which requires larger database for pre-generated wave kinematics in the whole wave field to be used in a global response analysis. Normally the database is so large that it exceeds the virtual memory limit of the simulation tool for wind turbine. Therefore, there is a need to scale down the data size to meet the requirement at the first place. In addition, it is so demanding to obtain accurate fully nonlinear wave kinematics due to complicated fully nonlinear FSBCs that a separate numerical wave tank (NWT) is needed to generate the wave. Build a link between the wave kinematics database and the simulation tool is also quite important.

The main objective of this paper is to study fully nonlinear wave effect on a semi-submersible floating wind turbine. The fully nonlinear waves are generated in a 2D numerical wave tank based on the Harmonic Polynomial Cell method which is an efficient field solver. The coupled dynamic analysis is carried out in HAWC2. In accordance to the first memory boundary challenge, a polynomial fitting method is proposed in order to decrease the data size. The wave kinematics at pre-defined grid points in the whole wave field is fitted to polynomial functions representing location coordinates and corresponding polynomial coefficients. The method is verified against HAWC2 default wave. The other contribution of this paper is extending the dynamic link library between wave kinematics database and HAWC2 from one dimensional to two dimensional so that it can be applied not only on bottom fixed wind turbine but also on floating wind turbine. The hydrodynamic wave load in HAWC2 is calculated using Morison's equation. The nonlinear effect considered in this paper mainly includes nonlinear wave kinematics generated from a numerical wave tank; hydrodynamic load calculation for the floater up to the instantaneous free surface of the incident waves, geometrical nonlinearity for mooring line. A regular wave case is performed for verification and two extreme irregular wave conditions are compared for the nonlinear effects. Wave kinematics, wave spectrum, floater motion, tower base force and mooring line tension are compared.

2. Wave theory

Ocean wave is a random and irregular process whose mathematical formulations can be determined based on several boundary conditions on water surface and sea bottom. Wave theories can be divided into linear and nonlinear groups according to the simplification level of boundary conditions. A linear regular wave has a sinusoidal surface profile with small amplitude and steepness, while a nonlinear wave has sharper crests and flatter troughs. The nonlinear regular waves can be described by Stokes, cnoidal, stream function or solitary wave theories according to the nonlinear properties of the waves. The applicability of various wave theories is discussed in DNV-RP-C205 DNVGL (2017) as shown in Fig. 1.

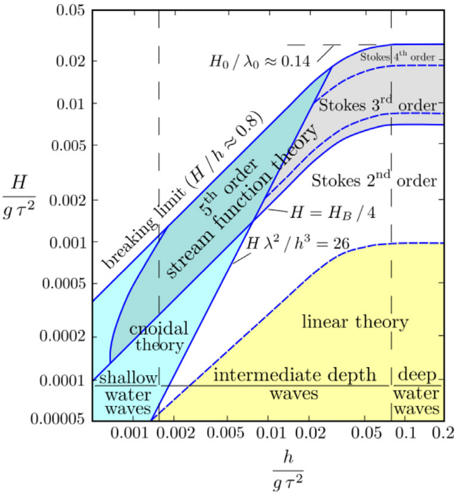

Fig. 1. Applicability of various wave theories.

Horizontal axis is a non-dimensional measurement of depth shallowness and the vertical axis is a measurement of wave steepness.

The nonlinearity of a large transient wave event can be described by higher order bound and resonant nonlinearities (Gibson and Swan, 2006). Bound nonlinearities are induced by higher order nonlinear harmonics which are phase locked to the first order wave component. They tend to modify the free surface profile by sharping the peaks and flattening the troughs. Resonant nonlinearities on the other hand influences the energy distribution within the wave spectrum by adjusting the phases and amplitudes of the first order wave components and produces new wave components satisfying dispersion relation.

2.1. Linear wave theory

Linear wave theory also known as Airy wave theory is the most widely used wave theory in offshore industry. It is based on the assumption that the contribution from the nonlinear terms in FSBCs are negligible. The mathematical expression can be derived considering a incompressible, inviscid and irrotational fluid.

1. Laplace equation is the governing equation in the fluid domain:

$$\bigtriangledown^2\phi = 0 \tag{1}$$

2. Considering wave elevation, η which is proportional to wave height H is small, the FSBCs can be linearized and described at the still water level (SWL) $z = 0$ instead of $z = \eta$ using Taylor's expansion. Dynamic FSBC is written as:

$$\frac{\partial\phi}{\partial t} = -g\eta \quad \text{on} \quad z = 0 \tag{2}$$

where the atmospheric pressure is assumed to be zero on the free surface.

3. Kinematic FSBC is expressed as

$$\frac{\partial\eta}{\partial t} = \frac{\partial\phi}{\partial z} \quad \text{on} \quad z = 0 \tag{3}$$

4. The impermeability condition, such as sea bottom and fixed body surfaces is described as:

$$\frac{\partial\phi}{\partial n} = 0 \tag{4}$$

2.2. Fully nonlinear wave theory

Linear wave theory is formulated on the basis that only the linear terms are kept in FSBCs while nonlinear terms are totally neglected. It can provide good estimation of the wave kinematics for small waves in deep water (water depth is larger than half of the wavelength). However, the contribution from nonlinear terms becomes significant when water depth is small. Therefore, fully nonlinear wave theory is a better option. The different FSBCs are written as:

- Fully nonlinear dynamic FSBC

$$\frac{\partial \phi}{\partial t} = -g\eta - \frac{1}{2} \nabla \phi \cdot \nabla \phi \qquad \text{on} \qquad z = \eta(x, y) \tag{5}$$

- Fully nonlinear kinematic FSBC

$$\frac{\partial \eta}{\partial t} = \frac{\partial \phi}{\partial z} - \overline{\nabla}\phi \cdot \overline{\nabla}\eta \qquad \text{on} \qquad z = \eta(x, y) \tag{6}$$

Here $\nabla = \vec{i}\frac{\partial}{\partial x} + \vec{j}\frac{\partial}{\partial y} + \vec{k}\frac{\partial}{\partial z}$ and $\overline{\nabla} = \vec{i}\frac{\partial}{\partial x} + \vec{j}\frac{\partial}{\partial y}$. $\vec{i}, \vec{j}$ and $\vec{k}$ are unit vectors along x-, y- and z-axis respectively.

When a material derivative following an arbitrary velocity $\vec{v} = \left\{v_x, v_y, v_z\right\}$ is introduced, the fully nonlinear FSBCs can be rewritten as:

$$\frac{\mathrm{D}\phi}{\mathrm{D}t} = -g\eta - \frac{1}{2} \nabla \phi \cdot \nabla \phi + \vec{v} \cdot \nabla \phi \qquad \text{on} \qquad z = \eta(x, y) \tag{7}$$

$$\frac{\mathrm{D}\eta}{\mathrm{D}t} = \frac{\partial \phi}{\partial z} - \overline{\nabla}\phi \cdot \overline{\nabla}\eta + \left\{v_x, v_y\right\}^T \cdot \overline{\nabla}\eta \qquad \text{on} \qquad z = \eta(x, y) \tag{8}$$

In this paper, a semi-Lagrangian approach will be used by following the vertical velocities of fluid particles on the free surface, which means in 2D case the following FSBCs shall be applied in the numerical implementation:

$$\frac{\mathrm{D}\phi}{\mathrm{D}t} = -g\eta - \frac{1}{2} \nabla \phi \cdot \nabla \phi + \frac{\partial \phi}{\partial z}(\frac{\partial \phi}{\partial z} - \frac{\partial \phi}{\partial x}\frac{\partial \eta}{\partial x}) - \mu(x)\phi \qquad \text{on} \qquad z = \eta(x, y) \tag{9}$$

$$\frac{\mathrm{D}\eta}{\mathrm{D}t} = \frac{\partial \phi}{\partial z} - \overline{\nabla}\phi \cdot \overline{\nabla}\eta + \left\{v_x, v_y\right\}^T \cdot \overline{\nabla}\eta - \mu(x)\phi \qquad \text{on} \qquad z = \eta(x, y) \tag{10}$$

Here $\mu(x)$ is a damping coefficient to dissipate the energy of the waves which exists only in the damping zone at the end of the numerical wave tank.

3. Hydrodynamic load modeling

Potential flow theory and Morison's equation are the two typical methods for hydrodynamic load calculation of floating wind turbine in global analysis. Computational Fluid Dynamics (CFD) has become more popular in recent years as well thanks to the rapid development of computer capacity. Matha et al. (2011) has discussed the advantages and limitations of all three methods.

3.1. Morison's equation

Morison's equation which is used in this paper is a semi-empirical method to calculate the wave loads on slender structures whose diameter-to-wavelength ratio is less than 1/5. The diffraction and radiation effects are considered not significant. It has been mostly applied on slender vertical surface-piercing cylinders such as monopile and spar. Some recent research results also proved the applicability for small-diameter floating wind turbine like semi-submersible in high sea states compared to model scale measurements (Robertson et al., 2013).

The hydrodynamic loading according to Morison's equation is expressed in terms of the undisturbed fluid-particle velocity and accelerations directly which allows Morison's equation to be applied in the case of nonlinear wave and current kinematics models (Santo et al., 2018).

The wave force dF on a strip of length dz of a rigid moving circular cylinder can be written as:

$$dF = \rho\frac{\pi D^2}{4}dzC_M a_n + \rho\frac{\pi D^2}{4}dz(C_M - 1)a_c + \frac{\rho}{2}C_D D dz|u_{rel}|u_{n,rel} \tag{11}$$

where D is the cylinder diameter, a_n is the undisturbed wave induced acceleration components normal to the cylinder axis, a_c is the normal component of cylinder acceleration, $u_{n,rel}$ is the component of the relative velocity normal to the cylinder, C_M and C_D are the mass and drag coefficients which are dependent of several parameters such as Reynolds number, the roughness number and the Keulegan–Carpenter number. The coefficients should be determined empirically and C_M can be determined according to the result from potential flow theory.

One advantage of Morison's equation is the hydrodynamic load calculation is based on undisturbed fluid particle velocity and acceleration instead of velocity potential which is expressed with frequency-dependent added mass, damping and wave excitation force. As a result, Morison's equation provides a more straightforward manner to consider nonlinear wave or current kinematics models. Accordingly in this paper, Morison's equation is used to carry out the hydrodynamic load calculation.

3.2. Radiation/diffraction theory

As the size of supporting floating substructure increases, wave diffraction and radiation effects become more significant and cannot inherently be captured by Morison's equation. In such case, potential flow theory is preferred. The first order potential problem solves diffraction and radiation problems separately with linearized boundary value problems whose solution is frequency-dependent and linearly related with wave amplitude. Added mass, damping and restoring matrices and incident wave excitation from diffraction are pre-computed in frequency domain. Viscosity is incorporated through drag term of the Morison's equation. Difference frequency and sum frequency effects are considered by second order potential theory which are important for slow drift motion of semi-submersible and ringing of TLP. Second order hydrodynamic effects can be obtained by either full quadratic transfer functions (QTF) which take into account the contribution from all six degrees of freedom or Newman's approximation which only requires the diagonal terms of the full QTF matrix while the off-diagonal terms are approximated by the diagonal terms for the two directions and periods involved. The frequency domain results are applied in time domain simulation through Cummins equation (Cummins, 1962). Take a floating single degree-of-freedom system including mooring system and viscous drag force as an example, the motion equation in time domain can be written as:

$$(M + A_\infty)\ddot{x}(t) + \int_{-\infty}^{+\infty} \kappa(t-\tau)\dot{x}(\tau)d\tau + Cx(t) + K(x(t)) = F^{FK} + F^{D} + C_q\,|u-\dot{x}|\,(u-\dot{x}) \tag{12}$$

where M is the mass of the body, A_∞ is the added mass at infinity frequency, $\kappa(t-\tau)$ is the retardation function consisting of frequency-dependent added mass and damping coefficient, C is the hydrostatic restoring force, $K(x(t))$ is the nonlinear restoring force from the mooring system, F^{FK} is the Froude–Krylov force, F^{D} stands for the diffraction force, the quadratic damping force is related to the relative velocity between body velocity and fluid particle velocity.

3.3. Computational fluid dynamics

Computational fluid dynamics (CFD) method can include all relevant linear and nonlinear hydrodynamic effects including viscous effects. Normally, finite-volume method is used to solve the Reynolds-Averaged Navier–Stokes (RANS) equations on grids while free surface can be represented by the volume of fluid (VOF) approach (Carrión et al., 2014). Viscous effects are included to describe vortex separation at mooring line and floater. Despite the accuracy in hydrodynamic wave modeling, high computational effort is expected which still requires a lot of effort before engineering application. Meanwhile, current CFD studies are restricted to wave-only simulation and it is challenging to include aerodynamic effects at the same time.

4. Harmonic polynomial cell method

4.1. 2D HPC method

The numerical wave tank used in this paper to generate fully nonlinear wave is based on 2D harmonic polynomial cell (HPC) method which was initially proposed by Shao and Faltinsen (2012) as a potential flow solver with approximately 4th order accuracy. The highlight of HPC method is that the fluid domain is divided into quadrilateral cells associated with harmonic polynomials which are used to describe the velocity potential in each cell. It has been compared with four other methods and demonstrates great efficiency and accuracy. The HPC method was developed to 3D case by Shao and Faltinsen (2014b), and implemented in fully-nonlinear wave body interaction problems such as sloshing in 3D tanks, shallow water wave tank, influence from seabed topography and nonlinear wave diffraction by a bottom-mounted vertical circular cylinder. Promising results again proved the applicability of HPC method when dealing with potential flow problems. Later on, the current effects was studied together with nonlinear wave diffraction by multiple bottom mounted cylinder in Shao and Faltinsen (2014a). Improvement of HPC method was made by Liang et al. (2015) in order to account for singular flows and discontinuous problems. Domain decomposition method combining with local potential flow solution was proposed to handle the singularity at sharp corners. A double-layer node technique is developed to model the velocity potential jump in a thin free shear layer in lifting problem.

Brief introduction of HPC method is given here while detailed theory can be referred to Shao and Faltinsen (2012, 2014a,b). According to 2D HPC method, the fluid domain is discretized into quadrilateral cells within which there are four quadrilateral elements and nine grid nodes as shown in Fig. 2. The stencil center is located in the middle node with index 9 while eight other nodes are boundary nodes numbering from 1 to 8. The velocity potential ϕ within the cell is expressed by harmonic polynomials which automatically satisfy Laplace equation. Therefore, the velocity potential at any point in the cell can be interpolated by a linear combination of the eight harmonic polynomials at the surrounding boundary nodes.

$$\phi(x, y) = \sum_{j=1}^{8} b_j f_j(x, y) \tag{13}$$

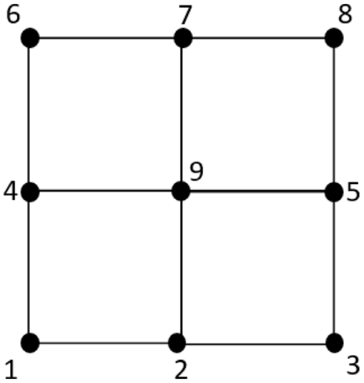

Fig. 2. Grid node indexes in a cell.

Where $f_1(x,y) = 1$; $f_2(x,y) = x$; $f_3(x,y) = y$; $f_4(x,y) = x^2 - y^2$; $f_5(x,y) = xy$; $f_6(x,y) = x^3 - 3xy^2$; $f_7(x,y) = 3x^2y - y^3$; $f_8(x,y) = x^4 - 6x^2y^2 + y^4$

Including higher order polynomials could reduce the wave dispersion errors in the time domain analysis and increase the accuracy of the solution.

The way to calculate the unknown coefficients b_j term is equivalent to a sub-Dirichlet boundary value problem with Laplace equation as the governing equation. Combining $x = x_j$, $y = y_j$, $\phi = \phi_j$ with Eq. (13), a linear equation with a precise form is achieved:

$$b_i = \sum_{j=1}^{8} c_{i,j}\phi_j \quad (i = 1, \ldots, 8) \tag{14}$$

here $c_{i,j}(i, j = 1, \ldots, 8)$ is the elements of the inverse of matrix $[D]$ which consists of elements $d_{i,j} = f_j(x_i, y_i)$. Therefore, the velocity potential at any grid point in the fluid domain could be described based on the eight surrounding boundary nodes in the same stencil cell. Considering the stencil center where $x = x_9 = 0$ and $y = y_9 = 0$, the resulting harmonic polynomials is expressed as $f_1(0,0) = 1$ and $f_j(0,0) = 0, j = 2, \ldots, 8$. Accordingly, the velocity potential at the cell center is described as:

$$\phi_9 = \phi(x = x_9 = 0, y = y_9 = 0) = \sum_{i=1}^{8} c_{1,i}\phi_i \tag{15}$$

The Dirichlet boundary condition is related to velocity potential at the boundary nodes, while the Neumann boundary condition is enforced by taking the normal derivative:

$$\frac{\partial\phi}{\partial n}(x,y) = \sum_{i=1}^{8}\left[\sum_{j=1}^{8} c_{j,i} \nabla f_j(x,y) \cdot n(x,y)\right]\phi_i \tag{16}$$

where n is the normal vector, defined as positive pointing outside of the fluid domain.

4.2. Time integration, wave generation and wave absorption

An explicit 4th order Runge–Kutta method is applied to integrate Eqs. (9) and (10) in time to update the wave elevation and velocity potential on the free surface. Auxiliary solutions at three time instants are needed in the 4-stage time integration. For each time step, four solutions of the boundary value problem for the velocity potential in the whole fluid domain are obtained by the HPC method, which has been described in Section 4.1.

Wavemaker at left end of the numerical wave tank is used to generate the target waves. It is known that a sudden start of a wavemaker will introduce instability and breakdown of the simulation eventually. Thus, a ramp function $r(t)$ is applied to the wavemaker signal $s(t)$ so that the modified signal becomes $s(t) = \bar{s}(t) \cdot r(t)$. In this study, the following ramp function is applied

$$r(t) = \begin{cases} \frac{1}{2}[1 - cos(\pi \frac{t}{T_{ramp}})], & t < T_{ramp} \\ 1, & t \geq T_{ramp} \end{cases} \tag{17}$$

Here T_{ramp} is the duration of the ramp, which is taken as 2 times of the peak period T_p of the wave spectrum.

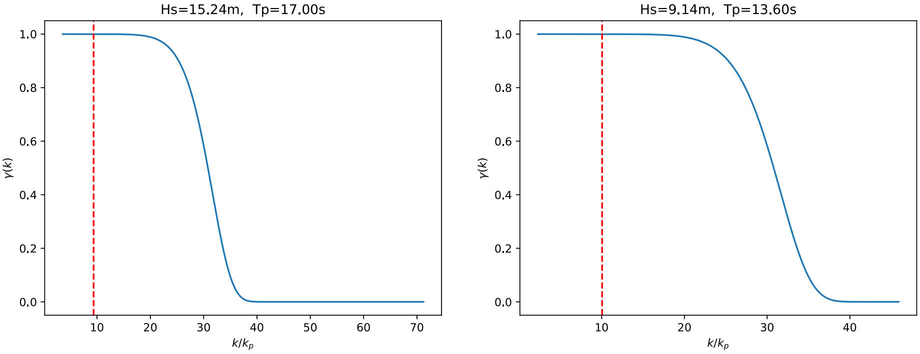

Fig. 3. Filter strength.

A numerical damping zone is implemented at the end of the numerical wave tank to dissipate the energy of the waves. A quadratic function, which has been suggested by Ning and Teng (2007) is applied:

$$\mu(x) = \begin{cases} \mu_0(\frac{x-x_b}{\lambda_b})^2, & x > x_b \\ 0, & x \leq x_b \end{cases} \tag{18}$$

Here x is the coordinate measured from the location of the wavemaker. x_b is the location where the damping zone starts and λ_b is the length of the damping zone. The length of the damping zone and the damping strength μ_0 are so chosen to minimize the wave reflection from the wall at the end of the tank.

It is necessary to apply a free-surface filter in order to simulate nonlinear steep waves over a long time duration without any instability developing. Without such a filter, sawtooth instability will eventually occur for waves over a certain steepness as consequence of aliasing effects due to the quadratic terms in fully nonlinear free surface conditions. In this study, the simulated wave elevation along the numerical wave tank is projected into wavenumber space through FFT technique, and the following filter is then applied to the resulting wave numbers

$$\gamma(k) = exp(-(\frac{k}{\alpha \cdot k_0})^\beta) \tag{19}$$

Here k_0 is a reference wave number, which normally corresponds to a characteristic wave number of the considered wave spectrum. In this study, k_0 is taken as k_p, which is the root of the dispersion relationship $\omega_p^2 = k_p h \cdot \tanh(k_p h)$. Here $\omega_p = 2\pi/T_p$. h is the water depth. α and β are constant coefficients.

An ideal filter should be able to sufficiently remove energy from very short waves while keep the important waves unchanged. α and β are determined through $\gamma(k_{max}) = 0.01$ and $\gamma(k_{min}) = 0.99$ which indicate that the filter takes away 99% wave amplitude from a short wave with wave number k_{max} and only 1% wave amplitude from a wave with wave number k_{min}. In this study, $k_{max} = 2\pi/(4\Delta x)$ and $k_{min} = 2\pi/(10\Delta x)$ are used in all the analysis with irregular waves. Δx is the size of the element along horizontal direction of the numerical wave tank. Since the filter strength is dependent on the discretization and the characteristic wave number $k_0 = k_p$, it is important to understand the effect of the filter before generating the nonlinear irregular waves.

Fig. 3 is an example of the filter strength $\gamma(k)$ as function of k/k_p for a sea state with $H_s = 15.24$ m and $T_p = 17.0$ s to the left and $H_s = 9.14$ m and $T_p = 13.6$ s to the right. The horizontal discretization is defined with $\Delta x = \frac{\lambda_p}{40} = \frac{2\pi}{k_p} \cdot \frac{1}{40}$, which means that 40 elements are uniformly distributed within a characteristic wave length, which corresponds to the peak-frequency of the spectrum. According to Fig. 3, the filter completely removes energy for waves with $k/k_p \geq 40$ while it has almost no effect for waves with $k/k_p \leq 20$.

When a wave spectrum is used to generate irregular waves in the time domain, it is common practice to truncate the wave spectrum by a lower-limit frequency ω_l and upper-limit frequency ω_u. The cut-off frequency limit in this paper is determined mainly based on two aspects: the important waves containing most of the energy cannot be cut off and extremely short wave which requires quite fine mesh should be cut off in order to avoid numerical breakdown and increase of CPU time. As recommended in Stansberg et al. (2008) and DNVGL (2017), the cut-off limit defined in this paper is: $\omega_u = \sqrt{2g/H_s}$ and $\omega_l = 0.4 * \omega_p$, which leads to only 0.9% and 1.1% loss of the zero-th moments of the wave spectra for ULS1 and ULS2 condition respectively. The vertical dashed lines in Fig. 4 represent the cut-off frequencies while the red lines represent the wave spectra.

At the same time, the vertical lines in Fig. 3 indicate the wave number corresponding to the upper-limit truncation frequency ω_u. It is quite obvious that the applied filter has negligible effects on the important waves that should be simulated through the truncated wave spectrum. If a finer mesh is used, the filter will have even less effects on the waves that are of practical interests in the studies presented in this paper.

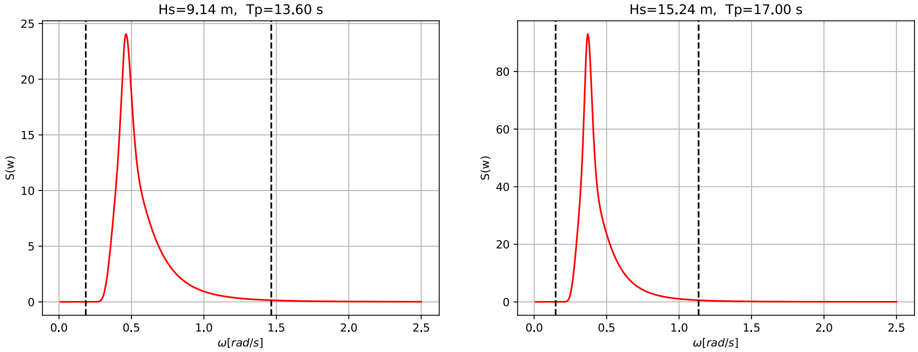

Fig. 4. Cut-off of wave spectra for ULS1 and ULS2 condition.

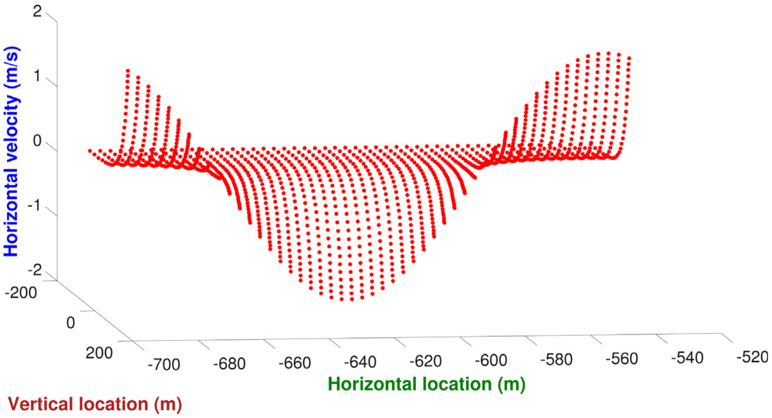

Fig. 5. Horizontal velocity at 200 s.

4.3. *Polynomial fitting of wave kinematics*

The velocity potential, wave elevation, velocity are directly calculated from 2D HPC wave tank, while acceleration is available by post-processing velocity and grid deformation. All the grids are fixed in the tank in linear wave making problem, while the grids deform vertically in nonlinear case which leads to the difference when calculating the acceleration. Bernoulli's equation is only valid in an inertial system. Therefore, material derivative is introduced to calculate the acceleration (Faltinsen and Timokha, 2009):

$$\frac{\partial U}{\partial t} = \frac{\delta U}{\delta t} - w_{grid} \cdot \nabla U \tag{20}$$

Since the grid deformation only appears in vertical direction, Eq. (20) can be further written as:

$$\frac{\partial U}{\partial t} = \frac{\delta U}{\delta t} - \frac{\partial z}{\partial t} \cdot \frac{\partial U}{\partial z} \tag{21}$$

Where U is the velocity, $\frac{\partial z}{\partial t}$ is the relative velocity representing the grid deformation in vertical direction.

The wave kinematics data obtained from the wave tank at each time step is expressed at discrete grid points across the whole wave field. Fig. 5 is an example of the horizontal velocity of wave particles in the wave field with corresponding horizontal and vertical coordinates at a certain time step. At the same time step, there are three other similar figures representing vertical velocity, horizontal acceleration and vertical acceleration which are not shown here. It takes about 18 h to calculate a 1 h irregular wave realization with 148 grids horizontally and 22 grids vertically in a normal computer when only 2 processors are engaged. However, the size of resulting wave kinematics files including wave elevation, velocity and acceleration in both horizontal and vertical directions is around 8 GB, which exceeds the memory requirement of the simulation tool for wind turbine, HAWC2 in this study. Besides, huge occupation of virtual memory will slow down the computation especially for floating wind turbine whose element number is normally very large. Therefore, there is an urgent need to scale down the size of input wave data.

Table 1
Polynomial function.

Order	Polynomial
0	1
1	xz
2	x^2xzz^2
3	$x^3x^2zxz^2z^3$
…	…
n	$x^nx^{n-1}zx^{n-2}z^2 \quad \dots \quad x^2z^{n-2}xz^{n-1}z^n$

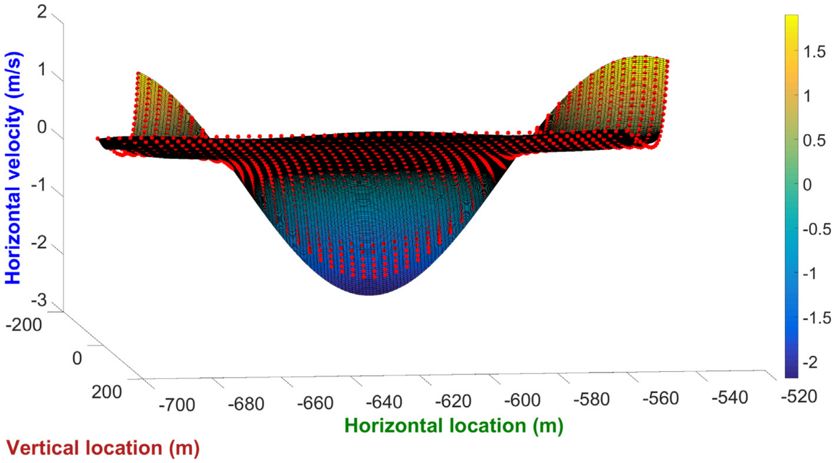

Fig. 6. Fitting surface and original data.

In accordance to the challenge, a polynomial fitting method is presented. First of all, the vertical and horizontal dimensions of the wave field are determined by water depth and footprint of the mooring system respectively. Normally, it is sufficient to use 50 grids horizontally per wavelength and 30 grids along water depth. Then the whole wave field is divided into a number of horizontal divisions based on the wavelength. The kinematics varies at both horizontal and vertical directions.

Therefore within each division, a 2 dimensional polynomial function representing horizontal and vertical coordinates up to a certain order n is introduced as shown in Table 1. The corresponding coefficients using least-squares method are calculated and arranged in a descending power regarding x coordinate. As a result, the kinematics data at each time step can be expressed in a function form instead with location coordinates as input variables:

$$U = c_1x^n + c_2x^{n-1}z + \cdots + c_{\frac{(n+1)(n+2)}{2}-2}xz^{n-1} + c_{\frac{(n+1)(n+2)}{2}-1}z^n + c_{\frac{(n+1)(n+2)}{2}} \tag{22}$$

Here x represents horizontal coordinate, z represents vertical coordinate and c_i is corresponding polynomial coefficient.

In nonlinear wave problem, the vertical coordinates of the grid points can be directly applied as input for z, since the grids deform vertically following instantaneous wave elevation up to the free surface. Meanwhile, in linear wave problem, the grid is fixed and the kinematics is calculated below mean water level. Therefore, Wheeler stretching method is applied to obtain the kinematics up to the free surface by scaling vertical coordinate:

$$z' = (z - \eta)\frac{d}{d + \eta} \tag{23}$$

Where z is original grid coordinate, z' is scaled coordinate, η is the instantaneous free surface elevation and d is water depth.

As a result, the wave kinematics at any locations in the whole wave field at each time step can be calculated based on Eq. (22), which include not only the original grid points directly from the wave tank as shown in Fig. 5 but also at the locations between the grid points. The resulting wave kinematics information can be expressed with a fitting surface where different color represent different amplitude of the kinematics. Fig. 6 is an example of the fitting surface for horizontal velocity and it can be seen that the velocity between the grid points are available as well represented by the fitting surface. The same procedure is applied to acceleration and velocity in both horizontal and vertical directions.

In the end, the original wave kinematics expressed at discrete grid points are replaced by coefficients c_i and corresponding polynomial functions x_i, z_i representing horizontal and vertical coordinates. The size of data is decreased

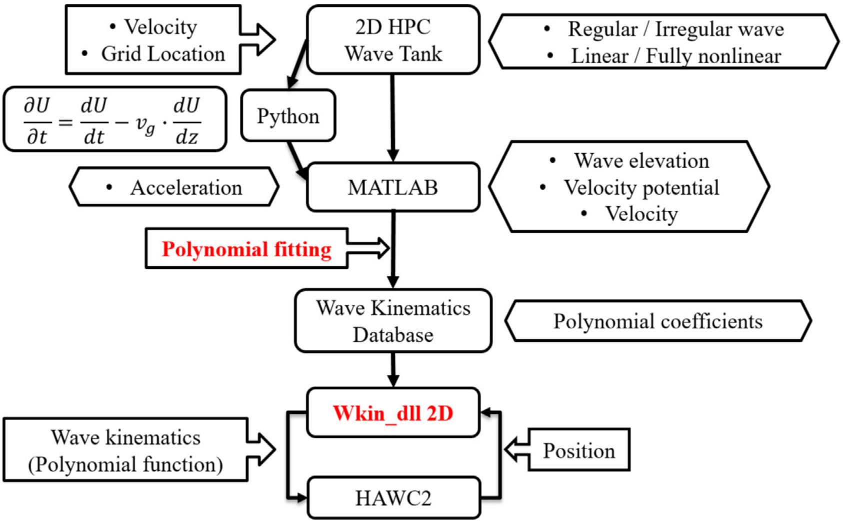

Fig. 7. Work flow.

from 8 GB to 1 GB for a 1 h irregular wave problem using 148 grids horizontally and 22 grids vertically, which fulfills the memory requirement of HAWC2 and can be imported through reading pre-generated wave kinematics manner. The order of the polynomial function applied should be carefully chosen in order to achieve good result especially for irregular wave problems whose variation of wave kinematics is harder to predict.

5. Methodology

5.1. Work flow

The main focus of this paper is to study the fully nonlinear wave effects on floating wind turbine using 2D HPC wave tank and HAWC2 with extended Wkin.dll 2D to handle wave kinematics polynomial coefficients. The work procedure is demonstrated in Fig. 7. The contribution of this paper are marked with red color.

1. Step1: 2D HPC numerical wave tank is first used to generate regular or irregular wave with linear or fully nonlinear FSBCs. Wave elevation, velocity and velocity potential are directly available from the tank while the acceleration is obtained through post-processing based on information of velocity and grid location. The calculation of acceleration is based on Eq. (21) and performed in Python.
2. Step2: A Matlab code package based on polynomial fitting method Eq. (22) is developed and applied to fit wave velocity and acceleration data to polynomial coefficients and store as a wave kinematics database.
3. Step3: Finally the coupled dynamic time domain analysis based on Morison's equation is carried out in HAWC2 and the wave kinematics at required location is calculated through Wkin.dll 2D using location coordinates sent from HAWC2 and polynomial coefficients sent from wave kinematics database.

5.2. Modeling theory

HAWC2 (Horizontal Axis Wind turbine simulation Code 2nd generation) is an aeroelastic code developed at DTU Wind Energy in 2003–2006. It is intended for calculating the response of offshore floating and fixed wind turbines in the time domain Larsen and Hansen (2007).

In HAWC2, multibody formulation is the basis of the structural modeling strategy meaning that the wind turbine is divided into several bodies and each body is modeled using a number of Timoshenko beam elements. The coupling constraints connecting individual bodies make it possible to account for the nonlinear structural effects due to body rotation or deformation.

The aerodynamic modeling is based on blade element momentum theory (BEM) and was extended by Hansen et al. (2004) to include dynamic stall, skew inflow and operation in sheared inflow etc. Turbulent inflow can be generated using Mann model and potential flow method is applied to describe tower shadow effects. Control of the turbine is achieved through several DLLs.

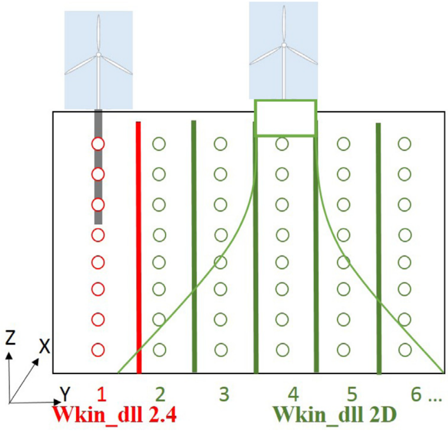

Fig. 8. Wave field structure of wkin.dll in HAWC2.

One option of the hydrodynamic modeling in HAWC2 is based on potential flow theory coupling with output results from WAMIT (Borg et al., 2016) for large volume structures to account for diffraction effect. The other alternative is Morison's equation suitable for small-diameter structures. Buoyancy loads are included through integration of external pressure contribution and inserted as concentrated forces on end nodes and distributed forces over conical sections.

Mooring lines for floating wind turbine can be modeled in either a quasi-static or dynamic manner (Kim et al., 2013). Quasi-static mooring line model is based on pre-calculated results from MIMOSA where stiffness property is described using fairlead position against restoring forces from mooring line. In each time step, the mooring line tension is iterated according to the configuration of each mooring line with the assumption that each mooring line is in static equilibrium at the moment. Inertial effects and damping of the mooring system from wave, current are neglected in quasi-static model (Jonkman, 2009). Dynamic mooring line model was developed by Kallesøe and Hansen (2011) using a cable element with hydrodynamic drag and buoyancy forces. The bottom contact is modeled by a nonlinear spring stiffness. The stiffness of each element is influenced by deflection and orientation of the element. The formulation is applicable for cables with uniform properties so that sections with different cable types are modeled separately and connected by ball joint constraints. Clump weight and buoy can be included as point mass with linear and quadratic viscous damping terms. In this paper, dynamic mooring line model is applied to account for the dynamic effect.

5.3. *Wave kinematics (Wkin.dll)*

The wave kinematics applied in HAWC2 are provided externally through a defined DLL interface named Wkin.dll. In the current version Wkin.dll 2.4, the input wave types can be selected from: linear airy waves with Wheeler stretching; irregular Airy waves based on JONSWAP or PM spectrum with directional spreading; stream function wave and pre-generated wave kinematics.

When importing pre-generated wave kinematics, the wave field that Wkin.dll 2.4 is able to handle can be considered as a one dimensional field since the data are imported at discrete grid points at only one horizontal location along the water depth as the red part in Fig. 8. The wave kinematics variation only exists in one dimension. The kinematics at any point and the wave elevation are linearly interpolated using the neighboring points. This works sufficiently for bottom fixed wind turbine such as monopile where only the wave kinematics at the center of the structure is needed since the movement of monopile is very small.

However, it is not applicable for floating wind turbine where the variation along horizontal direction is needed as well due to the mooring system. Therefore, the Wkin.dll is further extended in this paper to include wave kinematics variation in horizontal direction in order to implement on floating wind turbine (green part in Fig. 8). It is named Wkin.dll 2D because it is able to handle wave field in two dimensions. Wave elevation is linearly interpolated at different horizontal locations. The wave kinematics including velocity and acceleration are first calculated in numerical wave tank and then fit into polynomial coefficients to scale down the size as introduced in Section 4.3. Wkin.dll 2D will receive the location coordinates sent from HAWC2 and delivers the exact wave kinematics value using the polynomial fitting method. The wave loads on both floater and mooring line are calculated based on Morison's equation.

The extension of the wave field from one dimensional to two dimensional makes it possible to perform hydrodynamic analysis for floating wind turbine using pre-generated wave kinematics method, which is the basis for fully nonlinear wave effect study.

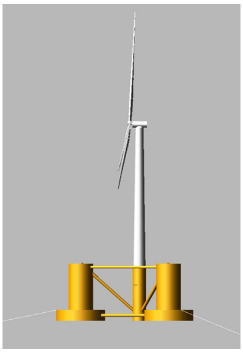

Fig. 9. OC4 semi-submersible wind turbine (Robertson et al., 2014a).

Table 2
Load cases.

	Type	H or Hs [m]	T or Tp [s]	Simulation time [s]	Time step [s]	No. of runs
REG	Regular	6	10	700	0.02	1
ULS1	Irregular	9.14	13.6	4200	0.02	20
ULS2	Irregular	15.24	17	4200	0.02	20

6. Case study

6.1. OC4 semi-submersible floating wind turbine

The floating wind turbine studied in this paper is 5MW OC4 semi-submersible wind turbine as shown in Fig. 9. The floater includes a center column connecting the tower and three side columns which is connected with main column through a number of smaller pontoons and braces (Robertson et al., 2014a). The design is aiming for 200 m water depth with 20 m draft. Three catenary mooring lines are arranged symmetrically about the platform vertical axis with 120° angle between them. The radius from the floater center is 40.87 m to fairlead and 837.6 m to anchor. Unstretched length of all three mooring lines is 835.5 m with 0.0776 m diameter and 108.63 kg/m apparent mass in fluid per unit length. The detailed layout and structural property is available in Robertson et al. (2014a).

Coupled dynamic analysis has been performed through a code comparison involving 23 organizations and 19 simulation tools (Robertson et al., 2014b) to study the structural behavior under different environmental conditions using different modeling philosophies. 23 load cases consisting of standstill frequency analysis without wind and wave loads; standstill case with wave loads; fully coupled dynamic analysis with both wind and wave loads were analyzed. Fully nonlinear wave effects has not been included. At the same time, potential flow theory and Morison's equation are also compared regarding hydrodynamic modeling. Diffraction effects are important to consider using potential flow theory when the structure diameter is larger than 0.2 times wavelength. The results from the comparison is that as for the main structures and pre-defined sea states, the diameter to wavelength ratio calculated only exceeds 0.2 for some lowest sea states, where hydrodynamic loads are small anyway. For the high sea states involved, Morison's equation is able to provide equally accurate results as potential flow theory. A detailed comparison is available in Robertson et al. (2014b). In this paper, Morison's equation is applied for hydrodynamic modeling in HAWC2 while mooring line is represented with dynamic model. The hydrodynamic load on the floater is calculated by integrating the force up to the free surface. The force acting on the mooring line is also calculated based on Morison's equation.

6.2. Load cases

It is important to check beforehand that whether the polynomial fitting method is able to provide reliable results compared with current available code with respect to predicting wave kinematics and responses e.g. floater motion and mooring line tension. Accordingly, a wave-only linear regular wave case is first performed to verify the polynomial fitting method. Afterwards, two irregular wave-only cases representing extreme sea states are considered to study the effect due to fully nonlinear wave.

The sea states selected in this paper is based on the pre-defined condition as listed in Robertson et al. (2014b) and the metocean data at Norway 5 site in North sea (Li et al., 2015). Water depth considered is 200 m. A regular wave condition is selected for verification as a representative case labeled as *REG* in Table 2. Polynomial fitting method is compared with default input wave from HAWC2 as a reference. Regular wave verification simulation is run for 700 s and the system

Table 3
Nonlinear effect.

	Linear wave	Fully nonlinear wave
Nonlinear wave kinematics	Not included	Included
Instantaneous water level	Included	Included
Nonlinear mooring line	Included	Included

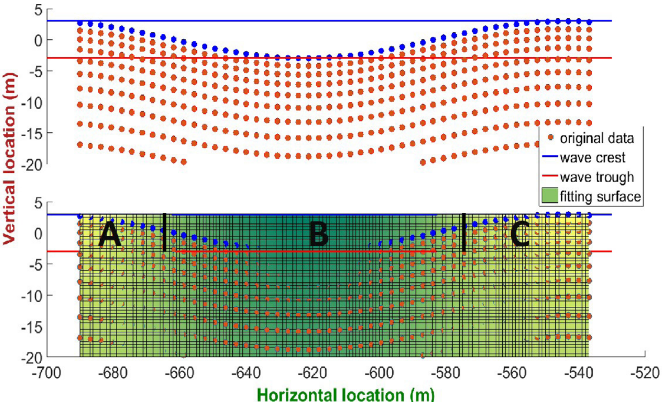

Fig. 10. Location coordinates of the grid points and fitting surface. (For interpretation of the references to color in this figure legend, the reader is referred to the web version of this article.)

becomes stable after 200 s. Only the results from 400 s to 450 s are presented in the following section due to the similarity. The two ultimate-limit-state (ULS) irregular wave conditions are based on JONSWAP spectrum. In each ULS condition, 20 simulations of linear and fully nonlinear wave are performed respectively and same random seed is used for the two wave models within each simulation so that the wave generated follows the same trend but with different amplitude. The total length of the simulation is 4200 s while first 600 s is removed due to transient effect. The following result is taken as the average of 20 simulation results to account for stochastic uncertainty as much as possible. In the following tables and figures, the notation of *HAWC2-Linear* stands for the results using default linear wave from HAWC2 while notation of *HPC-Linear* stands for the results using the new method — polynomial fitting kinematics from HPC wave tank. *Linear* and *Nonlinear* represent waves generated using linear and fully nonlinear FSBCs respectively.

The main objective of this paper is to study the nonlinear effect due to wave. Therefore, all the other nonlinear effects involved in the modeling are kept the same for the two models including calculation of hydrodynamic load up to instantaneous water level and nonlinearity in the mooring line model. The only difference is the nonlinear effect in wave kinematics as shown in Table 3.

6.3. Verification of the analysis procedure

The verification of the proposed analysis procedure (using 2D HPC method, polynomial fitting method and Wkin.dll 2D) for linear wave case against pure HAWC2 analysis is considered with respect to wave kinematics obtained from fitting function compared with original data; wave kinematics observed from HAWC2 simulation; floater motion and mooring line tension predicted using polynomial fitting method and default wave.

6.3.1. Wave kinematics

The polynomial fitting results are checked in the following section regarding how well it represents original data and predicts wave kinematics at other locations in the field. Meanwhile, the output from HAWC2 simulation is also compared between the new method and default regular wave.

Wave kinematics data is fit to polynomial coefficients after being generated fromt the 2D HPC numerical wave tank. Fig. 10 shows the location coordinates of original grid points whose vertical coordinates follows the wave elevation and the resulting fitting surface. It can be considered as the top view of original data (Fig. 5) and fitting surface (Fig. 6) where only the location coordinates are shown without the actual kinematics value. Fig. 11 is the cross-section of the fitting surface (Fig. 6) at wave crest and wave trough. It is used as an example to judge whether fitting surface can coincide with original data at different water depth from free surface to seabed.

Since the vertical coordinates of the data points have been Wheeler stretched using Eq. (23), all the data points follow the instantaneous wave elevation in vertical direction. Therefore in Fig. 10, the original data at free surface (blue dots) are not located at exact wave crest level (blue line) or wave trough level (red line) but at different levels in between.

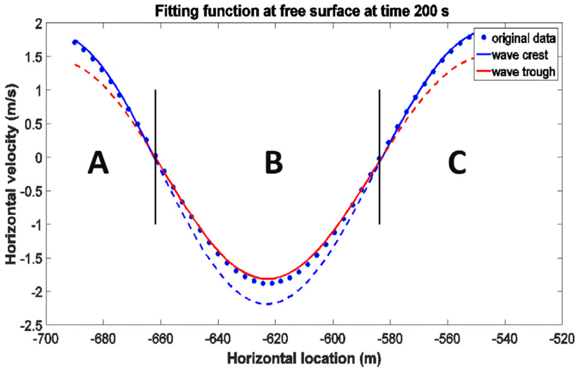

Fig. 11. Cross-section of the fitting surface at free surface.

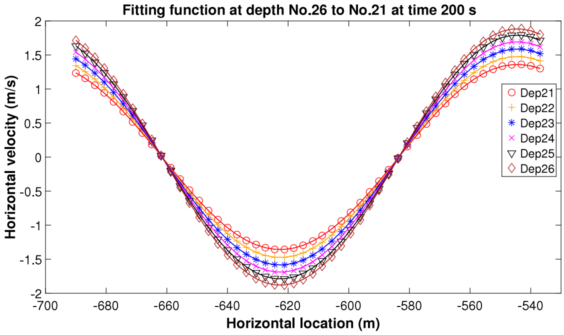

Fig. 12. Fitting function along various water depths.

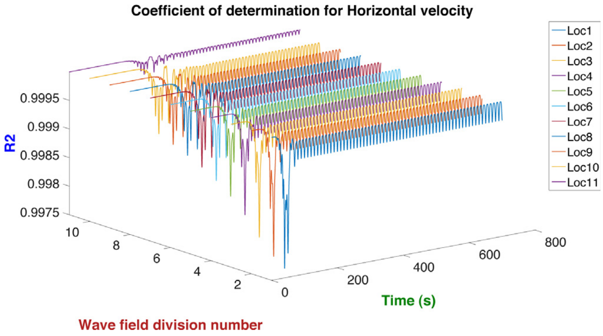

Fig. 13. Coefficient of determination.

The cross section of the fitting surface (Fig. 6) at wave crest and wave trough level do not go through all the free surface points (blue dots) exactly since the vertical coordinates are different as shown in Fig. 10, but it will provide an indication about how close original and predicted data are when their coordinates are close. Accordingly, original data is compared with wave crest level (blue solid line) in region A and C and wave trough level (red solid line) in region B considering close vertical coordinates. In Fig. 11, the dashed part of fitting curves are not used for comparison because they are less close to original data by contrast. It is observed that the fitting curves (solid part) predict quite close to original data. It is safe to conclude that the coincidence will be even better when the cross section at exact coordinate as the data is used.

The fitting result is checked at several other different water depths in Fig. 12. The two parts of each fitting line are determined based on the same principle as Fig. 11: the maximum and minimum vertical coordinate at that depth level. Different colors and markers are used to distinguish different water depths.

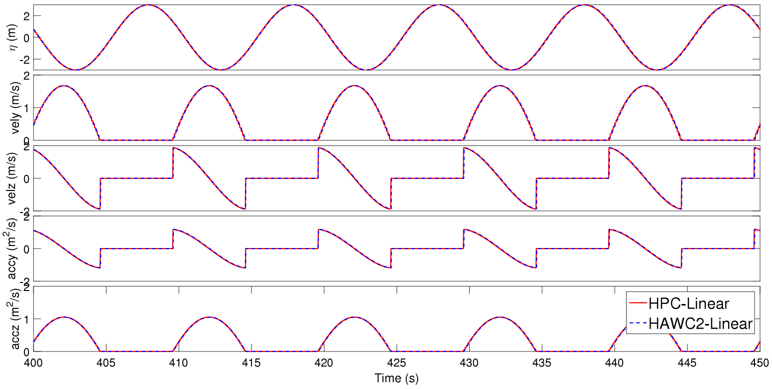

Fig. 14. Wave kinematics at (0 m, 0 m, 0 m). (For interpretation of the references to color in this figure legend, the reader is referred to the web version of this article.)

From statistical point of view, coefficient of determination, denoted R^2 is a measure of how well predicted model has represented original data.

$$R^2 = 1 - \frac{\sum_i (y_i - f_i)^2}{\sum_i (y_i - \bar{y})^2} \tag{24}$$

Where y_i is original data, f_i is predicted data and $\bar{y}$ is the mean of original data. The closer R^2 is to 1, the better linear regression results fit original data. R^2 are calculated for all the wave field divisions at each time step in Fig. 13, as the wave is slowly generated to steady state after 200 s, R^2 becomes stationary with minimum value being 0.9993 for all the divisions, which indicates that the fitting surface provides great representation of original data.

The wave-only regular wave dynamic analysis is performed using the polynomial fitting method and compared with default regular wave in HAWC2. The wave kinematics output of the simulation are also checked. Since HAWC2 is a 2D simulation tool, both velocity and acceleration in x direction are negligible. The wave kinematics observed at location (0 m, 0 m, 0 m) are shown in Fig. 14 including wave elevation; horizontal and vertical velocity; horizontal and vertical acceleration.

The blue line is the results calculated using default wave in HAWC2 while the red line is obtained from polynomial fitting method. Wave elevation from HPC method is linearly interpolated using data at nearest two discrete grid points while result from HAWC2 default wave is calculated based on the analytical expression. The kinematics at the observed point is only non-zero below instantaneous free surface, therefore it drops to zero when free surface goes below the point which is between 0 m and 3 m in Fig. 14 (the positive z direction in HAWC2 points downwards towards seabed). The prediction from the two methods is so close to hardly distinguish from the figure.

The wave kinematics decay along water depths which is captured in Fig. 15 where the data at three depths below free surface are plotted. There is almost no difference between the two methods. In conclusion, HPC polynomial fitting method is able to calculate wave kinematics correctly.

6.3.2. Floater motion

Surge, heave and pitch responses are shown in Fig. 16. Surge response will oscillate about zero-mean position if Morison's equation is calculated at the undisplaced position of the body without wave stretching. However, there should be a slight non-zero drift surge motion in reality. The phenomenon can be captured as illustrated in Fig. 16 when Morison's equation is integrated up to the instantaneous wave elevation using a stretching method. Meanwhile, the buoyancy force in HAWC2 is calculated by integrating static pressure over the bottom and conical sections of the structure with additional contribution from Archimedes method which only includes the normal component to the structure. Therefore, the FK term in the Morison's equation is used by HAWC2 to represent the dynamic pressure integration in the transverse direction (Karimirad et al., 2011). Heave and pitch motion oscillate about zero mean position while HPC method predicts slightly larger heave motion than HAWC2. The difference is due to the error during the polynomial fitting of the wave kinematics using HPC method and the fitting error is more obvious in vertical direction whose kinematics variation is large. However, the heave and pitch response prediction is not significantly affected considering the total response and can be accepted.

6.3.3. Mooring line tension

Mooring line 2 is in the upwind direction oriented with zero wind wave incoming direction while line 1 and 3 are symmetric in the downwind direction. The mean tension and maximum tension are pretty close predicted by the two

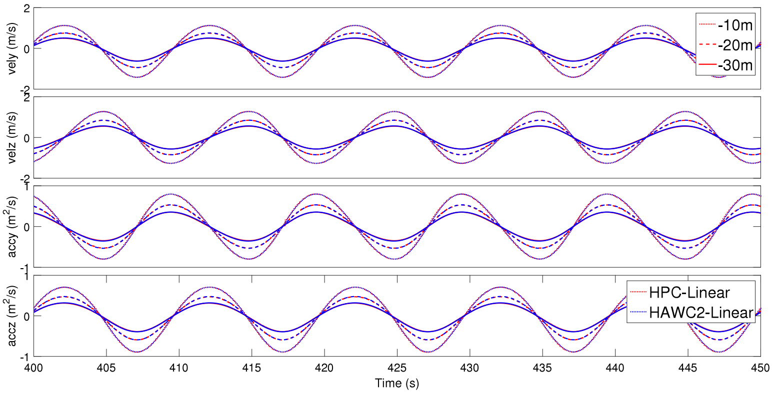

Fig. 15. Wave kinematics along different water depths.

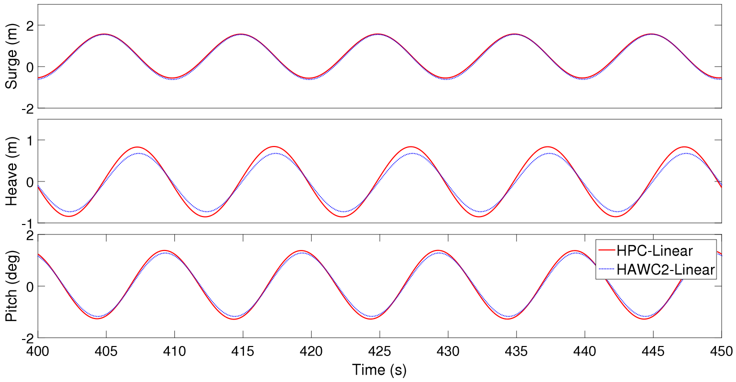

Fig. 16. Motion response.

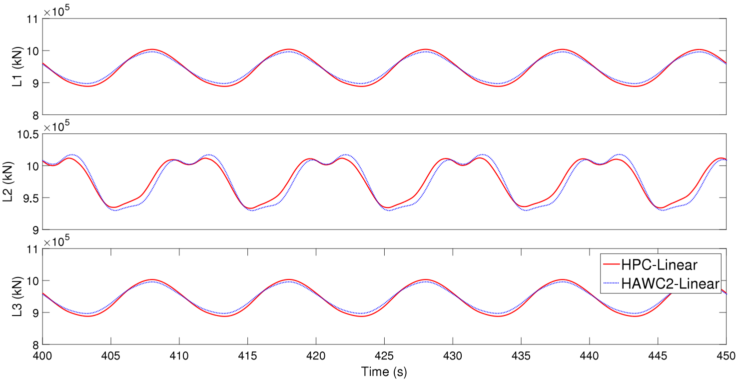

Fig. 17. Mooring line tension.

methods. The two continuing peak detected in mooring line 2 is due to the excitation of mooring line from the wave, which is captured by the dynamic mooring modeling method. If a quasi-static modeling method is applied, only one peak will be found (Robertson et al., 2014b).

In conclusion, wave kinematics from new proposed HPC polynomial fitting method not only saves the data size but also keeps the accuracy at a high level. The corresponding motion and tension response are also predicted correctly (see Fig. 17).

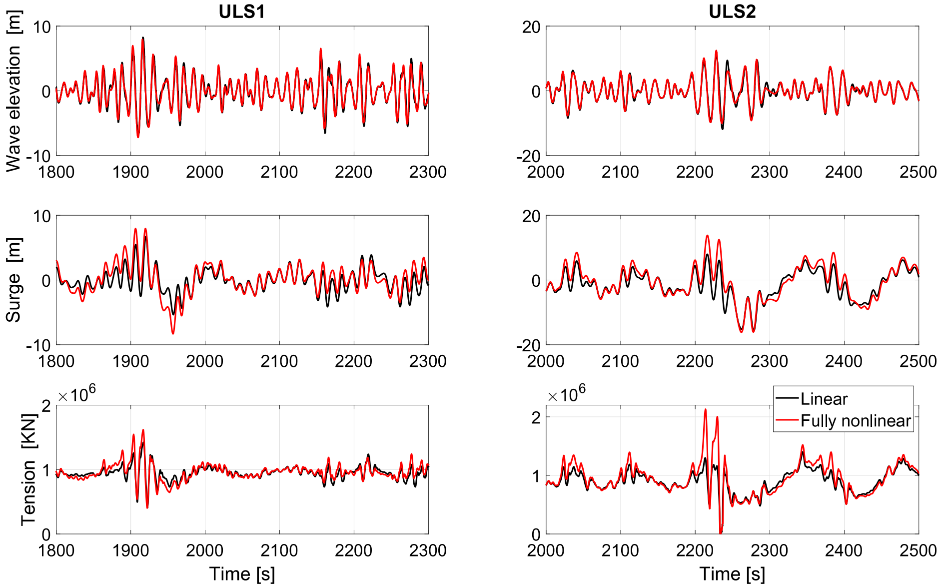

Fig. 18. Time series.

6.4. Irregular wave

The previous regular wave case has proved the accuracy and applicability of the polynomial fitting method. In the following section, the two irregular sea states are compared based on results from 20 simulations. The sea states are defined in Table 2. Both linear and fully nonlinear analysis are run for 4200 s while first 600 s is removed in order to get results for one hour simulation. The following figures and statistics are based on all the 20 simulation results. Fig. 18 is an example of time series for wave elevation, floater surge motion and mooring line tension in the two conditions. Black line represents results due to linear wave and red line represents results due to fully nonlinear wave.

6.4.1. Global maxima

Since the same seed number is used to generate the wave for linear and fully nonlinear wave , the time series of the wave and response follow the same trend just with different amplitudes. The peak amplitude illustrates the difference between the two wave models, which is the basis of the statistical study of this paper. From statistical point of view, probability of exceeding a given threshold by an random maximum provides direct indication of the distribution of maximum response and it can be fit with asymptotic extreme value probability distribution model when the number of sample is large enough. Accordingly, the occurrence probability of a certain level of response can be then predicted. The probability of exceedance is calculated as:

$$P(X_i) = 1 - \frac{i}{N+1} \tag{25}$$

Where X_i is the response sorted in an increasing order. N is the total number of peaks.

Normally, global response maxima of a stationary Gaussian narrow-band process can be well modeled by a Rayleigh distribution (Fu et al., 2017). However, when non-Gaussian and nonlinear property of the process increases, in order to get an accurate expression of the upper tail distribution, Weibull distribution is preferred instead of Rayleigh distribution. In this paper, the largest maximum response between adjacent zero-up-crossing above the mean response level is selected as the global response maxima. Fig. 19 is an example of the global maxima selection of the wave elevation. Blue line is the realization of the wave elevation and green line is the level of mean value and the red dots represent the selected global maxima. The exceedance probability above 0.1 is fitted with Rayleigh distribution while the tail part with probability below 0.1 is decided to be fitted with Weibull distribution. The global maxima of the responses with exceedance probability level of 10^{-4} for the fitted probability function are extrapolated and marked as extreme 10^{-4} in the following tables, which are mainly used to give a direct comparison of the two wave models. In the following section, results of linear and nonlinear wave from ULS1 and ULS2 conditions are shown together with different colors and markers. The fitting probability distribution are plotted using dashed line with the same color as the original maxima data. The horizontal axis represents the global maxima of the response and the vertical axis representing the probability of exceedance is expressed in a logarithmic scale for better representation.

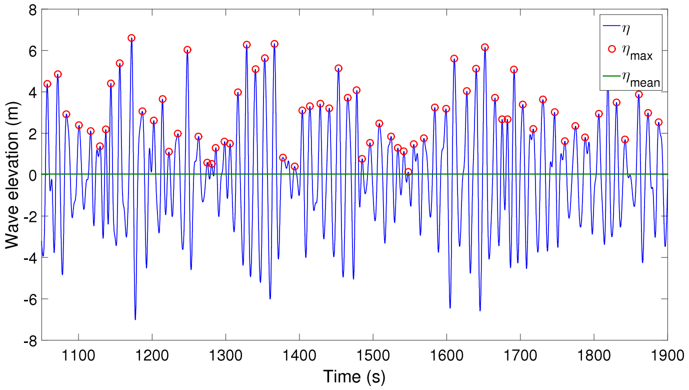

Fig. 19. Selection of global maxima of the wave elevation. (For interpretation of the references to color in this figure legend, the reader is referred to the web version of this article.)

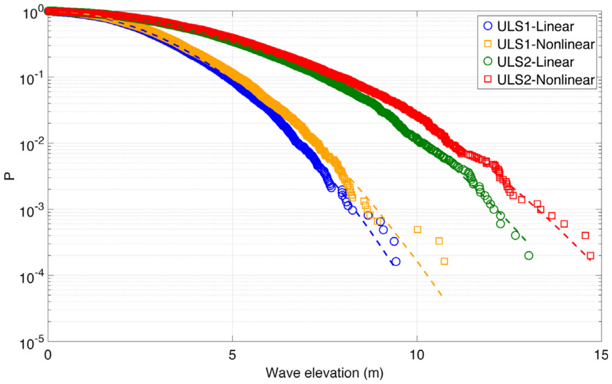

Fig. 20. Global maxima of positive wave peaks at (0 m, 0 m, 0 m).

Table 4
Statistics of wave elevation.

	ULS1 linear	ULS1 nonlinear	ULS2 linear	ULS2 nonlinear
Mean [m]	9.79e−5	6.27e−4	3.55e−4	7.36e−3
Maximum [m]	7.85	8.67	11.3	12.2
Standard deviation [m]	2.24	2.23	3.43	3.40
Skewness	0.00287	0.120	0.00883	0.170
Kurtosis	3.02	3.05	2.90	2.94
Extreme 10^{-4} [m]	9.79	10.60	13.78	15.59

6.4.2. *Wave realization*

The property of the wave observed at location (0 m, 0 m, 0 m) is first compared with time realization and wave spectrum.

Fig. 20 shows the probability of exceedance for positive wave peaks observed at (0 m, 0 m, 0 m) obtained from linear and nonlinear wave in two conditions. The peaks are selected according to the definition of global maxima in Eq. (25). In general, distinction is not obvious between linear and nonlinear curves at probability level larger than 0.1 for smaller wave peaks. It is mainly the higher maxima with probability level below 0.1 that has clear difference. Higher peaks are predicted from nonlinear wave than linear wave and the difference is more obvious in higher sea state (ULS2). When the same exceedance probability is considered, fully nonlinear wave tends to predict higher value. The mixed Rayleigh–Weibull distributions is able to predict the probability of the original data quite well.

Maximum elevation, skewness and kurtosis of wave elevation taken as the average of all 20 simulations are presented in Table 4. Nonlinear wave in general predicts larger maximum elevations than linear wave for both cases, which is mainly due to the additional contribution from the nonlinear terms. The standard deviations calculated for the linear and fully nonlinear wave are quite close with slightly higher value for linear wave, indicating that linear wave contains a bit higher

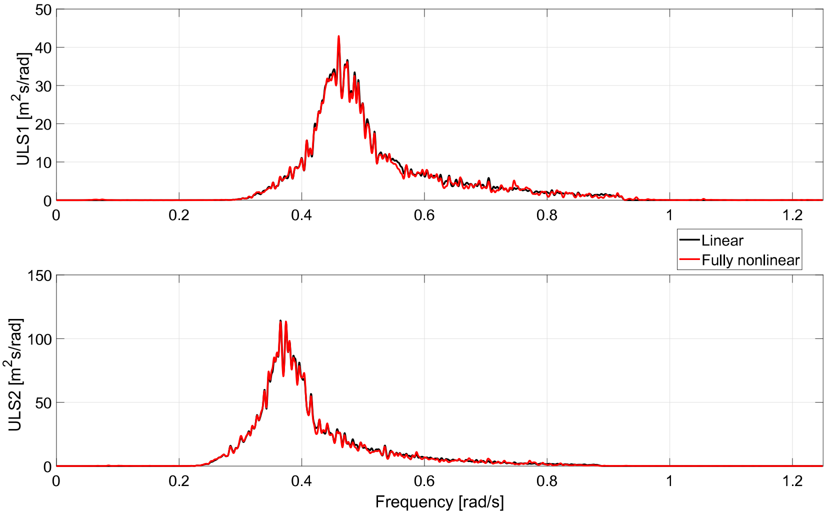

Fig. 21. Wave spectrum.

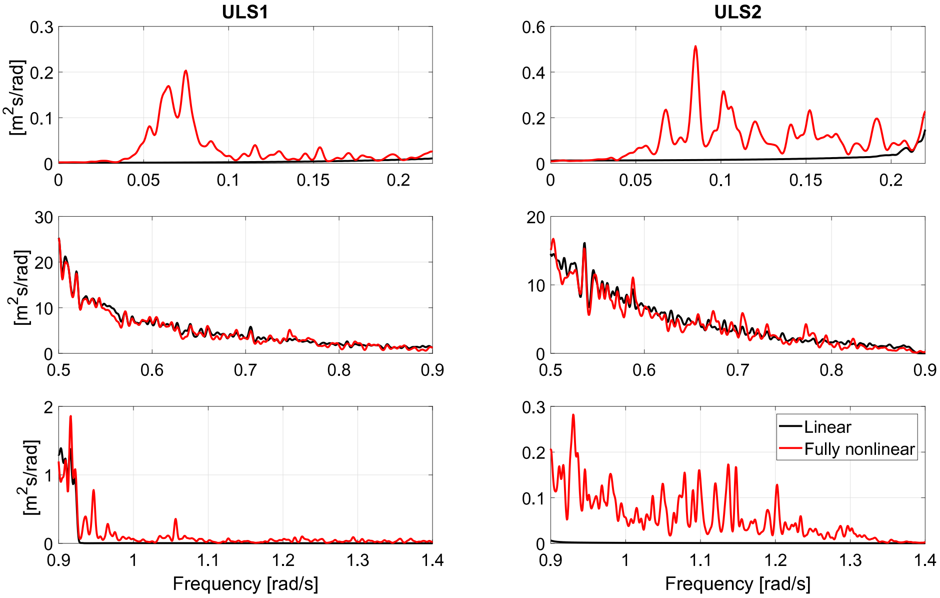

Fig. 22. Wave spectra at different frequency ranges.

energy than fully nonlinear wave when same random seed is used to generate the wave. Skewness is a measurement of the asymmetry of the maximum and minimum values of a process away from its mean value. The larger the skewness is, the shorter and more peaked the crests of the waves are while the troughs become longer and flatter. In this study, skewness is close to zero for both linear waves which means the peak and trough are equally close to the mean value. Meanwhile, the skewness is larger than zero for nonlinear waves which indicates the asymmetry of the wave profile. Larger kurtosis value for nonlinear wave on the other hand indicates higher nonlinearity than linear wave as expected.

Wave spectrum determines the energy distribution of the wave at different frequencies, which will influence the dynamic response of different natures. The linear and nonlinear spectrum of wave elevation for both cases are compared in Fig. 21. The spectral energy density are calculated for all 20 simulations and the average is used to plot the spectra to get a better representation especially for the low frequency part. The spectra at wave frequency range (ULS1: [0.3 rad/s–1 rad/s] & ULS2: [0.25 rad/s–1 rad/s]) are quite similar for linear and nonlinear wave containing most of the energy. The

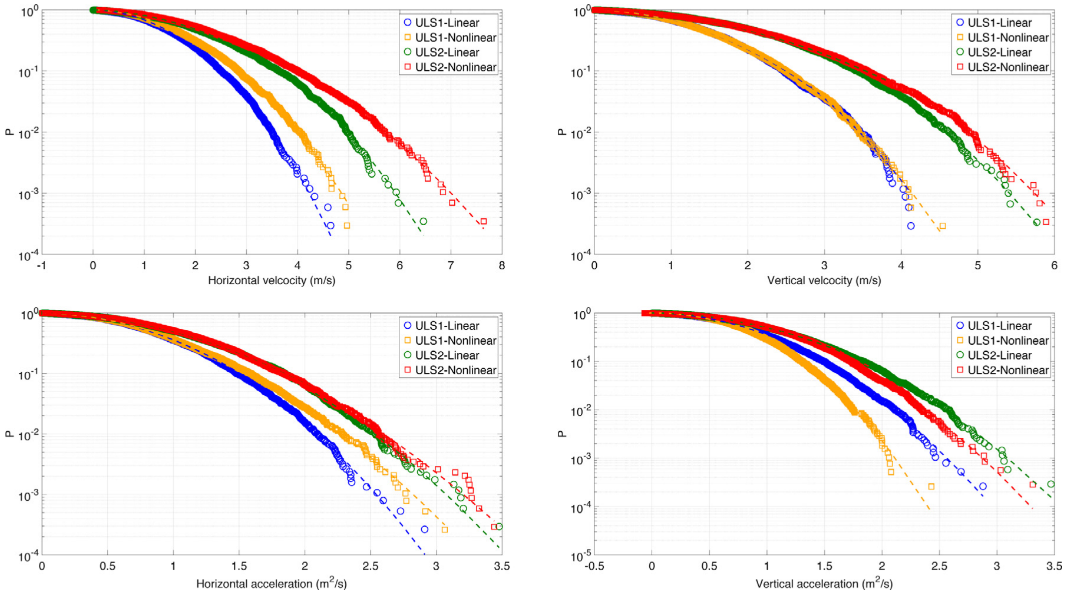

Fig. 23. Global maxima of wave kinematics at instantaneous water level above (0 m, 0 m, 0 m).

main difference is located at higher and lower frequency. The wave spectra are zoomed in at three frequency ranges as shown in Fig. 22. It is seen that linear wave tends to have more energy at range [0.5 rad/s–0.9 rad/s] than nonlinear wave. At the same time, nonlinear wave relocates more energy at higher range [0.9 rad/s–1.4 rad/s] and lower range [0 rad/s–0.2 rad/s]. Initially, the wave spectrum used for generating the irregular wave is the same for linear and fully nonlinear wave and the difference of the energy distribution in the resulting wave spectrum for different frequency range is due to nonlinear free surface effect and contact effect from seabed during wave development. Different responses are directly affected by wave energy distribution at corresponding range, such as surge motion in low frequency range and tower base shear force and bending moment at wave frequency range. The influence will be seen later in the response results.

6.4.3. Wave kinematics

The hydrodynamic wave load in HAWC2 is calculated based on Morison's equation (Eq. (11)) where wave kinematics including wave particle velocity and acceleration are the input variables. Therefore, prediction of the wave kinematics will directly affect the load calculation and further response level. Long-crested wave approximation is the basis of the wave formulation in HAWC2 which means that the wave energy propagates in one direction, i.e. 2D waves. Due to the decay of wave kinematics from free surface to seabed, the global maxima of wave kinematics at instantaneous water level above location (0 m, 0 m, 0 m) is compared in Fig. 23. In horizontal direction, linear wave model predicts smaller value for both velocity and acceleration in both conditions. At the same time, close prediction is seen for vertical velocity while linear wave model estimates higher vertical acceleration than fully nonlinear wave model.

6.4.4. Floater motion

Floater motion of a semi-submersible floating wind turbine is influenced by not only the wave-frequency wave load but also higher-order (low-frequency) wave load to a great extent. The statistics of motion response shown in Table 5 is calculated as the mean of all 20 simulations. Overall, larger motion response is observed at higher sea states as expected in Fig. 24. Little difference is found in heave and pitch motion for all the statistics from the two wave models. However, significant difference is observed for surge motion regarding mean value, maximum value and standard deviation. Linear wave model underestimates both the maximum and standard deviation for surge motion significantly.

The motion response spectra are compared in Fig. 25. For surge motion, little contribution is from wave frequency component while significant contribution is from surge resonance whose natural frequency is located between [0 rad/s–0.2 rad/s] where fully nonlinear wave contains more energy than linear wave due to energy relocation as shown in Fig. 22. Therefore, linear wave underestimates surge response compared with fully nonlinear wave, which is one of the most important findings in this paper. As for heave and pitch motion, both of them are governed by wave frequency response where linear and fully nonlinear wave contains similar energy and very little contribution is due to motion resonance. Therefore almost identical power spectra and statistics are estimated from two wave models.

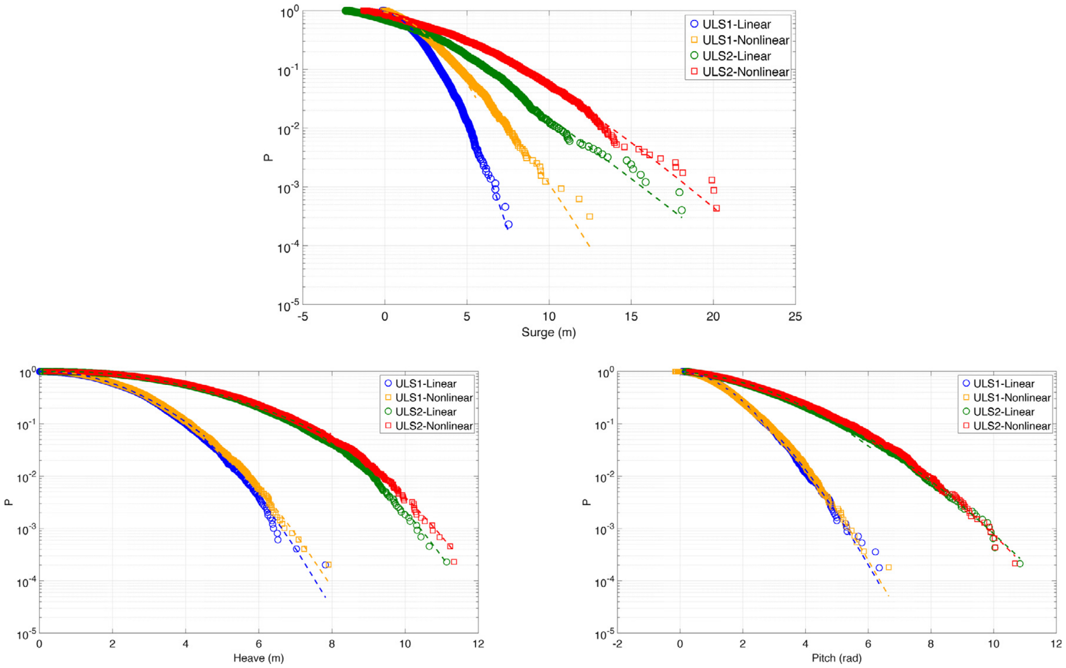

Fig. 24. Global maxima of floater motions.

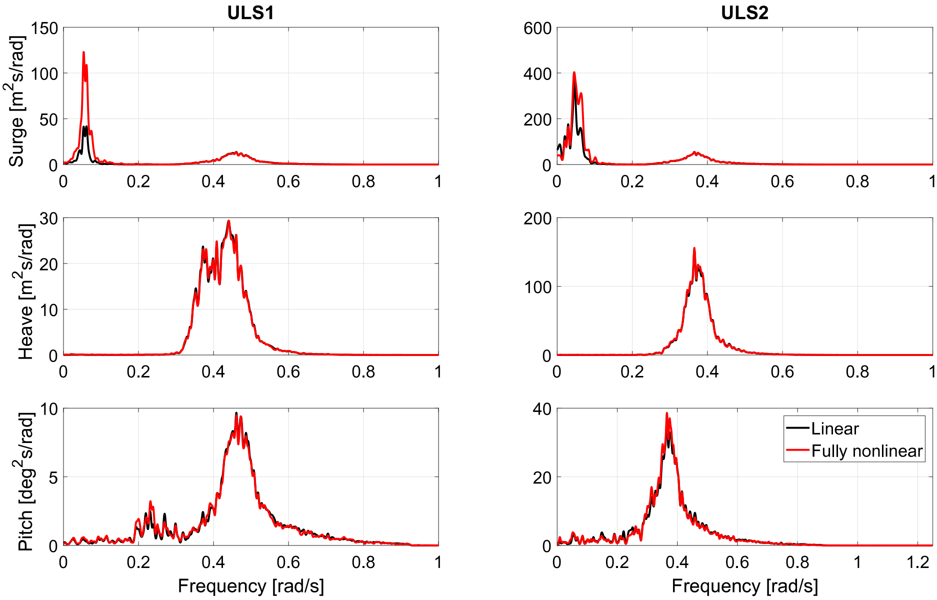

Fig. 25. Motion spectrum.

6.4.5. Tower base

The shear force and bending moment parallel to incoming wave direction at the tower base are studied in Fig. 26. It is very interesting to notice that both shear force and bending moment predicted from linear wave model are in general

Table 5
Statistics of motion response.

		ULS1 linear	ULS1 nonlinear	ULS2 linear	ULS2 nonlinear
Surge	Mean [m]	0.0981	0.126	0.921	1.96
	Maximum [m]	5.94	8.80	10.2	14.0
	Std [m]	1.56	2.10	4.09	4.41
	Skewness	0.152	0.242	−0.268	−0.0493
	Kurtosis	3.29	3.59	3.09	4.07
	Extreme 10^{-4} [m]	7.99	13.67	23.87	26.74
Heave	Mean [m]	0.0189	0.112	0.0482	0.179
	Maximum [m]	6.21	6.43	9.63	10.0
	Std [m]	1.85	1.84	3.29	3.29
	Skewness	0.0760	0.122	0.0435	0.0931
	Kurtosis	2.73	2.74	2.48	2.48
	Extreme 10^{-4} [m]	7.53	7.81	11.29	11.78
Pitch	Mean [deg]	0.0713	0.0606	0.203	0.295
	Maximum [deg]	5.13	5.10	8.70	8.86
	Std [deg]	1.19	1.18	2.10	2.11
	Skewness	0.249	0.313	0.415	0.519
	Kurtosis	3.35	3.38	3.56	3.51
	Extreme 10^{-4} [deg]	6.58	6.55	11.58	11.33

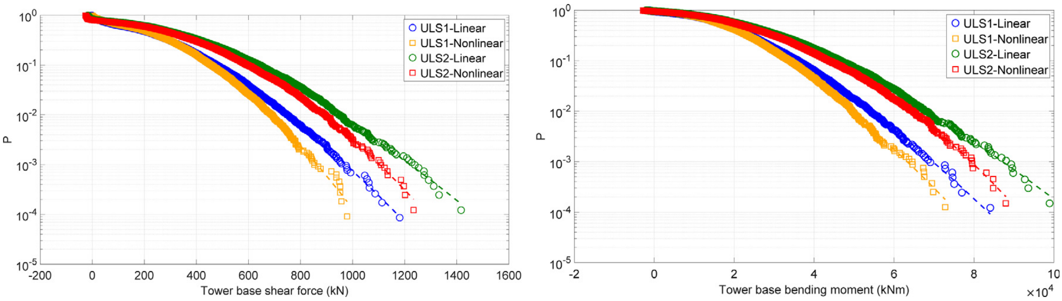

Fig. 26. Global maxima of tower base shear force and bending moment.

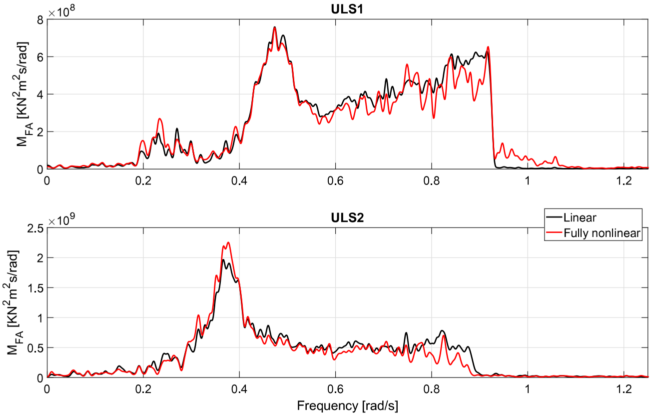

Fig. 27. Tower base bending moment spectrum.

larger than from nonlinear wave model. This is because both of them are mainly influenced by the wave frequency effect where linear wave contains more energy as shown in Fig. 22.

The power spectrum for the bending moment is compared in Fig. 27 for both conditions. More energy is located between [0.6 rad/s–0.9 rad/s] for linear wave which leads to larger response for shear force and bending moment while fully nonlinear transfers more energy to the frequency beyond cut-off limit to which tower base response is not very sensitive to.

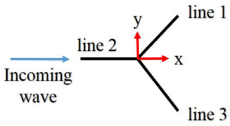

Fig. 28. Mooring configuration and incoming wave direction.

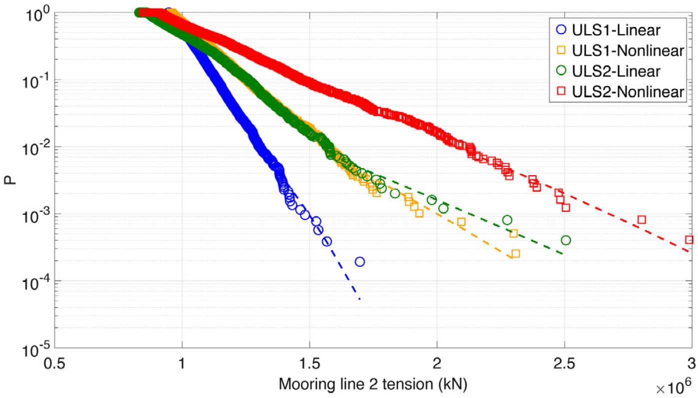
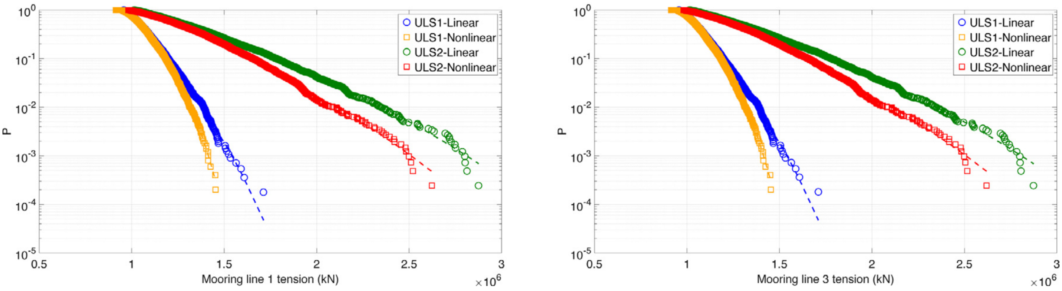

Fig. 29. Global maxima of mooring line tension.

6.4.6. *Mooring line tension*

Three mooring lines are equally spaced with angle of 120 degrees between each line as illustrated in Fig. 28 with the numbering. Maximum mooring line tension is located at fairlead which is mainly influenced by motion of the floater. The tension of the two mooring lines (line 1&3) in downwind direction are quite similar with each other. Because linear wave predicts smaller surge motion, the mooring line in downwind direction is relatively less slack than fully nonlinear wave condition which leads to higher tension response predictions. As for the upwind mooring line (line 2), since it faces incoming wave directly, the difference is quite obvious even for smaller sea state and becomes more significant for higher wave condition. The maximum, skewness and kurtosis of the tension response are listed in Table 6.

The maximum tension predicted from linear wave is smaller than from nonlinear wave in ULS1 and ULS2 condition respectively. Higher skewness and kurtosis are found for nonlinear wave model which indicates higher nonlinear and non-Gaussian property of the tension due to effects from nonlinear wave and nonlinear mooring line character. The difference is quite obvious for high sea state. Meanwhile, the combination of Rayleigh and Weibull distribution has been proved to be a really good probability model to predict the probability distribution of the tension response especially regarding the extreme response at the tail part (see Fig. 29).

The power spectrum for mooring line 2 is compared in Fig. 30. Surge resonance dominates the mooring line tension response with additional contribution from wave frequency. The difference from linear and fully nonlinear wave is more significant in the surge resonant range (low frequency range) than wave frequency range.

7. Conclusion

Fully nonlinear wave effects on OC4 semi-submersible floating wind turbine at intermediate water depth has been studied in this paper. An innovative way of dealing with big wave kinematics data is proposed and a complete simulation

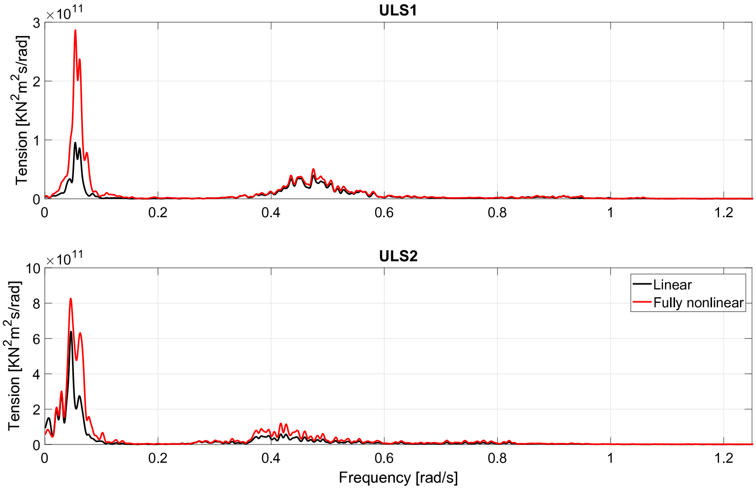

Fig. 30. Mooring line tension spectrum.

Table 6
Statistics of upwind mooring line (Line 2) tension.

	ULS1 linear	ULS1 nonlinear	ULS2 linear	ULS2 nonlinear
Mean [KN]	8.64e+05	9.12e+05	9.48e+05	9.61e+05
Maximum [KN]	1.403e+06	1.758e+06	1.706e+06	2.458e+06
Std [KN]	8.215e+04	1.130e+05	1.687e+05	2.096e+05
Skewness	0.214	1.01	0.743	1.08
Kurtosis	5.31	5.91	6.46	10.1
Extreme 10^{-4} [KN]	1.657e+06	2.438e+06	2.732e+06	3.215e+06

tool is developed which fills the gap in studying fully nonlinear wave effects on floating wind turbine in an engineering way. The comparison of global maxima for the response between linear wave model and fully nonlinear wave model illustrates the importance to consider wave nonlinear effect in hydrodynamic analysis.

In this paper, the linear irregular wave and fully nonlinear irregular wave are generated in 2D HPC numerical wave tank with linear and fully nonlinear free surface boundary conditions respectively. The HPC method once again shows its advantage regarding the accuracy and efficiency in dealing with instantaneous fully nonlinear free surface boundary conditions in time domain. It is able to provide fully nonlinear wave kinematics in an acceptable time without even using super computer.

Due to the configuration of mooring system, the wave field intended for floating wind turbine is much larger than bottom fixed wind turbine which leads to large size of wave kinematics data files. In order to solve the memory barrier of HAWC2 when reading pre-generated wave kinematics file, a polynomial fitting method is proposed to scale down the data size to meet the memory requirement. The wave kinematics is fitted into polynomial functions representing location coordinates associated with polynomial coefficients, which expresses wave kinematics information in a function manner instead of exact value. The fitting polynomial result is checked with original data from wave tank and the accuracy of using the polynomial function in time domain simulation is also verified with a regular wave case study against HAWC2 default wave.

The external dynamic link library used to provide wave kinematics to HAWC2 is extended from one dimensional (Wkin.dll 2.4) to two dimensional (Wkin.dll 2D). The development includes the variation of wave kinematics along horizontal direction which is relevant for floating wind turbine. The fully nonlinear wave kinematics is imported through the extended DLL to HAWC2 in the form of polynomial coefficients. Wkin.dll 2D receives location coordinates from HAWC2 and sends back the exact wave kinematics value for hydrodynamic wave load calculation.

Two irregular wave sea states representing extreme environmental conditions are compared to study fully nonlinear wave effects. Fully nonlinear irregular wave is compared with linear irregular wave generated with same random seed. The wave elevation is clearly underestimated by linear wave model especially for higher sea states. This could be in addition relevant for air gap analysis of offshore oil and gas platform. The different energy distribution is observed from the wave spectrum between linear and nonlinear wave. The nonlinear wave is able to capture contribution from higher and lower range than wave frequency. Comparatively, more energy is relocated by linear wave to the range slightly higher than wave frequency. Higher shear force and bending moment at tower base predicted from linear wave than fully nonlinear wave is a result of this energy distribution. Heave and pitch motion of the floater are predicted quite close with different wave models since they are mainly wave-frequency load dominating. However, surge motion and mooring line tension which in addition are also greatly influenced by low-frequency wave load is underpredicted using linear wave model. It is well explained by the motion response spectrum with respect to wave spectrum. High nonlinear and non-Gaussian property is captured by nonlinear wave especially when sea states becomes more extreme.

In conclusion, the paper not only proves the importance to include fully nonlinear wave effect in hydrodynamic analysis for floating wind turbine exposed to high sea states in shallow and intermediate water depth but also provides a corresponding engineering practical solution.

Acknowledgment

The first author gratefully acknowledges the financial support from China Scholarship Council.

References

Bai, W., Hannan, M., Ang, K., 2014. Numerical simulation of fully nonlinear wave interaction with submerged structures: Fixed or subjected to constrained motion. J. Fluids Struct. 49, 534–553.

Borg, M., Hansen, A.M., Bredmose, H., 2016. Floating substructure flexibility of large-volume 10 MW offshore wind turbine platforms in dynamic calculations. J. Phys. 753.

Bredmose, H., 2013. Fully nonlinear wave forcing of a TLP wind turbine. Deliverable report 4.21 on INNWIND.EU, DTU.

Carrión, M., Steijl, R., Woodgate, M., Barakos, G., Munduate, X., Gomez-Iradi, S., 2014. Aeroelastic analysis of wind turbines using a tightly coupled CFD–CSD method. J. Fluids Struct. 50, 392–415.

Cummins, W.E., 1962. The impulse response function and ship motions. In: Symposium on Ship Theory. University Hamburg.

DNVGL, 2017. DNV-RP-C205 Environmental Conditions and Environmental Loads.

Engsig-Karup, A.P., Bingham, H.B., Lindberg, O., 2009. An efficient flexible-order model for 3D nonlinear water waves. J. Comput. Phys. 228, 2100–2118.

Faltinsen, O.M., Timokha, A.N., 2009. Sloshing. Cambridge University Press.

Fu, P., Leira, B.J., Myrhaug, D., 2017. Reliability analysis of wake-induced collision of flexible risers. Appl. Ocean Res. 62, 49–56.

Gibson, R., Swan, C., 2006. The evolution of large ocean waves: the role of local and rapid spectral changes. Proc. R. Soc. A 463 (2077), 21–48.

Hansen, M.H., Gaunaa, M., Madsen, H.A., 2004. A Beddoes-Leishman type dynamic stall model in state-space and indicial formulations. Risø National Laboratory.

Jonkman, J.M., 2009. Dynamics of offshore floating wind turbines model development and verification. Wind Energy 12 (5), 459–492.

Kallesøe, B.S., Hansen, A.M., 2011. Dynamic mooring line modeling in hydro-aero-elasticwind turbine simulations. In: The Twenty-First International Offshore and Polar Engineering Conference.

Karimirad, M., Meissonnier, Q., Gao, Z., Moan, T., 2011. Hydroelastic code-to-code comparison for a tension leg spar-type floating wind turbine. Mar. Struct. 24 (4), 412–435.

Kim, B.W., Sung, H.G., Kim, J.H., Hong, S.Y., 2013. Comparison of linear spring and nonlinear FEM methods in dynamic coupled analysis of floating structure and mooring system. J. Fluids Struct. 42, 205–227.

Larsen, T.J., Hansen, A.M., 2007. How 2 HAWC2, the user's manual. Risø National Laboratory.

Larsen, T.J., Kim, T., Schløer, S., Bredmose, H., 2011. Comparisons of wave kinematics models for an offshore wind turbine mounted on a jacket substructure. In: Proceedings European Wind Energy Association (EWEA).

Li, L., Gao, Z., Moan, T., 2015. Joint distribution of environmental condition at five european offshore sites for design of combined wind and wave energy devices. J. Offshore Mech. Arctic Eng. 137.

Liang, H., Faltinsen, O.M., Shao, Y.-L., 2015. Application of a 2D harmonic polynomial cell (HPC) method to singular flows and lifting problems. Appl. Ocean Res. 53, 75–90.

Matha, D., Schlipf, M., Cordle, A., Pereira, R., Jonkman, J., 2011. Challenges in simulation of aerodynamics, hydrodynamics, and mooring-line dynamics of floating offshore wind turbines. In: 21st Offshore and Polar Engineering Conference.

Nematbakhsh, A., Bachynski, E.E., Gao, Z., Moan, T., 2015. Comparison of wave load effects on a TLP wind turbine by using computational fluid dynamics and potential flow theory approaches. J. Appl. Ocean Res. 53, 142–154.

Ning, D., Teng, B., 2007. Numerical simulation of fully nonlinear irregular wave tank in three dimension. Internat. J. Numer. Methods Fluids 53, 1847–1862.

Øye, S., 1996. FLEX4 simulation of wind turbine dynamics. In: Proceedings for the 28th IEA Meeting of Experts Concerning State of the Art of Aero-Elastic Codes for Wind Turbine Calculations.

Pegalajar-Jurado, A., Borg, M., Robertson, A., Jonkman, J., Bredmose, H., 2017. Effect of second-order and fully nonlinear wave kinematics on a tension-leg-platform wind turbine in extreme wave conditions. In: 36th International Conference on Ocean, Offshore and Arctic Engineering.

Robertson, A.N., Jonkman, J.M., Masciola, M.D., Molta, P., Goupee, A.J., Coulling, A.J., Prowell, I., Browning, J., 2013. Summary of conclusions and recommendations drawn from the deepcwind scaled floating offshore wind system test campaign. In: 32nd International Conference on Ocean, Offshore and Arctic Engineering.

Robertson, A., Jonkman, J., Masciola, M., Song, H., Goupee, A., Coulling, A., Luan, C., 2014a. Definition of the Semisubmersible Floating System for Phase II of OC4. NREL technical report.

Robertson, A., Jonkman, J., Vorpahl, F., Popko, W., Qvist, J., Froyd, L., Chen, X., Azcona, J., Uzungoglu, E., Guedes Soares, C., et al., 2014b. Offshore code comparison collaboration continuation within IEA wind task 30: Phase II results regarding a floating semi-submersible wind system. In: Proceeding of 33rd International Conference on Ocean, Offshore and Arctic Engineering, vol. 9B.

Santo, H., Taylor, P., Williamson, C., 2018. On the morison hydrodynamic forces on perforated flat plates in combined steady, low frequency and high frequency motion. J. Fluids Struct. 81, 514–527.

Schløer, S., Bredmose, H., Bingham, H.B., 2011. Irregular wave forces on monopile foundations. Effect af full nonlinearity and bed slope. In: 30th International Conference on Ocean, Offshore and Arctic Engineering, vol. 5. American Society of Mechanical Engineers. pp. 581–588.

Schløer, S., Bredmose, H., Bingham, H.B., 2012. The influence of fully nonlinear wave forces on aero-hydro-elastic calculations of monopile wind turbines. In: Proceedings of the ASME 31st International Conference on Ocean, Offshore and Arctic Engineering, vol. 7. pp. 393–402.

Schløer, S., Bredmose, H., Bingham, H.B., 2016. The influence of fully nonlinear wave forces on aero-hydro-elastic calculations of monopile wind turbines. Mar. Struct. 50, 162–188.

Shao, Y.-L., Faltinsen, O.M., 2012. Towards efficient fully-nonlinear potential-flow solvers in marine hydrodynamics. In: ASME 2012 31st International Conference on Ocean, Offshore and Arctic Engineering. American Society of Mechanical Engineers, pp. 369–380.

Shao, Y.-L., Faltinsen, O.M., 2014a. Fully-nonlinear wave-current-body interaction analysis by a harmonic polynomial cell method. J. Offshore Mech. Arct. Eng. 136 (3), 031301.

Shao, Y.-L., Faltinsen, O.M., 2014b. A harmonic polynomial cell (HPC) method for 3D Laplace equation with application in marine hydrodynamics. J. Comput. Phys. 274, 312–332.

Stansberg, C.T., Gudmestad, O.T., Haver, S.K., 2008. Kinematics under extreme waves. J. Offshore Mech. Arct. Eng. 130 (2), 021010.

A.5 Paper 5

Paper 5:
Effect of wave nonlinearity on fatigue damage and extreme responses of a semi-submersible floating wind turbine.
Authors: Kun Xu, Min Zhang, Yanlin Shao, Zhen Gao, Torgeir Moan
Published in *Applied Ocean Research*, 2019
DOI: https://doi.org/10.1016/j.apor.2019.101879

Applied Ocean Research 91 (2019) 101879

Contents lists available at ScienceDirect

Applied Ocean Research

journal homepage: www.elsevier.com/locate/apor

Effect of wave nonlinearity on fatigue damage and extreme responses of a semi-submersible floating wind turbine

Kun Xu[a,*], Min Zhang[b], Yanlin Shao[c,d], Zhen Gao[a,e,f], Torgeir Moan[a,e,f]

[a] Department of Marine Technology, Norwegian University of Science and Technology (NTNU), Trondheim 7491, Norway
[b] Shandong Provincial Key Lab of Ocean Engineering, Ocean University of China, Qingdao 266100, China
[c] Department of Mechanical Engineering, Technical University of Denmark, 2800 Kgs. Lyngby, Denmark
[d] Shipbuilding Engineering Institute, Harbin Engineering University, 150001 Harbin, China
[e] Centre for Ships and Ocean Structures (CESOS), NTNU, Trondheim 7491, Norway
[f] Centre for Autonomous Marine Operations and Systems (AMOS), NTNU, Trondheim 7491, Norway

ARTICLE INFO

Keywords:
Fully nonlinear wave effect
Floating wind turbine
Extreme value
Fatigue damage

ABSTRACT

Floating wind turbine has been the highlight in offshore wind industry lately. There has been great effort on developing highly sophisticated numerical model to better understand its hydrodynamic behaviour. A engineering-practical method to study the nonlinear wave effects on floating wind turbine has been recently developed. Based on the method established, the focus of this paper is to quantify the wave nonlinearity effect due to nonlinear wave kinematics by comparing the structural responses of floating wind turbine when exposed to irregular linear Airy wave and fully nonlinear wave. Critical responses and fatigue damage are studied in operational conditions and short-term extreme values are predicted in extreme conditions respectively. In the operational condition, wind effects are dominating the mean value and standard deviation of most responses except floater heave motion. The fatigue damage at the tower base is dominated by wind effects. The fatigue damage for the mooring line is more influenced by wind effects for conditions with small wave and wave effects for conditions with large wave. The wave nonlinearity effect becomes significant for surge and mooring line tension for large waves while floater heave, pitch motion, tower base bending moment and pontoon axial force are less sensitive to the nonlinear wave effect. In the extreme condition, linear wave theory underestimates wave elevation, floater surge motion and mooring line tension compared with fully nonlinear wave theory while quite close results are predicted for other responses.

1. Introduction

A significant development of floating wind technology has been witnessed over the last decade. To achieve wind turbines which are safe and serviceable, numerical methods which balance accuracy and efficiency are needed. For instance, high-fidelity numerical methods such as computational-fluid-dynamics (CFD) model and fully nonlinear wave model have been developed to deal with the hydrodynamic loading on wind turbine.

The hydrodynamic analysis of an offshore structure normally consists of determining the sea states at the relevant site depth; selecting applicable wave theory; choosing appropriate hydrodynamic load computation method; calculating structural response. Since offshore wind farms are normally deployed at relatively shallow water area where wave becomes more nonlinear and will lead to a considerable increase of hydrodynamic loads, wave nonlinearity and water depth therefore are two keywords in the hydrodynamic analysis for both bottom-fixed and floating wind turbine.

Wave nonlinearity according to Gibson and Swan [1], can be divided into higher-order bound nonlinearity and resonant nonlinearity at third order and above. The bound nonlinearities in regular waves are the higher-order terms derived by Stokes [2] which are phase locked to the corresponding linear wave component and intend to sharpen the wave peak and broaden the wave trough. Meanwhile, the resonant nonlinearity tends to redistribute the wave spectral energy by exchanging energy between various wave components when the interaction between wave components satisfies the dispersion relationship. As a result, more spectral energy of nonlinear wave are relocated to higher and lower frequency. Camp et al. [3] investigates the overturning moment of a monopile wind turbine based on linear wave theory and stream function wave at 6 m and 21 m water depths. For the same wave height, significant underestimation is found using linear wave and the

---

[*] Corresponding author.
E-mail addresses: kun.xu@ntnu.no (K. Xu), violet@ouc.edu.cn (M. Zhang).

https://doi.org/10.1016/j.apor.2019.101879
Received 6 May 2019; Received in revised form 29 June 2019; Accepted 17 July 2019
0141-1187/ © 2019 The Authors. Published by Elsevier Ltd. This is an open access article under the CC BY-NC-ND license
(http://creativecommons.org/licenses/BY-NC-ND/4.0/).

difference increases as water depth decreases. Schløer et al. [4] compared the wave loads on monopile foundation using linear and fully nonlinear irregular waves. Redistribution of energy between free and bound components in the nonlinear wave spectra is clearly observed and more energy at the first natural frequency is found in linear wave spectra, which greatly influences the fatigue calculation. For large sea states, the difference between linear and nonlinear extreme wave loads appears to be quite large. The influence of varying water depth on the wave-induced structural behaviour is studied by Li et al. [5] by comparing mooring line tension response at 500 m, 1000 m and 1500 m with same mooring line material. As the water depth decreases, the non-Gaussian property of mooring line tension response increases significantly. Therefore, even stronger non-Gaussianity of mooring line tension is expected for floating wind turbines at shallower water depth. The dynamic structural response of offshore structures in different environmental conditions is the driving factor in the design process. The ultimate structural response and fatigue damage of a spar floating wind turbine has been studied by Li et al. [6]. Mean up-crossing rate method is used to predict the extreme response while S-N curve method is used to calculate the fatigue damage.

The objective of this paper is to investigate the effect of wave nonlinearity by comparing the structural response of a semi-submersible floating wind turbine between linear wave theory and fully nonlinear wave theory. The numerical code to implement fully nonlinear wave kinematics in the irregular stochastic wave train was recently developed and verified by Xu et al. [7]. In this paper, the fatigue damage is calculated for tower base and mooring line in operational conditions and the extreme values are predicted for critical responses in extreme conditions.

2. Methodology

2.1. Floating wind turbine model

The floating wind turbine selected for this study is the OC4 semi-submersible wind turbine at 200 m water depth which was developed in the International Energy Agency (IEA) Wind Task 30 Offshore Code Comparison Collaboration Continuation (OC4) project. The semi-submersible platform consists of four columns connected by smaller pontoons and braces as illustrated in Fig. 1. A NREL 5MW wind turbine is mounted on top whose cut-in, rated and cut-out wind speed are: 3 m/s, 11.4 m/s and 25 m/s respectively. Three catenary mooring lines are connected at the top of the base columns at a depth of 14 m below the still water level. More details about the structure are given in Robertson et al. [8].

2.2. Fully coupled dynamic analysis

The fully coupled time-domain analysis is performed using HAWC2 (Horizontal Axis Wind turbine simulation Code 2nd generation) which is developed at DTU Wind Energy by Larsen and Hansen [9]. It is able to capture the nonlinear coupling effect from aerodynamics, hydrodynamics, structural dynamics, mooring line dynamics and control system dynamics. The floating wind turbine is divided into several bodies and each body is modeled with a number of Timoshenko beam elements. The turbulent wind field is generated with the Mann model [10]. The hydrodynamic forces acting on the floater and mooring line are calculated based on the Morison's formula.

$$dF = \rho\frac{\pi D^2}{4}dzC_M a_n + \rho\frac{\pi D^2}{4}dz(C_M - 1)a_c + \frac{\rho}{2}C_D Ddz|u_{\text{rel}}|u_{n,\text{rel}} \tag{1}$$

where D is the cylinder diameter, a_n is the undisturbed wave induced acceleration components normal to the cylinder axis, a_c is the normal component of cylinder acceleration, $u_{n,rel}$ is the component of the relative velocity normal to the cylinder, C_M and C_D are the mass and drag coefficients. The wave kinematics of the Morison's equation is provided by an external dynamic link library – *wkin_d ll*. In the original version *wkin 2.4*, importing external wave field is limited to one dimension (vertical) which is intended for bottom fixed wind turbine. It was extended by Xu et al. [7] to two dimensions (both vertical and horizontal) in *wkin 2D* which can apply external wave kinematics on floating wind turbine and its mooring system.

2.3. Wave generation and polynomial fitting

The linear and fully nonlinear irregular waves are generated in the 2D Harmonic Polynomial Cell (HPC) numerical wave tank developed by Shao and Faltinsen [11] and Shao and Faltinsen [12] with linear and fully nonlinear free surface boundary conditions respectively. It was improved by Liang et al. [13] regarding singular flows and discontinuous problems. HPC method is able to solve the velocity potential in each cell by dividing the fluid domain into quadrilateral cells associated with harmonic polynomials. An explicit 4th order Runge–Kutta method is used to update wave elevation and velocity potential on the free surface at each time step. A free surface filter is applied to model nonlinear steep wave to avoid numerical instability.

Because of the large footprint of floating wind turbine, the relevant wave field is also quite large which leads to huge database for the wave kinematics data including wave elevation, particle velocity and acceleration in horizontal and vertical directions. In order to use the kinematics data in HAWC2 and limit the need for memory, the kinematics data at discrete grid points are further processed to polynomial coefficients as shown in Fig. 2. The exact value of wave kinematics is consequently replaced by 2D polynomial coefficients up to a certain order

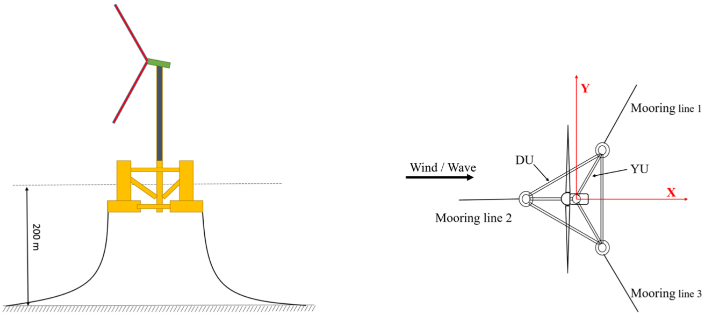

Floating wind turbine

Mooring system

Fig. 1. OC4 semi-submersible floating wind turbine. (a) Floating wind turbine. (b) Mooring system.

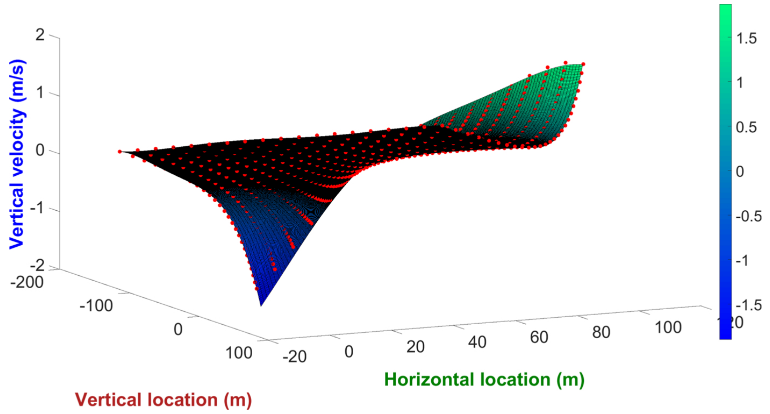

Fig. 2. Polynomial fitting of wave kinematics.

with location coordinates as input variables. The details about the polynomial fitting method are described by Xu et al. [7].

2.4. Fatigue damage calculation

Fatigue analysis in frequency domain has been developed and verified with acceptable accuracy and efficiency by Gao and Moan [14]. However, due to the complicated interaction between different parts of the structures and nonlinearity of the response, the fatigue analysis for floating wind turbine is preferably performed in the time domain despite the computational efforts required. A comprehensive fatigue assessment of a semi-submersible floating wind turbine in the time domain has been conducted by Kvittem and Moan [15] which focuses on the influence of simulation length, seed number, wind-wave misalignment, wave-wind dominating role and bin size of environmental conditions on fatigue prediction. However, the irregular wave trains used are based on linear wave theory, therefore the effect due to wave nonlinearity was not studied.

The total structural fatigue damage can be determined as the sum of the fatigue damage that arises from each individual design sea state. The damage for each sea state can be calculated based on Miner-Palmgren hypothesis by adding together the damage from each stress or tension level.

$$D = \sum_{j}^{N_{\text{total}}} \frac{n_j}{N_j} \tag{2}$$

where n_j is the number of cycles at the jth stress range in the time history and N_j is the number of cycles to failure at corresponding stress range according to the design curve. According to Wöhler, the number of cycles until fatigue failure (N) is given by:

$$N = \mathrm{KS}^{-m} \quad \text{or} \quad N = \mathrm{KT}^{-m} \tag{3}$$

where N is the number of permissible cycles of stress or tension range, K is the coefficient in the curve, m is the inverse slope factor and S is the stress range while T is the tension range in the time history. Normally, number of cycles to failure for high level stress cycles is fewer compared to lower level stress cycles. If the applied stress level is below the endurance limit of the material, the structure is assumed to be able to function infinitely. Therefore a two-sloped S-N curve is normally preferred to account for different stress levels.

The fatigue assessment in this paper is carried out in the time domain using Rainflow counting method to count the cycles. The fatigue damage at the tower base due to axial stress is calculated using S-N curve method. The coordinate system for tower base is illustrated in Fig. 3 and the nominal axial stress at tower base for a location (r, θ) is calculated as:

$$\sigma = \frac{N_x}{A} + \frac{M_y}{I_y} r\cdot\sin\theta + \frac{M_z}{I_z} r\cdot\cos\theta \tag{4}$$

where N_x is the axial force, M_y and M_z are moment about local y- and z-axis respectively, A is the area of the cross section, θ is the angle of the point for fatigue analysis. In general, all locations on the cross section should be considered for fatigue damage calculation. Since wind and wave are aligned in this paper, it is sufficient to take the point on the out radius with $\theta = 270^\circ$ as an example for fatigue evaluation.

The parameter used in the S-N curve is defined as in Eq. (5) and given in Table 1, where N is the number of cycles, t is the thickness, $\Delta\sigma$ is the stress range and the stress concentration factor is set to 1 for simplicity. The fatigue damage for mooring line is calculated using T-N curve method based on API [16]. The parameters defined in Eq. (3) are given in Table 2. The mooring line type studied in this paper is assumed to be studless.

$$\log \mathrm{N} = \log \bar{a} - \mathrm{m}\log\left(\Delta\sigma\left(\frac{t}{t_{\mathrm{ref}}}\right)^{k}\right) \tag{5}$$

2.5. Extreme value prediction

Take a random stochastic process $X(t)$ over a time period T as an example. The extreme value of the process is defined as the largest maximum from a sequence of individual maxima

$$X_e = \max\{X_{m1}, X_{m2}, \ldots, X_{mn}\} \tag{6}$$

where X_e stands for the largest maximum value and X_{mi} represents the individual maxima as shown in Fig. 4. Based on the assumption that all the individual maxima are independent and identically distributed with a common distribution function $F_{Xm}(x)$, the distribution for X_e is described as:

$$F_{\mathrm{Xe}}(x) = \mathrm{Prob}\{X_e \le x\} = [F_{\mathrm{Xm}}(x)]^n \tag{7}$$

Several methods have been developed for predicting the extreme value distribution, while two of them are used in this paper: type I asymptotic extreme value distribution i.e. the Gumbel fitting method and ACER (average conditional exceedance rate) method.

2.5.1. Gumbel fitting method

When the sample number n is large enough, the extreme value distribution Eq. (7) has been proved that it will converge towards one of three types of distributions: Gumbel, Fréchet and Weibull also known as type I, II and III extreme value distributions whose cumulative

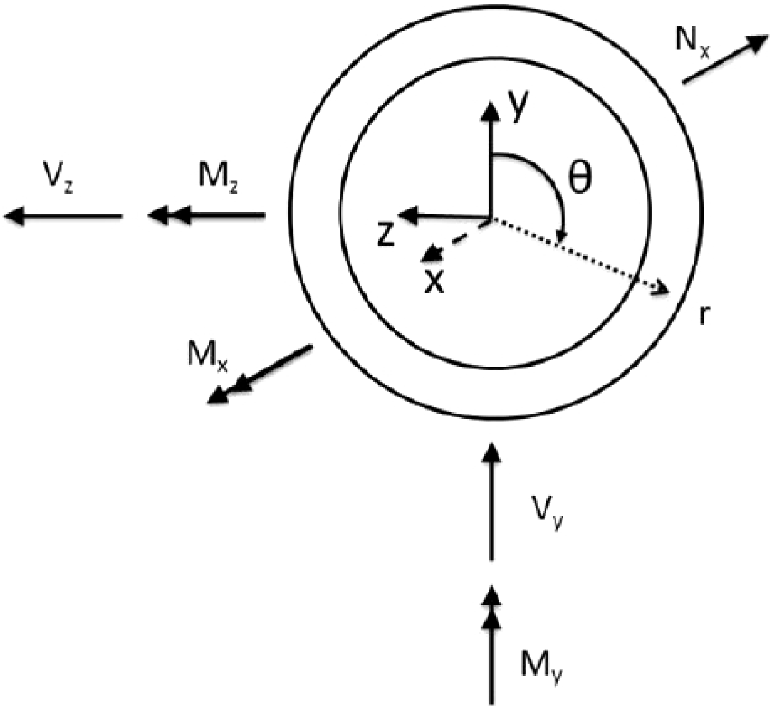

Fig. 3. Coordinate system for tower base fatigue damage calculation.

Table 1
S-N curve parameter for tower base.

$N \le 10^7$ cycles		$N > 10^7$ cycles		Fatigue limit at 10^7 cycles	k	t_{ref}
m	$\log \bar{a}$	m	$\log \bar{a}$	[MPa]		[mm]
3.0	12.164	5.0	15.606	52.63	0.20	25

Table 2
T-N curve parameter for mooring line.

Component	M	K
Studlink	3.0	1000
Studless link	3.0	316

distribution probability can be assembled as the generalized extreme value (GEV) distribution:

$$F_{\mathrm{Xe}}(x) = \exp\left\{-1 + \gamma\left(\frac{x-\mu}{\sigma}\right)^{-\frac{1}{\gamma}}\right\} \tag{8}$$

Here μ is the location parameter and σ is the scale parameter and γ is the shape parameter. The limiting case when $\gamma \rightarrow 0$ will result in the Gumbel distribution which is the most recommended model for marine structures [17].

$$F_{\mathrm{Xe}}(x) = \exp(-\exp(-\alpha(x-\mu))) \tag{9}$$

where α is the scale parameter and μ is the location parameter which can be determined by Gumbel probability paper method. Rewrite Eq. (9) with logarithm of both sides, a linear function is introduced as:

$$-\ln[-\ln(F_{\mathrm{Xe}}(x))] = \alpha(x-\mu) \tag{10}$$

The cumulative distribution probability is represented with a straight line in the probability paper where parameters α and μ can be estimated by the least-square fitting method of the original sample data [18]. An example of Gumbel probability paper for extreme wave elevation is shown in Fig. 5.

2.5.2. Average conditional exceedance rate method

The average conditional exceedance rate (ACER) method proposed by Næss and Gaidai [19] predicts the exact extreme value distribution by building up a sequence of non-parametric distribution functions known as ACER functions instead of the parametric distribution functions. It considers all the global maxima peaks while the dependence between successive peaks in a sampled time-series are taken into account as well which makes it available for both the stationary and non-stationary process. It has been used by Cheng et al. [20] to predict extreme structural responses for floating vertical axis wind turbines.

The extreme value probability distribution according to ACER method is written as:

$$F_{\mathrm{Xe}}(x) \approx P_k(x) \approx \exp\{-(N-k+1)\hat{\varepsilon}(x)\} \tag{11}$$

where k is the order of the ACER function which represents the immediately preceding non-exceedances, $\hat{\varepsilon}(x)$ is the empirical ACER function of order k which is determined by fitting available global maxima peaks from time series [21].

The empirical ACER function follows the form:

$$\hat{\varepsilon}(x) = q_k \cdot \exp\{-a_k(x-b_k)^{c_k}\}, \quad x \ge x_0 \tag{12}$$

Due to the fact that the ACER function behaves close to $\exp\{-a(x-b)^c\}$ in the upper tail region, the coefficients a_k, b_k, c_k and q_k depending on the order k can be determined by extrapolation using mean-square-error function:

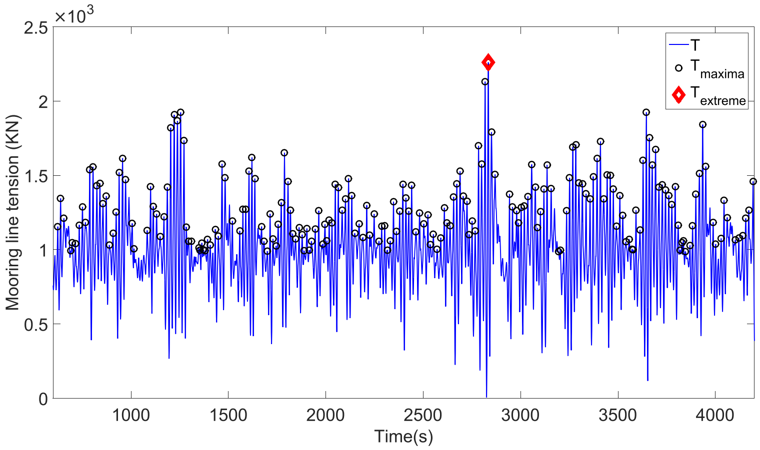

Fig. 4. Global maxima and extreme peak.

$$F(q_k, a_k, b_k, c_k) = \sum_{i=1}^{N} \rho_j |\ln \hat{\varepsilon_k}(x_{\mathrm{mi}}) - \ln q + a(x_{\mathrm{mi}-b})^c|^2 \tag{13}$$

The weight factor ρ_j is described as $\rho_j = (\ln CI^+(x_i) - \ln CI^-(x_i))^{-2}$ where it represents the 95% confidence interval:

$$\mathrm{CI}^{\pm}(x_{\mathrm{mi}}) = \hat{\varepsilon_k}(x_{\mathrm{mi}})\left\{\frac{1.96}{\sqrt{(N-k+1)\hat{\varepsilon_k}(x_{\mathrm{mi}})}}\right\} \tag{14}$$

An example of the ACER function for extreme wave elevation in LC7 condition with linear wave model is given in Fig. 6 representing the empirical ACER function for different orders of k from 1 to 6. The estimated confidence interval for ACER function with $k = 1$ is plotted in Fig. 7.

3. Load cases and environmental conditions

The focus of this paper is to quantify the difference due to wave nonlinearity rather than perform a realistic design of offshore wind turbine, so a series of representative load cases with turbulent wind and irregular wave are selected for the calculation of fatigue load and extreme load respectively. The environmental conditions are determined based on the wind and wave data at Statfjord site in the Northern North Sea. A joint wind and wave distributions was established by Johannessen et al. [22] considering 1-h mean wind speed at 10 m above sea water level (U_{10}), the significant wave height (H_s) and the spectral peak period (T_p).

$$f_{U_{10}H_sT_p}(u_{10}, h_s, t_p) = f_{U_{10}}(u_{10})\cdot f_{H_s|U_{10}}(h_s|u_{10})\cdot f_{T_p|H_sU_{10}}(t_p|h_s, u_{10}) \tag{15}$$

The joint distribution representing 100-year wind and 100-year wave condition consists of a marginal distribution of wind speed U_{10}, a conditional distribution of H_s for given U_{10} and a conditional distribution of T_p for given U_{10} and H_s. Design wind speed is first determined and the expected significant wave height can then be calculated based on the conditional distribution of H_s for given U_{10} which is a two-parameter Weibull distribution. Likewise, the expected spectral peak period T_p can then be calculated according to the conditional distribution of T_p for given H_s and U_{10} as a log-normal distribution proposed by Johannessen et al. [22].

The wind speed considered in this paper ranges from cut-in, rated and cut-out wind speed with a bin size of 4 m/s. The three dimensional turbulent wind fields are generated using turbulent model by Mann

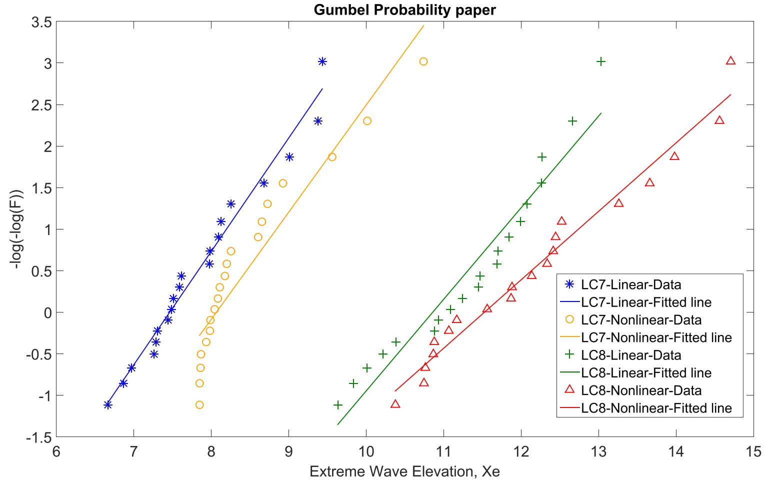

Fig. 5. Gumbel probability paper for extreme wave elevation.

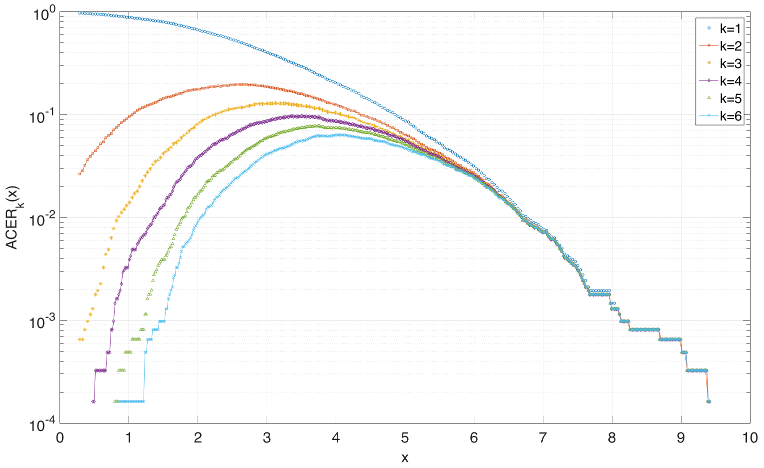

Fig. 6. ACER function for $k = 1, 2, \ldots, 6$.

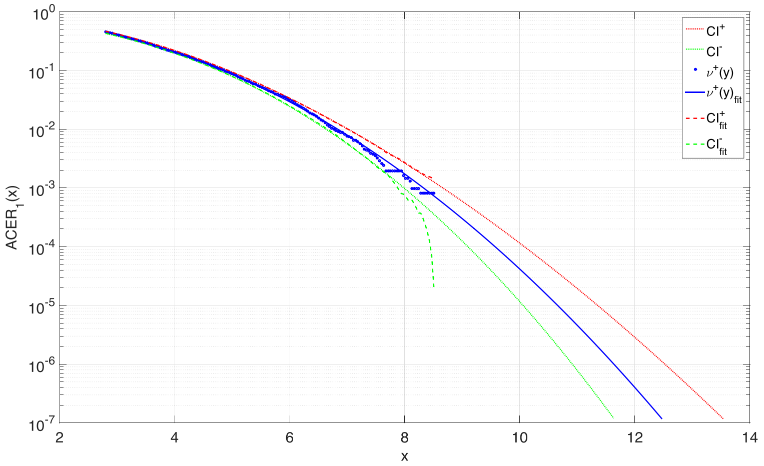

Fig. 7. Confidence interval for ACER function with $k = 1$.

Table 3
Load cases.

	U_w [m/s]	T_I	H_s [m]	T_p [s]	Seeds	Simulation length [s]	Turbine status
LC1	4	0.258	1.96	9.72	10	4200	Operational
LC2	8	0.174	2.53	9.85	10	4200	Operational
LC3	12	0.146	3.20	10.11	10	4200	Operational
LC4	16	0.132	3.97	10.44	10	4200	Operational
LC5	20	0.124	4.80	10.82	10	4200	Operational
LC5_2	24	0.118	4.80	10.82	10	4200	Operational
LC6	24	0.118	5.69	11.23	10	4200	Operational
LC6_2	20	0.124	5.69	11.23	10	4200	Operational
LC7	40	0.110	9.77	12.95	20	4200	Parked
LC8	60	0.094	15.75	15.10	20	4200	Parked

[10] while the turbulence intensity is determined according to IEC Class C IEC [23]. The vertical wind shear as the variation of the mean wind speed U_z with height z above the ground is considered using the normal wind profile model proposed in IEC [24]:

$$U(z) = U_{\mathrm{ref}}\left(\frac{z}{z_{\mathrm{ref}}}\right)^{\alpha} \tag{16}$$

where U_{ref} is the reference wind speed and z_{ref} is the height of the reference wind speed and α is the power law coefficient. The reference height is set to 90 m above mean water level as the center of totor and α was chosen to be 0.14 for floating wind turbine based on IEC [24]. The irregular linear and fully nonlinear wave trains are then generated based on JONSWAP spectrum with given H_s and T_p. As a result, a set of load cases with correlated wind and wave are available as given in Table 3. The most probable normal operational conditions with directionally aligned wind and wave are labeled as LCs 1–6 while LCs 7–8 are extreme conditions where wind turbine is under parked condition. In addition, two more operational conditions with specific wind and wave parameters are chosen to study the wind and wave effect labeled as LC5_2 and LC6_2.

All the simulations are run for 4200 s while the transient phase at first 600 s is eliminated to get a 1-h simulation. For the operational conditions, ten different random seeds of wind and wave are applied for each sea states while twenty random seeds of wave are used for the two extreme conditions in order to obtain a proper prediction of the extreme

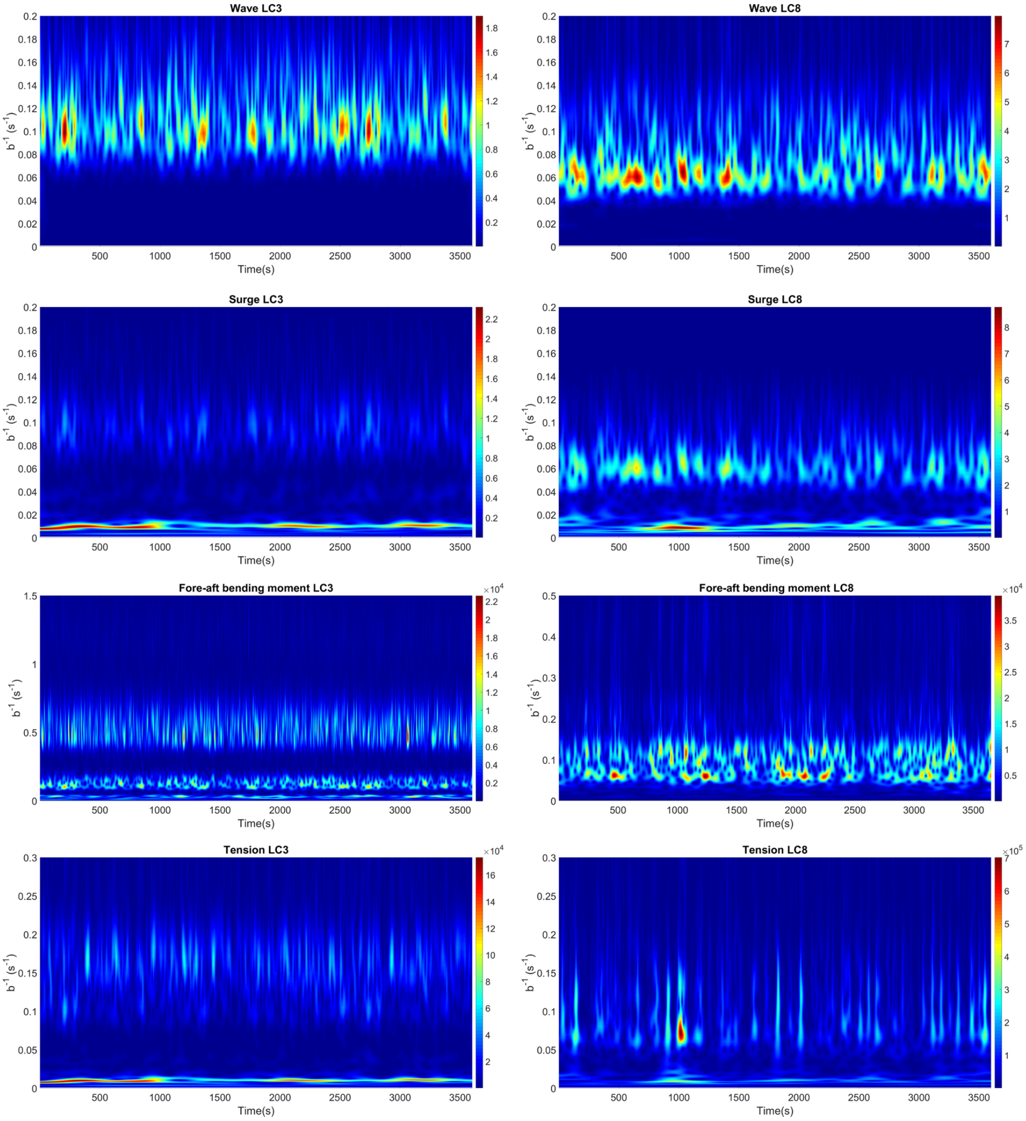

Fig. 8. Wavelet transformation of wave elevation, surge motion, tower base fore-aft bending moment and mooring line tension in LC3 and LC8.

value. The same random seed of wave is used within each load case for the irregular linear and fully nonlinear wave models.

4. Results and discussions

The results of coupled time-domain dynamic simulations are presented and discussed in this section for both operational and extreme conditions. The structural behavior is studied under different load cases in which different load effects are dominating. Same random seed of the irregular wave is used to generate the linear and fully nonlinear wave train to make it possible to investigate the discrepancy due to wave nonlinearity effect. In the following figures, black line represents results due to linear wave and red line represents results due to fully nonlinear wave. The circle marker indicates the mean response with a bar indicating the standard deviation. All the statistics are obtained by averaging all 10 or 20 one-hour simulations for each load case.

In operational condition where the blades are rotating, the stochastic characteristics of some critical dynamic responses and fatigue damage are studied. As for extreme condition where the wind turbine is parked with blades pitched to feather position, the extreme structural responses are predicted. Above all, the focus of the study is to compare the difference of structural response prediction from linear and fully nonlinear wave.

4.1. Comparison of operational and extreme condition

In operational condition where both wind and wave are functioning, floating wind turbine with turbine rotating behaves quite differently from that in extreme condition with turbine parked. Wavelet transformation which is a contour plot as shown in Fig. 8 illustrates the energy

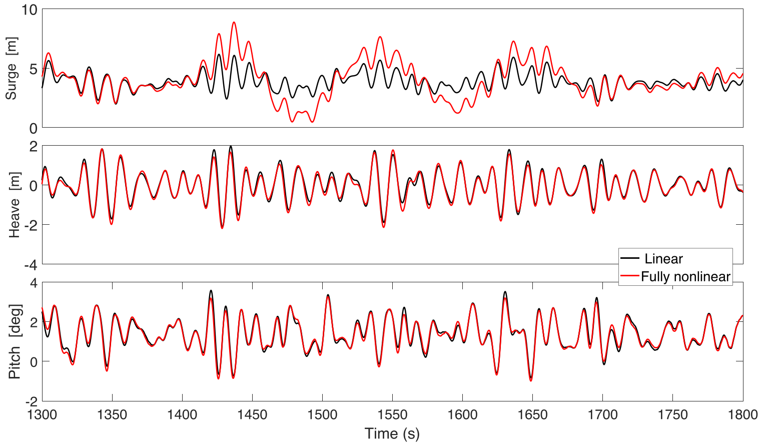

Fig. 9. Time series of floater motions in LC6.

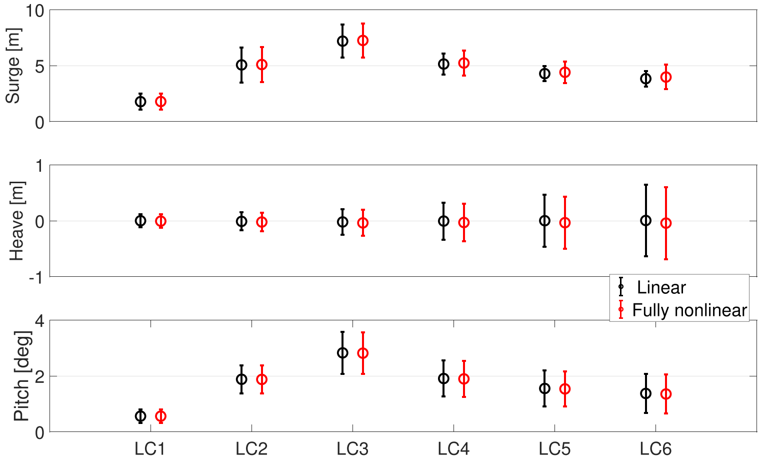

Fig. 10. Mean and standard deviation of floater motions.

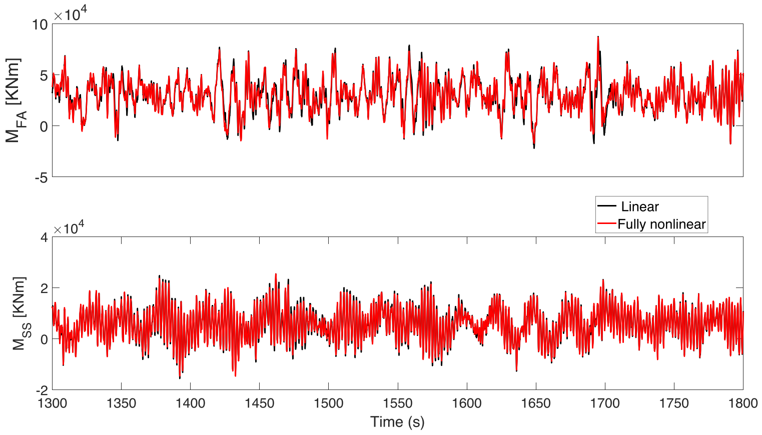

Fig. 11. Time series of tower base bending moment at LC6.

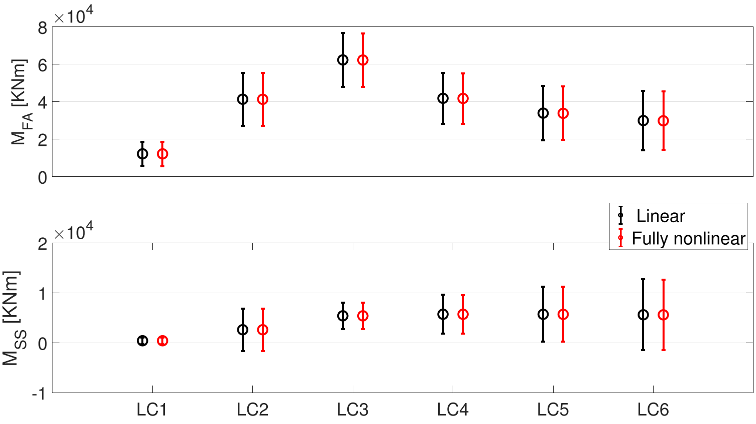

Fig. 12. Mean and standard deviation of tower base bending moment.

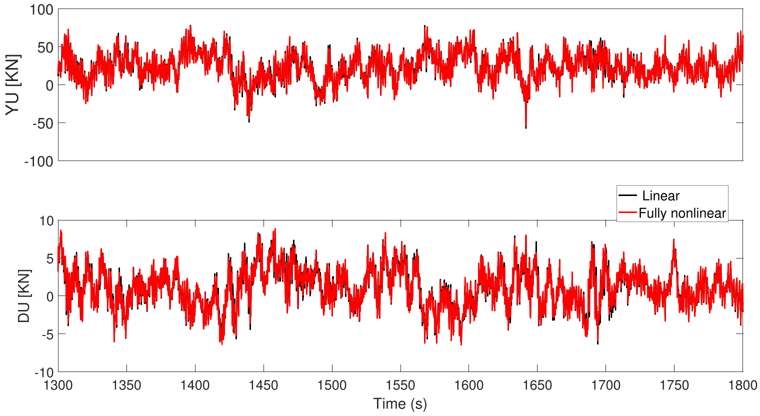

Fig. 13. Time series of axial force in YU and DU pontoon at LC6.

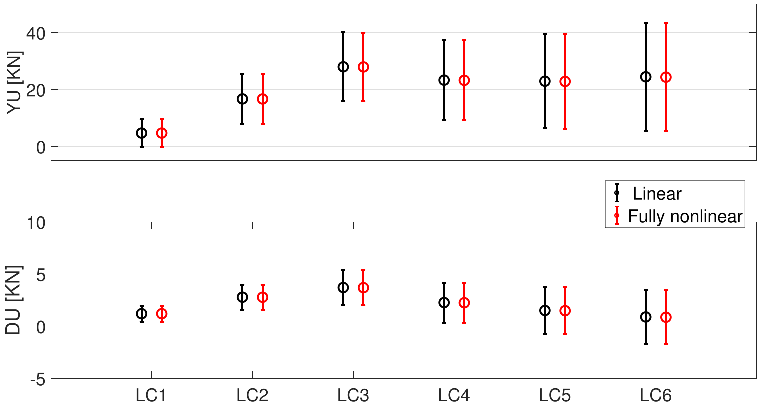

Fig. 14. Mean and standard deviation of axial force in YU and DU pontoon.

distribution of a signal at certain time and frequency with *x*-axis is time and *y*-axis is a scaled parameter which is equivalent to frequency.

From Fig. 8, the energy of surge motion in the operational condition (LC3) is concentrated at low frequency range which is mainly wind-induced while the energy is equally distributed at both wave frequency and wave-induced low frequency in extreme condition (LC8). Since tower base fore-aft bending moment is quite sensitive to the blade passing (3P) effect and tower natural bending effect in operational condition, the energy of M_{FA} in LC3 is distributed at wind-induced low frequency, wave frequency and higher frequency range. Meanwhile, the

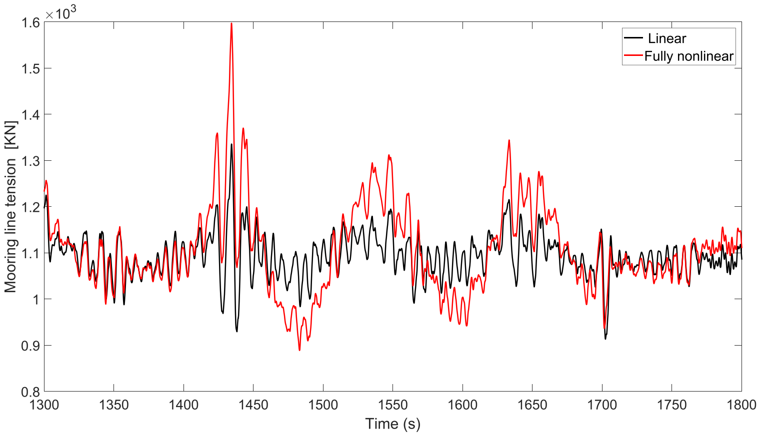

Fig. 15. Time series of mooring line tension at LC6.

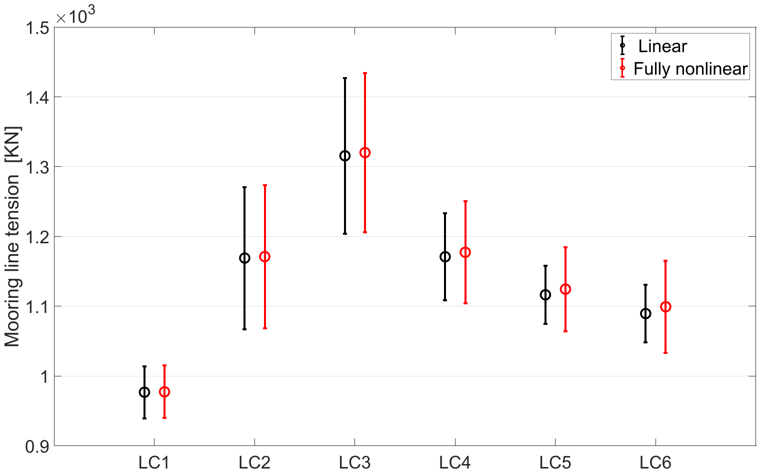

Fig. 16. Mean and standard deviation of mooring line tension.

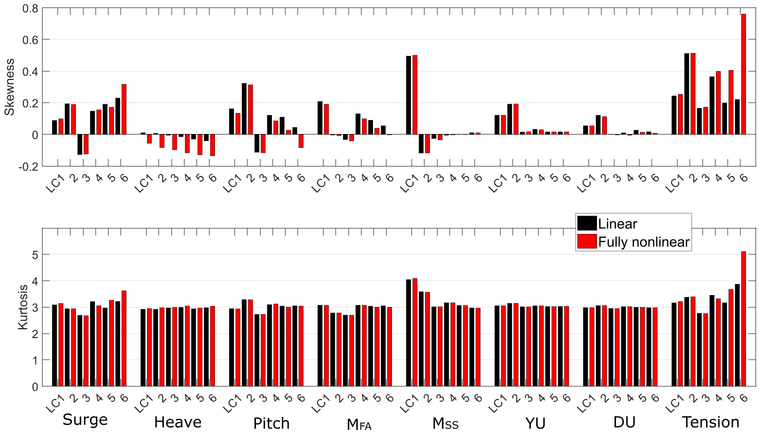

Fig. 17. Skewness and kurtosis.

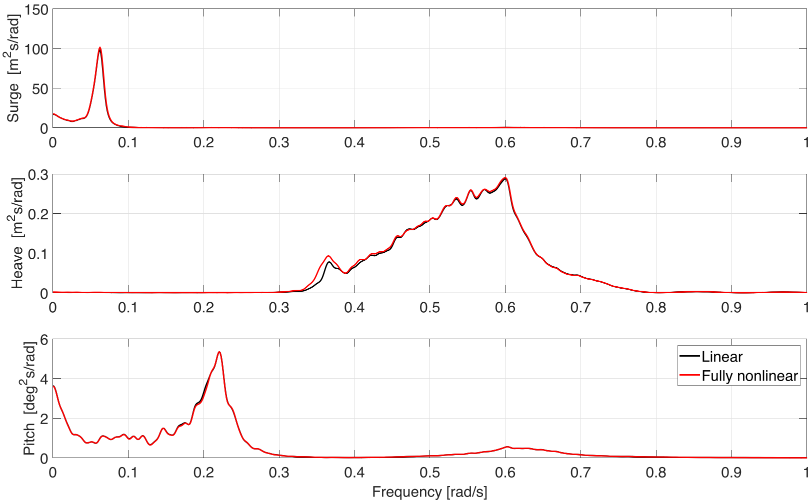

LC3

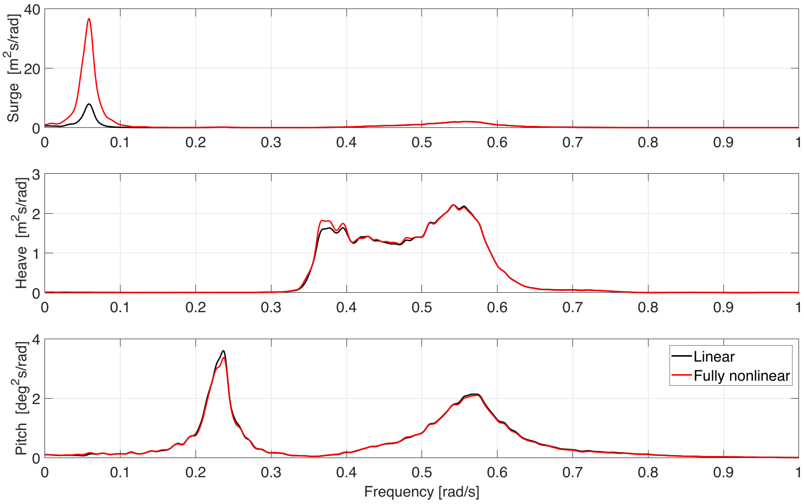

LC6

Fig. 18. Spectra for floater motions at LC3 and LC6.

energy of M_{FA} is mainly located around wave frequency in extreme condition (LC8) since the turbine is under parked condition. Mooring line tension is mainly affected by surge resonant effect at low frequency in operational condition (LC3) while in extreme condition (LC8), surge resonance and extreme wave contribute equally to the total response.

4.2. Operational conditions

4.2.1. Response statistics

4.2.1.1. Floater motions. The fact that the configuration of the floater is symmetric and the incoming wave & wind directions are in the symmetric plane leads to negligible sway and roll motion. Therefore the floater motion in surge, heave and pitch are selected as critical responses to study in this section. The mean value and standard deviation is given in Fig. 10 with an example time series of the motions in LC6 in Fig. 9.

From the time series, floater movement exposed to linear and fully nonlinear wave generally follows the same orbit since same random seed is used for generation of wave and wind respectively. Prediction of heave and pitch are almost the same while significant difference is found for surge motion.

In operational condition where both turbulent wind and irregular wave are considered, surge and pitch motions of the floater are mainly wind dominating while heave motion is primarily wave dominating as shown in Fig. 10. For surge and pitch motion, the mean values are non-zero due to mean wind and wave force. Both mean and standard

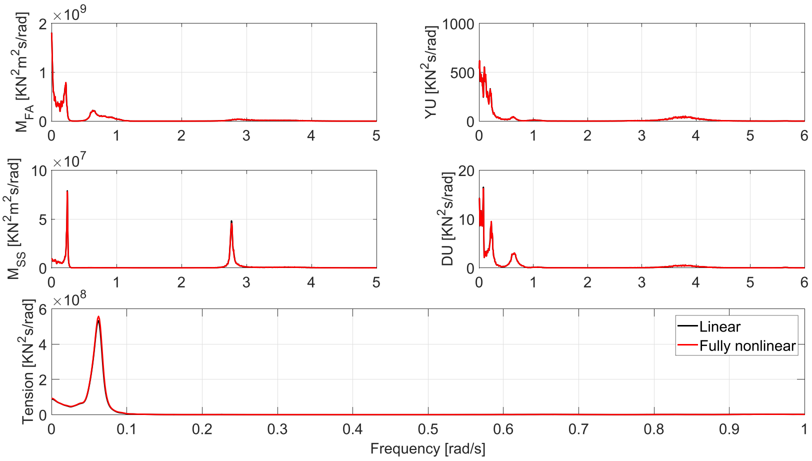

LC3

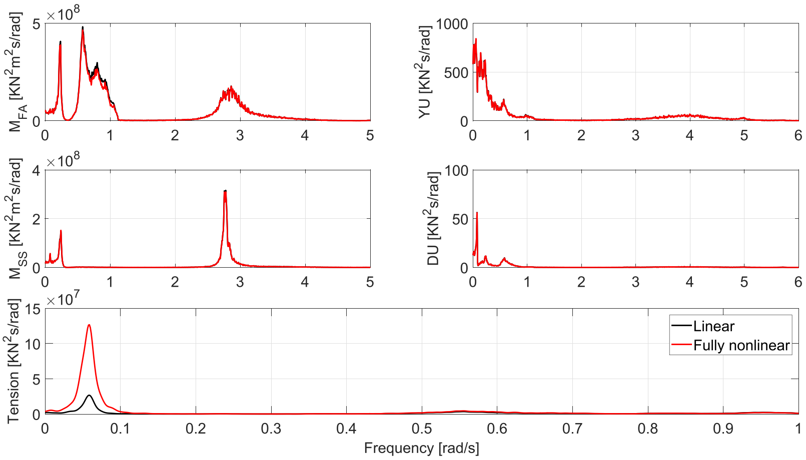

LC6

Fig. 19. Spectra for tower base bending moment, pontoon axial force and mooring line tension at LC3 and LC6.

Table 4
Relevant natural frequencies, unit: [rad/s].

	Surge	Heave	Pitch	3P
Natural frequency	0.054	0.369	0.244	3.79

deviation increase as wind speed increase from cut-in wind speed (4 m/s) in LC1 and reach maximum when wind speed is around rated wind speed (12 m/s) in LC3. As wind speed continues to increase, the blade pitch angle starts to increase due to the activated control system which leads to decreasing thrust force. Accordingly, the mean value of surge and pitch motion start to drop until around cut-out wind speed (24 m/s) in LC6.

As for heave motion, the mean values are close to zero and the standard deviation increases from LC1 to LC6 as the environmental condition becomes more severe, which is mainly wave-induced and it will be explained later in Section 4.2.4. Meanwhile, linear wave estimates slightly larger heave and pitch response for all LCs while fully nonlinear predicts higher surge response especially in LCs 4–6 where environmental conditions are more severe.

4.2.1.2. Tower base bending moment. The tower base bending moment is mainly due to thrust force acting on rotor and wave excitation force acting on the platform. The fore-aft (M_{FA}) and side-side (M_{SS}) bending moment considered in this paper are parallel and perpendicular to the incoming wind direction respectively. An example of time series and the statistics are given in Figs. 11 and 12.

From the time series, linear and fully nonlinear wave predict quite close result. So are the mean and standard deviation for both (M_{FA}) and (M_{SS}) with slightly higher response from linear wave. The mean value of M_{FA} is mainly affected by thrust force and floater pitch motion, which increases as wind speed increases below rated wind speed and decreases above rated wind speed. The standard deviation of M_{FA} varies not significantly in all LCs except LC1. On the other hand, the mean

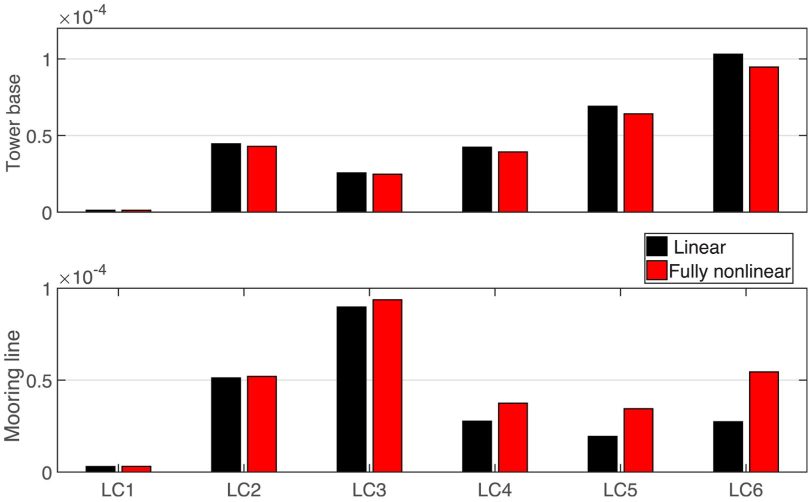

Fig. 20. Hourly fatigue damage at the tower base and the mooring line.

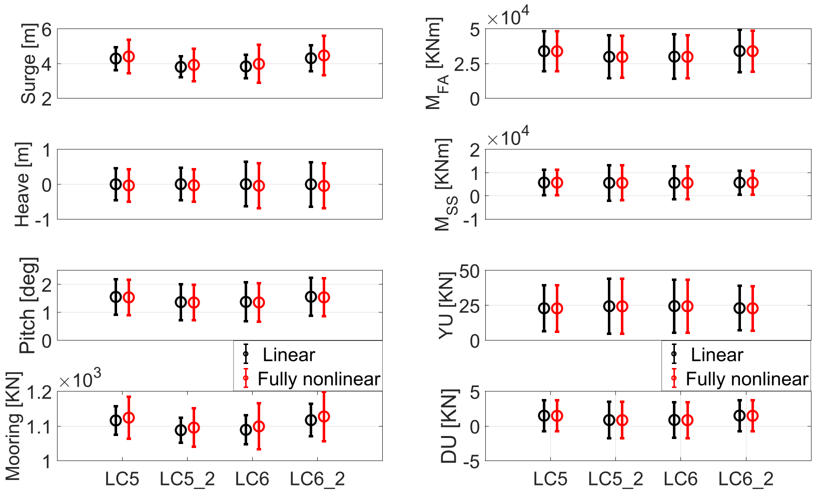

Fig. 21. Response statistics.

value of M_{SS} increases at below rated wind speed and it remains at a constant level as wind speed continues to increase. However, the standard deviation increases as sea state increases and this is mainly wind-induced and it will be discussed in Section 4.2.4. One interesting point to notice is that the bending moment at LC2 uniquely stands out which is due to the excitation of the tower natural bending mode around wind speed of 8 m/s at LC2 and it is more obvious for M_{SS} than M_{FA} as shown in Fig. 12.

4.2.1.3. Pontoon axial force. As shown in Fig. 1, the upper delta pontoon (DU) connecting the offset columns and the upper Y-shaped pontoon (YU) connecting the offset column with main column are studied in this section. The pontoons are modeled with beam elements, it is therefore possible to study the axial force under the load effects due to the external wind and wave and the structural elasticity effect at the ends of the pontoon. Fig. 13 provides an example of the time series of axial force in YU and DU pontoon at LC6.

For conditions below rated wind speed in Fig. 14, the axial force for both YU and DU pontoons increase as environmental conditions increases. As environmental conditions continue to increase, YU axial force remains at almost the same level while DU axial force starts to decrease. The difference between linear and fully nonlinear wave is not significant, which indicates that the supporting pontoon of the semi-submersible is not sensitive to nonlinear wave effect.

4.2.1.4. Mooring line tension. Among all three mooring lines, the upwind mooring line 2 was selected for study since it is aligned with the incoming wind and wave direction and subjected to the largest tension.

In the operational condition, mooring line tension is directly influenced by floater surge motion and is mainly dominated by low-frequency turbulent wind induced response. Largest mean and standard deviation of mooring line tension occurs in LC3 where wind speed is closest to rated wind speed. It becomes smaller for both lower and higher wind speed as shown in Fig. 16.

Linear and fully nonlinear wave provide quite close predictions of

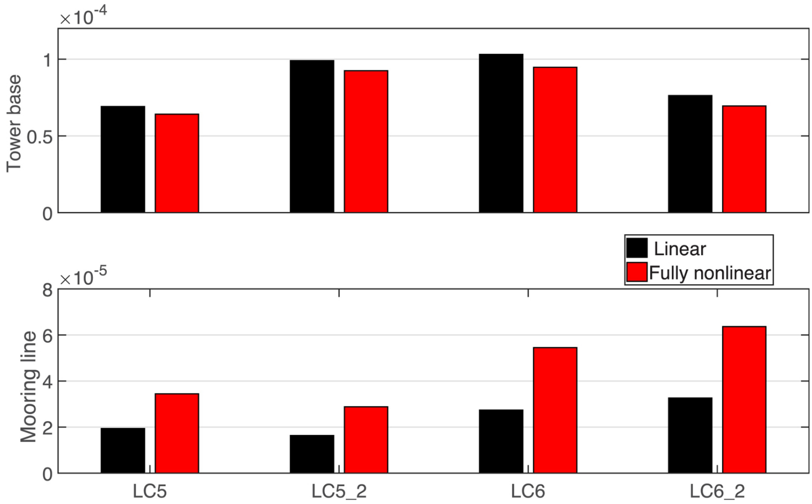

Fig. 22. Fatigue damage.

the mooring line tension for small sea states (LCs 1–3). However in large sea state, fully nonlinear wave predicts larger response than linear wave and the difference increases as sea state becomes more severe. Quite conspicuous difference is found in LCs 4–6, which proves the significance of wave nonlinear effect at large sea state and the time series in Fig. 15 also shines a light on this discrepancy.

4.2.1.5. *Non-Gaussian characteristics*.

The non-Gaussianity of the response can be characterized by its skewness and kurtosis. Skewness measures the asymmetrical degree of distortion of the distribution from the symmetrical bell curve. Kurtosis on the other hand describes the tailedness of the distribution. The skewness and kurtosis for any univariate Gaussian reponse are 0 and 3 respectively. Positive or negative skewness indicates longer tail on the right or left side. Larger or smaller kurtosis indicates heavy tails with many outliers or light tails with few outliers.

The skewness and kurtosis of all the relevant responses are shown in Fig. 17. Generally all the responses seem quite close to Gaussian process except mooring line tension. As for the comparison between linear and fully nonlinear wave, negative skewness is found for heave motion from fully nonlinear wave, which indicates larger heave response is expected from linear wave and it turns out to be the case. High non-Gaussianity due to wave nonlinearity in large wave is demonstrated by mooring line tension at LC5 and LC6, which lead to higher extreme tension estimation from fully nonlinear wave.

4.2.2. *Spectral analysis*

Power spectral analysis is used to indicate the contribution of different frequency component. LC3 and LC6 are selected as representative case as one with rated wind speed and one with the largest wave. The power spectra of floater motions are shown in Fig. 18 while the power spectra of tower bending moment, pontoon axial force and mooring line tension are shown in Fig. 19. Wind speeds in LC3 and LC6 are above rated wind speed, therefore the rotor the turbine is operating at its rated rotor speed of 12.1 rpm, which leads to the blade passing (3P) frequency to be around 3.79 rad/s as listed in Table 4.

In LC3 where wind speed is close to rated wind speed, surge resonance dominates surge motion with very little contribution from wave frequency response. Heave motion on the contrary is governed by wave frequency response and a small contribution from heave resonant response. As for pitch motion, the main contribution comes from pitch resonance and low-frequency wind induced response. Wave frequency response is relatively small. Almost identical power spectra are estimated from linear and fully nonlinear wave in LC3.

First of all, the response amplitude is smaller in LC6. Surge resonant response is also dominating surge motion. However, the contribution from wave frequency response is noticeable and so is the underestimation from linear wave. This is because surge motion is strongly influenced by wave effect at low-frequency where wave nonlinearity is mainly located. Heave resonant component contributes equally as wave frequency component to total heave response. For pitch motion, the low-frequency wind induced response decreases while the response from wave frequency increases.

The spectra for tower base bending moment, pontoon axial force and mooring line tension are illustrated in Fig. 19. The M_{FA} in LC3 is dominated by low-frequency wind induced response. Pitch resonance and wave induced response contribute relatively smaller. M_{SS} on the other hand is mainly influenced by not only pitch resonance but also tower first bending mode and 3P effect. The resonant responses at higher frequency range are larger for M_{SS} since there are limited aerodynamic damping as compared to M_{FA}. Both YU and DU pontoon are mainly influenced by slow varying wind effect, pitch resonance and wave frequency component. The contribution from high frequency component due to tower natural bending mode and 3P effect is relatively small. Almost all the mooring line tension response at LC3 is located at surge resonance range. Close predictions are obtained from the two wave models.

When the wave height increases as in LC6, the contribution from wave frequency response to M_{FA} becomes as important as pitch resonant response. Contribution due to tower natural bending response and 3P effect becomes significant for both M_{FA} and M_{SS}. The main influencing frequency factors for YU and DU axial force are almost the same as in LC3. Surge resonance still dominates the mooring line tension response. However, the difference from the two wave models becomes more significant than in LC3 which indicates that the wave nonlinear effect is important to consider for mooring line response especially for large wave.

4.2.3. *Fatigue damage*

The fatigue damage of mooring line and tower base is compared in Fig. 20. Generally, the fatigue damage at conditions with lower wind speed and smaller wave than LC1 can be expected not significant. The

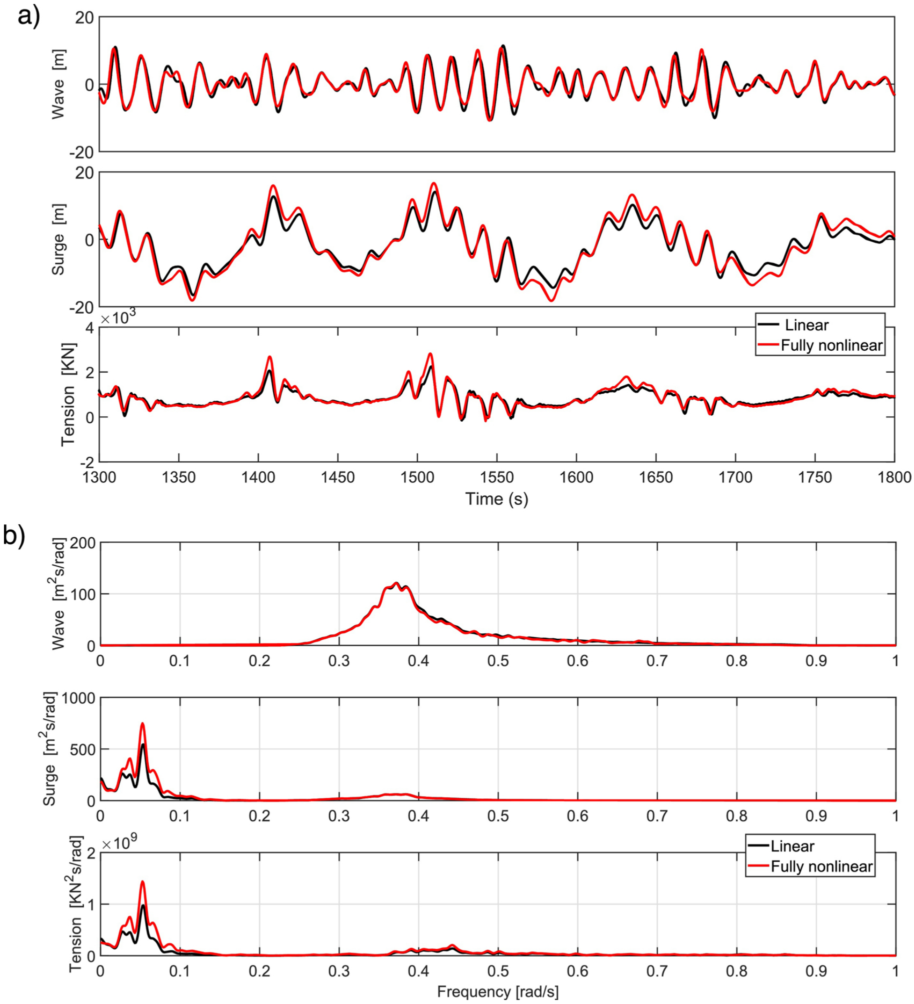

Fig. 23. Time series and spectra for wave elevation, surge motion and mooring line tension in LC7.

fatigue damage at the tower base increases as sea state increases, which is mainly due to increase of wind speed and will be discussed in Section 4.2.4. The excitation of the tower natural bending mode in LC2 significantly increases the fatigue damage level compared with other LCs. Linear wave predicts slightly higher fatigue damage than fully nonlinear wave because more energy is located around wave frequency range for linear wave. However, the difference is not quite significant. Compared with the statistics in Fig. 12, largest mean level of tower base bending moment in LC3 does not necessarily lead to the largest fatigue damage in the tower base.

In general, when exposed to wave only condition, the fatigue damage of the mooring line is proportional to wave height and inversely proportional to wave period [25]. For a given wind speed, fatigue damage tends to increase with increasing wave height and decreasing wave period. From Fig. 20, the fatigue damage level of mooring line follows the same trend as surge response which are wind dominated and reaches the maximum at LC3. From LC4 to LC6, the increase of wind speed actually leads to decreasing fatigue damage while the increase of wave condition on the contrary leads to increasing fatigue damage. The fatigue damage level in LC6 is found to be higher than in LC4 and LC5, which marks the greater contribution of fatigue damage due to wave than wind. The fatigue damage due to wave nonlinearity effect also increases from LC4 to LC6 as the wave height increases.

4.2.4. Wind and wave load effects

As mentioned before, some responses are mainly wind governed while others are wave dominated. In this section, four representative load cases are selected to distinguish wind-induced and wave-induced response in operational conditions. The same wave conditions are defined for LC5 as LC5_2 and LC6 as LC6_2 respectively while same wind conditions are defined for LC5 as LC6_2 and LC6 as LC5_2 respectively as listed in Table 3. Therefore, wind and wave effect on different responses can be studied comparatively.

The statistics of responses in the four load cases are given in Fig. 21 while the fatigue damage is compared in Fig. 22. When wind speed is above rated wind speed which is the case for the four LCs in this section, the mean and standard deviation of floater surge and pitch motion response in LC5 and LC6 are close to LC6_2 and LC5_2 respectively, which proves that both of them are wind-dominated while the influence from waves is less significant. For heave motion, the reversed result proves

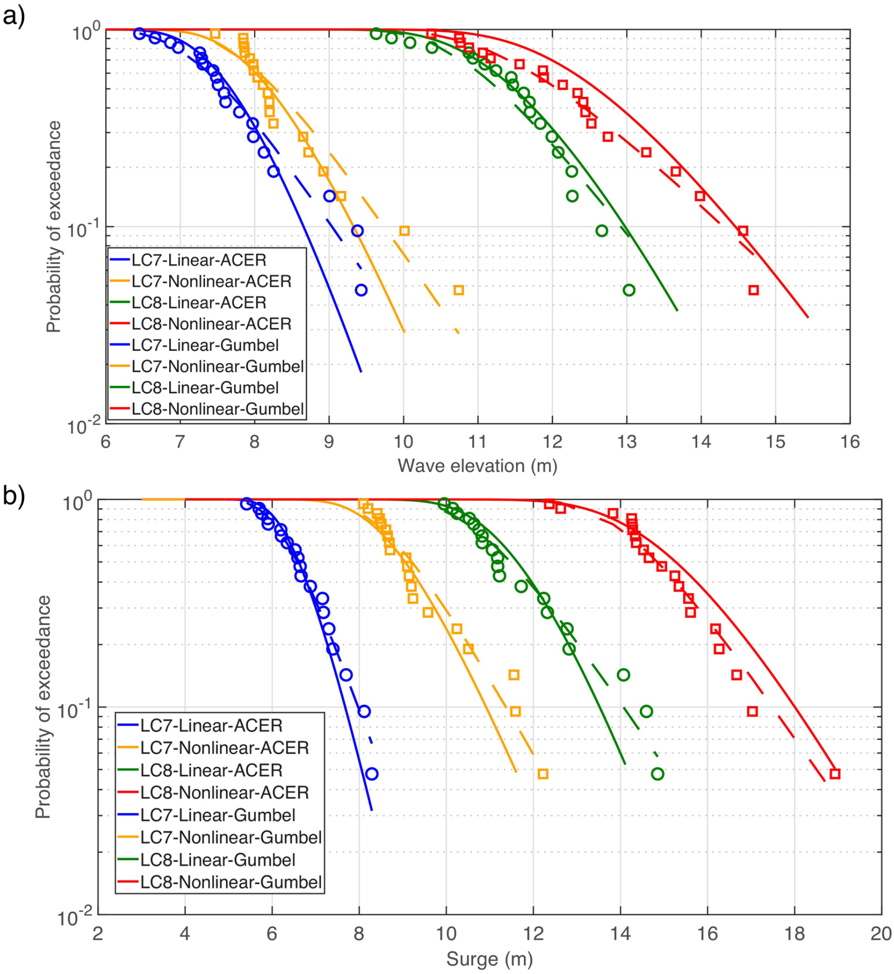

Fig. 24. Exceedance probability for wave elevation and surge motion. (For interpretation of the references to color in the text, the reader is referred to the web version of this article.)

that it is mainly affected by wave effects. As for the tower base bending moment and axial force in YU and DU pontoon, they are all wind-governed response based on close prediction from LC5 as LC6_2 and LC6 as LC5_2. However, the wave nonlinearity effect calculated as the difference between fully nonlinear wave and linear wave is found to be the same for LC5_2 as LC5 and LC6_2 as LC6 where the same wave condition is applied within each pair. As for mooring line tension, the mean value and standard deviation is wind dominating.

The fatigue damage level at tower base is mainly affected by wind effect as shown in Fig. 22. Generally speaking, wind is also dominating the fatigue level for mooring line at below rated wind speed where wave condition is small too. However, the contribution from wave becomes comparable to influence the total fatigue level at above rated wind speed when the wave is normally large too. Therefore, LC6_2 and LC6 with larger wave lead to clearly larger fatigue damage than LC5 and LC5_2. Meanwhile, the amplitude of wave nonlinearity effect is related to wave parameter too.

4.3. Extreme conditions

As concluded in operational condition, floater surge motion and mooring line tension are relatively more sensitive to wave nonlinear effect compared with other responses. Fig. 23 gives a corresponding example of time series and spectra in extreme condition (LC7) where the wind turbine is under parked condition and the wave load effect is dominating compared with wind load which mainly provides a drag force on the blades and tower. Clear difference is found from the two wave models. In extreme conditions (LC7 & LC8), the extreme value for the critical responses will be predicted in this section based on the Gumbel fitting method and ACER method as mentioned in Section 2.5.

As for Gumbel fitting method, the maximum value identified in the 20 simulations with 1-h effective duration with different random seeds are plotted in Gumbel probability paper as shown in Fig. 5. Then the shape and location parameters are determined accordingly. Once the unknown coefficients are estimated, the probability distribution function for Gumbel distribution is available. A large simulation sample is required in order to predict the Gumbel distribution with acceptable accuracy. Meanwhile, only the largest maxima is used for estimation

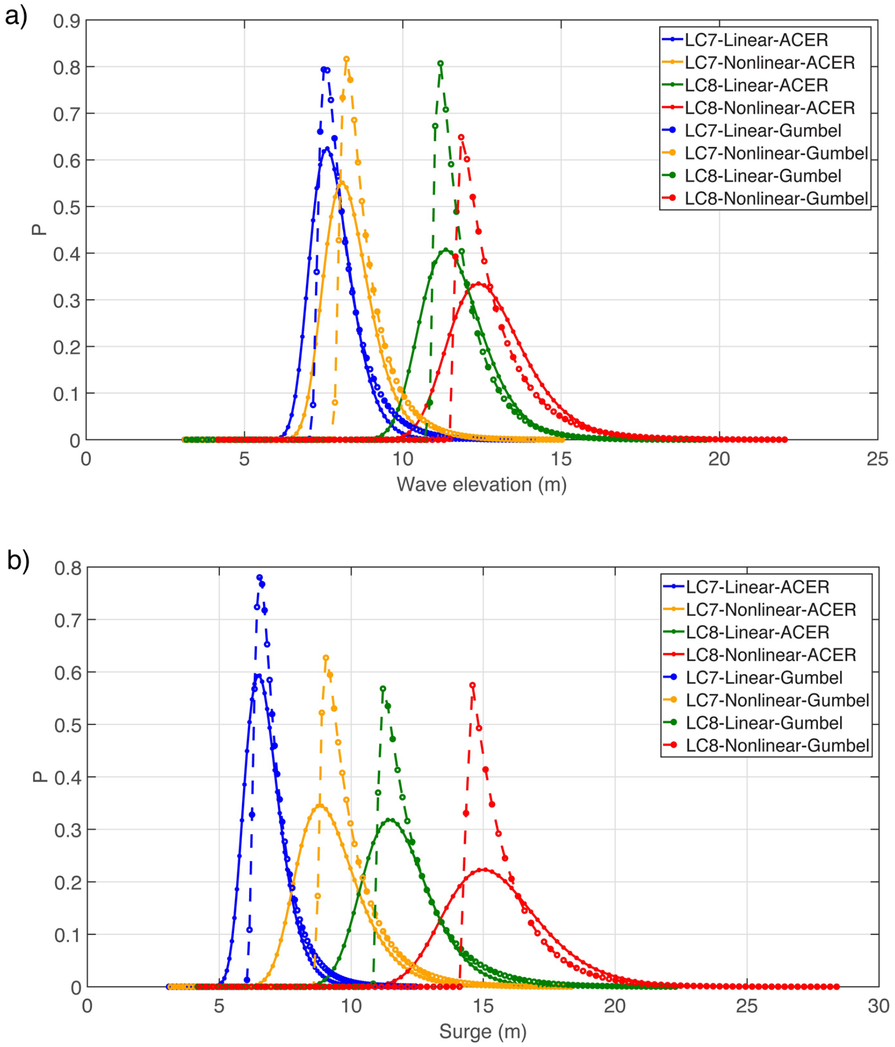

Fig. 25. Probability density function of extreme wave elevation and surge motion.

while the other maxima peaks did not really contribute.

Different from the Gumbel fitting method, all individual peaks as shown in Fig. 4 are involved in ACER method for predicting the extreme value. In addition, all the peaks from the 20 simulations are utilized while the number of exceeding peaks per hour is taken as the total number of peaks divided by the number of seeds. The empirical ACER function, $\hat{\varepsilon}_k(x)$ with order k from 1 to 6 is plotted in Fig. 6. Noticeable variation of ACER function with different order is discovered at lower range of the individual maxima indicating the significant dependence between data points. However, the variation disappears in the tail region for all functions which allows the first-order ACER function $\hat{\varepsilon}_1(x)$ to be chosen for extrapolation which involves most data for estimation and offers same level of accuracy as higher order functions at the same time. Meanwhile, the empirical ACER function in the tail region is close to a straight line which indicates the applicability of Gumbel distribution to describe the extreme value in this study because Gumbel distribution will be illustrated as a straight line in ACER plot ideally. The empirical function $\hat{\varepsilon}_1(x)$ is presented in Fig. 7 including the 95% confidence interval fitted by time series peaks as well as the estimation from extrapolation scheme. Previous studies by Fu et al. [21] show that the prediction is not sensitive to the choice of the tail marker x_0 which is used to define the tail region, therefore the default value is chosen. Finally, the extrapolation scheme leads to the estimation of all the coefficients required in ACER function.

Once all the coefficients for both methods are determined, the one-hour exceedance probability is plotted in Fig. 24 for wave elevation and surge motion where the solid line represents ACER function and dashed line stands for Gumbel function while original maximum peaks from each simulations are shown as markers with different colors. Exceedance probability not only indicates how well the probability models fit with original data but also provides a direct way to determine the extreme value over a certain probability occurrence level. In general, linear wave models predicts smaller extreme value than fully nonlinear wave model for a given exceedance level while the predictions from ACER method and Gumbel method are pretty close to each other.

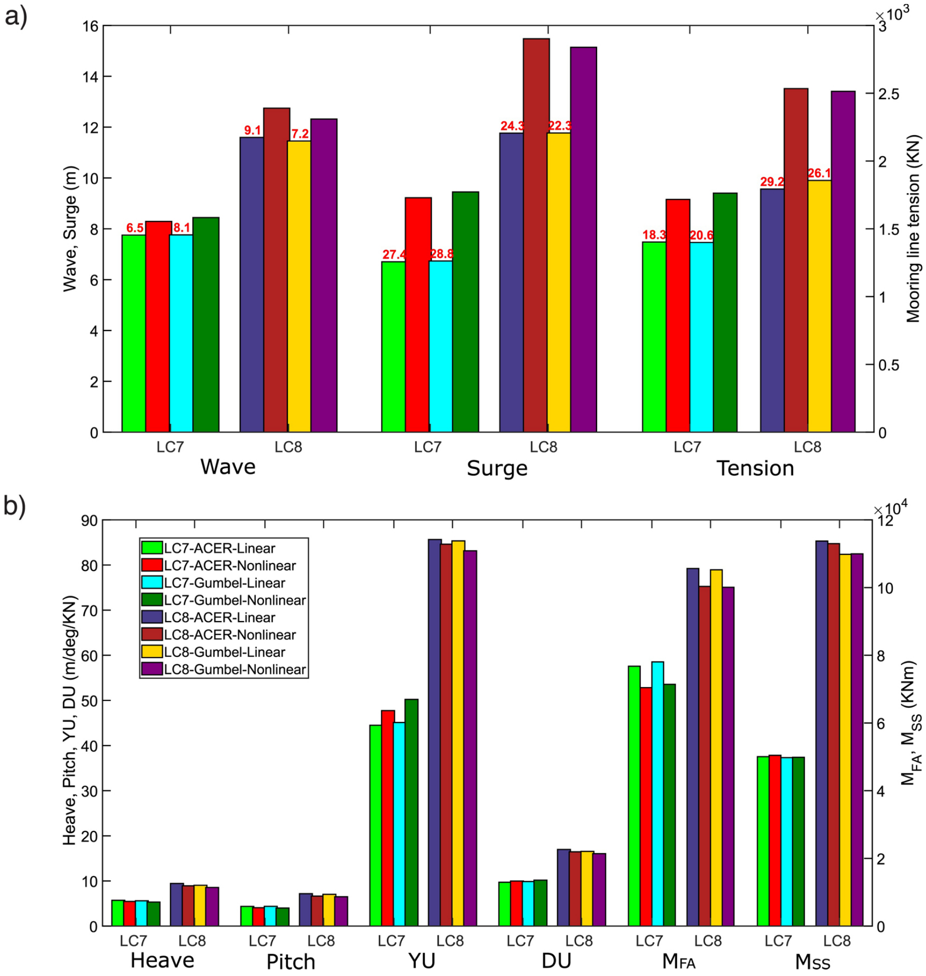

Fig. 26. Extreme response (The red numbers on top of the bar column quantify the under-estimation of linear wave theory as the percentage of the difference to the results of fully nonlinear wave theory). (For interpretation of the references to color in this figure legend, the reader is referred to the web version of this article.)

Meanwhile, the probability density functions can also be derived respectively from Eqs. (9) and (11) and plotted in Fig. 25:

$$f_{\mathrm{Gumbel}}(x) = \alpha\cdot\exp(-\alpha(x-\mu) - \exp(-\alpha(x-\mu))) \tag{17}$$

$$f_{\mathrm{ACER}}(x) = (N-k+1)\cdot q\cdot a\cdot c\cdot\exp\{-(N-k+1)\cdot q\cdot\exp[-a(x-b)^c] - a(x-b)^c\}\cdot(x-b)^{c-1} \tag{18}$$

Accordingly, the expected maximum value for both methods can be expressed as:

$$E_{\mathrm{Gumbel/ACER}}[X] = \int x\cdot f_{\mathrm{Gumbel/ACER}}(x)\mathrm{d}x \tag{19}$$

The expected extreme values are predicted for all the relevant responses as shown in Fig. 26 where different colors are used to represent the predictions from two methods in two load cases. The responses which are sensitive to nonlinear wave effect are distinguished from others.

First of all, as wave height increases, the extreme response due to higher sea states (LC8) is predicted larger than smaller sea states (LC7). Secondly, Gumbel fitting method generally predicts quite close results as ACER method for all cases even though latter method utilizes more data from time series. Most importantly, linear wave model significantly under-predicts extreme floater surge motion and mooring line tension compared with the fully nonlinear wave model for both LC7 and LC8 conditions and it becomes more significant as sea state becomes more severe. Underestimation is found for wave elevation, surge motion and mooring line tension with approximately 10%, 25% and 25% respectively. Meanwhile, the extreme value predictions are quite close for other responses.

5. Conclusions

This paper investigates the hydrodynamic behaviour of floating wind turbines based on linear and fully nonlinear wave kinematics theory. Several load cases are considered including operational conditions with turbine rotating and extreme conditions with turbine parked. Fatigue damage has been calculated and extreme values have been predicted by Gumbel fitting method and ACER method. Representative load cases are selected to distinguish wind-induced and wave-induced response.

In operational conditions, the floater heave motion is mainly wave-induced and increases as wave becomes larger while wind effect is governing surge and pitch motion which reaches maximum when the wind speed is close to rated wind speed. Linear wave theory predicts slightly higher heave and pitch motions while the fully nonlinear wave theory predicts larger surge motion and the difference increases significantly as the wave height increases. This is because wave energy is redistributed to the higher and lower frequency range than wave frequency due to wave nonlinearity effects and it greatly influences surge motion whose natural period is in the low frequency range. The tower base bending moment in both fore-aft and side-side direction is more influenced by wind-induced thrust force. The excitation of tower natural period increases the response level significantly. However, the bending moment estimates from the two wave theories are quite close with slightly larger value from the linear wave theory since it contains more energy around wave frequency range. The axial forces in YU and DU pontoon are mainly influenced by slowly varying wind effect, pitch resonance and wave-frequency response, while the wave nonlinear effect is not significant. Mooring line tension is mainly influenced by floater surge resonance and considerable contribution comes from wave frequency range when wave is large, therefore the tension reaches the maximum around rated-wind speed following similar trend as surge motion. Linear wave theory underestimates tension response when the waves become large. Moreover, mooring line tension tends to be quite non-Gaussian at large sea states while other response processes appear to be quite Gaussian. In extreme conditions, Gumbel fitting method and ACER method are used to predict the extreme value of some responses and both of them are able to give similar estimations. Linear wave generally underestimates wave elevation, floater surge motion and mooring line tension compared with fully nonlinear wave by 10%, 25% and 25% respectively.

The fatigue damage level at tower base is mainly wind dominating with outstanding result when tower natural mode is excited. Below rated wind speed, the fatigue level of mooring line is primarily governed by wind. When wind speed goes above rated wind speed where wave normally is large too, the contribution from wave becomes considerable and so is the wave nonlinearity effect.

In conclusion, nonlinear wave kinematics is important to consider in the design and analysis for floating wind turbine especially regarding predicting the fatigue damage at high sea states in operational condition and the extreme value of wave elevation, floater surge motion and mooring line tension in extreme condition.

Acknowledgement

The first and second author would like to thank the financial support from China Scholarship Council. The second author gratefully acknowledges the support from the National Natural Science Foundation of China (51879247) and the Natural Science Foundation of Shandong Province (ZR2018MEE049). Appreciation also goes to Dr. Ping Fu at DNV GL for discussion regarding the extreme value analysis.

References

[1] R. Gibson, C. Swan, The evolution of large ocean waves: the role of local and rapid spectral changes, Proc. R. Soc. A: Math. Phys. Eng. Sci. 463 (2006) 21–48.
[2] G.G. Stokes, On the Theory of Oscillatory Waves. Volume 1 of Cambridge Library Collection – Mathematics, Cambridge University Press, 2009, pp. 197–229.
[3] T. Camp, M. Morris, R. van Rooij, J. van der Tempel, M. Zaaijer, A. Henderson, K. Argyriadis, S. Schwartz, H. Just, W. Grainger, D. Peace, Design Methods for Offshore Wind Turbines at Exposed Sites, The European Commission, 2003 Technical Report.
[4] S. Schløer, H. Bredmose, H.B. Bingham, The influence of fully nonlinear wave forces on aero-hydro-elastic calculations of monopile wind turbines, Mar. Struct. 50 (2016) 162–188.
[5] H. Li, J. Du, S. Wang, M. Sun, A. Chang, Investigation on the probabilistic distribution of mooring line tension for fatigue damage assessment, Ocean Eng. 124 (2016) 204–214.
[6] L. Li, Z. Cheng, Z. Yuan, Y. Gao, Short-term extreme response and fatigue damage of an integrated offshore renewable energy system, Renew. Energy 126 (2018) 617–629.
[7] K. Xu, Y. Shao, Z. Gao, T. Moan, A study on fully nonlinear wave load effects on floating wind turbine, J. Fluids Struct. 88 (2019) 216–240.
[8] A. Robertson, J. Jonkman, M. Masciola, H. Song, A. Goupee, A. Coulling, C. Luan, Definition of the Semisubmersible Floating System for Phase II of OC4, National Renewable Energy Lab. (NREL), Golden, CO (United States), 2014 Technical Report.
[9] T.J. Larsen, A.M. Hansen, How 2 hawc2, The User's Manual, (2007).
[10] J. Mann, Wind field simulation, Probab. Eng. Mech. 13 (1998) 269–282.
[11] Y.L. Shao, O.M. Faltinsen, Towards efficient fully-nonlinear potential-flow solvers in marine hydrodynamics, ASME 2012 31st International Conference on Ocean, Offshore and Arctic Engineering, American Society of Mechanical Engineers, 2012, pp. 369–380.
[12] Y.L. Shao, O.M. Faltinsen, A harmonic polynomial cell (hpc) method for 3d laplace equation with application in marine hydrodynamics, J. Comput. Phys. 274 (2014) 312–332.
[13] H. Liang, O.M. Faltinsen, Y.L. Shao, Application of a 2d harmonic polynomial cell (hpc) method to singular flows and lifting problems, Appl. Ocean Res. 53 (2015) 75–90.
[14] Z. Gao, T. Moan, Frequency-domain fatigue analysis of wide-band stationary gaussian processes using a trimodal spectral formulation, Int. J. Fatigue 30 (2008) 1944–1955.
[15] M.I. Kvittem, T. Moan, Time domain analysis procedures for fatigue assessment of a semi-submersible wind turbine, Mar. Struct. 40 (2015) 38–59.
[16] API, 2sk, Recommended Practice for Design and Analysis of Stationkeeping Systems for Floating Structures, American Petroleum Institute, 1996.
[17] A. Næss, T. Moan, Stochastic Dynamics of Marine Structures, Cambridge University Press, 2013.
[18] P. Fu, B.J. Leira, D. Myrhaug, Reliability analysis of wake-induced collision of flexible risers, Appl. Ocean Res. 62 (2017) 49–56.
[19] A. Næss, O. Gaidai, Estimation of extreme values from sampled time series, Struct. Saf. 31 (2009) 325–334.
[20] Z. Cheng, H.A. Madsen, W. Chai, Z. Gao, T. Moan, A comparison of extreme structural responses and fatigue damage of semi-submersible type floating horizontal and vertical axis wind turbines, Renew. Energy 108 (2017) 207–219.
[21] P. Fu, B.J. Leira, D. Myrhaug, Assessment of methods for short-term extreme value analysis of riser collision, ASME 2018 37th International Conference on Ocean, Offshore and Arctic Engineering, American Society of Mechanical Engineers, 2018.
[22] K. Johannessen, T.S. Meling, S. Haver, et al., Joint distribution for wind and waves in the northern north sea, The Eleventh International Offshore and Polar Engineering Conference, International Society of Offshore and Polar Engineers, 2001.
[23] IEC, Iec 61400-3: Wind Turbines Part 3: Design Requirements for Offshore Wind Turbines, International Electrotechnical Commission, 2009.
[24] IEC, Iec 61400-1: Wind Turbines Part 1: Design Requirements, International Electrotechnical Commission, 2005.
[25] P.R. Thies, L. Johanning, V. Harnois, H.C. Smith, D.N. Parish, Mooring line fatigue damage evaluation for floating marine energy converters: field measurements and prediction, Renew. Energy 63 (2014) 133–144.

Appendix B

List of previous PhD theses at Dept. of Marine Tech.

Previous PhD theses published at the Department of Marine Technology
(earlier: Faculty of Marine Technology)
NORWEGIAN UNIVERSITY OF SCIENCE AND TECHNOLOGY

Report No.	Author	Title
	Kavlie, Dag	Optimization of Plane Elastic Grillages, 1967
	Hansen, Hans R.	Man-Machine Communication and Data-Storage Methods in Ship Structural Design, 1971
	Gisvold, Kaare M.	A Method for non-linear mixed -integer programming and its Application to Design Problems, 1971
	Lund, Sverre	Tanker Frame Optimalization by means of SUMT-Transformation and Behaviour Models, 1971
	Vinje, Tor	On Vibration of Spherical Shells Interacting with Fluid, 1972
	Lorentz, Jan D.	Tank Arrangement for Crude Oil Carriers in Accordance with the new Anti-Pollution Regulations, 1975
	Carlsen, Carl A.	Computer-Aided Design of Tanker Structures, 1975
	Larsen, Carl M.	Static and Dynamic Analysis of Offshore Pipelines during Installation, 1976
UR-79-01	Brigt Hatlestad, MK	The finite element method used in a fatigue evaluation of fixed offshore platforms. (Dr.Ing. Thesis)
UR-79-02	Erik Pettersen, MK	Analysis and design of cellular structures. (Dr.Ing. Thesis)
UR-79-03	Sverre Valsgård, MK	Finite difference and finite element methods applied to nonlinear analysis of plated structures. (Dr.Ing. Thesis)
UR-79-04	Nils T. Nordsve, MK	Finite element collapse analysis of structural members considering imperfections and stresses due to fabrication. (Dr.Ing. Thesis)
UR-79-05	Ivar J. Fylling, MK	Analysis of towline forces in ocean towing systems. (Dr.Ing. Thesis)
UR-80-06	Nils Sandsmark, MM	Analysis of Stationary and Transient Heat Conduction by the Use of the Finite Element Method. (Dr.Ing. Thesis)
UR-80-09	Sverre Haver, MK	Analysis of uncertainties related to the stochastic modeling of ocean waves. (Dr.Ing. Thesis)
UR-81-15	Odland, Jonas	On the Strength of welded Ring stiffened cylindrical Shells primarily subjected to axial Compression
UR-82-17	Engesvik, Knut	Analysis of Uncertainties in the fatigue Capacity of

		Welded Joints
UR-82-18	Rye, Henrik	Ocean wave groups
UR-83-30	Eide, Oddvar Inge	On Cumulative Fatigue Damage in Steel Welded Joints
UR-83-33	Mo, Olav	Stochastic Time Domain Analysis of Slender Offshore Structures
UR-83-34	Amdahl, Jørgen	Energy absorption in Ship-platform impacts
UR-84-37	Mørch, Morten	Motions and mooring forces of semi submersibles as determined by full-scale measurements and theoretical analysis
UR-84-38	Soares, C. Guedes	Probabilistic models for load effects in ship structures
UR-84-39	Aarsnes, Jan V.	Current forces on ships
UR-84-40	Czujko, Jerzy	Collapse Analysis of Plates subjected to Biaxial Compression and Lateral Load
UR-85-46	Alf G. Engseth, MK	Finite element collapse analysis of tubular steel offshore structures. (Dr.Ing. Thesis)
UR-86-47	Dengody Sheshappa, MP	A Computer Design Model for Optimizing Fishing Vessel Designs Based on Techno-Economic Analysis. (Dr.Ing. Thesis)
UR-86-48	Vidar Aanesland, MH	A Theoretical and Numerical Study of Ship Wave Resistance. (Dr.Ing. Thesis)
UR-86-49	Heinz-Joachim Wessel, MK	Fracture Mechanics Analysis of Crack Growth in Plate Girders. (Dr.Ing. Thesis)
UR-86-50	Jon Taby, MK	Ultimate and Post-ultimate Strength of Dented Tubular Members. (Dr.Ing. Thesis)
UR-86-51	Walter Lian, MH	A Numerical Study of Two-Dimensional Separated Flow Past Bluff Bodies at Moderate KC-Numbers. (Dr.Ing. Thesis)
UR-86-52	Bjørn Sortland, MH	Force Measurements in Oscillating Flow on Ship Sections and Circular Cylinders in a U-Tube Water Tank. (Dr.Ing. Thesis)
UR-86-53	Kurt Strand, MM	A System Dynamic Approach to One-dimensional Fluid Flow. (Dr.Ing. Thesis)
UR-86-54	Arne Edvin Løken, MH	Three Dimensional Second Order Hydrodynamic Effects on Ocean Structures in Waves. (Dr.Ing. Thesis)
UR-86-55	Sigurd Falch, MH	A Numerical Study of Slamming of Two-Dimensional Bodies. (Dr.Ing. Thesis)
UR-87-56	Arne Braathen, MH	Application of a Vortex Tracking Method to the Prediction of Roll Damping of a Two-Dimension Floating Body. (Dr.Ing. Thesis)

UR-87-57	Bernt Leira, MK	Gaussian Vector Processes for Reliability Analysis involving Wave-Induced Load Effects. (Dr.Ing. Thesis)
UR-87-58	Magnus Småvik, MM	Thermal Load and Process Characteristics in a Two-Stroke Diesel Engine with Thermal Barriers (in Norwegian). (Dr.Ing. Thesis)
MTA-88-59	Bernt Arild Bremdal, MP	An Investigation of Marine Installation Processes – A Knowledge - Based Planning Approach. (Dr.Ing. Thesis)
MTA-88-60	Xu Jun, MK	Non-linear Dynamic Analysis of Space-framed Offshore Structures. (Dr.Ing. Thesis)
MTA-89-61	Gang Miao, MH	Hydrodynamic Forces and Dynamic Responses of Circular Cylinders in Wave Zones. (Dr.Ing. Thesis)
MTA-89-62	Martin Greenhow, MH	Linear and Non-Linear Studies of Waves and Floating Bodies. Part I and Part II. (Dr.Techn. Thesis)
MTA-89-63	Chang Li, MH	Force Coefficients of Spheres and Cubes in Oscillatory Flow with and without Current. (Dr.Ing. Thesis
MTA-89-64	Hu Ying, MP	A Study of Marketing and Design in Development of Marine Transport Systems. (Dr.Ing. Thesis)
MTA-89-65	Arild Jæger, MH	Seakeeping, Dynamic Stability and Performance of a Wedge Shaped Planing Hull. (Dr.Ing. Thesis)
MTA-89-66	Chan Siu Hung, MM	The dynamic characteristics of tilting-pad bearings
MTA-89-67	Kim Wikstrøm, MP	Analysis av projekteringen for ett offshore projekt. (Licenciat-avhandling)
MTA-89-68	Jiao Guoyang, MK	Reliability Analysis of Crack Growth under Random Loading, considering Model Updating. (Dr.Ing. Thesis)
MTA-89-69	Arnt Olufsen, MK	Uncertainty and Reliability Analysis of Fixed Offshore Structures. (Dr.Ing. Thesis)
MTA-89-70	Wu Yu-Lin, MR	System Reliability Analyses of Offshore Structures using improved Truss and Beam Models. (Dr.Ing. Thesis)
MTA-90-71	Jan Roger Hoff, MH	Three-dimensional Green function of a vessel with forward speed in waves. (Dr.Ing. Thesis)
MTA-90-72	Rong Zhao, MH	Slow-Drift Motions of a Moored Two-Dimensional Body in Irregular Waves. (Dr.Ing. Thesis)
MTA-90-73	Atle Minsaas, MP	Economical Risk Analysis. (Dr.Ing. Thesis)
MTA-90-74	Knut-Aril Farnes, MK	Long-term Statistics of Response in Non-linear Marine Structures. (Dr.Ing. Thesis)
MTA-90-75	Torbjørn Sotberg, MK	Application of Reliability Methods for Safety Assessment of Submarine Pipelines. (Dr.Ing.

		Thesis)
MTA-90-76	Zeuthen, Steffen, MP	SEAMAID. A computational model of the design process in a constraint-based logic programming environment. An example from the offshore domain. (Dr.Ing. Thesis)
MTA-91-77	Haagensen, Sven, MM	Fuel Dependant Cyclic Variability in a Spark Ignition Engine - An Optical Approach. (Dr.Ing. Thesis)
MTA-91-78	Løland, Geir, MH	Current forces on and flow through fish farms. (Dr.Ing. Thesis)
MTA-91-79	Hoen, Christopher, MK	System Identification of Structures Excited by Stochastic Load Processes. (Dr.Ing. Thesis)
MTA-91-80	Haugen, Stein, MK	Probabilistic Evaluation of Frequency of Collision between Ships and Offshore Platforms. (Dr.Ing. Thesis)
MTA-91-81	Sødahl, Nils, MK	Methods for Design and Analysis of Flexible Risers. (Dr.Ing. Thesis)
MTA-91-82	Ormberg, Harald, MK	Non-linear Response Analysis of Floating Fish Farm Systems. (Dr.Ing. Thesis)
MTA-91-83	Marley, Mark J., MK	Time Variant Reliability under Fatigue Degradation. (Dr.Ing. Thesis)
MTA-91-84	Krokstad, Jørgen R., MH	Second-order Loads in Multidirectional Seas. (Dr.Ing. Thesis)
MTA-91-85	Molteberg, Gunnar A., MM	The Application of System Identification Techniques to Performance Monitoring of Four Stroke Turbocharged Diesel Engines. (Dr.Ing. Thesis)
MTA-92-86	Mørch, Hans Jørgen Bjelke, MH	Aspects of Hydrofoil Design: with Emphasis on Hydrofoil Interaction in Calm Water. (Dr.Ing. Thesis)
MTA-92-87	Chan Siu Hung, MM	Nonlinear Analysis of Rotordynamic Instabilities in Highspeed Turbomachinery. (Dr.Ing. Thesis)
MTA-92-88	Bessason, Bjarni, MK	Assessment of Earthquake Loading and Response of Seismically Isolated Bridges. (Dr.Ing. Thesis)
MTA-92-89	Langli, Geir, MP	Improving Operational Safety through exploitation of Design Knowledge - an investigation of offshore platform safety. (Dr.Ing. Thesis)
MTA-92-90	Sævik, Svein, MK	On Stresses and Fatigue in Flexible Pipes. (Dr.Ing. Thesis)
MTA-92-91	Ask, Tor Ø., MM	Ignition and Flame Growth in Lean Gas-Air Mixtures. An Experimental Study with a Schlieren System. (Dr.Ing. Thesis)
MTA-86-92	Hessen, Gunnar, MK	Fracture Mechanics Analysis of Stiffened Tubular Members. (Dr.Ing. Thesis)

MTA-93-93	Steinebach, Christian, MM	Knowledge Based Systems for Diagnosis of Rotating Machinery. (Dr.Ing. Thesis)
MTA-93-94	Dalane, Jan Inge, MK	System Reliability in Design and Maintenance of Fixed Offshore Structures. (Dr.Ing. Thesis)
MTA-93-95	Steen, Sverre, MH	Cobblestone Effect on SES. (Dr.Ing. Thesis)
MTA-93-96	Karunakaran, Daniel, MK	Nonlinear Dynamic Response and Reliability Analysis of Drag-dominated Offshore Platforms. (Dr.Ing. Thesis)
MTA-93-97	Hagen, Arnulf, MP	The Framework of a Design Process Language. (Dr.Ing. Thesis)
MTA-93-98	Nordrik, Rune, MM	Investigation of Spark Ignition and Autoignition in Methane and Air Using Computational Fluid Dynamics and Chemical Reaction Kinetics. A Numerical Study of Ignition Processes in Internal Combustion Engines. (Dr.Ing. Thesis)
MTA-94-99	Passano, Elizabeth, MK	Efficient Analysis of Nonlinear Slender Marine Structures. (Dr.Ing. Thesis)
MTA-94-100	Kvålsvold, Jan, MH	Hydroelastic Modelling of Wetdeck Slamming on Multihull Vessels. (Dr.Ing. Thesis)
MTA-94-102	Bech, Sidsel M., MK	Experimental and Numerical Determination of Stiffness and Strength of GRP/PVC Sandwich Structures. (Dr.Ing. Thesis)
MTA-95-103	Paulsen, Hallvard, MM	A Study of Transient Jet and Spray using a Schlieren Method and Digital Image Processing. (Dr.Ing. Thesis)
MTA-95-104	Hovde, Geir Olav, MK	Fatigue and Overload Reliability of Offshore Structural Systems, Considering the Effect of Inspection and Repair. (Dr.Ing. Thesis)
MTA-95-105	Wang, Xiaozhi, MK	Reliability Analysis of Production Ships with Emphasis on Load Combination and Ultimate Strength. (Dr.Ing. Thesis)
MTA-95-106	Ulstein, Tore, MH	Nonlinear Effects of a Flexible Stern Seal Bag on Cobblestone Oscillations of an SES. (Dr.Ing. Thesis)
MTA-95-107	Solaas, Frøydis, MH	Analytical and Numerical Studies of Sloshing in Tanks. (Dr.Ing. Thesis)
MTA-95-108	Hellan, Øyvind, MK	Nonlinear Pushover and Cyclic Analyses in Ultimate Limit State Design and Reassessment of Tubular Steel Offshore Structures. (Dr.Ing. Thesis)
MTA-95-109	Hermundstad, Ole A., MK	Theoretical and Experimental Hydroelastic Analysis of High Speed Vessels. (Dr.Ing. Thesis)
MTA-96-110	Bratland, Anne K., MH	Wave-Current Interaction Effects on Large-Volume Bodies in Water of Finite Depth. (Dr.Ing. Thesis)
MTA-96-111	Herfjord, Kjell, MH	A Study of Two-dimensional Separated Flow by a Combination of the Finite Element Method and

		Navier-Stokes Equations. (Dr.Ing. Thesis)
MTA-96-112	Æsøy, Vilmar, MM	Hot Surface Assisted Compression Ignition in a Direct Injection Natural Gas Engine. (Dr.Ing. Thesis)
MTA-96-113	Eknes, Monika L., MK	Escalation Scenarios Initiated by Gas Explosions on Offshore Installations. (Dr.Ing. Thesis)
MTA-96-114	Erikstad, Stein O., MP	A Decision Support Model for Preliminary Ship Design. (Dr.Ing. Thesis)
MTA-96-115	Pedersen, Egil, MH	A Nautical Study of Towed Marine Seismic Streamer Cable Configurations. (Dr.Ing. Thesis)
MTA-97-116	Moksnes, Paul O., MM	Modelling Two-Phase Thermo-Fluid Systems Using Bond Graphs. (Dr.Ing. Thesis)
MTA-97-117	Halse, Karl H., MK	On Vortex Shedding and Prediction of Vortex-Induced Vibrations of Circular Cylinders. (Dr.Ing. Thesis)
MTA-97-118	Igland, Ragnar T., MK	Reliability Analysis of Pipelines during Laying, considering Ultimate Strength under Combined Loads. (Dr.Ing. Thesis)
MTA-97-119	Pedersen, Hans-P., MP	Levendefiskteknologi for fiskefartøy. (Dr.Ing. Thesis)
MTA-98-120	Vikestad, Kyrre, MK	Multi-Frequency Response of a Cylinder Subjected to Vortex Shedding and Support Motions. (Dr.Ing. Thesis)
MTA-98-121	Azadi, Mohammad R. E., MK	Analysis of Static and Dynamic Pile-Soil-Jacket Behaviour. (Dr.Ing. Thesis)
MTA-98-122	Ulltang, Terje, MP	A Communication Model for Product Information. (Dr.Ing. Thesis)
MTA-98-123	Torbergsen, Erik, MM	Impeller/Diffuser Interaction Forces in Centrifugal Pumps. (Dr.Ing. Thesis)
MTA-98-124	Hansen, Edmond, MH	A Discrete Element Model to Study Marginal Ice Zone Dynamics and the Behaviour of Vessels Moored in Broken Ice. (Dr.Ing. Thesis)
MTA-98-125	Videiro, Paulo M., MK	Reliability Based Design of Marine Structures. (Dr.Ing. Thesis)
MTA-99-126	Mainçon, Philippe, MK	Fatigue Reliability of Long Welds Application to Titanium Risers. (Dr.Ing. Thesis)
MTA-99-127	Haugen, Elin M., MH	Hydroelastic Analysis of Slamming on Stiffened Plates with Application to Catamaran Wetdecks. (Dr.Ing. Thesis)
MTA-99-128	Langhelle, Nina K., MK	Experimental Validation and Calibration of Nonlinear Finite Element Models for Use in Design of Aluminium Structures Exposed to Fire. (Dr.Ing. Thesis)
MTA-99-	Berstad, Are J., MK	Calculation of Fatigue Damage in Ship Structures.

129		(Dr.Ing. Thesis)
MTA-99-130	Andersen, Trond M., MM	Short Term Maintenance Planning. (Dr.Ing. Thesis)
MTA-99-131	Tveiten, Bård Wathne, MK	Fatigue Assessment of Welded Aluminium Ship Details. (Dr.Ing. Thesis)
MTA-99-132	Søreide, Fredrik, MP	Applications of underwater technology in deep water archaeology. Principles and practice. (Dr.Ing. Thesis)
MTA-99-133	Tønnessen, Rune, MH	A Finite Element Method Applied to Unsteady Viscous Flow Around 2D Blunt Bodies With Sharp Corners. (Dr.Ing. Thesis)
MTA-99-134	Elvekrok, Dag R., MP	Engineering Integration in Field Development Projects in the Norwegian Oil and Gas Industry. The Supplier Management of Norne. (Dr.Ing. Thesis)
MTA-99-135	Fagerholt, Kjetil, MP	Optimeringsbaserte Metoder for Ruteplanlegging innen skipsfart. (Dr.Ing. Thesis)
MTA-99-136	Bysveen, Marie, MM	Visualization in Two Directions on a Dynamic Combustion Rig for Studies of Fuel Quality. (Dr.Ing. Thesis)
MTA-2000-137	Storteig, Eskild, MM	Dynamic characteristics and leakage performance of liquid annular seals in centrifugal pumps. (Dr.Ing. Thesis)
MTA-2000-138	Sagli, Gro, MK	Model uncertainty and simplified estimates of long term extremes of hull girder loads in ships. (Dr.Ing. Thesis)
MTA-2000-139	Tronstad, Harald, MK	Nonlinear analysis and design of cable net structures like fishing gear based on the finite element method. (Dr.Ing. Thesis)
MTA-2000-140	Kroneberg, André, MP	Innovation in shipping by using scenarios. (Dr.Ing. Thesis)
MTA-2000-141	Haslum, Herbjørn Alf, MH	Simplified methods applied to nonlinear motion of spar platforms. (Dr.Ing. Thesis)
MTA-2001-142	Samdal, Ole Johan, MM	Modelling of Degradation Mechanisms and Stressor Interaction on Static Mechanical Equipment Residual Lifetime. (Dr.Ing. Thesis)
MTA-2001-143	Baarholm, Rolf Jarle, MH	Theoretical and experimental studies of wave impact underneath decks of offshore platforms. (Dr.Ing. Thesis)
MTA-2001-144	Wang, Lihua, MK	Probabilistic Analysis of Nonlinear Wave-induced Loads on Ships. (Dr.Ing. Thesis)
MTA-2001-145	Kristensen, Odd H. Holt, MK	Ultimate Capacity of Aluminium Plates under Multiple Loads, Considering HAZ Properties. (Dr.Ing. Thesis)
MTA-2001-146	Greco, Marilena, MH	A Two-Dimensional Study of Green-Water

		Loading. (Dr.Ing. Thesis)
MTA-2001-147	Heggelund, Svein E., MK	Calculation of Global Design Loads and Load Effects in Large High Speed Catamarans. (Dr.Ing. Thesis)
MTA-2001-148	Babalola, Olusegun T., MK	Fatigue Strength of Titanium Risers – Defect Sensitivity. (Dr.Ing. Thesis)
MTA-2001-149	Mohammed, Abuu K., MK	Nonlinear Shell Finite Elements for Ultimate Strength and Collapse Analysis of Ship Structures. (Dr.Ing. Thesis)
MTA-2002-150	Holmedal, Lars E., MH	Wave-current interactions in the vicinity of the sea bed. (Dr.Ing. Thesis)
MTA-2002-151	Rognebakke, Olav F., MH	Sloshing in rectangular tanks and interaction with ship motions. (Dr.Ing. Thesis)
MTA-2002-152	Lader, Pål Furset, MH	Geometry and Kinematics of Breaking Waves. (Dr.Ing. Thesis)
MTA-2002-153	Yang, Qinzheng, MH	Wash and wave resistance of ships in finite water depth. (Dr.Ing. Thesis)
MTA-2002-154	Melhus, Øyvin, MM	Utilization of VOC in Diesel Engines. Ignition and combustion of VOC released by crude oil tankers. (Dr.Ing. Thesis)
MTA-2002-155	Ronæss, Marit, MH	Wave Induced Motions of Two Ships Advancing on Parallel Course. (Dr.Ing. Thesis)
MTA-2002-156	Økland, Ole D., MK	Numerical and experimental investigation of whipping in twin hull vessels exposed to severe wet deck slamming. (Dr.Ing. Thesis)
MTA-2002-157	Ge, Chunhua, MK	Global Hydroelastic Response of Catamarans due to Wet Deck Slamming. (Dr.Ing. Thesis)
MTA-2002-158	Byklum, Eirik, MK	Nonlinear Shell Finite Elements for Ultimate Strength and Collapse Analysis of Ship Structures. (Dr.Ing. Thesis)
IMT-2003-1	Chen, Haibo, MK	Probabilistic Evaluation of FPSO-Tanker Collision in Tandem Offloading Operation. (Dr.Ing. Thesis)
IMT-2003-2	Skaugset, Kjetil Bjørn, MK	On the Suppression of Vortex Induced Vibrations of Circular Cylinders by Radial Water Jets. (Dr.Ing. Thesis)
IMT-2003-3	Chezhian, Muthu	Three-Dimensional Analysis of Slamming. (Dr.Ing. Thesis)
IMT-2003-4	Buhaug, Øyvind	Deposit Formation on Cylinder Liner Surfaces in Medium Speed Engines. (Dr.Ing. Thesis)
IMT-2003-5	Tregde, Vidar	Aspects of Ship Design: Optimization of Aft Hull with Inverse Geometry Design. (Dr.Ing. Thesis)
IMT-	Wist, Hanne Therese	Statistical Properties of Successive Ocean Wave

2003-6		Parameters. (Dr.Ing. Thesis)
IMT-2004-7	Ransau, Samuel	Numerical Methods for Flows with Evolving Interfaces. (Dr.Ing. Thesis)
IMT-2004-8	Soma, Torkel	Blue-Chip or Sub-Standard. A data interrogation approach of identity safety characteristics of shipping organization. (Dr.Ing. Thesis)
IMT-2004-9	Ersdal, Svein	An experimental study of hydrodynamic forces on cylinders and cables in near axial flow. (Dr.Ing. Thesis)
IMT-2005-10	Brodtkorb, Per Andreas	The Probability of Occurrence of Dangerous Wave Situations at Sea. (Dr.Ing. Thesis)
IMT-2005-11	Yttervik, Rune	Ocean current variability in relation to offshore engineering. (Dr.Ing. Thesis)
IMT-2005-12	Fredheim, Arne	Current Forces on Net-Structures. (Dr.Ing. Thesis)
IMT-2005-13	Heggernes, Kjetil	Flow around marine structures. (Dr.Ing. Thesis
IMT-2005-14	Fouques, Sebastien	Lagrangian Modelling of Ocean Surface Waves and Synthetic Aperture Radar Wave Measurements. (Dr.Ing. Thesis)
IMT-2006-15	Holm, Håvard	Numerical calculation of viscous free surface flow around marine structures. (Dr.Ing. Thesis)
IMT-2006-16	Bjørheim, Lars G.	Failure Assessment of Long Through Thickness Fatigue Cracks in Ship Hulls. (Dr.Ing. Thesis)
IMT-2006-17	Hansson, Lisbeth	Safety Management for Prevention of Occupational Accidents. (Dr.Ing. Thesis)
IMT-2006-18	Zhu, Xinying	Application of the CIP Method to Strongly Nonlinear Wave-Body Interaction Problems. (Dr.Ing. Thesis)
IMT-2006-19	Reite, Karl Johan	Modelling and Control of Trawl Systems. (Dr.Ing. Thesis)
IMT-2006-20	Smogeli, Øyvind Notland	Control of Marine Propellers. From Normal to Extreme Conditions. (Dr.Ing. Thesis)
IMT-2007-21	Storhaug, Gaute	Experimental Investigation of Wave Induced Vibrations and Their Effect on the Fatigue Loading of Ships. (Dr.Ing. Thesis)
IMT-2007-22	Sun, Hui	A Boundary Element Method Applied to Strongly Nonlinear Wave-Body Interaction Problems. (PhD Thesis, CeSOS)
IMT-2007-23	Rustad, Anne Marthine	Modelling and Control of Top Tensioned Risers. (PhD Thesis, CeSOS)
IMT-2007-24	Johansen, Vegar	Modelling flexible slender system for real-time simulations and control applications
IMT-2007-25	Wroldsen, Anders Sunde	Modelling and control of tensegrity structures.

		(PhD Thesis, CeSOS)
IMT-2007-26	Aronsen, Kristoffer Høye	An experimental investigation of in-line and combined inline and cross flow vortex induced vibrations. (Dr. avhandling, IMT)
IMT-2007-27	Gao, Zhen	Stochastic Response Analysis of Mooring Systems with Emphasis on Frequency-domain Analysis of Fatigue due to Wide-band Response Processes (PhD Thesis, CeSOS)
IMT-2007-28	Thorstensen, Tom Anders	Lifetime Profit Modelling of Ageing Systems Utilizing Information about Technical Condition. (Dr.ing. thesis, IMT)
IMT-2008-29	Refsnes, Jon Erling Gorset	Nonlinear Model-Based Control of Slender Body AUVs (PhD Thesis, IMT)
IMT-2008-30	Berntsen, Per Ivar B.	Structural Reliability Based Position Mooring. (PhD-Thesis, IMT)
IMT-2008-31	Ye, Naiquan	Fatigue Assessment of Aluminium Welded Box-stiffener Joints in Ships (Dr.ing. thesis, IMT)
IMT-2008-32	Radan, Damir	Integrated Control of Marine Electrical Power Systems. (PhD-Thesis, IMT)
IMT-2008-33	Thomassen, Paul	Methods for Dynamic Response Analysis and Fatigue Life Estimation of Floating Fish Cages. (Dr.ing. thesis, IMT)
IMT-2008-34	Pákozdi, Csaba	A Smoothed Particle Hydrodynamics Study of Two-dimensional Nonlinear Sloshing in Rectangular Tanks. (Dr.ing.thesis, IMT/ CeSOS)
IMT-2007-35	Grytøyr, Guttorm	A Higher-Order Boundary Element Method and Applications to Marine Hydrodynamics. (Dr.ing.thesis, IMT)
IMT-2008-36	Drummen, Ingo	Experimental and Numerical Investigation of Nonlinear Wave-Induced Load Effects in Containerships considering Hydroelasticity. (PhD thesis, CeSOS)
IMT-2008-37	Skejic, Renato	Maneuvering and Seakeeping of a Singel Ship and of Two Ships in Interaction. (PhD-Thesis, CeSOS)
IMT-2008-38	Harlem, Alf	An Age-Based Replacement Model for Repairable Systems with Attention to High-Speed Marine Diesel Engines. (PhD-Thesis, IMT)
IMT-2008-39	Alsos, Hagbart S.	Ship Grounding. Analysis of Ductile Fracture, Bottom Damage and Hull Girder Response. (PhD-thesis, IMT)
IMT-2008-40	Graczyk, Mateusz	Experimental Investigation of Sloshing Loading and Load Effects in Membrane LNG Tanks Subjected to Random Excitation. (PhD-thesis, CeSOS)
IMT-2008-41	Taghipour, Reza	Efficient Prediction of Dynamic Response for Flexible amd Multi-body Marine Structures. (PhD-

		thesis, CeSOS)
IMT-2008-42	Ruth, Eivind	Propulsion control and thrust allocation on marine vessels. (PhD thesis, CeSOS)
IMT-2008-43	Nystad, Bent Helge	Technical Condition Indexes and Remaining Useful Life of Aggregated Systems. PhD thesis, IMT
IMT-2008-44	Soni, Prashant Kumar	Hydrodynamic Coefficients for Vortex Induced Vibrations of Flexible Beams, PhD thesis, CeSOS
IMT-2009-45	Amlashi, Hadi K.K.	Ultimate Strength and Reliability-based Design of Ship Hulls with Emphasis on Combined Global and Local Loads. PhD Thesis, IMT
IMT-2009-46	Pedersen, Tom Arne	Bond Graph Modelling of Marine Power Systems. PhD Thesis, IMT
IMT-2009-47	Kristiansen, Trygve	Two-Dimensional Numerical and Experimental Studies of Piston-Mode Resonance. PhD-Thesis, CeSOS
IMT-2009-48	Ong, Muk Chen	Applications of a Standard High Reynolds Number Model and a Stochastic Scour Prediction Model for Marine Structures. PhD-thesis, IMT
IMT-2009-49	Hong, Lin	Simplified Analysis and Design of Ships subjected to Collision and Grounding. PhD-thesis, IMT
IMT-2009-50	Koushan, Kamran	Vortex Induced Vibrations of Free Span Pipelines, PhD thesis, IMT
IMT-2009-51	Korsvik, Jarl Eirik	Heuristic Methods for Ship Routing and Scheduling. PhD-thesis, IMT
IMT-2009-52	Lee, Jihoon	Experimental Investigation and Numerical in Analyzing the Ocean Current Displacement of Longlines. Ph.d.-Thesis, IMT.
IMT-2009-53	Vestbøstad, Tone Gran	A Numerical Study of Wave-in-Deck Impact usin a Two-Dimensional Constrained Interpolation Profile Method, Ph.d.thesis, CeSOS.
IMT-2009-54	Bruun, Kristine	Bond Graph Modelling of Fuel Cells for Marine Power Plants. Ph.d.-thesis, IMT
IMT 2009-55	Holstad, Anders	Numerical Investigation of Turbulence in a Sekwed Three-Dimensional Channel Flow, Ph.d.-thesis, IMT.
IMT 2009-56	Ayala-Uraga, Efren	Reliability-Based Assessment of Deteriorating Ship-shaped Offshore Structures, Ph.d.-thesis, IMT
IMT 2009-57	Kong, Xiangjun	A Numerical Study of a Damaged Ship in Beam Sea Waves. Ph.d.-thesis, IMT/CeSOS.
IMT 2010-58	Kristiansen, David	Wave Induced Effects on Floaters of Aquaculture Plants, Ph.d.-thesis, CeSOS.

IMT 2010-59	Ludvigsen, Martin	An ROV-Toolbox for Optical and Acoustic Scientific Seabed Investigation. Ph.d.-thesis IMT.
IMT 2010-60	Hals, Jørgen	Modelling and Phase Control of Wave-Energy Converters. Ph.d.thesis, CeSOS.
IMT 2010- 61	Shu, Zhi	Uncertainty Assessment of Wave Loads and Ultimate Strength of Tankers and Bulk Carriers in a Reliability Framework. Ph.d. Thesis, IMT/ CeSOS
IMT 2010-62	Shao, Yanlin	Numerical Potential-Flow Studies on Weakly-Nonlinear Wave-Body Interactions with/without Small Forward Speed, Ph.d.thesis,CeSOS.
IMT 2010-63	Califano, Andrea	Dynamic Loads on Marine Propellers due to Intermittent Ventilation. Ph.d.thesis, IMT.
IMT 2010-64	El Khoury, George	Numerical Simulations of Massively Separated Turbulent Flows, Ph.d.-thesis, IMT
IMT 2010-65	Seim, Knut Sponheim	Mixing Process in Dense Overflows with Emphasis on the Faroe Bank Channel Overflow. Ph.d.thesis, IMT
IMT 2010-66	Jia, Huirong	Structural Analysis of Intect and Damaged Ships in a Collission Risk Analysis Perspective. Ph.d.thesis CeSoS.
IMT 2010-67	Jiao, Linlin	Wave-Induced Effects on a Pontoon-type Very Large Floating Structures (VLFS). Ph.D.-thesis, CeSOS.
IMT 2010-68	Abrahamsen, Bjørn Christian	Sloshing Induced Tank Roof with Entrapped Air Pocket. Ph.d.thesis, CeSOS.
IMT 2011-69	Karimirad, Madjid	Stochastic Dynamic Response Analysis of Spar-Type Wind Turbines with Catenary or Taut Mooring Systems. Ph.d.-thesis, CeSOS.
IMT - 2011-70	Erlend Meland	Condition Monitoring of Safety Critical Valves. Ph.d.-thesis, IMT.
IMT – 2011-71	Yang, Limin	Stochastic Dynamic System Analysis of Wave Energy Converter with Hydraulic Power Take-Off, with Particular Reference to Wear Damage Analysis, Ph.d. Thesis, CeSOS.
IMT – 2011-72	Visscher, Jan	Application of Particla Image Velocimetry on Turbulent Marine Flows, Ph.d.Thesis, IMT.
IMT – 2011-73	Su, Biao	Numerical Predictions of Global and Local Ice Loads on Ships. Ph.d.Thesis, CeSOS.
IMT – 2011-74	Liu, Zhenhui	Analytical and Numerical Analysis of Iceberg Collision with Ship Structures. Ph.d.Thesis, IMT.
IMT – 2011-75	Aarsæther, Karl Gunnar	Modeling and Analysis of Ship Traffic by Observation and Numerical Simulation. Ph.d.Thesis, IMT.

Imt – 2011-76	Wu, Jie	Hydrodynamic Force Identification from Stochastic Vortex Induced Vibration Experiments with Slender Beams. Ph.d.Thesis, IMT.
Imt – 2011-77	Amini, Hamid	Azimuth Propulsors in Off-design Conditions. Ph.d.Thesis, IMT.
IMT – 2011-78	Nguyen, Tan-Hoi	Toward a System of Real-Time Prediction and Monitoring of Bottom Damage Conditions During Ship Grounding. Ph.d.thesis, IMT.
IMT-2011-79	Tavakoli, Mohammad T.	Assessment of Oil Spill in Ship Collision and Grounding, Ph.d.thesis, IMT.
IMT-2011-80	Guo, Bingjie	Numerical and Experimental Investigation of Added Resistance in Waves. Ph.d.Thesis, IMT.
IMT-2011-81	Chen, Qiaofeng	Ultimate Strength of Aluminium Panels, considering HAZ Effects, IMT
IMT-2012-82	Kota, Ravikiran S.	Wave Loads on Decks of Offshore Structures in Random Seas, CeSOS.
IMT-2012-83	Sten, Ronny	Dynamic Simulation of Deep Water Drilling Risers with Heave Compensating System, IMT.
IMT-2012-84	Berle, Øyvind	Risk and resilience in global maritime supply chains, IMT.
IMT-2012-85	Fang, Shaoji	Fault Tolerant Position Mooring Control Based on Structural Reliability, CeSOS.
IMT-2012-86	You, Jikun	Numerical studies on wave forces and moored ship motions in intermediate and shallow water, CeSOS.
IMT-2012-87	Xiang ,Xu	Maneuvering of two interacting ships in waves, CeSOS
IMT-2012-88	Dong, Wenbin	Time-domain fatigue response and reliability analysis of offshore wind turbines with emphasis on welded tubular joints and gear components, CeSOS
IMT-2012-89	Zhu, Suji	Investigation of Wave-Induced Nonlinear Load Effects in Open Ships considering Hull Girder Vibrations in Bending and Torsion, CeSOS
IMT-2012-90	Zhou, Li	Numerical and Experimental Investigation of Station-keeping in Level Ice, CeSOS
IMT-2012-91	Ushakov, Sergey	Particulate matter emission characteristics from diesel enignes operating on conventional and alternative marine fuels, IMT
IMT-2013-1	Yin, Decao	Experimental and Numerical Analysis of Combined In-line and Cross-flow Vortex Induced Vibrations, CeSOS

IMT-2013-2	Kurniawan, Adi	Modelling and geometry optimisation of wave energy converters, CeSOS
IMT-2013-3	Al Ryati, Nabil	Technical condition indexes doe auxiliary marine diesel engines, IMT
IMT-2013-4	Firoozkoohi, Reza	Experimental, numerical and analytical investigation of the effect of screens on sloshing, CeSOS
IMT-2013-5	Ommani, Babak	Potential-Flow Predictions of a Semi-Displacement Vessel Including Applications to Calm Water Broaching, CeSOS
IMT-2013-6	Xing, Yihan	Modelling and analysis of the gearbox in a floating spar-type wind turbine, CeSOS
IMT-7-2013	Balland, Océane	Optimization models for reducing air emissions from ships, IMT
IMT-8-2013	Yang, Dan	Transitional wake flow behind an inclined flat plate-----Computation and analysis, IMT
IMT-9-2013	Abdillah, Suyuthi	Prediction of Extreme Loads and Fatigue Damage for a Ship Hull due to Ice Action, IMT
IMT-10-2013	Ramìrez, Pedro Agustìn Pèrez	Ageing management and life extension of technical systems- Concepts and methods applied to oil and gas facilities, IMT
IMT-11-2013	Chuang, Zhenju	Experimental and Numerical Investigation of Speed Loss due to Seakeeping and Maneuvering. IMT
IMT-12-2013	Etemaddar, Mahmoud	Load and Response Analysis of Wind Turbines under Atmospheric Icing and Controller System Faults with Emphasis on Spar Type Floating Wind Turbines, IMT
IMT-13-2013	Lindstad, Haakon	Strategies and measures for reducing maritime CO2 emissons, IMT
IMT-14-2013	Haris, Sabril	Damage interaction analysis of ship collisions, IMT
IMT-15-2013	Shainee, Mohamed	Conceptual Design, Numerical and Experimental Investigation of a SPM Cage Concept for Offshore Mariculture, IMT
IMT-16-2013	Gansel, Lars	Flow past porous cylinders and effects of biofouling and fish behavior on the flow in and around Atlantic salmon net cages, IMT
IMT-17-2013	Gaspar, Henrique	Handling Aspects of Complexity in Conceptual Ship Design, IMT
IMT-18-2013	Thys, Maxime	Theoretical and Experimental Investigation of a Free Running Fishing Vessel at Small Frequency of Encounter, CeSOS
IMT-19-2013	Aglen, Ida	VIV in Free Spanning Pipelines, CeSOS

IMT-1-2014	Song, An	Theoretical and experimental studies of wave diffraction and radiation loads on a horizontally submerged perforated plate, CeSOS
IMT-2-2014	Rogne, Øyvind Ygre	Numerical and Experimental Investigation of a Hinged 5-body Wave Energy Converter, CeSOS
IMT-3-2014	Dai, Lijuan	Safe and efficient operation and maintenance of offshore wind farms ,IMT
IMT-4-2014	Bachynski, Erin Elizabeth	Design and Dynamic Analysis of Tension Leg Platform Wind Turbines, CeSOS
IMT-5-2014	Wang, Jingbo	Water Entry of Freefall Wedged – Wedge motions and Cavity Dynamics, CeSOS
IMT-6-2014	Kim, Ekaterina	Experimental and numerical studies related to the coupled behavior of ice mass and steel structures during accidental collisions, IMT
IMT-7-2014	Tan, Xiang	Numerical investigation of ship's continuous- mode icebreaking in leverl ice, CeSOS
IMT-8-2014	Muliawan, Made Jaya	Design and Analysis of Combined Floating Wave and Wind Power Facilities, with Emphasis on Extreme Load Effects of the Mooring System, CeSOS
IMT-9-2014	Jiang, Zhiyu	Long-term response analysis of wind turbines with an emphasis on fault and shutdown conditions, IMT
IMT-10-2014	Dukan, Fredrik	ROV Motion Control Systems, IMT
IMT-11-2014	Grimsmo, Nils I.	Dynamic simulations of hydraulic cylinder for heave compensation of deep water drilling risers, IMT
IMT-12-2014	Kvittem, Marit I.	Modelling and response analysis for fatigue design of a semisubmersible wind turbine, CeSOS
IMT-13-2014	Akhtar, Juned	The Effects of Human Fatigue on Risk at Sea, IMT
IMT-14-2014	Syahroni, Nur	Fatigue Assessment of Welded Joints Taking into Account Effects of Residual Stress, IMT
IMT-1-2015	Bøckmann, Eirik	Wave Propulsion of ships, IMT
IMT-2-2015	Wang, Kai	Modelling and dynamic analysis of a semi-submersible floating vertical axis wind turbine, CeSOS
IMT-3-2015	Fredriksen, Arnt Gunvald	A numerical and experimental study of a two-dimensional body with moonpool in waves and current, CeSOS
IMT-4-2015	Jose Patricio Gallardo Canabes	Numerical studies of viscous flow around bluff bodies, IMT

IMT-5-2015	Vegard Longva	Formulation and application of finite element techniques for slender marine structures subjected to contact interactions, IMT
IMT-6-2015	Jacobus De Vaal	Aerodynamic modelling of floating wind turbines, CeSOS
IMT-7-2015	Fachri Nasution	Fatigue Performance of Copper Power Conductors, IMT
IMT-8-2015	Oleh I Karpa	Development of bivariate extreme value distributions for applications in marine technology,CeSOS
IMT-9-2015	Daniel de Almeida Fernandes	An output feedback motion control system for ROVs, AMOS
IMT-10-2015	Bo Zhao	Particle Filter for Fault Diagnosis: Application to Dynamic Positioning Vessel and Underwater Robotics, CeSOS
IMT-11-2015	Wenting Zhu	Impact of emission allocation in maritime transportation, IMT
IMT-12-2015	Amir Rasekhi Nejad	Dynamic Analysis and Design of Gearboxes in Offshore Wind Turbines in a Structural Reliability Perspective, CeSOS
IMT-13-2015	Arturo Jesùs Ortega Malca	Dynamic Response of Flexibles Risers due to Unsteady Slug Flow, CeSOS
IMT-14-2015	Dagfinn Husjord	Guidance and decision-support system for safe navigation of ships operating in close proximity, IMT
IMT-15-2015	Anirban Bhattacharyya	Ducted Propellers: Behaviour in Waves and Scale Effects, IMT
IMT-16-2015	Qin Zhang	Image Processing for Ice Parameter Identification in Ice Management, IMT
IMT-1-2016	Vincentius Rumawas	Human Factors in Ship Design and Operation: An Experiential Learning, IMT
IMT-2-2016	Martin Storheim	Structural response in ship-platform and ship-ice collisions, IMT
IMT-3-2016	Mia Abrahamsen Prsic	Numerical Simulations of the Flow around single and Tandem Circular Cylinders Close to a Plane Wall, IMT
IMT-4-2016	Tufan Arslan	Large-eddy simulations of cross-flow around ship sections, IMT

IMT-5-2016	Pierre Yves-Henry	Parametrisation of aquatic vegetation in hydraulic and coastal research,IMT
IMT-6-2016	Lin Li	Dynamic Analysis of the Instalation of Monopiles for Offshore Wind Turbines, CeSOS
IMT-7-2016	Øivind Kåre Kjerstad	Dynamic Positioning of Marine Vessels in Ice, IMT
IMT-8-2016	Xiaopeng Wu	Numerical Analysis of Anchor Handling and Fish Trawling Operations in a Safety Perspective, CeSOS
IMT-9-2016	Zhengshun Cheng	Integrated Dynamic Analysis of Floating Vertical Axis Wind Turbines, CeSOS
IMT-10-2016	Ling Wan	Experimental and Numerical Study of a Combined Offshore Wind and Wave Energy Converter Concept
IMT-11-2016	Wei Chai	Stochastic dynamic analysis and reliability evaluation of the roll motion for ships in random seas, CeSOS
IMT-12-2016	Øyvind Selnes Patricksson	Decision support for conceptual ship design with focus on a changing life cycle and future uncertainty, IMT
IMT-13-2016	Mats Jørgen Thorsen	Time domain analysis of vortex-induced vibrations, IMT
IMT-14-2016	Edgar McGuinness	Safety in the Norwegian Fishing Fleet – Analysis and measures for improvement, IMT
IMT-15-2016	Sepideh Jafarzadeh	Energy effiency and emission abatement in the fishing fleet, IMT
IMT-16-2016	Wilson Ivan Guachamin Acero	Assessment of marine operations for offshore wind turbine installation with emphasis on response-based operational limits, IMT
IMT-17-2016	Mauro Candeloro	Tools and Methods for Autonomous Operations on Seabed and Water Coumn using Underwater Vehicles, IMT
IMT-18-2016	Valentin Chabaud	Real-Time Hybrid Model Testing of Floating Wind Tubines, IMT
IMT-1-2017	Mohammad Saud Afzal	Three-dimensional streaming in a sea bed boundary layer
IMT-2-2017	Peng Li	A Theoretical and Experimental Study of Wave-induced Hydroelastic Response of a Circular Floating Collar
IMT-3-2017	Martin Bergström	A simulation-based design method for arctic maritime transport systems

IMT-4-2017	Bhushan Taskar	The effect of waves on marine propellers and propulsion
IMT-5-2017	Mohsen Bardestani	A two-dimensional numerical and experimental study of a floater with net and sinker tube in waves and current
IMT-6-2017	Fatemeh Hoseini Dadmarzi	Direct Numerical Simualtion of turbulent wakes behind different plate configurations
IMT-7-2017	Michel R. Miyazaki	Modeling and control of hybrid marine power plants
IMT-8-2017	Giri Rajasekhar Gunnu	Safety and effiency enhancement of anchor handling operations with particular emphasis on the stability of anchor handling vessels
IMT-9-2017	Kevin Koosup Yum	Transient Performance and Emissions of a Turbocharged Diesel Engine for Marine Power Plants
IMT-10-2017	Zhaolong Yu	Hydrodynamic and structural aspects of ship collisions
IMT-11-2017	Martin Hassel	Risk Analysis and Modelling of Allisions between Passing Vessels and Offshore Installations
IMT-12-2017	Astrid H. Brodtkorb	Hybrid Control of Marine Vessels – Dynamic Positioning in Varying Conditions
IMT-13-2017	Kjersti Bruserud	Simultaneous stochastic model of waves and current for prediction of structural design loads
IMT-14-2017	Finn-Idar Grøtta Giske	Long-Term Extreme Response Analysis of Marine Structures Using Inverse Reliability Methods
IMT-15-2017	Stian Skjong	Modeling and Simulation of Maritime Systems and Operations for Virtual Prototyping using co-Simulations
IMT-1-2018	Yingguang Chu	Virtual Prototyping for Marine Crane Design and Operations
IMT-2-2018	Sergey Gavrilin	Validation of ship manoeuvring simulation models
IMT-3-2018	Jeevith Hegde	Tools and methods to manage risk in autonomous subsea inspection,maintenance and repair operations
IMT-4-2018	Ida M. Strand	Sea Loads on Closed Flexible Fish Cages
IMT-5-2018	Erlend Kvinge Jørgensen	Navigation and Control of Underwater Robotic Vehicles

IMT-6-2018	Bård Stovner	Aided Intertial Navigation of Underwater Vehicles
IMT-7-2018	Erlend Liavåg Grotle	Thermodynamic Response Enhanced by Sloshing in Marine LNG Fuel Tanks
IMT-8-2018	Børge Rokseth	Safety and Verification of Advanced Maritime Vessels
IMT-9-2018	Jan Vidar Ulveseter	Advances in Semi-Empirical Time Domain Modelling of Vortex-Induced Vibrations
IMT-10-2018	Chenyu Luan	Design and analysis for a steel braceless semi-submersible hull for supporting a 5-MW horizontal axis wind turbine
IMT-11-2018	Carl Fredrik Rehn	Ship Design under Uncertainty
IMT-12-2018	Øyvind Ødegård	Towards Autonomous Operations and Systems in Marine Archaeology
IMT-13-2018	Stein Melvær Nornes	Guidance and Control of Marine Robotics for Ocean Mapping and Monitoring
IMT-14-2018	Petter Norgren	Autonomous Underwater Vehicles in Arctic Marine Operations: Arctic marine research and ice monitoring
IMT-15-2018	Minjoo Choi	Modular Adaptable Ship Design for Handling Uncertainty in the Future Operating Context
MT-16-2018	Ole Alexander Eidsvik	Dynamics of Remotely Operated Underwater Vehicle Systems
IMT-17-2018	Mahdi Ghane	Fault Diagnosis of Floating Wind Turbine Drivetrain- Methodologies and Applications
IMT-18-2018	Christoph Alexander Thieme	Risk Analysis and Modelling of Autonomous Marine Systems
IMT-19-2018	Yugao Shen	Operational limits for floating-collar fish farms in waves and current, without and with well-boat presence
IMT-20-2018	Tianjiao Dai	Investigations of Shear Interaction and Stresses in Flexible Pipes and Umbilicals
IMT-21-2018	Sigurd Solheim Pettersen	Resilience by Latent Capabilities in Marine Systems
IMT-22-2018	Thomas Sauder	Fidelity of Cyber-physical Empirical Methods. Application to the Active Truncation of Slender Marine Structures
IMT-23-2018	Jan-Tore Horn	Statistical and Modelling Uncertainties in the Design of Offshore Wind Turbines

IMT-24-2018	Anna Swider	Data Mining Methods for the Analysis of Power Systems of Vessels
IMT-1-2019	Zhao He	Hydrodynamic study of a moored fish farming cage with fish influence
IMT-2-2019	Isar Ghamari	Numerical and Experimental Study on the Ship Parametric Roll Resonance and the Effect of Anti-Roll Tank
IMT-3-2019	Håkon Strandenes	Turbulent Flow Simulations at Higher Reynolds Numbers
IMT-4-2019	Siri Mariane Holen	Safety in Norwegian Fish Farming – Concepts and Methods for Improvement
IMT-5-2019	Ping Fu	Reliability Analysis of Wake-Induced Riser Collision
IMT-6-2019	Vladimir Krivopolianskii	Experimental Investigation of Injection and Combustion Processes in Marine Gas Engines using Constant Volume Rig
IMT-7-2019	Anna Maria Kozlowska	Hydrodynamic Loads on Marine Propellers Subject to Ventilation and out of Water Condition.
IMT-8-2019	Hans-Martin Heyn	Motion Sensing on Vessels Operating in Sea Ice: A Local Ice Monitoring System for Transit and Stationkeeping Operations under the Influence of Sea Ice
IMT-9-2019|	Stefan Vilsen	Method for Real-Time Hybrid Model Testing of Ocean Structures – Case on Slender Marine Systems
IMT-10-2019	Finn-Christian W. Hanssen	Non-Linear Wave-Body Interaction in Severe Waves
IMT-11-2019	Trygve Olav Fossum	Adaptive Sampling for Marine Robotics
IMT-12-2019	Jørgen Bremnes Nielsen	Modeling and Simulation for Design Evaluation
IMT-13-2019	Yuna Zhao	Numerical modelling and dyncamic analysis of offshore wind turbine blade installation
IMT-14-2019	Daniela Myland	Experimental and Theoretical Investigations on the Ship Resistance in Level Ice
IMT-15-2019	Zhengru Ren	Advanced control algorithms to support automated offshore wind turbine installation
IMT-16-2019	Drazen Polic	Ice-propeller impact analysis using an inverse propulsion machinery simulation approach
IMT-17-2019	Endre Sandvik	Sea passage scenario simulation for ship system performance evaluation

IMT-18-2019	Loup Suja-Thauvin	Response of Monopile Wind Turbines to Higher Order Wave Loads
IMT-19-2019	Emil Smilden	Structural control of offshore wind turbines – Increasing the role of control design in offshore wind farm development
IMT-20-2019	Aleksandar-Sasa Milakovic	On equivalent ice thickness and machine learning in ship ice transit simulations
IMT-1-2020	Amrit Shankar Verma	Modelling, Analysis and Response-based Operability Assessment of Offshore Wind Turbine Blade Installation with Emphasis on Impact Damages
IMT-2-2020	Bent Oddvar Arnesen Haugaløkken	Autonomous Technology for Inspection, Maintenance and Repair Operations in the Norwegian Aquaculture
IMT-3-2020	Seongpil Cho	Model-based fault detection and diagnosis of a blade pitch system in floating wind turbines
IMT-4-2020	Jose Jorge Garcia Agis	Effectiveness in Decision-Making in Ship Design under Uncertainty
IMT-5-2020	Thomas H. Viuff	Uncertainty assessment of wave-and current-induced global response of floating bridges
IMT-6-2020	Fredrik Mentzoni	Hydrodynamic Loads on Complex Structures in the Wave Zone
IMT-7-2020	Senthuran Ravinthrakumar	Numerical and Experimental Studies of Resonant Flow in Moonpools in Operational Conditions
IMT-8-2020	Stian Skaalvik Sandøy	Acoustic-based Probabilistic Localization and Mapping using Unmanned Underwater Vehicles for Aquaculture Operations
IMT-9-2020	Kun Xu	Design and Analysis of Mooring Systems for Semi-submersible Floating Wind Turbines in Shallow Water